Hemodynamics in abdominal aorta aneurysms

By Richard J. Lozowy

A Thesis submitted to the Faculty of Graduate Studies of

The University of Manitoba in Partial Fulfillment of the

Requirements for the Degree of Doctor of Philosophy

Department of Mechanical Engineering

The University of Manitoba, Winnipeg, Manitoba

Acknowledgement

I would like to express my sincere gratitude to my thesis advisors, Professor David C. S. Kuhn and Professor April J. Boyd for the advise and support over the course of this project. Their comments were considerable help during this work. I would also like to acknowledge financial support provided by the University Medical Group, Department of Surgery, University of Manitoba and high performance computer resources provided by Compute Canada WestGrid. My gratitude also goes to the members of my Ph.D. committee, Professor Bing-Chen Wang and Professor Jason Morrison for their useful suggestions during this project and for reviewing my thesis.

I would like to also express my appreciation to my friends and colleagues that I worked with in the computational thermofluids research lab. Last, but definitely not least, my appreciation goes to my parents and my friend Barsha for their support during the graduate degree.

Abstract

This thesis presents results from numerical simulations of pulsatile fluid flow in canonical channel geometry and patient-specific abdominal aortic aneurysms (AAA). An AAA is a dilatation of the aortic segment between the renal arteries and the iliac bifurcation. The continuing expansion of an AAA weakens the wall and potentially leads to rupture. Intraluminal thrombus (ILT) deposition is the coagulation of platelets and often accumulates along the wall in AAA. The presence of ILT may decrease the flow of oxygen to the wall and the region of the AAA with ILT could be more susceptible to further expansion or rupture. Knowledge of AAA shapes that cause adverse hemodynamics could be used to establish criteria to help determine when to operate on a particular AAA to prevent rupture.

It was determined that some AAA shapes experience non-disturbed hemodynamics that do not significantly deviate from normal-sized aorta. For other AAA shapes a turbulent jet forms distal to the aneurysms neck and impinges against the AAA wall. It was found that at the location the jet impinges the wall was devoid of ILT and away from this location ILT often accumulated. It was suspected that the high wall-tangent shearing force from the impact of flow vortexes prevents attachment of cellular material to the wall. Although impingement prevents ILT, in all cases the AAA was found to be expanding in the direction

the neck angled the flow vortexes and it was reasoned that the wall-normal pressure force from vortex impact causes the expansion.

The triple decomposition method is used to segment blood flow into its periodic and turbulent components. Another segmentation method, dynamic mode decomposition (DMD) is used to segment blood flow into modes oscillating at specific frequencies. A low-order representation of the velocity field was then reconstructed using only the modes oscillating at the pulse frequency. This procedure removes both the higher-frequency turbulent and periodic oscillations from the velocity field. The resulting reconstruction shows a simplified representation of the blood flow dynamics in the AAA, such that it consists of a single large-scale vortex.

Contents

List of Figures

List of Tables

List of Symbols

Abbreviations

AAA abdominal aortic aneurysm

APG adverse pressure gradient

CFD computational fluid dynamics

CFL Courant-Friedrichs-Lewy number

CTA computed tomography angiography

DMD dynamic mode decomposition

DNS direct numerical simulation

FPG favorable pressure gradient

OSI oscillatory shear index

P.D.F. probability density function

PISO pressure-implicit with splitting of operators

rAAA ruptured abdominal aortic aneurysm

r.m.s. root mean square

sPOD snaptshot proper orthogonal decomposition

SVD singular value decomposition

TAWSS time-averaged wall shear stress

TKE turbulent kinetic energy

transWSS transverse wall shear stress

WSS wall shear stress

Dimensionless numbers

β oscillating-to-mean flow rate ratio

Re_b bulk Reynolds number

Re_τ friction Reynolds number

Wo Womersley number

Mathematical functions

arg complex argument

cos cosine

cosh hyperbolic cosine

exp exponential

log natural logarithm

i complex number

$\Im$ imaginary component of complex number

Jo bessel function zero

$\Re$ real component of complex number

sin sine

tan tangent

Greek letters

$\mathbf{\Phi}$ DMD mode matrix

$\boldsymbol{\phi}$ DMD mode vector

$\mathbf{\Psi}$ snapshot matrix

$\mathbf{\Psi'}$ snapshot matrix shifted forward in time

$\boldsymbol{\psi}$ snapshot vector

η Kolmogorov length scale

ϵ dissipation of TKE

$\boldsymbol{\kappa}$ von Karman constant

$\boldsymbol{\tau}_w$ wall shear stress vector

τ_w	wall shear stress scalar
δ	viscous length scale
μ	dynamic viscosity
ν	kinematic viscosity
ν_t	eddy viscosity
ω	angular frequency
$\mathbf{\Omega}$	rotation-rate tensor
ρ	density
ϕ	phase lag
φ	phase position
Π_k	viscous diffusion of TKE
α	DMD growth rate
λ	DMD ritz value
$\mathbf{\Lambda}$	eigenvalues of $\mathbf{C}$
λ_2	lambda$_2$-criterion
Δt	time-step
$\mathbf{\Sigma}$	singular value matrix

Matrix and vector operations

diag() diagonal matrix

$\mathbf{A}^{\mathrm{T}}$ transpose of a matrix

$\mathbf{A}^{-1}$ inverse of a matrix

$\mathbf{A}^{\dagger}$ Moore-Penrose pseudoinverse of a matrix

$\mathbf{A}^{*}$ complex-conjugate-transpose of a matrix

$\boldsymbol{a} : \boldsymbol{a}$ double inner product of two vectors or tensors

$\boldsymbol{a} \cdot \boldsymbol{a}$ dot product of two vectors or tensors

$\|\boldsymbol{a}\|$ magnitude of a vector or tensor

$\|\mathbf{A}\|_2$ $\mathscr{L}^2$-norm of a matrix

Roman letters

A AC component

$\mathbf{A}$ best-fit operator relating $\boldsymbol{\Psi}'$ and $\boldsymbol{\Psi}$

$\mathcal{A}_n$ pulsatile pressure gradient

$\mathcal{A}$ single harmonic oscillating pressure gradient

$\mathbf{C}$ low-order approximation of $\mathbf{A}$

C_f skin friction coefficient

C_p pressure coefficient

d DMD amplitude

$\mathbf{D}$ DMD amplitude matrix

D_k viscous diffusion of TKE

e variance fraction contained in frequencies higher than the fundamental

$\mathcal{E}$ volume integrated total kinetic energy

$E_{u'u'}$ energy spectrum of streamwise velocity fluctuation

h channel half-height

$\mathbf{I}$ identity matrix

k wave number

l_s Stokes length

l_t turbulent stokes length

$\mathbf{M}$ diagonal matrix with entries that give the volume ratio of a grid cell

$\boldsymbol{n}_s$ surface normal vector

P pressure

p P/ρ

P_k production of TKE

Q Q-criterion

Q_i quadrant components $i = (1 \cdots 4)$

R radius

$R_{u'u'}$ correlation function of streamwise velocity fluctuation

r radial coordinate

$\boldsymbol{r}$ DMD residual

$\mathbf{S}$ strain-rate tensor

$\mathbf{S}'$ fluctuating strain-rate tensor

T period

T_k turbulent transport of TKE

$\mathbf{T}$ Vandermode matrix

t time

$\mathbf{t}$ surface traction vector

$\boldsymbol{u} = (u, v, w)$ velocity field

$\mathbf{U}$ left singular value matrix

u_b bulk velocity

u_c centerline velocity

u_p bulk velocity from steady Poiseuille flow

u_τ friction velocity

u_{osc} amplitude of the oscillation in flow rate

$\mathbf{W}$ right singular value matrix

$\boldsymbol{x} = (x, y, z)$ Cartesian coordinate system

$\mathbf{Y}$ eigenvectors of low-order approximation of $\mathbf{A}$ calculated using SVD

$\mathbf{Z}$ eigenvectors of $\mathbf{C}$

Chapter 1

Introduction

1.1 Motivation

An abdominal aortic aneurysm (AAA) is a dilatation of 50% or greater in the diameter of the aortic segment between the renal arteries and the iliac bifurcation. A simplified sketch of the aorta is shown in figure 1.1 and a majority of aortic aneurysms occur in the segment below the renal arteries. The aorta is the largest artery in the human cardiovascular system. It descends down the abdomen until it bifurcates into the common iliac arteries that lead into the legs. There are usually no symptoms associated with an AAA; however, dilatation weakens the aortic wall making it susceptible to rupture. The rupture of an AAA is life-threating and the risk of rupture increases with diameter and is being significant at diameters grearer than 5.5 cm (Lederle et al. [64]). As such, the decision to repair an AAA is based on a diameter criterion of 5.5 cm in men and 5 cm in women. However, ruptured AAAs (RAAA) may have diameters smaller than 5 cm, while other AAA can reach sizes of $10-12$ cm without rupture. The typical size of the male aorta is 2 cm; female 1.6 cm. The fact that

rupture occurs at a wide range of sizes indicates additional criteria must be used to evaluate a particular AAA's susceptibility to rupture. Being able to identify low-risk AAA shapes would be beneficial to surgeons, because the risk associated with surgery may be greater than the risk of AAA rupture. Aortic diameter is a static measure that does not take into consideration the dynamic interactions between local hemodynamic forces and the biology of the aortic wall. Pulsatile blood flow in an AAA may result in zones of stagnant blood, turbulent fluctuations and flow impingement. These conditions in turn may damage the endothelium, contribute to further AAA development and the degradation of the aneurysm wall.

It was stated by Tarbell [116] that vascular disease occurs due to a combination of both biological and hemodynamic factors. The biological factors, such as cholesterol, smoking and high blood pressure, act throughout the entire cardiovascular system but vascular disease only occurs at certain locations (Lasheras [63]). Generally these locations are arteries with shapes that differ from a straight artery, i.e. bends, arches and bifurcations. The hypothesis

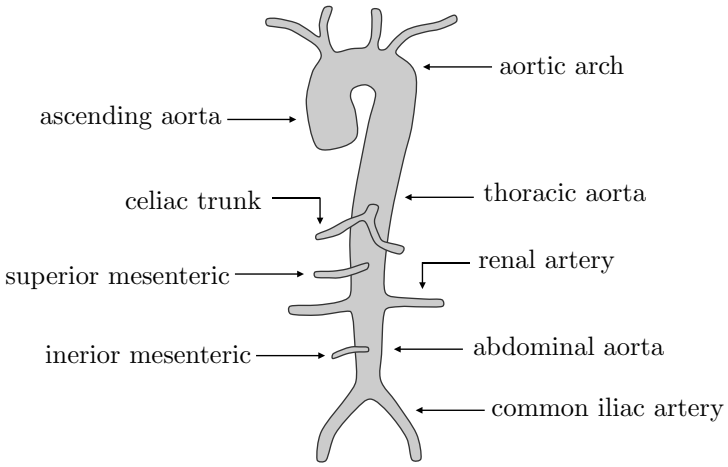

Figure 1.1: Sketch of the aorta. Major visceral arteries that branch off the aorta are indicated.

that adverse blood flow dynamics that develop at such locations may play an important role in the development vascular disease is an inspiration of this theses work. Adverse blood flow behavior includes dynamics such as recirculation, impingement and turbulent fluctuations. The tangential force exerted on the arterial wall by blood flow, referred to as wall shear stress (WSS), is thought to be an important hemodynamic factor that regulates arterial health. In a review article by Peiffier et al. [92] a summary was provided showing how the hypotheses on WSS have changed in the cardiovascular community over the last half century. Initially it was thought that high WSS can cause damage to the arterial wall and lead to atherosclerosis lesions (Fry [37]). Atherosclerosis is the accumulation of white blood cells and other cellular material at a site of endothelial injury, leading to a plaque like deposit on the vascular wall. In the ground-breaking work by Caro et al. [18] the prevailing high WSS hypothesis was challenged and they suggested that in fact it is low WSS that leads to atherosclerosis. The hypothesis outlined by Caro et al. [18] proposed that a low gradient in the velocity profile close to the wall prevents mixing and causes a buildup of cellular material. Caro et al. [18] further reasoned that high WSS has the opposite effect and actually removes or prevents cellular material from being deposited on the wall. This was expanded upon by Ku et al. [59], who suggested that low WSS combined with oscillations in direction of blood flow is the dominant mechanism leading to arterial disease. To study their hypothesis they defined the parameter oscillatory shear index (OSI) that quantities the oscillations in the blood flow. Ku et al. [59] was inspired by the study of blood flow in a diseased carotid bifurcation, which is an artery that leads to the brain. Within a healthy carotid bifurcation there is a continuous supply of blood that is unidirectional without oscillations. In diseased cases, a zone of recirculating blood was present and within this zone the blood flow oscillated

in direction and WSS was lower. Specifically the region of the arterial wall that developed atherosclerosis was exposed to the oscillating recirculation zone and this is shown in figure 1.2.

The general consensus that has developed in the cardiovascular community is that low WSS combined with oscillations in blood flow direction is a dominant mechanisms that contributes to vascular disease (Tarbell et al. [116]). Interest has also been renewed in investigating the possibility that very high WSS causes a remodeling of the arterial wall (Dolan et al. [31]). Such elevated WSS can occur in regions of blood flow impingement and in a stenosed artery. Meng et al. [78] suggested that in intracranial aneurysms high WSS from impingement led to a thinning of the arterial wall.

Although a large number of publications have focused on blood flow in AAA, including Les et al. [67], Suh et al. [112], Arzani and Shadden [4], Arzani et al. [2], among others, the exact mechanism that causes an abdominal aorta to dilate in size is not known. During resting conditions, a large amount of the blood flow that enters the thoracic aorta is directed

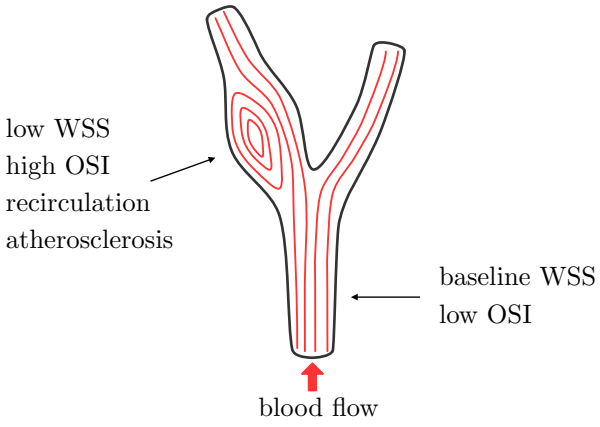

Figure 1.2: Sketch of blood flow dynamics in a diseased carotid bifurcation. Based on a similar figure from Dolan et al. [31] and OSI data is from Ku et al. [59].

into the renal arteries towards the kidneys, and does not enter the abdominal segment of the aorta. As a consequence the flow rate and WSS are substantially lower in the abdominal segment of the aorta (Tang et al. [115]). The lower WSS, relative to the upstream segment, allows cellular material to deposit on the wall leading to atherosclerosis and a weakening of the arterial wall. This is one possible explanation to why 95% of aortic aneurysms are localized to the abdominal aorta.

During exercise conditions, due to the increased demand for blood from the legs, considerably more blood flow enters the abdominal aorta. This raises WSS within the abdominal segment and it has been suggested that individuals that are physically active could have a lower occurrence of AAA (Caro et al. [18]). Studies have verified that exercise conditions raise WSS and produce unidirectional flow in normal-sized aorta (Tang et al. [115], Taylor et al. [118]) and AAA (Suh et al. [113], Les et al. [67]). A flaw in linking reduced WSS in the abdominal segment of the aorta to the formation of an AAA is that low WSS in the abdominal aorta is a universal occurrence, while AAA is not. Another limitation in linking AAA growth to the low WSS theory is that WSS is proportional to artery diameter. As an AAA increases in size the blood flow velocity and WSS will proportionally be reduced. Because of this correlation it is relatively easy to identify that large AAA have lower WSS compared to small AAA (Dalman et al. [24]). Although this correlation exists, it does not necessarily mean that low WSS causes all AAAs to expand, rather it may only be a consequence of the AAA becoming larger.

The theory mentioned above that oscillating blood flow is linked to vascular disease is applied in the literature to all locations in the cardiovascular system; however, it is problematic to apply this theory to the aorta. The aortic blood pulse consists of a spike in

flow rate as the heart contracts and this is followed by a prolonged period where the flow rate is low or effectively zero. This behavior results in blood flow velocity that naturally oscillates in direction close to the arterial wall and with a high OSI under normal resting conditions in the abdominal aorta (Taylor et al. [120]). As a result, it is questionable as to whether or not oscillations in blood flow direction are causally linked to aortic wall deterioration. If the aorta is capable of withstanding blood flow oscillations without adverse affects, it is fair to speculate that all cardiovascular locations are similarly capable of not being affected by oscillations. At best the concept that flow with a high OSI leads to vascular disease is an incomplete theory and it is possible that blood flow oscillations in isolation have no impact on arterial health. Peiffier et al. [92] questioned the affect of OSI on vasculature health. A significant focus in the cardiovascular literature is to identify parameters derived from WSS and link these parameters to growth or rupture. For example, Arzani and Shadden [5] compared the results from 18 different WSS based parameters and the focus of vascular research papers is often defining new WSS based parameters (Peiffer et al. [91], Achille et al. [28]). However, if WSS is less relevant to AAA then first thought, this draws into question the direction of current research.

The second hemodynamic force that acts upon the arterial wall is the wall-normal pressure force. Regions with locally high pressure can result from asymmetry in the blood flow caused by bends in an artery and blood flow impingement. It has been shown that patients with a single above-knee leg amputation are more likely to develop AAA (Vollmar et al. [128]). In addition to further lowering WSS in the abdominal aorta, due to the reduced blood requirement of the amputated leg, a single above-knee leg amputation causes an asymmetrical flow pattern at the aortic bifurcation. The majority of the blood flow being directed down a

single iliac artery of the non-amputated leg causes a higher wall-normal pressure force to be applied along the side with the amputation and expansion was found to be more prevalent on this side. This finding suggests that non-symmetric pressure distribution in the aorta plays an important role in AAA formation and growth. In Lasheras [62] it was suggested that pressure forces may be more influential to AAA growth then shearing forces.

Intraluminal thrombus (ILT) deposition may also play a role in AAA formation and growth. It is the coagulation of platelets and red blood cells that can form along the arterial wall. Once a layer of ILT forms the aortic wall is no longer directly exposed to the blood flow. This fact further challenges the relevance that low and oscillating WSS has on AAA growth and rupture. Since the shear from the blood flow is now acting on a layer of dead cellular material and not the arterial wall, WSS can no longer be considered the direct cause of wall deterioration (Lasheras [62]). Furthermore aortic wall receives oxygen primarily from luminal blood flow and a layer of ILT may decrease the flow of oxygen (hypoxia). This lack of oxygen could cause a reduction in arterial wall integrity and the region of the AAA with ILT could be more susceptible to further expansion or rupture (Vorp et al. [130]). It has been shown that the presence of ILT deposition increased AAA growth rate (Parr et al. [88], Wolf et al. [137], Zambrano et al. [143]), regions of the AAA wall with ILT experienced localized hypoxia (Vorp et al. [129]), were thinner with more inflammation (Kazi et al. [53]) and Koole et al. [56] showed that wall degradation was correlated with ILT thickness. Several studies have performed finite element analysis (FEA) on AAA and have found that a layer of ILT reduces the wall stress in the arterial wall (Di Martino et al. [30], Mower et al. [84], Wang et al. [133], Xenos et al. [141]). This has lead to the speculation that ILT is protective and shields the aortic wall from pressure forces. However this hypothesis was brought into

question with the work by Speelman et al. [109], where AAA wall stress was lower when a large ILT volume was present but growth rate was also higher. The authors stated that the deterioration of the aortic wall from ILT may be more influentially than the hemodynamic forces acting on the wall. It has been suggested that ILT thickness could be used as a criterion, in addition to diameter, when determining risk of rupture (Satta et al. [103]) and ILT deposition in small-sized AAA should be a factor when considering early surgical repair (Stenbark et al. [111], Wolf et al. [137]). Studies that have attempted to link OSI to ILT in AAA have found a correlation between low OSI and ILT deposition (Arzani et al. [6], O'Rourke et al. [85]). This is in opposition with the original theory regarding blood flow oscillations.

Generally ILT does not encompass the AAA wall at a uniform thickness. Shown in figure 1.3 (a) is a mid-sagittal computed tomography angiography (CTA) and sketch of lumen and ILT for a patient with both posterior-eccentric ILT in the upper portion and eccentric-equal ILT in the lower portion of the AAA. For this patient the AAA has dilated to a very large diameter of 11 cm and the maximum ILT thickness is 4.4 cm. This is well beyond the diameter criterion used to determine when to operate. The aorta segment directly upstream of the dilation is highly angulated. Interestingly this patient experienced a rupture that can be seen in the CTA on the posterior side below the conical neck. In figure 1.3 (b) a upper-axial CTA and sketch of lumen and ILT is shown. Here the ILT is thickest along the posterior wall, then reduces in thickness along the left and right walls and the anterior wall is devoid of ILT. For axial CTA the left and right sides are flipped. The front and back sides of the AAA are referred to as anterior and posterior, respectively. Figure 1.4 shows a mid-axial CTA and sketch of lumen and ILT for a patient with anterior-eccentric ILT.

Although this patient has an AAA with a diameter of approximately 5 cm, a thick layer of ILT along the anterior wall has resulted in a small lumen flow channel. Thrombus is also present along the posterior wall but it is relatively thin. Figure 1.5 shows a mid-axial CTA and sketch of lumen and ILT for patient where the ILT is along the right wall. This patient also has an AAA with a diameter of approximately 5 cm but since it only has a thin layer of ILT the lumen flow channel is considerably larger then the above patient. Previous studies have shown it to be more common for ILT to be anterior-eccentric in AAA (Hans et al. [41], Pillari et al. [94], Metaxa et al. [79]). In a study by Metaxa et al. [79] it was found that AAA with posterior-eccentric ILT have lower growth rates when compared to AAA with anterior-eccentric ILT. This indicates that the the location of the ILT along the wall may be more important in growth than any adverse hemodynamic conditions, i.e. the layer of ILT weakens the anterior wall and causes it to expand. When there is no ILT along the anterior wall it will maintain its integrity and expansion is slower. If ILT is located along the posterior wall, this does not necessarily result in growth as the spine blocks growth in the posterior direction.

Although it is possible for an AAA to dilate to a very large size prior to rupturing, a majority of the previous studies in the literature have focused on AAA with diameters less than 5 cm, such as Les et al. [67] and Arzani et al. [6]. One reason for the lack of large-sized AAA in the literature is the common practice to operate on AAA when they dilate to approximately 5 cm and therefore large-sized AAA are less available for use in numerical simulation. For a fixed blood viscosity, density and pulse period, the ratio of pulsatile inertia forces to viscous forces is dependent only on arterial diameter. As an AAAs diameter increases inertia has a greater affect on the hemodynamics and therefore the behavior of the blood

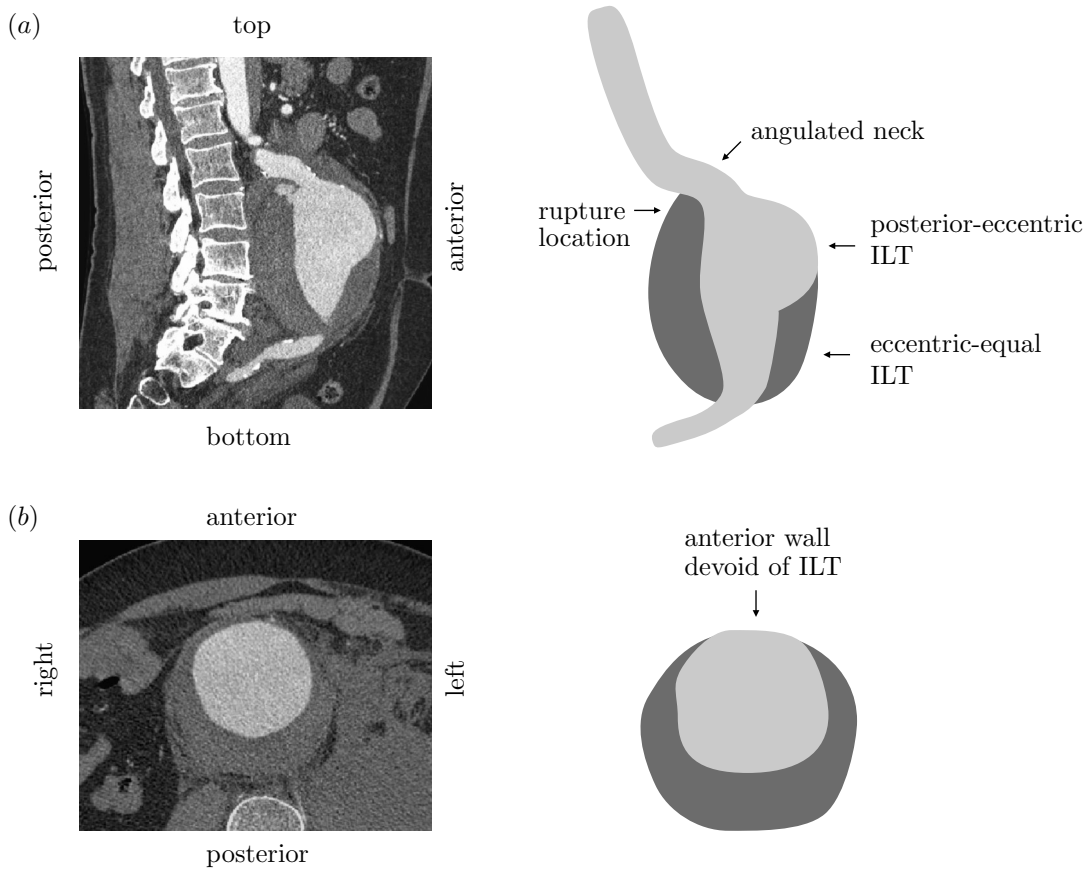

Figure 1.3: (a) Mid-sagittal CTA and sketch of lumen and ILT for patient with both posterior-eccentric and eccentric-equal ILT. (b) Upper-axial CTA and sketch of lumen and ILT showing posterior-eccentric ILT. Dark gray is ILT and light gray is lumen.

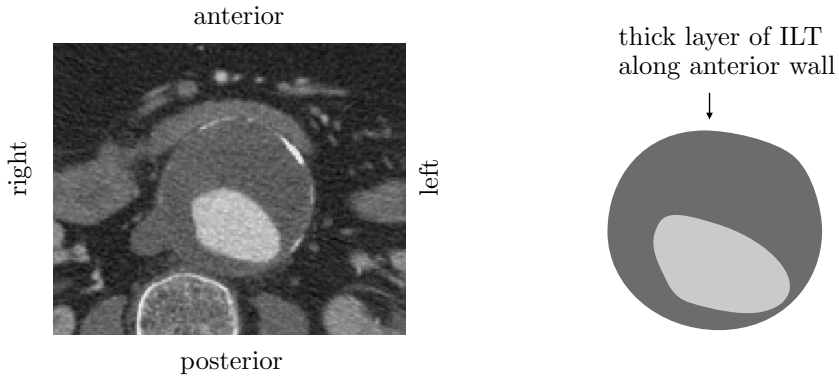

Figure 1.4: Mid-axial CTA and sketch of lumen and ILT for patient with anterior-eccentric ILT. Dark gray is ILT and light gray is lumen.

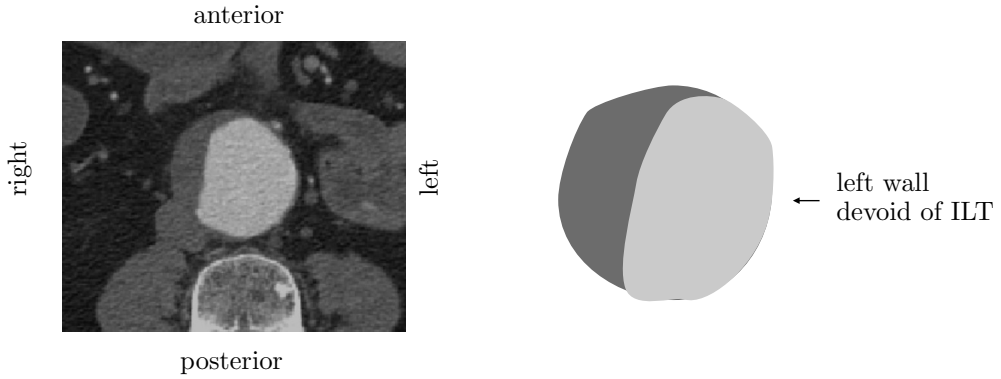

Figure 1.5: Mid-axial CTA and sketch of lumen and ILT for patient with right-eccentric ILT. Dark gray is ILT and light gray is lumen.

flow could differ substantially for AAAs with diameters > 5 cm.

There has also been significant literature on intracranial aneurysms (Valen-Sendstad et al. [125], Varble et al. [126]). Intracranial arteries are significantly smaller than the aorta and pulsatile inertia forces have even less affect on their blood flow dynamics. Any observations made for intracranial aneurysms, cannot be applied to AAA due to the large size difference in the vessels, their relatively thin walls and the fact the the cerebral circulation is a low resistance flow situation. There is a significant gap in the literature in the understanding of the flow dynamics in medium to large-sized AAA, with the work by Zambrano et al. [143] and Doyle et al. [33] being two of the few studies to include AAA greater than 5 cm. Both of these studies only investigated time-averaged flow behavior and did not examine the instantaneous dynamics of the blood flow. There is also a gap in the literature relating the hemodynamics from a numerical simulation to biological data such as, ILT location, growth and rupture. The work by Zambrano et al. [143], Doyle et al. [33], Arzani et al. [6] and O'Rourke et al. [85] being the few studies to do this.

It is possible that zones of stagnant blood, turbulent fluctuations and flow impingement produce a hemodynamic environment that contributes to AAA expansion, ILT deposition and rupture. As an AAA increases in size adverse hemodynamic conditions may worsen, further increasing the risk of rupture. Since an AAA can have a wide variety of shapes, it is possible that particular geometries have greater disturbances in blood flow. Some AAAs may dilate to very large sizes while maintaining stable non-disturbed blood flow and therefore could potentially be at a lower risk for rupture. It would be beneficial to be able to identify the flow dynamics associated with particular aortic geometries. Again since a majority of previous AAA studies have focused on AAA with diameters less than 5 cm, these flow dynamics have not been fully explored.

The objective of this thesis is to determine what affect AAA size and shape have on the blood flow dynamics. This was achieved by computationally investigating pulsatile blood flow dynamics in a large set of patient-specific AAA. AAA from these patients cover a wide range of shapes and sizes. The open source computational fluid dynamic (CFD) code OpenFOAM was used to perform direct numerical simulations (DNS) of the blood flow. The term DNS refers to solving the governing equations for mass and momentum without the use of any models and all relevant scales of motion are computed. It is hypothesized that as AAA increase in size the hemodynamic environment progressively worsens with the blood flow becoming more disturbed and this is one of the reasons rupture risk increases with size. When AAA are less than 5 cm it is suspected that the blood flow is predominately non-disturbed and this could explain why small-sized AAA are at a low risk to rupture. It is investigated if the numerical simulations can explain why ILT accumulates in certain locations or why AAA experience different growth rates. The overarching goal is to identify AAA shapes that are

at a high risk to rupture. Knowledge of these shapes could be used to establish additional criterion to help determine when to operate on a particular AAA.

1.2 Thesis outline

In chapters 4, 5 and 7 the analysis focuses on comparing the numerical results to biological data such as, ILT location, growth and rupture. Chapters 3, 6 and 8 focus on the development, validation and application of engineering methods to pulsatile turbulent flow. A outline of the contents of the chapters in this thesis is provided here. Chapter 2 details the methods used to obtain and analyze the data. Chapter 3 presents a numerical simulation of turbulent low-Reynolds pulsatile flow in a channel has been performed. Additionally, this chapter presents the validation of the OpenFOAM source code is against a canonical simulation of non-pulatile turbulent channel flow and verifies that the code is suitable to perform simulations of pulsatile flow. The work from this chapter has been prepared into a draft of a journal paper. In chapter 4 data is presented from pulsatile numerical simulations of a group of 23 patient-specific AAA. The blood flow dynamics are compared to AAA shape and ILT deposition. The effectiveness of the OSI parameter is evaluated for AAA. This work has been published in Lozowy et al. [73]. Serial growth data from patient-specific AAA is presented for 3 cases in chapter 5. The blood flow dynamics are compared to the change in AAA size and ILT thickness for two of these cases. The work from this chapter has been prepared into a draft of a journal paper. In chapter 6 triple decomposition and dynamic mode decomposition (DMD) are applied to turbulent pulsatile blood flow for a single patient-specific AAA. The challenges of implementing the DMD method for pulsatile turbulent flow are discussed. The

work from this chapter has been prepared into a draft of a journal paper. In chapter 7 simulations from a group of 7 patient-specific rupture AAA is presented and the blood flow dynamics are compared to the location of rupture. This work has been published in Boyd et al. [15] and was presented at the CSME Congress (Lozowy et al. [71]). The final writing and preperation of the published paper was performed by Dr. Boyd, based on the initial work performed by Richard Lozowy. In chapter 8 pulsatile simulations are compared between a medium and large sized AAA. Triple decomposition is used to calculate the phase-wise variation in the turbulent kinetic energy. This work has been presented at the Engineering Turbulence Modeling and Measurements conference (Lozowy et al. [72]). In the final chapter a conclusion is presented and possible future work is discussed.

1.3 Contributions of work

The primarily contribution of this work is that it provides insight into the types of flow dynamics that can occur in a wide range of AAA shapes. A total of 32 patient-specific AAA cases are presented in this thesis, with some of the cases appearing in multiple chapters. Novel observations were made on how shape influences blood flow dynamics and these observations were linked back to AAA growth, rupture and ILT deposition. It is described how specific AAA geometries produce an adverse hemodynamic environment while other geometries do not. Novel observations are made on the flow dynamics from pulsatile channel flow. While not a unique contribution, a python script has been developed that can perform DMD, using parallel computing, on data from a OpenFOAM simulation. This work is also the first to apply DMD to pulsatile turbulent blood flow in a patient-specific artery.

Chapter 2

Method

In this chapter the methods used to obtain and analyze the data are presented. The location within the thesis that a particular analysis method is used is indicated. All of the simulations in this thesis are performed using the open source CFD code OpenFOAM.

2.1 Equations and numerical method

In the following section the non-dimensional parameters, governing equations and an overview of the numerical procedure are given. The period of a blood pulse is given by T and the phase position within the period is represented as $\varphi(t) \in [0, T]$. Assuming an artery can be modeled as a constant radius pipe, the length scale is the radius R and the velocity scale is the time-averaged bulk velocity $\overline{u}_b$, where an overbar indicates a flow quantity has been averaged over time. The non-dimensional parameters that govern vascular flow are the bulk Reynolds number Re_b, Womersley number Wo and the oscillating-to-mean flow rate ratio β, which are, respectively,

$$Re_b = 2\overline{u}_b R/\nu, \tag{2.1}$$

$$Wo = R\sqrt{\omega/\nu}, \tag{2.2}$$

$$\beta = u_{osc}/\overline{u}_b. \tag{2.3}$$

Here $\nu = \mu/\rho$ is the kinematic viscosity, with μ and ρ being the dynamic viscosity and density, respectively, $\omega = 2\pi/T$ is the angular frequency and u_{osc} is the amplitude of the oscillating component of the pulse. These non-dimensional parameters vary substanially within the cardiovascular system. For fully developed non-oscillatory flow in a pipe, the Reynolds number cited as the critical value giving the onset of turbulence is $Re_{b,c} \approx 2300$ (Incropera and Dewitt [46]). Although in the absence of disturbances, laminar flow in a pipe can be maintained at much higher Re_b than the critical value. Aside from the great vessels, the blood flow rate is below the critical Reynolds number and any turbulence that occurs is influenced by the shape of the artery or pulsatile inertia effects. The Womersley number gives the ratio of pulsatile inertia to viscous forcse and its influence on blood flow is discussed in the following section. Although blood in a non-Newtonian fluid, in large arteries, such as the aorta, it can be assumed to behave as Newtonian (Ku [58]). A study by Marrero et al. [76] showed minimal qualitative difference in AAA when using blood flow with either Newtonian or non-Newtonian properties. The arterial wall is assumed to be rigid and only the fluid flow is considered for the simulation. The governing equations for the conservation of mass and momentum, in a Cartesian coordinate system $\boldsymbol{x} = (x, y, z)$, are as follows:

$$\nabla \cdot \boldsymbol{u} = 0 \tag{2.4}$$

$$\partial \boldsymbol{u}/\partial t + \boldsymbol{u} \cdot \nabla \boldsymbol{u} = -\nabla p + \nu \nabla^2 \boldsymbol{u} \tag{2.5}$$

where the velocity field is given by $\boldsymbol{u} = (u, v, w)$, t is the time unit and $p = P/\rho$, with P being the pressure field.

The open source unstructured finite-volume code OpenFOAM-2.2.2 (OpenCFD Ltd, Bracknell, United Kingdom) (Weller [134]) is used to directly solve the governing equations. The pressure and velocity are stored at the cell centres and in chapters $2-6$ and 8 the Pressure-Implicit with Splitting of Operators (PISO) algorithm (Issa [47]) is used for the pressure-velocity coupling. An overview of how the PISO algorithm is implemented in OpenFOAM is as follows: for its first step it solves the velocity field using the pressure field from the previous time-step. The Poisson equation for the pressure is then solved using the approximated velocity field and afterwards the velocity is adjusted based on the new pressure field. This step is repeated twice to obtain suitable accuracy (Issa [47]). In chapter 7 the SIMPLE algorithm is used. A detailed description on how numerical schemes are implemented within OpenFOAM on an unstructured grid can be found in Jasak [49], de Villiers [27] and Damian [25]. The PISO algorithm converges mass and momentum at each time step; where as the SIMPLE algorithm converges iteratively over consecutive time steps. Therefore, the SIMPLE algorithm does not capture transient flow features and only a final steady state for the flow field. The central-difference scheme is applied to the convection and Laplacian terms and a second-order implicit Euler method is used for time integration.

The Poisson equation is solved using an algebraic multi-grid solver and the equations are considered converged when the residuals become less than 1×10^{-6}. The residual is a measure of the error in the solution and are normalised to make it independent of the quantity being solved. To ensure numerical stability the the Courant-Friedrichs-Lewy (CFL), defined as

$$\mathrm{CFL} = \frac{\Delta t \|\boldsymbol{u}\|}{\Delta x} \tag{2.6}$$

must be less than 1, with Δt being the time step, $\|\boldsymbol{u}\|$ is the magnitude of the velocity is a grid cells centre and Δx is the grid cells width in the direction of the velocity.

The simulations from this thesis were solved using 48 processors provided by Compute Canada WestGrid high performance computer resources. It is found that when using the algebraic multi-grid solver the computational speed of the simulation does not scale linearly as the number of processors is increased. If substantially more then 48 processors are used for a simulation CPU speed would decrease. The computational grids have been generated using the commercial software Pointwise (version 17.2, Pointwise, Fork Worth, Texas) and three-dimensional surface models of AAA were generated from CTA using the commercial software Mimics (version 14.0, Materialize, Plymooth, Michigan). To simplify the geometry, arteries that branch off of the aorta, such as the visceral arteries, were excluded and the common iliac arteries were modeled to the bifurcation of the internal and external iliac arteries. Ethics approval for using patient CTA in this work was granted by the University of Manitoba Research Ethics Board, Research Protocol Number: REB B2013:130.

2.2 Blood pulse

In this section the underlying theory on oscillating fluid is presented. This is followed by a discussion on the aortic blood pulse and how the analytical theory can be applied to a realistic case. The term pulatile flow refers to a mean flow superimposed with oscillations. A purely oscillating flow has a mean component of zero.

2.2.1 Oscillating flow theory

For fully developed Poiseuille flow in a pipe segment of length L, radius R and radial coordinate r the velocity profile across the pipe is given by the well known equation

$$u(r) = -\frac{dP}{dx}\frac{R^2}{4\mu}\big(1 - r^2/R^2\big), \tag{2.7}$$

where the $dP/dx = (P_2 - P_1)/L$ is the pressure gradient along the pipe segment, P_1 and P_2 are the pressures at opposite ends of the pipe segment. The bulk flow rate for steady pipe flow is then

$$u_b = \frac{2}{R^2}\int_0^R u(r) r \mathrm{d}r = -\frac{R^2}{8\mu}\frac{dP}{dx} \tag{2.8}$$

and the pressure gradient driving the fluid is balanced by an opposing frictional force τ_w at the wall calculated as

$$\tau_w = \mu\frac{du(r,t)}{dr}|_{r=R} = -\frac{R}{2}\frac{dP}{dx}. \tag{2.9}$$

For the case where the pressure gradient undergoes some pulsatile motion it can be expressed as the real component of the Fourier series

$$-dP/dx = \mathcal{A}_0 + \sum_{n=1}^{\infty} \mathcal{A}_n \exp\left(\mathrm{i}\omega_n\right), \tag{2.10}$$

where $\mathcal{A}_0$ is the mean component of dP/dx, the terms $\mathcal{A}_n = \mathcal{A}_{c,n} + \mathrm{i}\mathcal{A}_{s,n}$ are the amplitudes, $\omega_n = 2\pi n/T$ and $\mathrm{i} = \sqrt{-1}$. Alternatively the oscillating component of the Fourier series can be expressed as

$$\begin{aligned} \sum_{n=1}^{\infty} \mathcal{A}_n \exp\left(\mathrm{i}\omega_n t\right) &= \sum_{n=1}^{\infty} \mathcal{A}_{c,n} \cos\left(\omega_n t\right) + \sum_{n=1}^{\infty} \mathcal{A}_{s,n} \sin\left(\omega_n t\right) \\ &= \sum_{n=1}^{\infty} a_n \sin\left(\omega_n t + \phi_n\right), \end{aligned} \tag{2.11}$$

where $a_n = \left(\mathcal{A}_{c,n} + \mathcal{A}_{s,n}\right)^{1/2}$ and $\phi_n = \tan^{-1}\left(\mathcal{A}_{s,n}/\mathcal{A}_{c,n}\right)$. The fully developed laminar velocity profile for pulsatile flow in a pipe can be calculated as the real component of

$$u(r,t) = \frac{\mathcal{A}_0 R^2}{4\mu}\left(1 - r^2/R^2\right) + \sum_{n=1}^{\infty} \frac{\mathcal{A}_n}{\mathrm{i}\omega_n \rho}\left[1 - \frac{J_0\left(Wo_n \mathrm{i}^{3/2} r/R\right)}{J_0\left(Wo_n \mathrm{i}^{3/2}\right)}\right] \exp\left(\mathrm{i}\omega_n t\right), \tag{2.12}$$

where J_0 is a Bessel function of order zero and $Wo_n = R\sqrt{\omega_n/\nu}$. The above equation represents the pulsatile velocity profile as a mean component that is based on steady Poiseuille flow and the summation of oscillating velocity profiles at progressively higher Wo_n. The analytical solution to the oscillating component is often referred to as the Stokes solution and the non-dimensional parameter Wo was first introduced in this form by Womersley [138]. The depth of the oscillating boundary layer is referred to as the Stokes' length and is calculated as $l_s = (2\nu/\omega)^{1/2}$. Therefore, Wo is proportional to the ratio of the outer length scale R to the oscillating length scale (Loudon & Tordesillas [70]). Derivations for eqn. (2.12) can be found in Uchida [124] and discussion on how the analytical solution changes for turbulent

flow can be found in chapter 3 of this thesis. For the case where dP/dx consists of a single harmonic oscillation of amplitude $\mathcal{A} = \mathcal{A}_c + \mathrm{i}\mathcal{A}_s$, eqn. (2.12) reduces to the real component of

$$u(r,t) = \frac{\mathcal{A}}{\mathrm{i}\omega\rho}\left[1 - \frac{J_0\big(Wo\mathrm{i}^{3/2}r/R\big)}{J_0\big(Wo\mathrm{i}^{3/2}\big)}\right]\exp\big(\mathrm{i}\omega t\big). \tag{2.13}$$

Applying a force balance on a single harmonic oscillation yields

$$\pi R^2\mathcal{A}\exp\big(\mathrm{i}\omega t\big) = \pi R^2\rho\frac{du_b(t)}{dt} + 2\pi R\tau_w(t), \tag{2.14}$$

where the first term on the right hand side is the contribution of the force by inertia effects, the second term on the right hand side is the contribution from the friction drag at the wall and the left hand side is the total force from pressure. The effect that increasing Wo has on the distribution of the force terms is shown in figure 2.1. The terms are normalized by u_p^2/R, where u_p is the bulk velocity from steady Poiseuille flow. When $Wo = 1$ a majority of the pressure gradient force goes towards overcoming friction drag and the friction drag is mostly aligned with the pressure gradient force. The amplitude of the inertia force is relatively low and its peak occurs during mid flow acceleration. When Wo is increased to 2 there is approximately an even split between inertia and frictional drag. The peak in the friction drag is delayed with respect to the peak in the pressure gradient force and the peak in the inertia force becomes more aligned. As Wo increases the inertia force offsets a greater portion of the pressure gradient force. The friction drag progressively offsets a smaller portion of the pressure gradient force and the peak in friction drag further lags behind the peak in the pressure gradient as Wo increases.

Figure 2.2 (a) shows the effect that increasing Wo has on the amplitude of oscillating bulk

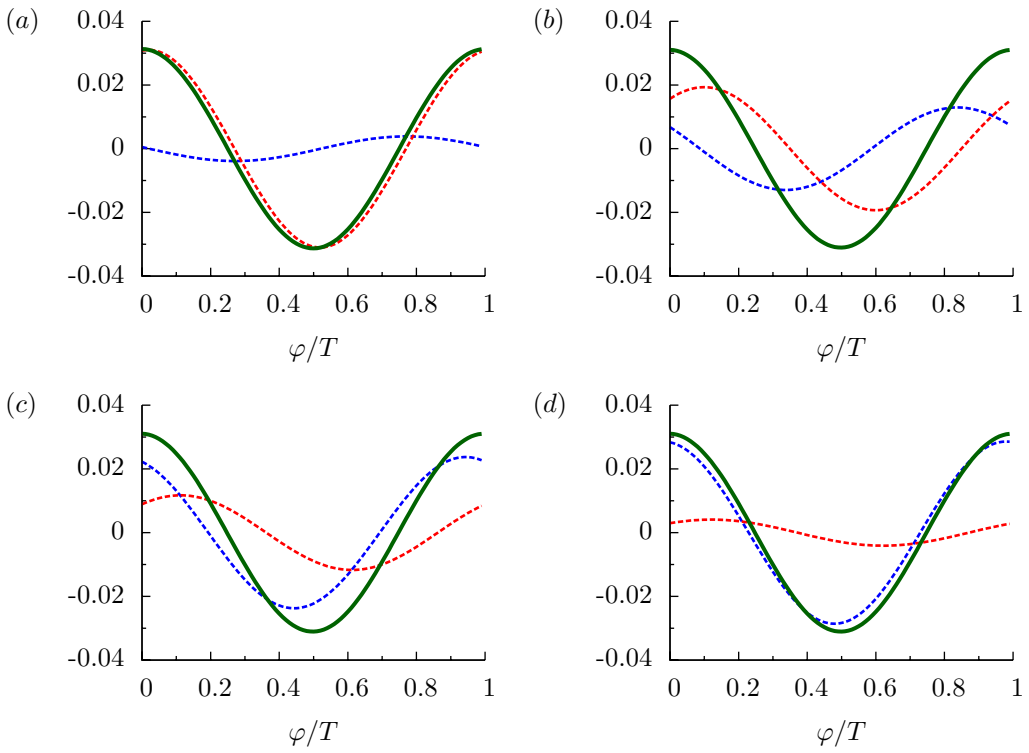

Figure 2.1: Phase-wise force balance with (a) $Wo = 1$, (b) $Wo = 2$, (c) $Wo = 5$ and (d) $Wo = 15$. Blue dashed line is the inertial force accelerating the bulk flow, red dashed line is wall friction force and green line is total force from the pressure gradient. Terms are normalized by u_p^2/R. Based on a similar figure from Uchida [124].

flow rate, relative to steady Poiseuille flow and figure 2.2 (b) shows the effect that Wo has on the phase lag between the peak value for the pressure gradient and both the peak value for the bulk flow rate and the friction drag. As Wo is increased, the amplitude decreases and the velocity's phase-lag increases, with the largest phase-lag at the center of the pipe. A majority of the change in amplitude and phase-lag occurs when Wo is less than 10 and afterwards these terms slowly approach asymptotic values. In the limit of very high Wo the phase-lag in u_b and friction drag approach asymptotic values of $T/4$ and $T/8$, respectively.

When $Wo < 1$ the velocity distribution across a pipe does not vary significantly from the parabolic profile given by eqn. 2.7. The fluid can be treated as quasi-steady and there is

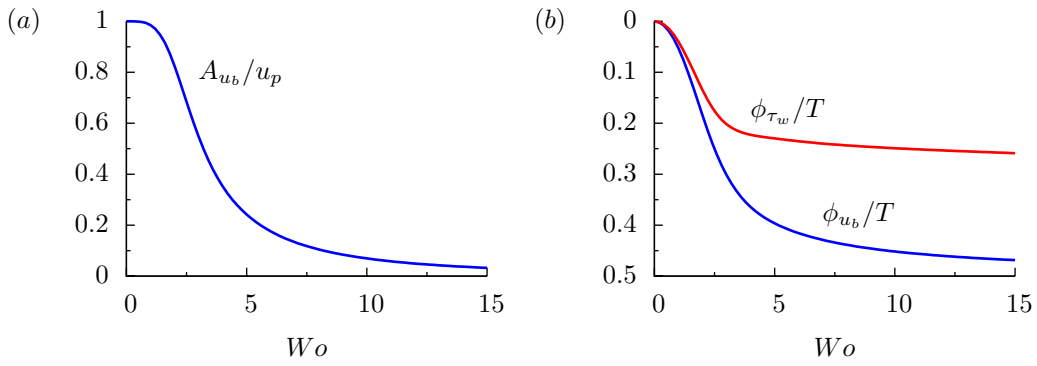

Figure 2.2: Effect of Wo on (a) amplitude of oscillating bulk flow rate A_{u_b}, relative to corresponding steady Poiseuille flow, (b) phase lag in the maximum bulk flow (blue line) and in the wall friction (red line) with-respect-to the maximum oscillating pressure gradient. Based on a similar figure from Womersley [138]

effectively no difference in the velocity's phase-lag at the pipe wall and center. As Wo is increased the velocity profile begins to deviate from a parabolic shape. Figure 2.3 shows unsteady velocity profiles across the pipe radius for (a) $Wo = 5$ and (b) $Wo = 15$ at various phase positions. The velocity reverses first at the wall and reversal is delayed in the central region of the pipe. As Wo is increased the shear layer is confined to a progressively smaller layer close to the wall. For very high Wo values the the outer region becomes flat with a very sharp gradient at the wall.

To assist in the calculation of the bulk flow rate from a known oscillating pressure gradient and Wo, Womersley [138] provided the following equation

$$u_b = \mathcal{M}\frac{\mathcal{A}R^2}{\mu}\sin\Big(n\omega t + \varphi_{u_b}\Big), \tag{2.15}$$

where $\mathcal{M}$ and φ_{u_b} are both functions of Wo. For very small Wo values $\mathcal{M} \approx 1/8$ and $\varphi_{u_b} \approx 0$. For $Wo > 10$ Womersley [138] gave correlations to determine these values, where

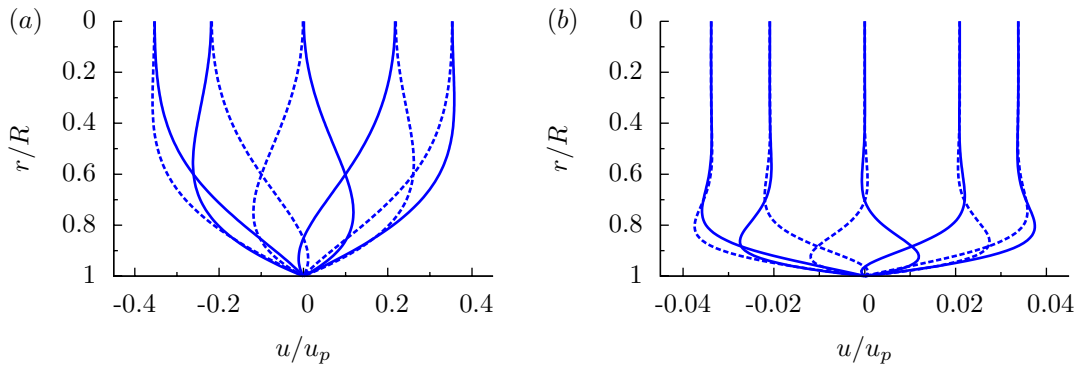

Figure 2.3: Oscillating velocity profile for (a) $Wo = 5$ and (b) $Wo = 15$ at phase positions $\varphi/T = 0, 0.1, ..., 0.8, 0.9$. Based on a similar figure from Uchida [124].

$$\mathcal{M} = \frac{\sqrt{2}}{Wo^2} - \frac{\sqrt{2}}{Wo^3} + \frac{1}{Wo^4} \tag{2.16}$$

$$\varphi_{u_b} = 57.296\left(\frac{\sqrt{2}}{Wo} + \frac{1}{Wo^2} + \frac{19}{24\sqrt{2}Wo^3}\right). \tag{2.17}$$

and for $Wo < 10$ the corresponding values for $\mathcal{M}$ and φ_{u_b} are tabulated in Womersley [138].

The length of pipe required for steady Poiseuille flow to fully develop was given in Incropera and Dewitt [46] on page 487 as

$$x/R \approx 0.1 Re_b. \tag{2.18}$$

It was determined by Wood [139] that the development length for the oscillating Stokes' solution can be approximated as

$$x/R \approx Re_{b,inst}/Wo^2, \tag{2.19}$$

where $Re_{b,inst}$ is calculated from the instantaneous bulk velocity. The instantaneous development length changes over the pulse period and as Wo increases the development length reduces.

2.2.2 Aortic blood pulse

Systole refers to when blood is ejected from the heart and diastole to when the heart muscle relaxes. The aorta is the largest artery in the human cardiovascular system. Blood flow exits the heart into the ascending aorta and which arches over the left pulmonary artery. Figure 2.4 shows an anterior view of an AAA with a diameter of approximately 5 cm. Arteries branching off of the aorta, referred to as visceral arteries, have been removed from the figure and are not considered. The blood flow descends down though the thoracic and abdominal segments of the aorta until it bifurcates into the common iliac arteries and flows into the legs. As the blood flows through the aorta it branches out into visceral arteries and the flow rate at the supraceliac level is substantially less then the infrarenal level. The term infrarenal refers to the segment of the aorta below the renal arteries and the term supraceliac is the segment of the aorta above the celiac axis. Since ν and T are fixed parameters within the cardiovascular system, the Womersley number Wo is dependent on the size of the artery. In small arteries and capillaries, where $Wo << 1$, the pressure gradient is aligned with the flow rate and the flow can be treated as quasi-steady, i.e. at any moment in the pulse the velocity profile has a parabolic Poiseuille shape that is based on the instantaneous bulk velocity. As the diameter of an artery increases, pulsatile inertia forces will have a progressively greater influence on the blood flow dynamics and it no longer behaves quasi-steady. In the thoracic and

abdominal segments of the aorta $Wo \approx 15$ and aside from the heart and diseased arteries this is approximately the largest Wo value that occurs in the cardiovascular system. Where the AAA has dilated to a diameter of approximately 5 cm, the local Wo is approximately 30 and pulsatile inertia effects are much more substantial compared to the upstream aorta. Where the aorta bifurcates into the common iliac arteries, the diameter is reduced to approximately 1 cm and the local Wo is now only approximately 5. In this region the influence of pulsatile inertia forces is greatly reduced compared to the upstream aorta. Referring back to figure 2.3 note how different Wo values affect the oscillating velocity profile. In the aorta and other greater vessels the blood flow profile is flat in the center region with a very steep gradient close to the arterial wall. In the AAA, since diameter is larger, the velocity gradient is restricted to a smaller portion of the velocity profile. While in the smaller diameter vessels, such as the downstream iliac arteries, the velocity gradient extends from the arterial wall to the center region.

The amount of blood flow that enters the aorta is dependent on the requirements of the

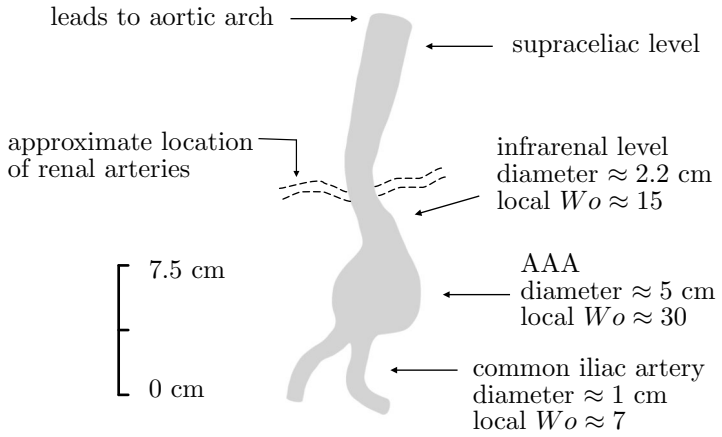

Figure 2.4: Typical shape of an AAA with approximate artery size and local Wo. Arteries that branch off of the aorta, such as the renal arteries, are not shown in image.

legs. Using data that was given in Pedersen et al. [90], table 2.1 summarizes the increase in supraceliac flow rate, the increase in heart rate and the percentage of the supraceliac flow rate that enters the abdominal aorta, going from rest to exercise conditions. During resting conditions only a small amount of the supraceliac flow enters the abdominal segment of the aorta, while during exercise a majority enters it.

Temporal variation in supraceliac and infrarenal bulk blood flow rate are shown in figure 2.5. During diastole the supraceliac flow rate is low but non-zero while the infrarenal flow rate is effectively zero. At the start of diastole infrarenal flow rate reverses and temporarily becomes negative while the supraceliac flow rate remains positive throughout the pulse. The mean supraceliac and infrarenal flow rate provided by Les et al. [68] are 51.2 $\pm$ 10.3 ml s^{-1} and 17.5 $\pm$ 5.44 ml s^{-1},respectively. In Les et al. [68] the pulse profile data was provided as $M = 24$ bulk flow data points $u_{b,n}$ spread equidistantly over a pulse and this data is used to calculated a 12 term Fourier Series represented as

$$u_b = \overline{u}_b + \sum_{m=1}^{M/2} a_m \cos\big(n\omega t\big) + \sum_{m=1}^{M/2} b_m \sin\big(n\omega t\big), \tag{2.20}$$

where the coefficients a_m and b_m are calculated as

	rest	medium exercise	exercise
supraceliac flow rate (l min^{-1})	2.53	3.74	5.15
heart rate (beats min^{-1})	60	90	120
flow entering abdominal segment	30.8 %	64.2 %	81.6 %

Table 2.1: Flow rate at the supraceliac level in the aorta, pulse beats per minute and percentage of supraceliac flow rate entering abdominal segment for rest, medium exercise and exercise conditions. Data originated from Pedersen et al. [90].

$$a_m = \frac{2}{M}\sum_{n=0}^{M-1} u_{b,n}\cos\left(n\omega t\right) \qquad b_m = \frac{2}{M}\sum_{n=0}^{M-1} u_{b,n}\sin\left(n\omega t\right). \tag{2.21}$$

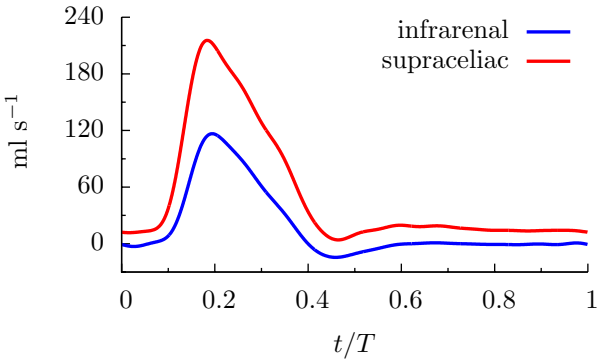

Figure 2.5: Temporal variation in supraceliac and infrarenal bulk flow rate. 12 term Fourier Series calculated using bulk flow rate data from Les et al. [68].

Figure 2.6 (a) shows infrarenal aortic bulk flow rate calculated using 12 terms in a Fourier Series. In figure 2.6 $(b)-(d)$ is shown how the pulse profile is constructed by adding additional harmonics at progressively higher frequency. After only 3 harmonics the pulse profile closely resembles the typical physiological shape.

To better understand the expected flow dynamics in the abdominal aorta, the analytical solution to a fully-developed pulsatile velocity profile is calculated for a pipe segment of radius R, radial coordinate r, $Wo = 15$ and the infrarenal aortic bulk flow rate shown in figure 2.6 (a). The calculation of an oscillating velocity profile requires the coefficients a_m and b_m of the bulk flow rate to be shifted to their corresponding pressure gradient and this is done using eqn. 2.16 and eqn. 2.17. In figure 2.7 the analytical velocity profile is shown at various times during systole and early-diastole. As the blood flow decelerates, close to the wall it reverses in direction at $t/T = 0.29$. During diastole the velocity profile consists of a low negative component close to the wall and a low positive component in the core

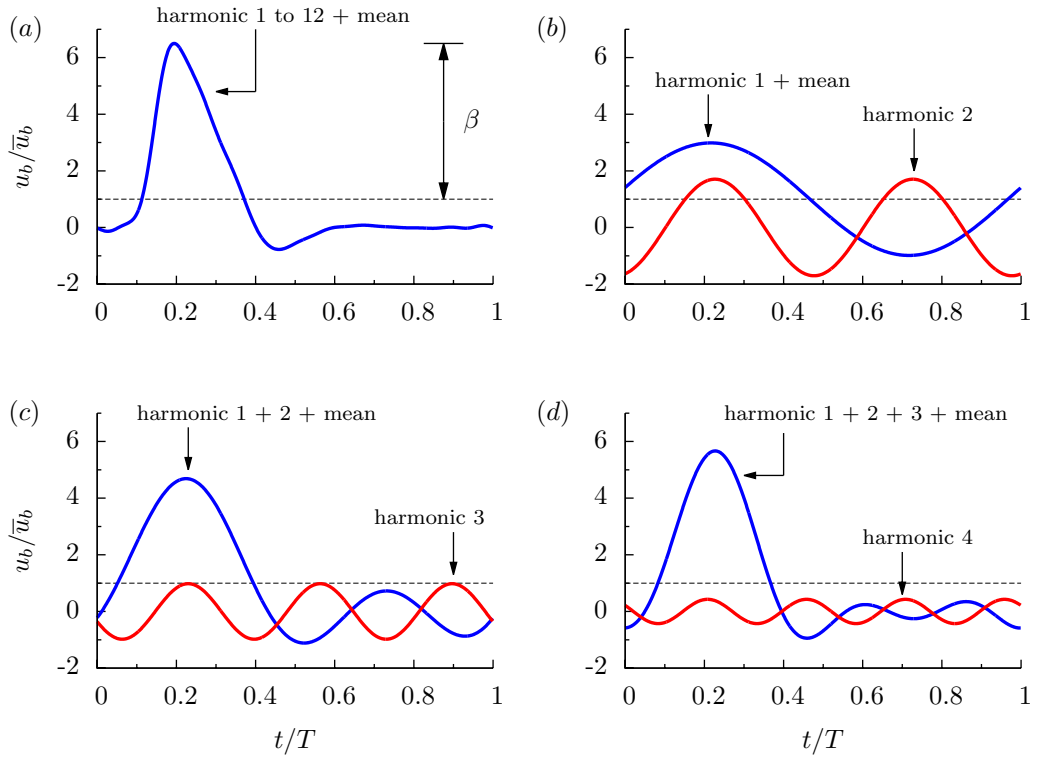

Figure 2.6: (a) 12 term Fourier Series of infrarenal aortic bulk flow rate. (b) Summation of harmonic 1 + mean and harmonic 3. (c) Summation of harmonic 1 + 2 + meanc and harmonic 3. (d) Summation of harmonic 1 + 2 + 3 + mean and harmonic 4. Fourier coefficients calculated using bulk flow rate data from Les et al. [68]. Figure is based on a similar figure from McDonald [77].

region. Blood flow that oscillates in direction while maintaining a net positive direction is referred to as flow reversal without separation (Tardu et al. [117]). Where as, blood flow with a flow direction at the wall that is opposite to the dominant direction is referred to as a recirculation zone. The extent of the flow reversal that occurs for a given pulse profile is governed by Wo. Close to the arterial wall, oscillations in the blood flow will be more aligned with the oscillations in the pressure gradient compared to the blood flow in the center region of an artery. As described by Hale et al. [40], near wall velocity is low, therefore it has less momentum and is more easily reversed by the pressure gradient.

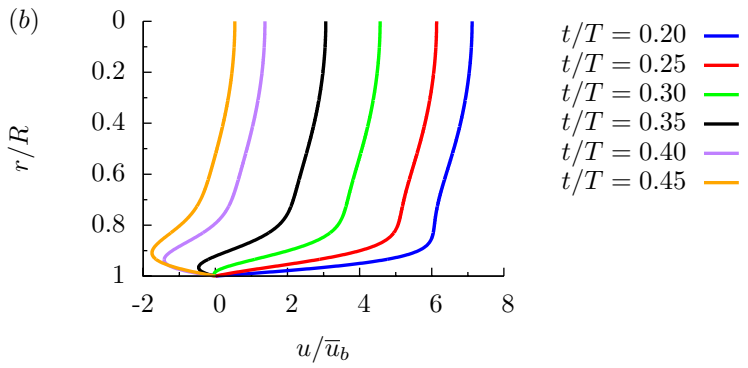

Figure 2.7: Analytical solution to a fully-developed pulsatile velocity profile in a pipe. Profiles calculated using bulk flow rate data from Les et al. [68]

Using the analytical solution shown in figure 2.7 and assuming a mean bulk blood flow rate of 20 ml s^{-1}, $\beta = 5.5$, $\mu = 0.0035$ kg m^{-1} s^{-1}, $\rho = 1050$ kg m^{-3} and $Wo = 15$, the highest WSS during the pulse is 2.4 N m^{-2}. This value occurs at $\phi/T = 0.17$, which is $\phi/T = 0.02$ prior to the maximum flow rate. As the flow decelerates during the later half of systole, the reversal in flow direction causes friction drag that acts opposite to the dominant flow direction. During the later half of diastole, WSS and the bulk flow are effectively zero. The mean WSS that occurs during a pulse can be calculated simply from the well-known Poiseuille equation as eqn. 2.22;

$$\overline{\tau}_w = -\mu 4\overline{u}_b/R. \tag{2.22}$$

Using the above parameters mean WSS is 0.04 N m^{-2}, which is not an accurate representation of the peak value caused by the pulsating flow. For cardiovascular flows where Wo and β values are substantially smaller than that which occur in the aorta, such as intracranial arteries, the Poiseuille equation can be used to give a reasonable approximation of the peak WSS.

Modeling assumptions applied to aortic flow

It is common in AAA studies to include the visceral arteries in the model of the aorta and an example of this can be seen in Les et al. [67]. In this thesis the visceral arteries have been removed from the aorta model and the infrarenal blood flow rate is applied at the supraceliac level in the aorta. This has been done previously in the literature by Biasetti et al. [13], Zambrano et al. [143], Poelma et al. [95], Basciano et al. [10] and reduces the complexity of the simulation since the blood flow behavior in the visceral arteries is not included in the simulation. It is assumed that removing the visceral arteries has minimal influence on the flow dynamics downstream in the AAA. Flow disturbances have been observed at the renal arteries (Ku [57]) but it is not suspected that they propagate downstream into the AAA. The validity of this assumption is supported by results that will be shown later in chapter 4 and 6. It is observed in these chapters that flow structures in the upstream neck region of an AAA stagnant at that location without interacting with the downstream AAA. This stagnation is due to the bulk flow rate being effectively zero during diastole.

It is also common in AAA studies to use patient-specific pulse profiles. Again an example of this can be found in Les et al. [67]. For the patients used in this thesis, data of their pulse profile is not available. Therefore the pulse profile found in Les et al. [68] is used for all patients. This profile was calculated using data from patients with AAA and therefore provides a good representation of the flow conditions that occur with patients having AAAs, as opposed to using pulse profiles from healthy patients.

Using eqn. 2.18 it can be determined that the length of the aorta is insufficient for the mean component of the Fourier series to fully develop (Caro et al. [18]) and the core

region of the aorta does not have the parabolic shape that is observed in steady Poiseuille flow. Real-life abdominal aortic flow deviates from the analytical solution shown in figure 2.6 in this regard. However, based on eqn. 2.19 the development length for the oscillating components of the Fourier series is only several cm (Wood [140]) before these components are fully developed. In chapters 4, 5 and 6 a bulk velocity profile is applied at the upstream inlet boundary. An oscillating boundary then quickly develops downstream in the inlet boundary. Chapter 7 and 8 are the first simulations that were completed for this thesis and different assumptions were made for the inlet conditions. In chapter 7 the blood flow is assumed to be steady and fully developed at the inlet. In chapter 8 the inlet condition is pulsatile and fully developed, which has been implemented in previous papers, such as Les et al. [67].

2.3 Hemodynamics analysis

The following is a summary of the methods used to perform analysis AAA hemodynamics in this thesis. Turbulent coherent structures are defined as regions of locally high vorticity that maintain their shape for an extended period of time. Here coherent structures are visualized using the Q-criterion (Hunt et al. [44]), where Q is defined as

$$Q = \left(\|\mathbf{\Omega}\|^2 - \|\mathbf{S}\|^2\right)/2 \tag{2.23}$$

with $\|\mathbf{S}\| = [\mathrm{tr}(\mathbf{S}\mathbf{S}^{\mathrm{T}})]^{1/2}$ and $\|\Omega\| = [\mathrm{tr}(\mathbf{\Omega}\mathbf{\Omega}^{\mathrm{T}})]^{1/2}$. The tensors $\mathbf{S} = \left(\nabla \boldsymbol{u} + \nabla \boldsymbol{u}^{\mathrm{T}}\right)/2$ and $\mathbf{\Omega} = \left(\nabla \boldsymbol{u} - \nabla \boldsymbol{u}^{\mathrm{T}}\right)/2$ are the strain and rotation-rate tensor, respectively. The quantity Q measures the amount that the rotation rate exceeds the strain rate. Coherent structures are identified using using this method in chapters $4-5$. Coherent structures can also be

identified using the λ_2-criterion introduced by Jeong & Hussain [50], where λ_2 is defined as the second largest eigenvalue of the tensor $\mathbf{S}^2 + \mathbf{\Omega}^2$. This method is used to identify coherent structures in chapter 8. The pressure coefficient C_p is defined as

$$C_p = 2\big(P - P_{ref}\big)/\big(\rho \overline{u}_b^2\big), \tag{2.24}$$

where the average pressure at the inlet boundary is used as the reference pressure P_{ref}. Results showing the pressure coefficient are presented in chapter 8. As mentioned in chapter 1, the friction drag exerted by blood flow on the arterial wall, referred to as wall shear stress (WSS), is thought to play an important role in regulating cardiovascular health. For laminar flow in a straight pipe, WSS can be calculated as a scalar using eqn. 2.22. In patient-specific arteries the geometry is more complex and WSS is calculated as a vector $\boldsymbol{\tau}_w = (\tau_{w,x}, \tau_{w,y}, \tau_{w,z})$ that is defined as the tangential component of the surface traction vector $\mathbf{t} = \boldsymbol{\tau}\boldsymbol{n}_s$, where $\boldsymbol{n}_s$ is a unit vector normal to the surface, $\boldsymbol{\tau} = 2\mu\mathbf{S}$ is the shear stress tensor. The tangential component of $\mathbf{t}$ is isolated by subtracting out the normal component through

$$\boldsymbol{\tau}_w = \mathbf{t} - (\mathbf{t} \cdot \boldsymbol{n}_s)\boldsymbol{n}_s. \tag{2.25}$$

The time-averaged WSS (TAWSS) is a scalar defined as

$$\text{TAWSS} = \frac{1}{t_f - t_i} \int_{t_i}^{t_f} \big\|\boldsymbol{\tau}_w\big\| dt, \tag{2.26}$$

where $\|.\|$ is the magnitude of a vector. A large number of time-averaged quantities have been derived in the literature based on the WSS vector (Arzani and Shadden [5]), two of which are used in this thesis. The oscillatory shear index (OSI), defined by He & Ku [43] is a

measure of the WSS vectors alignment during the pulse-cycle with its dominant direction and is defined as

$$\mathrm{OSI} = 0.5\left(1 - \frac{\left\|\overline{\boldsymbol{\tau}}_w\right\|}{\mathrm{TAWSS}}\right). \tag{2.27}$$

A high OSI value indicates oscillations about the dominant flow axis while low OSI indicates that the blood flows along a single direction during a pulse. The transverse time-averaged WSS (transWSS), first introduced by Peiffer et al. [91], defines the disturbance in the WSS vector and is defined as

$$\mathrm{transWSS} = \frac{1}{t_f - t_i}\int_{t_i}^{t_f}\left\|\boldsymbol{\tau}_w \cdot \left(\boldsymbol{n}_s \times \frac{\overline{\boldsymbol{\tau}}_w}{\left\|\overline{\boldsymbol{\tau}}_w\right\|}\right)\right\| dt, \tag{2.28}$$

where the term $\mathbf{n}_s \times \overline{\boldsymbol{\tau}}_w / \left\|\overline{\boldsymbol{\tau}}_w\right\|$ is a unit vector perpendicular to $\overline{\boldsymbol{\tau}}_w$ and tangent with the arterial wall. The metric transWSS is then the magnitude of $\boldsymbol{\tau}_w$ after being projected onto this vector and averaged over time. Low transWSS indicates the WSS vector is parallel with a single axis during the pulse-cycle. High transWSS is an indication that the instantaneous WSS vector fluctuations about the dominant axis and this can be an indication of turbulent flow conditions. Since a wide range of TAWSS values can occur in AAA, in this thesis transWSS is normalized by the local value for TAWSS. In Les et al. [67] and Suh et al. [113] OSI is calculated by time-averaging over 5 pulses. Results using these time-averaged WSS quantities are presented in chapter 4.

Peiffer et. al. [91] identified the following flow conditions that can occur during a cardiac cycle and their corresponding values of OSI and transWSS. Non-disturbed blood flowing along a single direction has an OSI = 0 and transWSS = 0. Blood flow that is oscillating

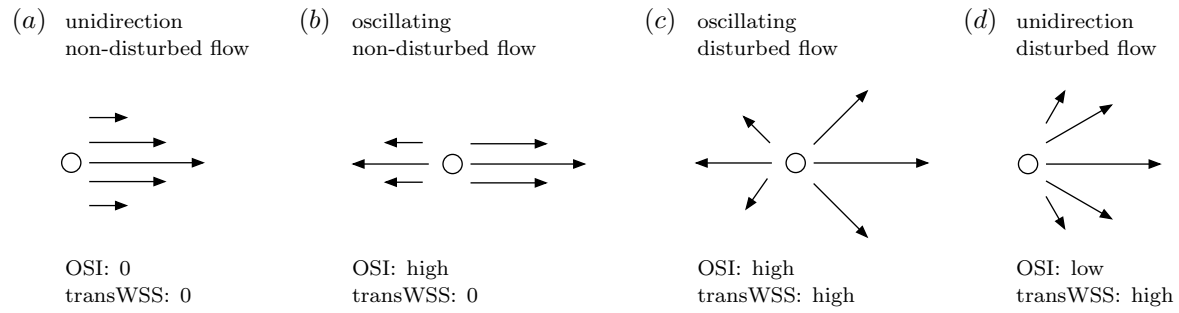

Figure 2.8: Graphical representation of instantaneous WSS vector allignment that can occur during a pulse-cycle. (a) Unidirection non-disturbed flow, (b) oscillating non-disturbed flow, (c) oscillating disturbed flow and (d) unidirection disturbed flow. Based on a similar figure from Peiffer et al. [91].

about a single axial direction has a high OSI and transWSS = 0, while oscillating and disturbed blood has both high OSI and transWSS. Unidirectional disturbed flow has a low OSI combined with a high transWSS and this condition identifies a turbulent flow that is traversing along a single direction.

2.4 Triple decomposition

Cardiovascular blood flow consists of a mean component superimposed with a oscillating pulse profile. For healthy arteries the blood flow are predominately laminar with the instantaneous velocity repeating every pulse with minimal variation. In large or diseased arteries with features, such as bends, bifurcations, aneurysms or stenosis the blood flow can transition to turbulence and there are additional stochastic oscillations superimposed on the periodic component. When a pulsatile flow is turbulent, the instantaneous velocity does not repeat every pulse, however flow statistics are stationary when taken at the same location within the period. Cantwell & Coles [17] observed from a study on turbulent vortex shedding, that

"turbulence is a local phenomenon, attached to and moving with the individual vortexes". It is shown in later chapters that this description also describes the turbulence that occurs in large AAA. The triple decomposition method introduced by Hussain & Reynolds [45] can be used to decompose a pulsatile turbulent flow quantity, such as the velocity vector $\boldsymbol{u}$, into

$$\boldsymbol{u} = \overline{\boldsymbol{u}} + \widetilde{\boldsymbol{u}} + \boldsymbol{u}', \tag{2.29}$$

where $\overline{\boldsymbol{u}}$ is the time average, $\widetilde{\boldsymbol{u}}$ is the periodic fluctuation, $\boldsymbol{u}'$ is the turbulent fluctuation and the total fluctuating component is defined as $\boldsymbol{u}'' = \widetilde{\boldsymbol{u}} + \boldsymbol{u}'$. This method is used to analyze data in chapters $3-4$, 6 and 8. Each period is segmented into M equidistant phase positions and at each phase N snapshots of the flow field are collected. The average of a flow quantity locked at a phase is calculated as

$$\langle \boldsymbol{u} \rangle|_m = \overline{\boldsymbol{u}} + \widetilde{\boldsymbol{u}}|_m = \frac{1}{N} \sum_{n=0}^{N-1} \boldsymbol{u}|_{t+nT}, \tag{2.30}$$

with the brackets $\langle . \rangle$ denoting the phase average of a quantity, the subscript m indicates phase position and the subscript $t + nT$ gives the temporal positions that the snapshots are collected. The time-average is then calculated by averaging the phase-locked values as

$$\overline{\boldsymbol{u}} = \frac{1}{M} \sum_{m=1}^{M} \langle \boldsymbol{u} \rangle|_m. \tag{2.31}$$

The time-average can also be calculated by integrating over the total number of pulses. Following Tardu et. al. [117] the phase average can be decomposed into a Fourier Series, such that

$$\langle \boldsymbol{u} \rangle = \overline{\boldsymbol{u}} + A_{\widetilde{\boldsymbol{u}},1} \cos\left(\omega t + \phi_{\widetilde{\boldsymbol{u}},1}\right) + \sum_{m=2}^{M/2} A_{\widetilde{\boldsymbol{u}},m} \cos\left(m\omega t + \phi_{\widetilde{\boldsymbol{u}},m}\right), \tag{2.32}$$

where $A_{\widetilde{\boldsymbol{u}},m}$ and $\phi_{\widetilde{\boldsymbol{u}},m}$ are the amplitude and phase, respectively, for the Fourier mode. The contribution of the fundamental Fourier mode to the phase average is

$$e_{\widetilde{\boldsymbol{u}}} = \langle \boldsymbol{u} \rangle - \overline{\boldsymbol{u}} - A_{\widetilde{\boldsymbol{u}},1} \cos\left(\omega t + \phi_{\widetilde{\boldsymbol{u}},1}\right) \tag{2.33}$$

and to quantify the extent that the phase average deviates from pure harmonic motion Scotti & Piomelli [106] defined the norm

$$\|e_{\widetilde{\boldsymbol{u}}}\|_v = \left(\frac{1}{T}\int_0^T e_{\widetilde{\boldsymbol{u}}}^2 / \langle \boldsymbol{u} \rangle^2 \mathrm{d}\varphi\right)^{1/2}. \tag{2.34}$$

Each component of the triple decomposition individually conserve mass and when phase averaging is applied to the momentum equation and the flow is both turbulent and pulsatile, it becomes

$$\partial\langle \boldsymbol{u} \rangle/\partial t + \langle \boldsymbol{u} \rangle \cdot \nabla \langle \boldsymbol{u} \rangle = -\nabla\langle p \rangle + \nu\nabla^2\partial\langle \boldsymbol{u} \rangle - \nabla\langle \boldsymbol{u}'\boldsymbol{u}' \rangle, \tag{2.35}$$

with the last term on the right hand side being the Reynolds stress tensor locked at a phase. The $\langle \boldsymbol{u}'\boldsymbol{u}' \rangle$ term is a function of both space and phase-position and is calculated as

$$\langle \boldsymbol{u}'\boldsymbol{u}' \rangle|_m = \frac{1}{N}\sum_{n=0}^{N-1} \boldsymbol{u}'\boldsymbol{u}'|_{t+nT}. \tag{2.36}$$

A large number of snapshots is required to obtain statistically converged phase-averages. For example, in a experimental study on vortex shedding by Zhou et al. [146] $N = 5800$ snapshots were collected. Although in another experimental study on pulsatile jets by Choutapalli

et al. [23] fewer snapshots were used and $N = 100$. For numerical studies N is limited to the computational resources required to simulate pulses. In a numerical vascular study by Chnafa et al. [22] $N = 30$ snapshots were used when phase-averaging the blood flow in a left ventricle. For the numerical simulation of accelerating channel flow by He & Seddighi [42] phase-averages were calculated using $N = 10$ snapshots and spatial averaging in homogeneous directions. For DNS, the quality of the phase-averaged statistics needs to be weighed against the computational resources and data storage requirements needed to collect the snapshots.

When time averaging is applied to the momentum and the flow is both turbulent and pulsatile, the momentum equation becomes

$$\overline{\boldsymbol{u}} \cdot \nabla \overline{\boldsymbol{u}} = -\nabla \overline{p} + \nu \nabla^2 \overline{\boldsymbol{u}} - \nabla \overline{\widetilde{\boldsymbol{u}}\widetilde{\boldsymbol{u}}} - \nabla \overline{\boldsymbol{u}'\boldsymbol{u}'}, \tag{2.37}$$

where the last two terms on the right hand side of the equation give the contribution to the time-averaged Reynolds stress tensor by periodic and turbulent fluxes, respectively. Since these terms are time-averages they are functions of space only and are calculated as

$$\overline{\widetilde{\boldsymbol{u}}\widetilde{\boldsymbol{u}}} = \frac{1}{M} \sum_{m=1}^{M} \widetilde{\boldsymbol{u}}\widetilde{\boldsymbol{u}}|_m \qquad \overline{\boldsymbol{u}'\boldsymbol{u}'} = \frac{1}{M} \sum_{m=1}^{M} \left\langle \boldsymbol{u}'\boldsymbol{u}' \right\rangle|_m \tag{2.38}$$

Cantwell & Coles [17] concluded that when developing a turbulence model for a time-averaged flow both the periodic and turbulent components of the Reynolds stresses need to by incorporated into the model. Using triple decomposition the phase-averaged fluctuating kinetic energy can be decomposed as

$$\left\langle \boldsymbol{u}'' \cdot \boldsymbol{u}'' \right\rangle / 2 = \widetilde{\boldsymbol{u}} \cdot \widetilde{\boldsymbol{u}} / 2 + \left\langle \boldsymbol{u}' \cdot \boldsymbol{u}' \right\rangle / 2, \tag{2.39}$$

where the periodic kinetic energy component is the first term on the right hand side and the turbulent kinetic energy (TKE) component is the second term on the right hand side. The phase-average equation for the transport of TKE is

$$\frac{\partial\langle \boldsymbol{u}' \cdot \boldsymbol{u}'\rangle/2}{\partial t} + \langle \boldsymbol{u}\rangle \cdot \nabla\langle \boldsymbol{u}' \cdot \boldsymbol{u}'\rangle/2 = \langle P_k\rangle + \langle T_k\rangle + \langle D_k\rangle + \langle \Pi_k\rangle + \langle \epsilon\rangle. \tag{2.40}$$

The terms on the right side are the phase-averaged turbulent production $\langle P_k\rangle$, turbulent transport $\langle T_k\rangle$, viscous diffusion $\langle D_k\rangle$, pressure transport $\langle \Pi_k\rangle$, dissipation due to viscosity $\langle \epsilon\rangle$ and are defined as follows

$$\langle P_k\rangle = -\langle \boldsymbol{u}'\boldsymbol{u}'\rangle{:}\nabla\langle \boldsymbol{u}\rangle \qquad \langle T_k\rangle = \nabla \cdot \langle \boldsymbol{u}' \cdot \boldsymbol{u}'\boldsymbol{u}'\rangle/2 \tag{2.41}$$

$$\langle D_k\rangle = \nu\nabla^2\langle \boldsymbol{u}' \cdot \boldsymbol{u}'\rangle/2 \qquad \langle \Pi_k\rangle = \nabla \cdot \langle p'\boldsymbol{u}'\rangle \tag{2.42}$$

$$\langle \epsilon\rangle = 2\nu\langle \mathbf{s}'{:}\mathbf{s}'\rangle \tag{2.43}$$

where $\mathbf{s}' = \left(\nabla \boldsymbol{u}' + \nabla \boldsymbol{u}'^{\mathrm{T}}\right)/2$ is the fluctuating strain-rate tensor and the operator **:** gives the double inner product of two tensors. For the case of two second-rank tensors this operation produces a scalar. Kinetic energy is transfered to the largest-scale turbulent fluctuations through the production $\langle P_k\rangle$, then transfers to progressively smaller scales and at the smallest scale present the kinetic energy is dissipated through $\langle \epsilon\rangle$ as heat. The production term can be viewed as the working of the Reynolds stress against the mean velocity gradient of the flow, similar to viscosity resisting deformation by the instantaneous velocity gradients and

dissipating the energy as heat (George [38]). The remaining terms in eqn. 2.40 involve the transport of TKE.

The Kolmogorov length scale gives an order of magnitude representation of the smallest length scale of turbulent motion (Pope [96]) and it's phase and time-averages are calculated as

$$\left\langle \eta \right\rangle = (\nu^3/\left\langle \epsilon \right\rangle)^{1/4} \tag{2.44}$$

$$\overline{\eta} = (\nu^3/\overline{\epsilon})^{1/4}, \tag{2.45}$$

respectively. The quantity $\left\langle \eta \right\rangle$ gives the smallest length scale of turbulent during a pulse and $\overline{\eta}$ gives an overall representation of the smallest scale during a pulse. Ideally for DNS the edge length of a computational grid cell should match the smallest scale of turbulence. Paraphrasing from Moin and Mahesh [82] "this requirement is probably too stringent. The smallest resolved length scale is required to be of $\mathcal{O}(\eta)$, not equal to η". Thus it is desirable when directly solving the governing equations to have the numerical grid resolution close to the smallest scale of turbulent motion but it is not necessary for the grid to be as small as the smallest length scale.

When the statistics are independent of the time origin, there will be no periodic fluctuation, i.e. $\widetilde{\boldsymbol{u}} = 0$ and the time-averaged Reynolds stress tensor reduces to $\overline{\boldsymbol{u}'\boldsymbol{u}'}$. This type of simulation applies to a case shown in chapter 3 section 3.2.1. In chapter 7 a modeling assumption is applied where it is assumed is that the blood flow is both laminar and non-pulsatile and for this chapter both $\widetilde{\boldsymbol{u}}$, $\boldsymbol{u}'$ and the Reynolds stress tensor are zero. For the

remaining cases presented in this thesis, the flow is both pulsatile and turbulent.

2.5 Dynamic mode decomposition

Dynamic mode decomposition (DMD) is a method where a set of data is decomposed into modes that oscillate at specific frequencies. This method was introduced by Rowley et al. [101], Schmid [105] and Bagheri et al. [7]. In this thesis it is used to analysis data in chapters 3 and 6. The DMD method has been previously applied to a range of diverse applications, such as bluff body wakes (Parkin et al. [87]), combustion in gas turbines (Motheau et al. [83]), wind turbine wakes (Sarmast et al. [102]), cyclic robot movement (Berger et al. [11]) and electrical power system oscillation (Barocio et al. [8]). It has been shown in figure 2.6 that a blood pulse can be represented as a Fourier series and as discussed in the previous section, there can be turbulent fluctuations superimposed on periodic oscillations. The DMD method segments a dataset into modes that correspond to specific frequencies. Afterwards a low-order model of the dataset can be constructed, where high-frequency modes are excluded from the reconstruction. Although not limited to this, the dataset can be snapshots of the velocity field from a patient-specific artery and collected over a pulse. This type of decomposition shares a close relationship with triple decomposition (Mezic [80]) and the low-order representation of the velocity field closely resembles the phase average. The DMD modes contain flow motion at a single frequency but the method does not make a distinction between periodic and turbulent oscillations. Therefore a DMD mode can contain both types of oscillation, where as triple decomposition distinguishes between periodic and turbulent oscillations. For fluid flow data, produced either through experiments or numerical simulations, a snapshot of the

instantaneous flow field is constructed that stores the individual components of velocity u, v and w in a vector $\boldsymbol{\psi}$. The total number of entries in the vector is n and the order that these entries are arranged is not important. The interval between consecutive snapshots is Δt and the entire dataset is stored in the matrix

$$\boldsymbol{\Psi} = \begin{pmatrix} \boldsymbol{\psi}_1 & \boldsymbol{\psi}_2 & \cdots & \boldsymbol{\psi}_m \end{pmatrix} \in \mathbb{R}^{n \times m}. \tag{2.46}$$

The total number of snapshots in the matrix is m and for engineering relevant flows, when the entire three-dimensional flow field is simulated $n >> m$. A second matrix is defined that gives the dataset shifted forward in time by Δt, where

$$\boldsymbol{\Psi}' = \begin{pmatrix} \boldsymbol{\psi}_2 & \boldsymbol{\psi}_3 & \cdots & \boldsymbol{\psi}_{m+1} \end{pmatrix} \in \mathbb{R}^{n \times m}. \tag{2.47}$$

The operator $\mathbf{A}$ is then defined as

$$\boldsymbol{\Psi}'\boldsymbol{\Psi}^{\dagger} = \mathbf{A} \in \mathbb{R}^{n \times n}, \tag{2.48}$$

where $\dagger$ is the Moore-Penrose pseudoinverse. The matrix $\mathbf{A}$ is a best-fit operator relating $\boldsymbol{\Psi}'$ and $\boldsymbol{\Psi}$ and it's eigenvalues and eigenvectors describe the dynamic behavior the system. Due to the large size of n it is not possible to directly calculate $\mathbf{A}$ and instead it must be projected onto a lower-dimensional subspace, which will result in a significantly smaller system that can be solved using direct methods (Bagheri et al. [7]). The objective of DMD is to calculate a low-order approximation of the operator $\mathbf{A}$. This allows the eigenvalues and eigenvectors of $\mathbf{A}$ to be approximated without having knowledge of $\mathbf{A}$. For the case where the final snapshot $\boldsymbol{\psi}_{m+1}$ is the linear combination of the previous snapshots, a low-order approximation of $\mathbf{A}$

that shifts the snapshots forward in time is defined as $\mathbf{C} \in \mathbb{R}^{m \times m}$ and 2.48 can be represented as

$$\mathbf{\Psi}' = \mathbf{A}\mathbf{\Psi} = \mathbf{\Psi}\mathbf{C}. \tag{2.49}$$

The low-order matrix is then

$$\mathbf{C} = \begin{pmatrix} 0 & 0 & \cdots & 0 & c_1 \\ 1 & 0 & \cdots & 0 & c_2 \\ \vdots & \vdots & \ddots & \vdots & \vdots \\ 0 & 0 & \cdots & 1 & c_m \end{pmatrix} \tag{2.50}$$

and by using the last column in $\mathbf{C}$, the final snapshot $\boldsymbol{\psi}_{m+1}$ can then be expressed as the linear combination of the preceding snapshots, where

$$\boldsymbol{\psi}_{m+1} = \boldsymbol{\psi}_1 c_1 + \boldsymbol{\psi}_2 c_2 + \cdots \boldsymbol{\psi}_m c_m. \tag{2.51}$$

For the case where $\boldsymbol{\psi}_{m+1} = \boldsymbol{\psi}_0$ then $c_1 = 1$ and $c_j = 0$ for all other values of j (Rowley et al. [101]). This will be the case when DMD is applied to phase-averaged data since oscillations repeat every pulse. Performing an decomposition on 2.49 yields

$$\mathbf{C} = \mathbf{Z}\mathbf{\Lambda}\mathbf{Z}^{-1} = \mathbf{T}^{-1}\mathbf{\Lambda}\mathbf{T}, \tag{2.52}$$

where $\mathbf{\Lambda} = \text{diag}(\lambda_1 \cdots \lambda_m)$ are the eigenvalues, often referred to as ritz values, $\mathbf{Z}$ are the eigenvectors, $\mathbf{T}$ is a Vandermode matrix defined as

$$\mathbf{T} \in \mathbb{R}^{m \times m} = \begin{pmatrix} 1 & \lambda_1^1 & \cdots & \lambda_1^{m-1} \\ 1 & \lambda_2^1 & \cdots & \lambda_2^{m-1} \\ \vdots & \vdots & \ddots & \vdots \\ 1 & \lambda_m^1 & \cdots & \lambda_m^{m-1} \end{pmatrix}. \tag{2.53}$$

The eigenvectors and eigenvalues from $\mathbf{C}$ are a subset of those from the larger matrix $\mathbf{A}$ (Rowley et al. [101]) and contain information on the dynamics of the data set. The eigenvectors $\mathbf{Z}$ are related to the Vandermode matrix $\mathbf{T}$, such that

$$\mathbf{Z} = \mathbf{T}^{-1}\mathbf{D}^{-1}. \tag{2.54}$$

The diagonal matrix $\mathbf{D} = \text{diag}(d_1 \cdots d_m)$ gives the mode amplitudes and the energy of a mode is defined as $\|d_k\|^2$. The rows in $\mathbf{T}$ give the dynamic behavior for a particular mode and therefore the modes $\mathbf{\Phi} = (\boldsymbol{\phi}_1 \cdots \boldsymbol{\phi}_m) \in \mathbb{R}^{n \times m}$ are calculated as

$$\mathbf{\Phi} = \mathbf{\Psi}\mathbf{T}^{-1}\mathbf{D}^{-1} = \mathbf{\Psi}\mathbf{Z}. \tag{2.55}$$

The modes are non-orthogonal with a $\mathscr{L}^2$-norm of $\|\boldsymbol{\phi}_k\|_2 = \left(\boldsymbol{\phi}_k^* \boldsymbol{\phi}_k\right)^{1/2} = 1$ and each mode represents the spatial structures oscillating at a specific frequency. The angular frequency ω_k corresponding to each mode is calculated as

$$\omega_k = \arg\left(\lambda_k\right)/\Delta t. \tag{2.56}$$

The largest angular frequency that can be determined by the decomposition is defined by the Nyquist criterion and is $\pi/\Delta t$. The mode with $\omega_k = 0$ gives the time-average of the data

contained in the matrix $\mathbf{\Psi}$. The growth rates α_k corresponding to each mode are calculated using

$$\alpha_k = \log\left(\|\lambda_k\|\right)/\Delta t. \tag{2.57}$$

Modes with large negative α_k values decay over time and may not contribute significantly to the reconstruction. The original matrix $\mathbf{\Psi}$ is then reassembled through

$$\mathbf{\Psi} = \begin{pmatrix} \boldsymbol{\phi}_1 & \boldsymbol{\phi}_2 & \cdots & \boldsymbol{\phi}_m \end{pmatrix} \begin{pmatrix} d_1 & 0 & \cdots & 0 \\ 0 & d_2 & \cdots & 0 \\ \vdots & \vdots & \ddots & \vdots \\ 0 & 0 & \cdots & d_m \end{pmatrix} \begin{pmatrix} 1 & \lambda_1^1 & \cdots & \lambda_1^{m-1} \\ 1 & \lambda_2^1 & \cdots & \lambda_2^{m-1} \\ \vdots & \vdots & \ddots & \vdots \\ 1 & \lambda_m^1 & \cdots & \lambda_m^{m-1} \end{pmatrix}. \tag{2.58}$$

For most datasets the final snapshot $\boldsymbol{\psi}_{m+1}$ is not a linear combination of the preceding snapshots and eqn. 2.49 becomes

$$\mathbf{\Psi}' = \mathbf{A}\mathbf{\Psi} = \mathbf{\Psi}\underbrace{\mathbf{T}^{-1}\mathbf{\Lambda}\mathbf{T}}_{\mathbf{C}} + \boldsymbol{r}\boldsymbol{e}^{\mathrm{T}}, \tag{2.59}$$

where $\boldsymbol{r}$ is the residual vector and $\boldsymbol{e} = (0, 0...1)$. It is desirable to chose the number of snapshots and the spacing between snapshots to minimize $\boldsymbol{r}$.

In practice computing $\mathbf{C} = \mathbf{\Psi}^{\dagger}\mathbf{\Psi}'$ may produce an ill-conditioned matrix (Chen et al. [21]). It was suggested by Schmid [105] that the matrix preconditioning technique singular value decomposition (SVD) can be used to compute the low-order map of $\mathbf{A}$. Performing SVD on $\mathbf{\Psi}$ yields

$$\mathbf{M}^{1/2}\mathbf{\Psi} = \mathbf{U}\mathbf{\Sigma}\mathbf{W}^{*}, \tag{2.60}$$

where $\mathbf{U} \in \mathbb{R}^{n\times m}$ and $\mathbf{W} \in \mathbb{R}^{m\times m}$ are orthogonal unitary matrices, $\mathbf{\Sigma} = \text{diag}(\sigma_1 \cdots \sigma_m)$ is a diagonal matrix with non-negative real numbers and the superscript $*$ is the complex-conjugate-transpose of a matrix. Here the diagonal matrix $\mathbf{M} \in \mathbb{R}^{n\times n}$ is introduced with diagonal entries that give the volume ratio of a grid cell and this matrix scales the velocity components based on the size of the computational grid cell. The singular values can be solved by constructing a weighted inner product matrix

$$\mathbf{\Psi}^*\mathbf{M}\mathbf{\Psi} \in \mathbb{R}^{m\times m}, \tag{2.61}$$

with the above calculation yielding a symmetric square matrix with diagonal entries that are proportional to the volume-averaged kinetic energy for the snapshot. Non-diagonal entries give the correlation between different snapshots. Performing an eigenvalue decomposition on (2.61) yields

$$\mathbf{\Psi}^*\mathbf{M}\mathbf{\Psi} = \big(\mathbf{W}\mathbf{\Sigma}\mathbf{U}^*\big)\big(\mathbf{U}\mathbf{\Sigma}\mathbf{W}^*\big) = \mathbf{W}\mathbf{\Sigma}^2\mathbf{W}^* \tag{2.62}$$

and the left singular values are calculated as $\mathbf{U} = \mathbf{M}^{1/2}\mathbf{\Psi}\mathbf{W}\mathbf{\Sigma}^{-1}$. The application of the above SVD in fluid mechanics is commonly referred to as snapshot proper orthogonal decomposition (sPOD) (Sirovich [108]). The columns of the left singular values $\mathbf{U}$ give orthogonal spatial modes and the rows of the right singular values $\mathbf{W}$ gives the temporal variation in the mode. The proportion of the total kinetic energy associated with each mode is $\sigma_k/\mathcal{E}$, where $\mathcal{E} = \sum_{k=1}^{m} \sigma_k$. Unlike the DMD modes, the modes from the matrix $\mathbf{U}$ will contain flow motion at multiple frequencies. Using the SVD of $\mathbf{\Psi}$, eqn. (2.48) can be modified such that

$$\mathbf{U}^*\mathbf{M}^{1/2}\boldsymbol{\Psi}'\boldsymbol{\Psi}^\dagger\mathbf{M}^{-1/2}\mathbf{U} = \mathbf{U}^*\mathbf{A}\mathbf{U} \in \mathbb{R}^{m\times m}. \tag{2.63}$$

and the above equation gives a low-order map of the larger matrix $\mathbf{A}$. Using the SVD to perform a Moore-Penrose pseudoinverse of $\boldsymbol{\Psi}^\dagger\mathbf{M}^{-1/2} = \mathbf{W}\boldsymbol{\Sigma}^{-1}\mathbf{U}^*$, the terms on the left hand side of eqn. 2.63 can be modified and performing an eigenvalue decomposition yields

$$\boldsymbol{\Sigma}^{-1}\mathbf{W}^*\boldsymbol{\Psi}^*\mathbf{M}\boldsymbol{\Psi}'\mathbf{W}\boldsymbol{\Sigma}^{-1} = \mathbf{Y}\boldsymbol{\Lambda}\mathbf{Y}^{-1}, \tag{2.64}$$

where $\mathbf{Y} \in \mathbb{R}^{m\times m}$ are eigenvectors and $\boldsymbol{\Lambda}$ containing the identical eigenvalues found in eqn. 2.52. An advantage of the above formation is that a majority of the entries in the weighted inner product $\boldsymbol{\Psi}^*\mathbf{M}\boldsymbol{\Psi}'$ were calculated previously in (2.61) and do not need to be recomputed (Tu and Rowley [123], Belson et al. [100]). The eigenvectors calculated from $\mathbf{C}$ are related to the eigenvectors from eqn. 2.64 through

$$\mathbf{Z} = \mathbf{W}\boldsymbol{\Sigma}^{-1}\mathbf{Y}. \tag{2.65}$$

The modes are then calculated by combining eqn. 2.65 and eqn. 2.55

$$\boldsymbol{\Phi} = \mathbf{M}^{-1/2}\mathbf{U}\mathbf{Y} = \boldsymbol{\Psi}\mathbf{W}\boldsymbol{\Sigma}^{-1}\mathbf{Y}. \tag{2.66}$$

and therefore the modes are the projection of the eigenvectors $\mathbf{Y}$ onto the vector space $\mathbf{U}$. A proof showing the eigenvectors and eigenvalues from eqn. 2.64 are a subset of those from the operator $\mathbf{A}$ was given by Tu [122] and is as follows:

$$\mathbf{U}^*\mathbf{A}\mathbf{U}\mathbf{Y} = \mathbf{Y}\boldsymbol{\Lambda} \qquad \mathbf{U}\mathbf{U}^*\mathbf{A}\mathbf{U}\mathbf{Y} = \mathbf{U}\mathbf{Y}\boldsymbol{\Lambda} \tag{2.67}$$

$$\underbrace{\mathbf{U}\mathbf{U}^*}_{\mathbf{I}}\mathbf{A}\mathbf{\Phi} = \mathbf{\Phi}\mathbf{\Lambda}, \tag{2.68}$$

where $\mathbf{I} \in \mathbb{R}^{n\times n}$ is the identity matrix. The amplitude of the modes can then be calculated using the method shown in Sarmast et al. [102], where by rearranging the below equation

$$\mathbf{\Psi} = \underbrace{\mathbf{M}^{-1/2}\mathbf{U}\mathbf{Y}}_{\mathbf{\Phi}}\mathbf{D}\mathbf{T} = \mathbf{M}^{-1/2}\mathbf{U}\mathbf{\Sigma}\mathbf{W}^* \tag{2.69}$$

the amplitudes can be calculated as

$$\mathbf{D} = \mathbf{Y}^*\mathbf{\Sigma}\mathbf{W}^*\mathbf{T}^{-1}. \tag{2.70}$$

By using the above method $\mathbf{D}$ can be calculated using only matrices of size $m \times m$. An alternative method that can be used to calculate $\mathbf{D}$ is the optimal amplitudes algorithm presented in Jovanovic et. al. [51]. It is also possible to calculate the amplitudes simply through $\mathbf{D} = \mathbf{\Phi}^{-1}\mathbf{\Psi}\mathbf{T}^{-1}$, but this procedure will involve using a matrices of size $n \times m$.

Since each mode represents the spatial structures oscillating at a specific frequency the flow field can be reconstructed as

$$\boldsymbol{\psi}_j = \sum_{k=1}^{m} \boldsymbol{\phi}_k d_k \underbrace{\exp\left(\alpha_k t_j + \mathrm{i}\omega_k t_j\right)}_{\lambda_k^{j-1}} \qquad j = (1 \cdots m), \tag{2.71}$$

where $t_j = (1-j)\Delta t$. By limiting eqn. 2.71 to only low frequency modes a low-order reconstruction of the flow field can be obtained that contains only the large-scale flow structures.

Belson et al. [100] presented the computational challenges of performing DMD and a summary of their discussion is follows. Since the size of the matrix $\mathbf{\Psi}^*\mathbf{M}\mathbf{\Psi}$ is relatively small,

it is trivial to perform an eigenvalue decomposition once it is calculated. The challenge arises from calculating the inner product matrix when either n or m are large. When the snapshots contain large amounts of data it is not possible to load the entire matrix $\mathbf{\Psi}$ into memory. When this is the case the individual vectors $\boldsymbol{\psi}$ are loaded into memory as needed. For the off-diagonal entries in $\mathbf{\Psi}^*\mathbf{M}\mathbf{\Psi}$ only two vectors need to loaded into memory at a given time and for the entries in $\mathbf{\Psi}^*\mathbf{M}\mathbf{\Psi}$ along the diagonal only a single vector is loaded. Since the computation of each individual entry in $\mathbf{\Psi}^*\mathbf{M}\mathbf{\Psi}$ is independent it is possible to parallelize the process among several processors. For example if $m = 400$ and taking into account symmetry, the matrix $\mathbf{\Psi}^*\mathbf{M}\mathbf{\Psi}$ contains 80200 entries that need to be calculated. This task could be divided amongst 48 processors where 47 of the processors calculate 1670 of the entries and a single processor calculates the remaining 1710 entries. Afterwards a single processor gathers the entries and assembles the inner product matrix. Here parallelization is done using the MPI Python module mpi4py. To calculate an individual mode $\boldsymbol{\phi}$ the matrix $\mathbf{\Psi}$ is required. Again since the entire matrix is too large be loaded into memory, to perform this calculation individual $\boldsymbol{\psi}$ vectors are loaded into memory.

Chapter 3

Dynamics of pulsatile low-Reynolds number channel flow

Abstract

Direct numerical simulation of pulsatile channel flow is performed at a low-Reynolds and intermediate frequency range. The non-dimensional parameters for the study are $Re_\tau = 180$, $Wo = 15$ and $A_{u_c}/\overline{u}_c = 0.44$. The periodic component of the velocity is found to deviate significantly from the laminar Stokes solution. This is due to the propagation of turbulent structures outward of the oscillating shear layer into the outer region of the boundary layer. The time-averaged velocity collapses onto a profile that is similar to the non-pulsatile case, except that the log region is shifted upward. It is found that close to the wall there is significantly less phase-lag in the streamwise Reynolds stress component compared to the other components. All Reynolds stress components deviate substantially from single harmonic motion. A quadrant analysis of the turbulent shear stress highlights the variation of fluid structure motions through different phases in the pulse. It is shown that these components

experience varying amounts of phase-lag. This work expands on the existing literature by investigating in detail a case with parameters comparable to a large artery. In the literature more focus has been given to high-frequency cases since these are more comparable to industrial applications.

3.1 Introduction

Complex turbulent flow structures can occur in large arteries with abnormal pathologies for example in abdominal aorta aneurysms. Under these conditions the oscillating shear layer has a significant influence on the turbulence. The objective of this study is to investigate turbulence variations in a simplified channel flow geometry using pulsatile flow conditions that are comparable to those found in large arteries in the human cardiovascular system. Direct numerical simulation of the pulsatile channel flow is performed using the open source code OpenFOAM. There is a gap in the understanding of the flow dynamics that occur for low-Reynolds and low-frequency pulsatile conditions.

The length scale is the channel half-height h and the velocity scale is the friction velocity $u_\tau = \sqrt{\tau_w/\rho}$, where $\tau_w = \mu \partial \overline{u}/\partial y|_{y=0}$, ρ is the density, μ is the dynamic viscosity and $\overline{u}$ is the time-averaged streamwise velocity. The non-dimensional parameters are the friction Reynolds number Re_τ, the Womersley number Wo defined as

$$Re_\tau = h/\delta \tag{3.1}$$

$$Wo = h\sqrt{\omega/\nu}. \tag{3.2}$$

and the ratio of the oscillating component of the centerline velocity to the time-averaged component $A_{u_c}/\overline{u}_c$. Where $\delta = \nu/u_\tau$ is the viscous length scale, $\omega = 2\pi/T$ is the angular frequency, $\nu = \mu/\rho$ is the kinematic viscosity. The superscript $^+$ denotes the viscous scaling of length by δ, velocity by u_τ and time by ν/u_τ^2. Oscillating shear is confined to a boundary layer of thickness $l_s = (2\nu/\omega)^{1/2}$, referred to as the Stokes length and this can be expressed in viscous units as

$$l_s^+ = \sqrt{2/\omega^+}. \tag{3.3}$$

Pulsatile flows can range from small arteries to oceanic and atmospheric flows. When $l_s^+ < 1$ the flow is considered to be in the high-frequency range and the oscillating Stokes layer is confined to a thin layer within the viscous region close to the wall. At this frequency the turbulence in the outer region is uncoupled from the oscillations. When $l_s^+ < 10$ the flow is referred to as quasi-laminar since the periodic component of the velocity corresponds to the analytical Stokes solution, where

$$\widetilde{u} = \frac{\mathcal{A}}{\mathrm{i}\omega\rho}\left[1 - \frac{\cosh\left(Wo\mathrm{i}^{1/2}y/h\right)}{\cosh\left(Wo\mathrm{i}^{1/2}\right)}\right]\exp\left(\mathrm{i}\omega t\right). \tag{3.4}$$

At this point the shear from the Stokes layer begins to propagate past the viscous layer and there is some influence on the flow in the outer region. When $10 < l_s^+ < 20$ the flow is considered to be in the intermediate-frequency range and there is significant pulsatile inertial effects on the turbulence. Most cardiovascular flows are laminar and at a frequency that is lower than most industry or environmental applications, thus the Stokes length extends well into the outer region of most arteries. The exception to this is in great vessels, such as the

aorta, where the flow is in the intermediate-frequency range. Other smaller arteries, such as intracranial arteries, may experience turbulent conditions but $l_s^+ > 20$ and the flow behaves in a quasi-steady state.

It was proposed by Scotti & Piomelli [106] that the Stokes length, which is based on laminar assumptions, does not capture the propagation of turbulent structures past the oscillating shear layer. Using the eddy viscosity the Stokes length can be written as $l_t = \left(2(\nu+\nu_t)/\omega\right)^{1/2}$. The eddy viscosity can be expressed as $\nu_t = \kappa \overline{u}_\tau l_t$, where κ is the von Karman constant. The turbulent Stokes length can be expressed as

$$l_t^+ = \kappa l_s^{+2}/2 + l_s^+ \sqrt{1 + \left(\kappa l_s^+/2\right)^2}. \tag{3.5}$$

At high frequencies $l_t^+ \approx l_s^+$ while at low frequencies $l_t^+ \approx \kappa (l_s^+)^2$.

There has been a significant amount of research previously performed on pulsatile and oscillating flows. In a seminal paper by Scotti & Piomelli [106], they investigated numerically pulsating channel flow at $Re_\tau = 350$, $A_{u_c}/\overline{u}_c \approx 0.7$ and $l_s^+ = 4.4-70$. Their study verified that when $2l_t^+$ is significantly smaller than h there is a decoupling between the Stokes boundary layer and the core region of the channel. They found that during the acceleration portion of the pulse the flow structures consisted of elongated streaks and by the deceleration phase the streaks had developed turbulent spots that eventually encompass the entire flow. In another seminal paper by Tardu et al. [117] pulsating channel flow was experimentally studied at $Re_c = \overline{u}_c h/\nu = 8500$, $\beta = 0.1 - 0.7$ and $l_s^+ = 2.9 - 34$. They showed that the time-averaged quantities are not significantly affected by the oscillations in the flow. This observation was also found to be true when the amplitude of the flow oscillations was sufficient to cause flow

reversal at the wall. A recent work by Papadopoulos & Vouros [86] looked at pulsating pipe flow in the high frequency region with $Re_\tau \approx 180$, $A_{u_c}/\overline{u}_c = 0.16 - 0.63$ and $l_s^+ = 2.4 - 6.8$. Their work further supported the notion that the laminar Stokes solution is valid for these high-frequency flows and amplitude has minimal affect while frequency is the dominant parameter. Their results identify that there is no distinction in flow behavior between a high or very-high frequency regimes. Sundstrom et al. [114] investigated pulsating pipe flow with the superposition of two pulsations at different frequencies and $Re_\tau \approx 900$ and $l_s^+ = 8 - 25$. The double frequency case was shown to closely match the superposition of the oscillating components from single frequencies and the time-averaged quantities are unaffected by the superposition of the oscillating components. Weng et al. [135] looked at low-amplitude pulsating channel flow at $Re_\tau = 350$, $A_{u_c}/\overline{u}_c \approx 0.1$ and $l_s^+ = 7.07 - 44.72$. The non-linear components of the perturbation field were found to increase with l_s^+, up to $l_s^+ = 18.26$.

In He & Seddighi [42] a channel flow was studied that underwent rapid increase in flow rate. Initially $Re_\tau \approx 178$ and after the increase $Re_\tau \approx 418$. The transitional process described by the authors shares similarities to the transitional process with the present pulsatile channel flow simulation. The wall-normal and spanwise turbulent fluctuations were found by He & Seddighi [42] to remain unchanged for a substantial period of time after the increase in flow rate, while the streamwise fluctuations increased immediately after the increase in flow rate. This was attributed by the authors to the formation of elongated streaks, which the authors described as large coherent structures that differ from the turbulence experienced in steady channel flow. The transitional process was described by the authors as a thin boundary layer of high strain that develops close to the wall and then propagates outward. The flow undergoes a pre-transition, transition and fully turbulent stage during this process.

During the pre-transition stage stable elongated streaks form and during the transition stage turbulent spots form. These spots grow in size and eventually merge, covering the entire surface of the wall and at this point the flow has entered the fully turbulent stage. At the start of the final stage the authors found that the newly generated turbulence is confined and the core region is still mostly unaffected. Gradually the turbulence spreads out to the outer region and the turbulence reaches its steady state value at the higher Reynolds number.

3.2 Method

An incompressible fluid with Newtonian properties is assumed. The domain is shown in figure 3.1 and is a $(L_x \times L_y \times L_z) = (4\pi h \times 2h \times 2\pi h)$ computational box with periodic boundary conditions applied in the x and z-directions and a no-slip boundary condition is applied in the y-direction. The parameters used for the steady and pulsatile simulation are summarized in table 3.1.

3.2.1 Steady case

The OpenFOAM source code is validated with a canonical channel flow simulation at $Re_\tau = 180$. The desired flow rate is achieved by applying a constant body force u_τ^2/h in the x-direction and there is no oscillating component. The grid consists of $256(x) \times 128(y) \times 256(z)$

Case	Re_τ	Wo	$A_{u_c}/\overline{u}_c$	l_s^+	l_t^+	Δx^+	Δy^+_{min}	Δy^+_{max}	Δz^+	Δt^+
steady	180	...	...	...	...	8.8	0.1	4.4	4.4	0.072
pulsatile	180	15	0.44	18.76	146.64	7.0	0.08	3.5	3.5	0.0452

Table 3.1: Summary of simulation parameters.

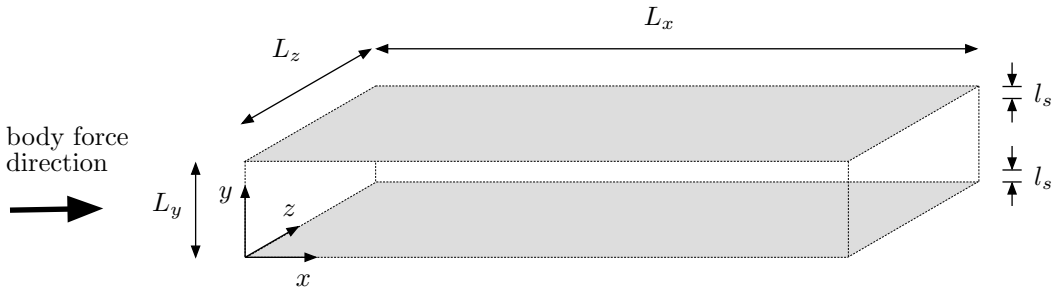

Figure 3.1: Coordinate system and domain geometry. An approximation of Stokes length l_s is shown.

grid points and the grid spacing in viscous units is $\Delta x^+ = 8.8$, $\Delta y^+_{min} = 0.1$, $\Delta y^+_{max} = 4.4$ and $\Delta z^+ = 4.4$. In Kolmogorov units the maximum grid spacing in the y-direction is $\left(\Delta/\overline{\eta}\right)_{max} = 2.38$, where $\Delta = (\Delta x \Delta y \Delta z)^{1/3}$. Statistics are obtained by ensemble averaging 50 uncorrelated snapshots separated in time by $0.5h/u_\tau$ and the eddy turnover time is defined as h/u_τ. In addition to temporal averaging, statistics are spatially averaged in the homogeneous x and z-directions and about the channel centre. The timestep in viscous units is $\Delta t^+ = 0.072$ and the CFL number does not exceed 0.3. The initial conditions for the simulation are random numbers and the flow is allowed to fully develop over $10h/u_\tau$. Figure 3.2 compares the time-averaged velocity, root-mean-square (r.m.s.) of the time-averaged Reynolds normal stresses and the Reynolds shear stresses to results from dataset FD2 in Vreman & Kuerten [132] and there is excellent qualitative agreement. In addition the present results are in good agreement with the time-averaged centerline values for $\overline{u}^+$ and the Reynolds normal stresses of 8 DNS studies summarized by Vreman & Kuerten [132]. It should be noted that the grid spacing in viscous units from dataset FD2 in Vreman & Kuerten [132] are $\Delta x^+ = 4.4$, $\Delta y^+_{min} = 0.49$, $\Delta y^+_{max} = 2.2$ and $\Delta z^+ = 2.9$, which is considerably more refined than what was used here. Figure 3.2 (c) also shows the shear from the mean velocity

with the total shear across the channel being linear and calculated as

$$-\overline{u'v'}^{+} + \partial\overline{u}^{+}/\partial y^{+} = \underbrace{1 - y^{+}/h^{+}}_{\text{total shear}}. \tag{3.6}$$

In figure 3.3 the time evolution in u'^{+} at $y^{+} \approx 30$ is plotted over $4h/u_{\tau}$. The length of the period shown in this figure is less then the period of the pulse from the pulsatile case.

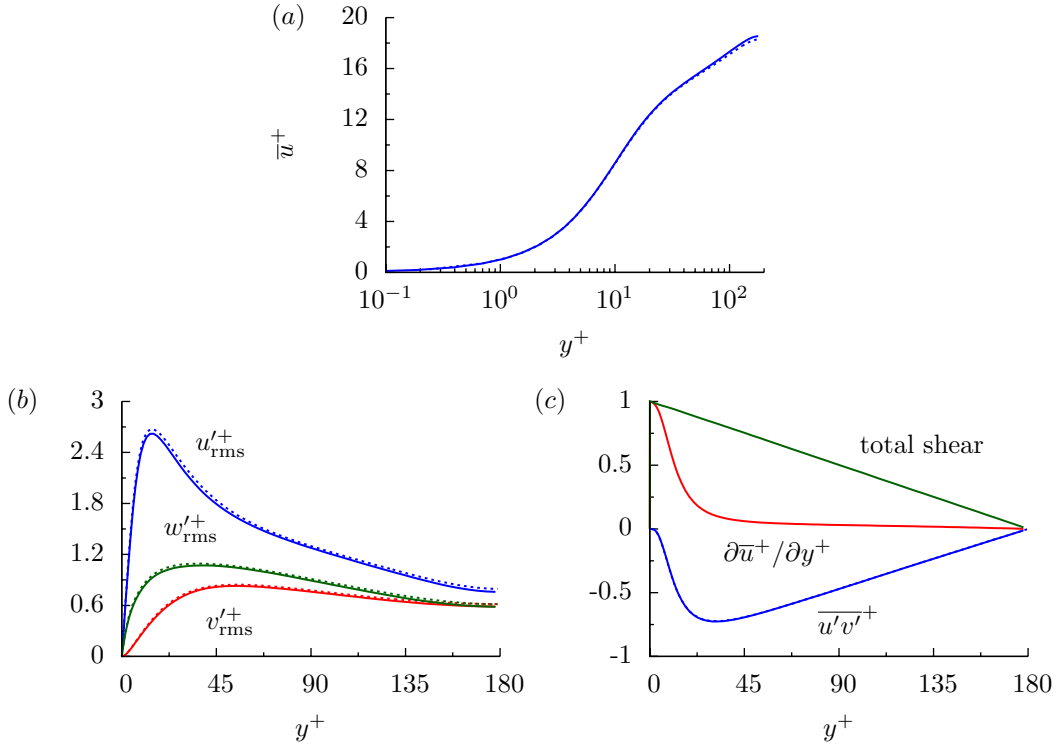

Figure 3.2: Steady case. (a) Time-averaged velocity $\overline{u}^{+}$, (b) r.m.s. of the Reynolds normal stresses and (c) the shear stress components $\overline{u'v'}^{+}$ and $\partial\overline{u}^{+}/\partial y^{+}$. Solid line is present data and dashed line is dataset FD2 from Vreman & Kuerten [132]

.

3.2.2 Pulsatile case

Pulsatile channel flow simulations are performed on a grid consisting of $320(x)\times160(y)\times320(z)$ grid points. The grid spacing in viscous units is $\Delta x^{+} = 7.0$, $\Delta y^{+}_{min} = 0.08$, $\Delta y^{+}_{max} = 3.5$ and

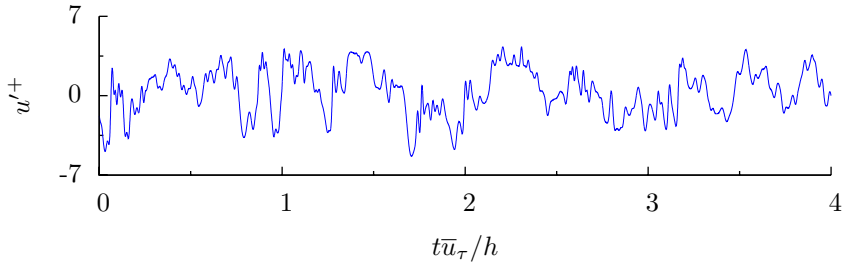

Figure 3.3: Time evolution in u'^+ at $y^+ \approx 30$ plotted over $4h/u_\tau$. The time orgin is arbitary.

$\Delta z^+ = 3.5$. The period of a pulse is equal to approximately $5h/u_\tau$. The flow is driven by mean component of u_τ^2/h and an oscillating component of $10u_\tau^2/h$ in the the x-direction. The non-dimensional parameters for the study are $Re_\tau = 180$, $Wo = 15$ and $A_{u_c}/\overline{u}_c = 0.44$. At $Wo = 15$ the simulation is comparable to pulsatile conditions in a artery of approximately 2 cm in diameter, such as the aorta. The resulting viscous and turbulent Stokes length is $l_s^+ = 18.76$ and $l_t^+ = 146.64$, respectively and therefore the influence of the oscillating shear extends well into the outer region of the boundary layer. The time step is fixed at $\Delta t = 0.5 \times 10^{-4}/T$ or in viscous units $\Delta t^+ = 0.0452$ and the CFL number does not exceed 0.3 during a pulse. The Re_τ used in this study is less than the value of $Re_\tau = 360$ used by Scotti and Piomelli [106]. Each period is segmented into $M = 50$ equidistant phase positions and phase-locked quantities are calculated at each phase position by ensemble averaging $N = 20$ snapshots. The time average is then calculated by averaging the $M = 50$ phase-locked values. The storage of 1000 velocity fields requires approximately 0.59 TB of memory. In addition to temporal averaging statistics are spatially averaged in the homogeneous x and z-directions and about the channel center. The initial conditions are fully developed turbulent flow at $Re_\tau = 180$ and to ensure fully developed unsteady conditions once the oscillating component is applied the flow is developed over 10 periods. In Scandura et al. [104] 10 initial pulses were

also used to fully develop the flow. Figure 3.4 shows the phase-wise variation in the maximum ratio of the grid spacing to the phase-averaged Kolmogorov length scale $\left(\Delta/\langle\eta\rangle\right)_{max}$. The maximum ratio is 2.47 and occurs at $\varphi/T = 0.4$ while the maximum time-averaged ratio is $\left(\Delta/\overline{\eta}\right)_{max} = 1.95$.

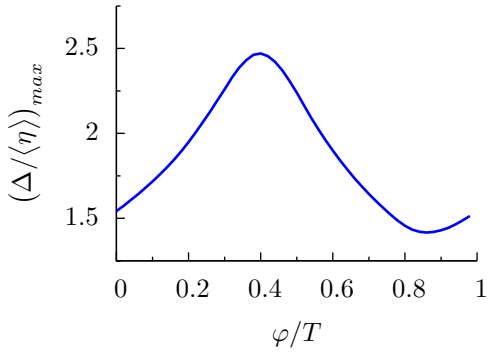

Figure 3.4: Phase-wise variation in the maximum ratio of the grid spacing to the phase-averaged Kolmogorov length scale $\left(\Delta/\langle\eta\rangle\right)_{max}$. The maximum time-averaged ratio is $\left(\Delta/\overline{\eta}\right)_{max} = 1.95$

3.3 Results and discussion

3.3.1 Velocity and Reynolds stress statistics

The flow within the channel is driven by a pulsatile body force in the x-direction that is shown in figure 3.5 (a). The mean component of the body force is significantly smaller then the amplitude of the oscillating component and the oscillation consists of a single harmonic. The phase-wise variation in the centerline velocity $\langle u_c \rangle^+$ is shown in figure 3.5 (b) and the amplitude in $\langle u_c \rangle^+$ is substantially smaller than the amplitude in the body force. In addition the peak value in $\langle u_c \rangle^+$ lags behind the body force by $\phi_{\widetilde{C_f}}/T = 0.25$ and at the center of the

channel the oscillations in velocity consist of a single harmonic. The numerical simulation is performed at $Wo = 15$ and at this Womersley number a considerable portion of the body force goes towards overcoming inertia with only a small portion of the body force being balanced by the skin friction at the wall, as shown in figure 2.1. If Wo were to be reduced, inertial effects will take a smaller portion of the body force and the amplitude and phase-lag in the velocity would become progressively more aligned with the body force. This flow phenomenon has been shown previously in figure 2.2 and 2.3. The phase-wise variation in the skin friction coefficient $\langle C_f \rangle$ is shown in figure 3.5 (c), where

$$\langle C_f \rangle = 2\langle \tau_w \rangle / \big(\rho \overline{u}_b\big). \tag{3.7}$$

At the wall the phase-lag is $\phi_{\widetilde{C_f}}/T = 0.13$ and this is considerably less then the phase-lag that occurs at the channel center. Since the fluid contains higher momentum towards the channel center it can better resist the oscillations in the body force. Although the pulsatile body force acts in the negative x-direction for a sizable period of the pulse, at no point does the phase-averaged velocity become negative. Unlike the velocity at the channel center, the skin friction deviates from single harmonic motion and during the deceleration period $\langle C_f \rangle$ stagnates at a relative constant value before further decreasing. The phase-wise variation in the turbulent fluctuations of the skin friction coefficient $\langle C_f' C_f' \rangle^{1/2}$ is shown in figure 3.5 (d) and there is considerably more phase-lag in this term compared to the velocity at either the wall or channel center. At peak $\langle C_f \rangle$, the turbulent fluctuations in C_f are relatively low and it is not until the deceleration period of the pulse that the fluctuations in $\langle C_f \rangle$ increase. This increase in turbulence at the wall corresponds with the period of the pulse

where $\langle C_f \rangle$ stagnates at a constant value. The turbulent fluctuations temporarily increase the momentum within the wall region and allow the fluid to resist, for a short period of time, the inertial force that is decelerating the fluid velocity.

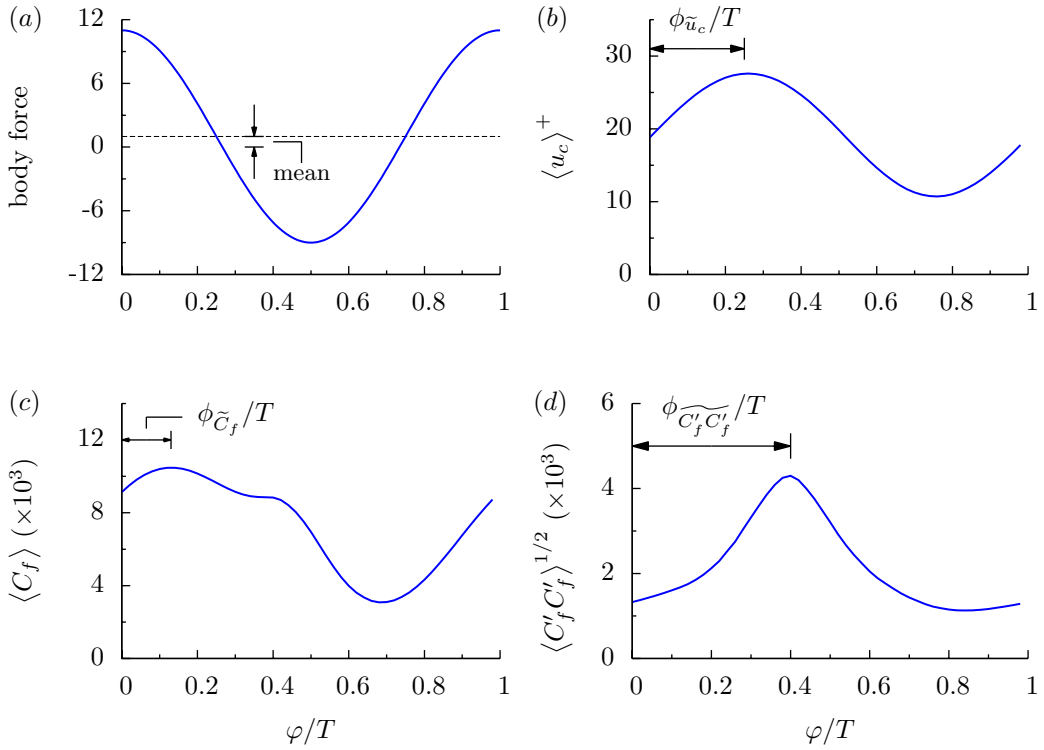

Figure 3.5: Phase-wise variation in the (a) pulsatile body force normalized by u_τ^2/h, (b) centerline velocity $\langle u_c \rangle^+$, (c) skin friction coefficient $\langle C_f \rangle$ and (d) turbulent fluctuations in the skin friction coefficient $\langle C'_f C'_f \rangle^{1/2}$.

Pulsatile flow can be though as analogous to a electrical circuit, where the time-average is the DC component and the amplitude in the oscillations is the AC component. When calculating the amplitude and phase-lag, since the oscillation in the fluids velocity deviate from a single harmonic, the signal is first reconstructed using the four modes from a Fourier decomposition. The phase-lag $\phi_{\tilde{u}}$ is then calculated from this reconstructed signal and the amplitude (DC component) is calculated as

$$A_u = (u_{max} - u_{min})/2. \tag{3.8}$$

Figure 3.6 (a) compares the time-averaged velocity $\overline{u}^+$ (DC component) from the present numerical simulation to the results from a steady simulation at $Re_\tau = 180$ from dataset FD2 in Vreman & Kuerten [132]. Within the viscous sublayer $\overline{u}^+$ from the pulsatile and steady case are the same and within the outer region of the channel $\overline{u}^+$ is shifted higher for the pulsatile case. Manna & Vacca [74] studied high-frequency pulsatile flow in a pipe and a similar overshoot in the log region for high amplitude osculations. This was again shown in the more recent work by Manna et al. [75], where they investigated high-frequency flow, the log profile deviated for the high-amplitude case. In the data from Tardu et al. [117] the time-averaged velocity collapses onto the log-profile. The low-amplitude simulations by Weng et al. [135] again showed a collapse of the time-averaged velocity profile. When the moderate-amplitude data from Scotti & Piomelli [106] was compared, their profile slightly overshot the log profile. Papadopoulos & Vouros [86] found that the pulsatile profile collapsed onto the steady profile for both different amplitudes and frequency. In a study on accelerating channel by Seddighi et al. [107], it was shown that during the pre-transitional phase the log layer overshoots the initial profile. Once the transition phase starts the log layer was found to gradually drops down to the steady log profile. Figure 3.6 (b) shows the AC component of $\langle u \rangle$ normalized by its centerline value $A_{\widetilde{u}_c}$ and phase-lag $(\phi_{\widetilde{u}_c} - \phi_{\widetilde{u}})/T$. The results from the numerical simulation are compared to the analytical Stokes solution. As expected since $l_t^+ = 146.64$, the numerical simulation deviates significantly from the analytical solution. Scotti & Piomelli [106] found that only for $l_s^+ = 4.4$ did the AC component match the Stokes

solution. They observed that the case with $l_s^+ = 14$ represented an intermediate case when momentum began to be transported into the outer region. A similar trend was observed by Tardu et al. [117].

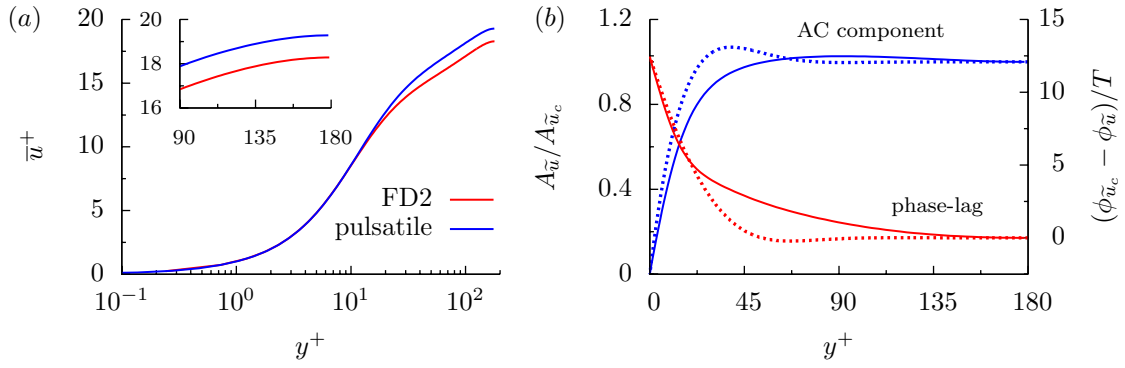

Figure 3.6: (a) Time-averaged velocity $\overline{u}^+$ from the pulsatile case and dataset FD2 from Vreman & Kuerten [132] at $Re_\tau = 180$. (b) AC component of $\langle u \rangle$ normalized by its centerline value and phase-lag $(\phi_{\widetilde{u}_c} - \phi_{\widetilde{u}})/T$. Solid line is pulsatile case and dashed line is Stokes solution at $Wo = 15$.

The periodic component of velocity $\widetilde{u}$, normalized by the amplitude of its center line value $A_{\widetilde{u}_c}$, is shown in figure 3.7. In this figure the data from the pulsatile simulation is compared to the analytical Stokes solution at $Wo = 15$. For the Stokes solution, the periodic velocity consists of a thin shear layer, confined to l_s close to the wall and a plug profile in the outer region. The analytical solution shows that the flow velocity close to the wall changes first followed by the fluid in the outer region. For the pulsatile simulation, since l_s^+ is outside of the viscous sublayer, turbulent structures perpetuate from the wall into the outer region and $\widetilde{u}$ deviates significantly from the analytical solution. Within the outer region the velocity profile no longer resembles plug flow. The turbulent fluctuations that develop close to the wall, as shown in figure 3.5 (d), temperately prevent the reversal in flow direction at the wall. This can be seen in figure 3.7 (d) and (e), where the region of fluid outside the Stokes

layer has reversed, while within the Stokes layer and in the outer region of the channel $\widetilde{u}$ is still positive. In the high frequency study by Papadopoulos & Vouros [86] the phase-lag and amplitude agreed with the Stokes solution. Although Manna et al. [75] found deviations in the log profile, for either low and high amplitude, the AC component and phase-lag did not deviate from the Stokes solution.

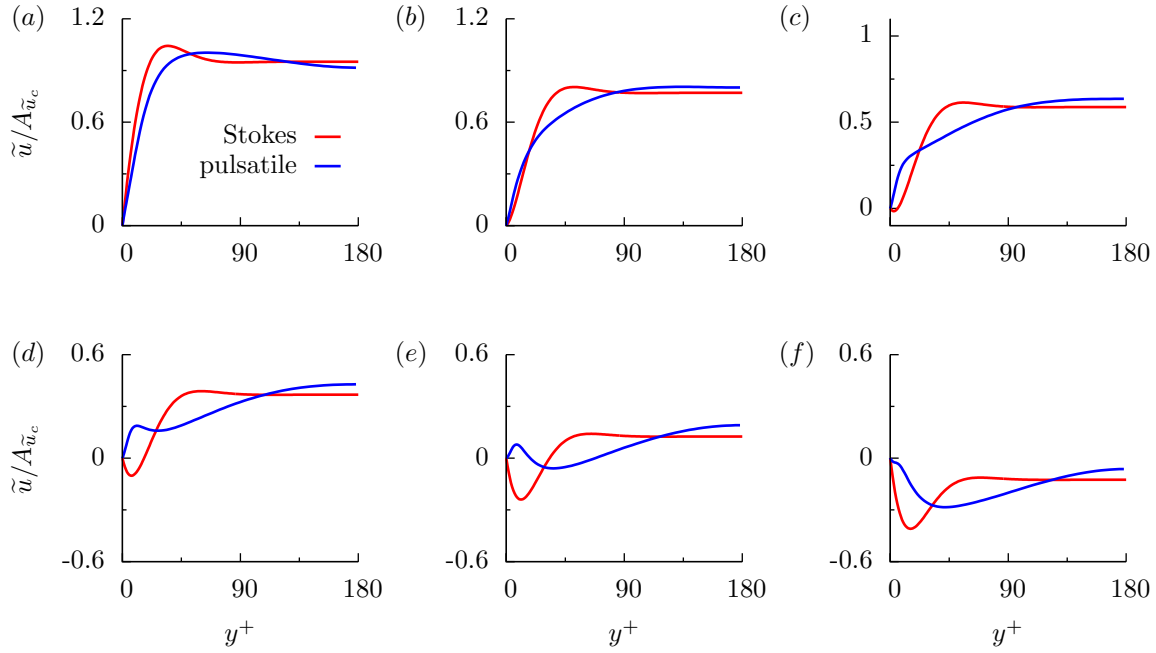

Figure 3.7: Phase-locked periodic component of velocity $\widetilde{u}/A_{\widetilde{u}_c}$ at phase positions (a) $\varphi/T = 0.2$, (b) $\varphi/T = 0.36$ and (c) $\varphi/T = 0.4$, (d) $\varphi/T = 0.44$, (e) $\varphi/T = 0.48$ and (f) $\varphi/T = 0.52$. Numerical simulation is compared to the Stokes solution at $Wo = 15$.

The variations in the instantaneous skin friction C_f during a pulse are investigated using a phase-locked probability density function (P.D.F.) in figure 3.8. The P.D.F. was computed using a python script. The data was placed into approximately $n^{1/3}$ equal-width bins along the range $-20 < C_f < 40$, where n is the size of the dataset. The P.D.F. was normalized such that the integral over its range is 1. A similar method was used for all other P.D.F. in this chapter. Although $\langle C_f \rangle$ is positive during the entirety of the pulse, as shown in figure

3.5 (c), as the velocity decelerates there is a low occurrence of negative C_f values. It can be seen at $\varphi/T = 0.4$ that although C_f is decreasing, the range of possible values increases and there is a slightly greater occurrence of high values. A phase-locked P.D.F. of the turbulent fluctuations in the skin friction C_f' is shown in figure 3.9 and during the acceleration period of the pulse the P.D.F. is close to symmetric about the zero x-axis. As the flow decelerates the peak in the P.D.F. shifts towards negative C_f' values and there is greater spread in positive C_f' values.

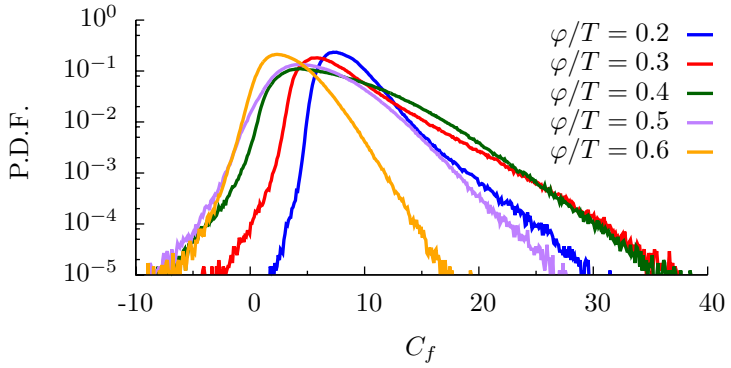

Figure 3.8: Phase-locked probability density function (P.D.F.) of the skin friction C_f at phase positions $\varphi/T = [0.2, 0.3, 0.4, 0.5, 0.6]$. Plotted on a linear-log scale.

Figure 3.10 showz the time evolution in u''^+ and v'^+ at $y^+ \approx 30$, plotted over two pulses. The streamwise total fluctuating component u''^+ consists of a periodic flux superimposed with turbulent fluctuations. Qualitatively it can be observed that the fluctuations increase during the deceleration period of the pulse. Since the pulsatile body force is directed in the x-direction, the wall-normal fluctuations experiences no periodic flux, i.e. $\widetilde{v} = 0$. During the early portion of the pulse the fluctuations in v'^+ are relatively small and there is minimal change in intensity of the fluctuations. This is followed by a sudden increase in the fluctuation amplitude and then a gradual decrease. Although the fluctuations in v'^+ become small at no

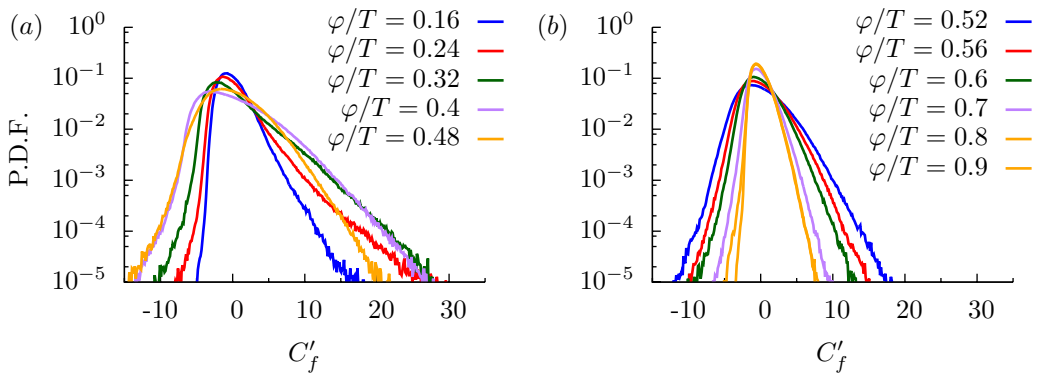

Figure 3.9: Phase-locked probability density function (P.D.F.) of the turbulent fluctuations in the skin friction C'_f at phase positions (a) $\varphi/T = [0.16, 0.24, 0.32, 0.4, 0.48]$ and (b) $\varphi/T = [0.52, 0.56, 0.6, 0.7, 0.8, 0.9]$. Plotted on a linear-log scale.

point during the pulse does the figure show the flow relaminarize at this location.

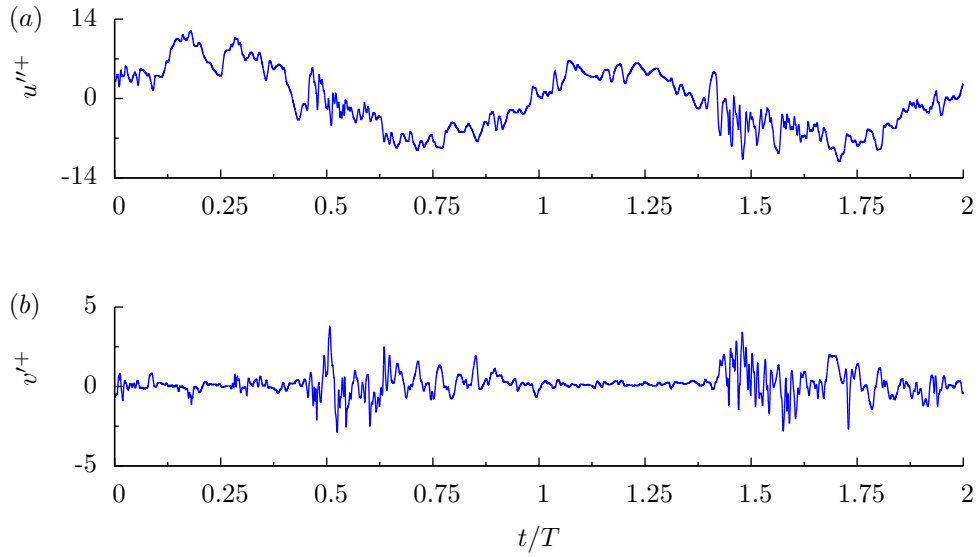

Figure 3.10: Time evolution at $y^+ \approx 30$, in (a) u''^+ and (b) v'^+ plotted over two pulses. The time origin is placed at the start of a pulse.

The AC and DC components of the Reynolds stresses are shown in figure 3.11, where the blue and red line are the AC component and time-average (DC component) from the pulsatile case, respectively and red dashed line is the steady case at $Re_\tau = 180$ in dataset FD2

from Vreman & Kuerten [132]. Although the intensity of the turbulent fluctuations varies significantly during the pulse-cycle, as shown in figure 3.10, when averaged over time, the pulsatile turbulent stresses collapse onto the same profile as the time-averaged non-pulsatile case at $Re_\tau = 180$. For all of the Reynolds stresses the AC component extends along the channel height, with the shear stress $\langle u'v' \rangle^+$ having proportionally the largest AC component. In results shown in Scotti & Piomelli [106], when $l_s^+ = 4.4$ the AC component was only present close to the wall and goes to zero in the outer region. At $l_s^+ = 7$ the AC component was non-zero for the full length of the channel and as l_s^+ increased so did the proportion of the AC component in the outer region. In Bhaganagar [12] the time-average of the normal Reynolds stresses from pulsatile simulations at various frequencies collapsed onto the steady cases profile. Similar to Scotti & Piomelli [106] for high frequency the AC component was only present close to the wall.

The phase-lags $\phi_{\widetilde{u'u'}}/T$, $\phi_{\widetilde{v'v'}}/T$, $\phi_{\widetilde{w'w'}}/T$ and $\phi_{\widetilde{u'v'}}/T$ are shown in figure 3.12 (a). For the Reynold stresses there is considerably more phase-lag compared to the steamwise velocity and in general phase-lag increases towards the channel center. Interestingly for $\langle u'u' \rangle$ the phase-lag first decreases away from the wall and then increases in the outer region. The phase-lag for $\langle v'v' \rangle$ does not behave in this way and only increases away from the wall. The phase-wise behavior of the spanwise stress is qualitatively similar to the wall-normal component and as such will not be shown in any further figures. The fact that close to the wall $\langle u'u' \rangle$ reaches its peak value earlier than the other stresses results in there being a brief portion of the pulse the fluid will be dominated by streamwise fluctuations only. A consequence of this is that although the flow is turbulent, it experiences reduced turbulent shear during this period of the pulse. Although the Reynold stresses experience different phase-lag close to

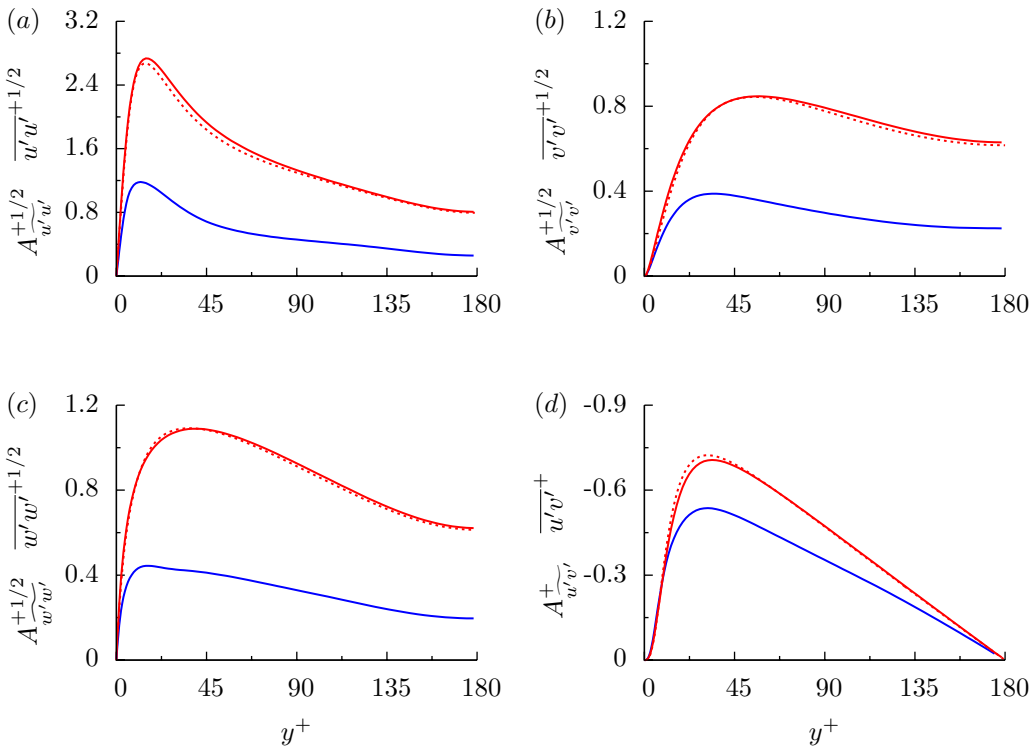

Figure 3.11: AC and DC components of the Reynolds stresses (*a*) $\langle u'u' \rangle^{+1/2}$, (*b*) $\langle v'v' \rangle^{+1/2}$, (*c*) $\langle w'w' \rangle^{+1/2}$ and (*d*) $\langle u'v' \rangle^{+}$. Blue line is AC component, red line is the time-average (DC component) and red dashed line is dataset FD2 from Vreman & Kuerten [132].

the wall, at the channel center the phase-lag is similar. The increased phase-lag that the wall-normal fluctuation experiences appears to be similar to the phenomenon observed by He & Seddighi [42] for accelerating channel flow. Scotti and Piomelli [106] found that at the intermediate frequency range of $l_s^+ = 14$, there was a linear increase in phase-lag for all Reynold stresses away from the wall and the $\langle u'u' \rangle$ term was frozen close to the channel center. At a lower frequency of $l_s^+ = 35$, $\langle u'u' \rangle$ was observed by these authors to not be frozen at the channel center. For accelerating channel flow by He & Seddighi [42], the streamwise turbulence increased immediately at the wall as the flow accelerated but this increase was delayed away from the wall. While the wall-normal and spanwise turbulence unchanged

during the start of acceleration. The authors stated that the increase in streamwise turbulence was from the stretching of the existing flow structures and this stretching is initiated at the wall. It was stated in Seddighi et al. [107] that increase in v' and w' is the initiation of turbulence during the transition process.

The variance fraction of $\langle u \rangle$, $\langle u'u' \rangle$, $\langle v'v' \rangle$, $\langle w'w' \rangle$ and $\langle u'v' \rangle$ is shown in figure 3.12 (b). The variance fraction is a measure of how these quantities deviate from single harmonic motion. For the streamwise velocity $\langle u \rangle$ the variance fraction is effectively zero in the outer region and then increases close to the wall. This increase in the non-linear behavior of $\langle u \rangle$ is caused by increased momentum from turbulent fluctuations resisting the pulsatile inertia close to the wall. For $\langle u'u' \rangle$ and $\langle w'w' \rangle$ the variance fraction is at a moderately high constant value in the outer region and further increases close to the wall. For $\langle v'v' \rangle$ the variance fraction is significantly higher at the wall and gradually decreases towards the channel center, where it approaches the same value as $\langle u'u' \rangle$. The turbulent shear stress $\langle u'v' \rangle$ is substantially more non-linear then the normal stresses and the variance fraction increases slightly in the outer region towards the center. Scotti & Piomelli [106] found that the periodic components deviate from single harmonic motion as frequency was lowered. They also found that the low-frequency regime shows higher non-linearity than the quasi-steady regime.

Contours of the phase-wise variation in $\widetilde{u'u'}^+$ and $\widetilde{v'v'}^+$ are shown in figure 3.13. The locations of the maximum and minimum values that occur during the pulse are highlighted in this figure. Both Reynolds stress components exhibit highly skewed profiles in the outer region. For the streamwise component $\widetilde{u'u'}^+$ despite having a skewed profile in the outer region, its minimum value occurs at approximately the same location as $\widetilde{u}^+$. The minimum value for the wall-normal component $\widetilde{v'v'}^+$ does not occur until the flow acceleration period

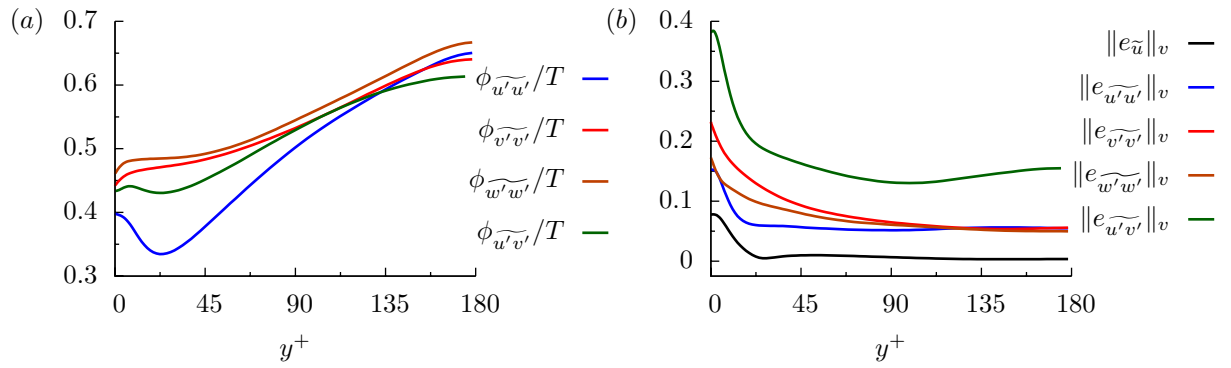

Figure 3.12: (a) Phase-lag $\phi_{\widetilde{u'u'}}/T$, $\phi_{\widetilde{v'v'}}/T$, $\phi_{\widetilde{w'w'}}/T$ and $\phi_{\widetilde{u'v'}}/T$. (b) Variance fraction of $\langle u \rangle$, $\langle u'u' \rangle$, $\langle v'v' \rangle$, $\langle w'w' \rangle$ and $\langle u'v' \rangle$ contained in frequencies higher than the fundamental.

of the next pulse.

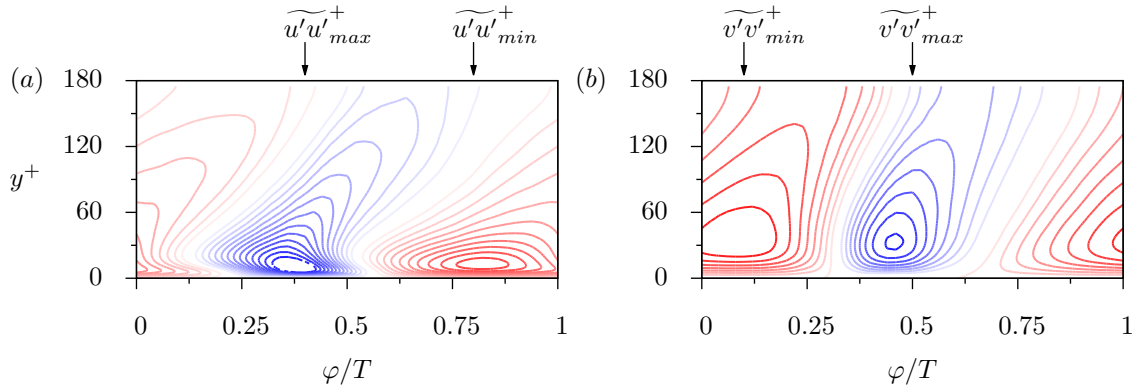

Figure 3.13: Phase-wise variation in (a) $\widetilde{u'u'}^+ \in [-1.4, 1.4]$ and (b) $\widetilde{v'v'}^+ \in [-0.5, 0.5]$. Blue and red contour lines are positive and negative values, respectively.

The phase-wise variation in $\langle u'u' \rangle^{+1/2}$ is further investigated in figure 3.14 (a), (b) and (c) at $y^+ \approx 5$, $y^+ \approx 21$ and the channel center $y^+ \approx 180$, respectively. These profiles highlight that the phase-lag for the streamwise Reynolds stress first decreases moving away from the wall and then increases. At the channel center, the minimum value does not occur until after peak flow rate of the following pulse. At $y^+ \approx 5$ the profile deviates most from single harmonic motion in comparison to the profiles at $y^+ \approx 21$ and the channel center. In figure

3.14 $(d) - (f)$ the phase-wise variation in $\left\langle v'v' \right\rangle^{+1/2}$ is shown at the same locations along the channel height. At $y^+ \approx 5$ and 21, the wall-normal is flat during the early period of the pulse and it is this feature that leads to the greater deviation from single harmonic motion that is show in figure 3.12 (b). At the channel center both the streamwise and wall-normal stresses exhibit similar behavior and experience qualitatively the same phase-lag.

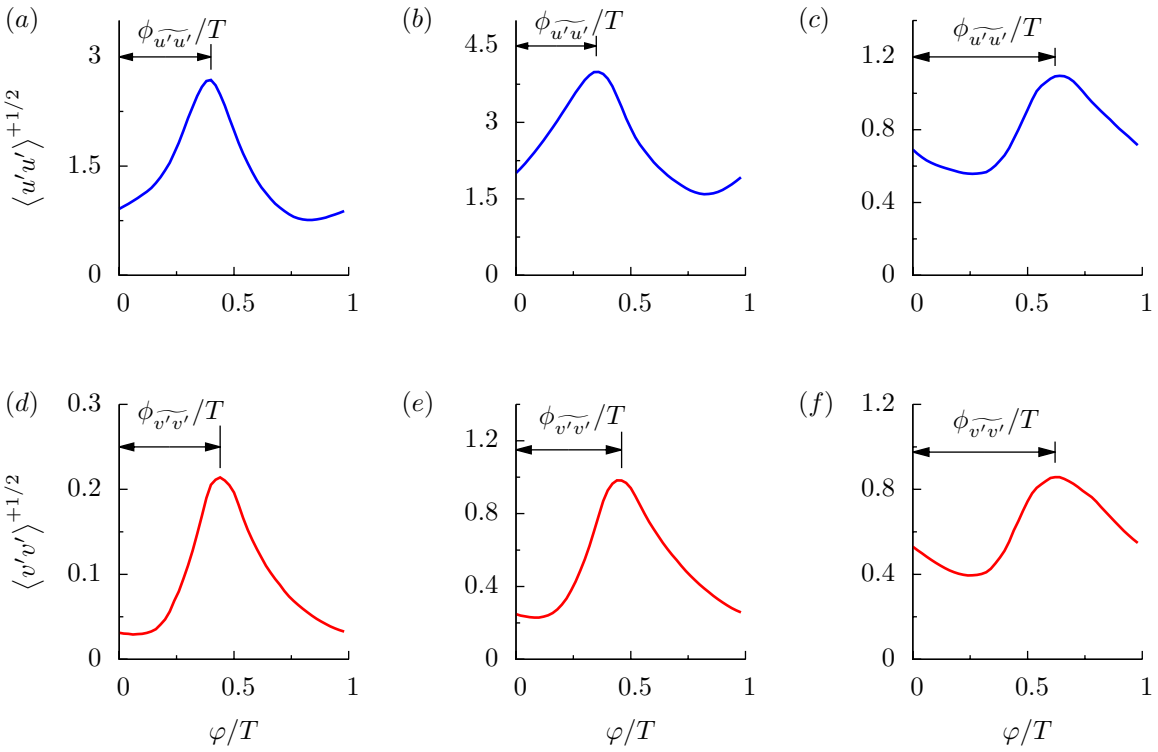

Figure 3.14: Phase-wise variation in $\left\langle u'u' \right\rangle^{+1/2}$ at (a) $y^+ \approx 5$, (b) $y^+ \approx 21$ and (c) the channel center $y^+ \approx 180$. Phase-wise variation in $\left\langle v'v' \right\rangle^{+1/2}$ at (d) $y^+ \approx 5$, (e) $y^+ \approx 21$ and (f) the channel center $y^+ \approx 180$.

Profiles of the phase-locked streamwise stress $\left\langle u'u' \right\rangle^{+1/2}$ at various phase positions are shown in figure 3.15. The phase-wise variation is shown as a blue line and is compared to the time-averaged profile $\overline{u'u'}^+$ shown as a dashed red line. Increases in $\left\langle u'u' \right\rangle^{+1/2}$ occur first centered at the location of the peak time-averaged value. The streamwise turbulence

then spreads into the outer wall region. As $\langle u'u' \rangle^{+1/2}$ increases, its peak value moves slightly closer to the wall. During the late half of the pulse, $\langle u'u' \rangle^{+1/2}$ begins to decrease close to the wall while it is still increasing at the channel center. This feature is highlighted in the inset graph in figure 3.15 (b). Profiles of the phase-locked wall-normal stress $\langle v'v' \rangle^{+1/2}$ at various phase positions are shown in figure 3.16. Similar to the streamwise stress, the increase in $\langle v'v' \rangle^{+1/2}$ occurs first at the location of the peak time-averaged value and later into the pulse as $\langle v'v' \rangle^{+1/2}$ decreases its profile flattens in the outer region. Profiles of the phase-locked shear stress $\langle u'v' \rangle^{+}$ locked at various phase positions are shown in figure 3.17. Similar to the streamwise component, $\langle u'v' \rangle^{+}$ first increase around the peak time-averaged value. During the deceleration period of the pulse the peak value in $\langle u'v' \rangle^{+}$ moves away from the wall and the profile flattens. The Reynolds stress profiles were found behaved similarly by He & Seddighi [42] when channel flow accelerating channel flow. The turbulent was found to first increase close to the wall and then spread out to the outer region.

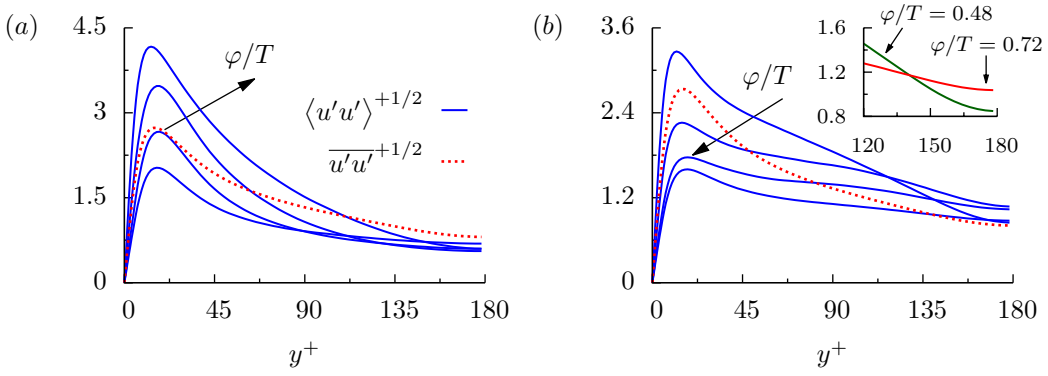

Figure 3.15: Phase-locked Reynolds normal stress $\langle u'u' \rangle^{+1/2}$ at phase positions (a) $\varphi/T = [0, 0.12, 0.24, 0.36]$ and (b) $\varphi/T = [0.48, 0.6, 0.72, 0.84]$. Blue line is phase-average data and red dashed line is time-average data.

The phase-locked production of TKE for a pulsatile flow in a channel can be calculated as

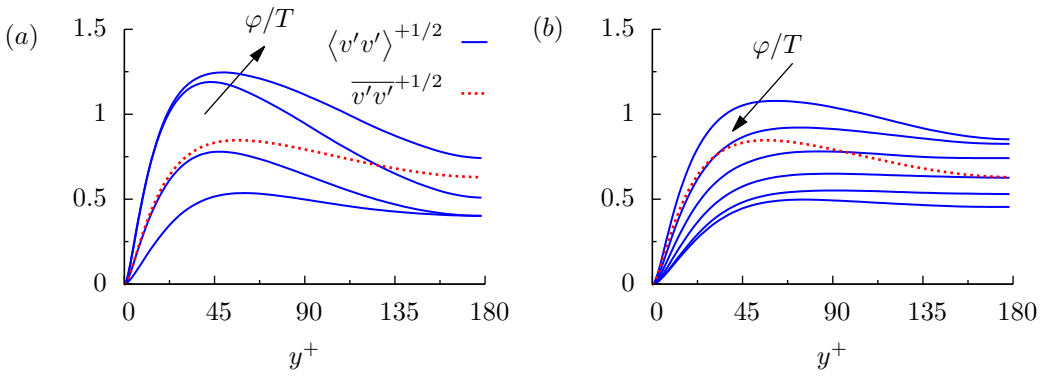

Figure 3.16: Phase-locked Reynolds normal stress $\langle v'v' \rangle^{+1/2}$ at phase positions (a) $\varphi/T = [0.2, 0.3, 0.4, 0.5]$ and (b) $\varphi/T = [0.6, 0.7, 0.8, 0.9, 0, 0.1]$. Blue line is phase-average data and red dashed line is time-average data.

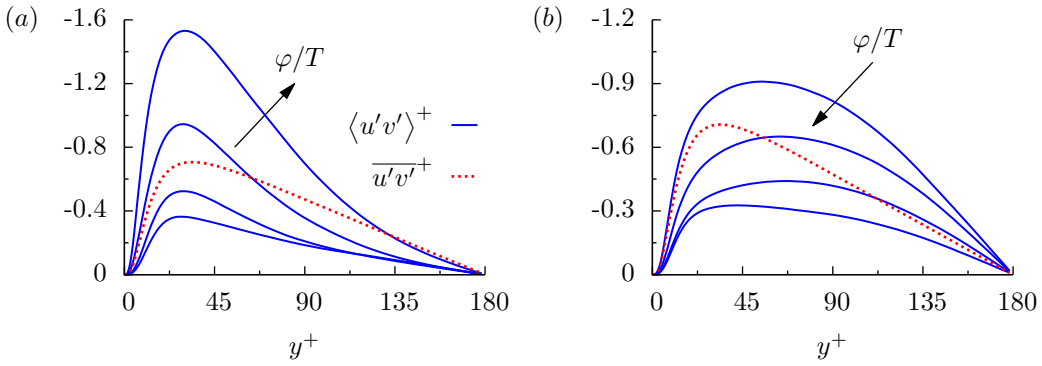

Figure 3.17: Phase-locked Reynolds shear stress $\langle u'v' \rangle^{+}$ at phase portions (a) $\varphi/T = [0.1, 0.2, 0.3, 0.4]$ and (b) $\varphi/T = [0.6, 0.7, 0.8, 0.9]$. Blue line is phase-average data and red dashed line is time-average data.

$$\langle P_k \rangle = -\langle u'v' \rangle \frac{d\langle u \rangle}{dy}. \tag{3.9}$$

The time-averaged production of TKE for a pulsatile flow is then calculated as

$$\overline{P_k} = -\overline{\langle u'v' \rangle \frac{d\langle u \rangle}{dy}} = -\overline{u'v'} \frac{d\overline{u}}{dy} - \overline{\widetilde{u'v'} \frac{d\widetilde{u}}{dy}} \tag{3.10}$$

and contains contributions from the time-averaged and periodic components of the flow.

Production from the oscillating component is small compared to the contribution from $\overline{u'v'}d\overline{u}/dy$. It was found in Manna et al. [75] that at high amplitude $\overline{\widetilde{u'v'}d\widetilde{u}/dy}$ contributed significantly to the total turbulent production and only a small amount for a moderate amplitude. Figure 3.18 (a) shows the time-averaged balance of production and dissipation $\overline{P}_k/\overline{\epsilon} - 1$. Similar to the time-average of the Reynolds stress shown in figure 3.11, the balance of production and dissipation TKE collapses onto the same profile as the steady simulation and shows good agreement with steady channel flow data of Lee & Moser [65] at $Re_\tau = 180$. Production exceeds dissipation close to the wall and in the outer region there is a close to equal balance with dissipation slightly exceeding production Approaching the channel center the production of TKE ceases and dissipation becomes relatively small. The phase-locked balance of production and dissipation $\langle P_k \rangle / \langle \epsilon \rangle - 1$ is shown in figure 3.18 (b) and (c). During the early period of the pulse, close to the wall there is an excess in production, relative to the dissipation and in the outer region of the channel there is a deficit. During $\varphi/T = 0.4 - 0.6$, the proportion of production in the outer region increases while it decreases close to the wall, i.e. there is a close-to equal balance during the mid-portion of the pulse. The phase-wise variation in production $\langle P_k \rangle$ and dissipation $\langle \epsilon \rangle$ is shown in figure 3.19 with the terms being normalized by $\overline{u}_\tau^4/\nu$. The peak in both $\langle P_k \rangle$ and $\langle \epsilon \rangle$ occurs as the flow is decelerating and both terms have relatively similar phase-lag, with the phase-lag increasing towards the channel center.

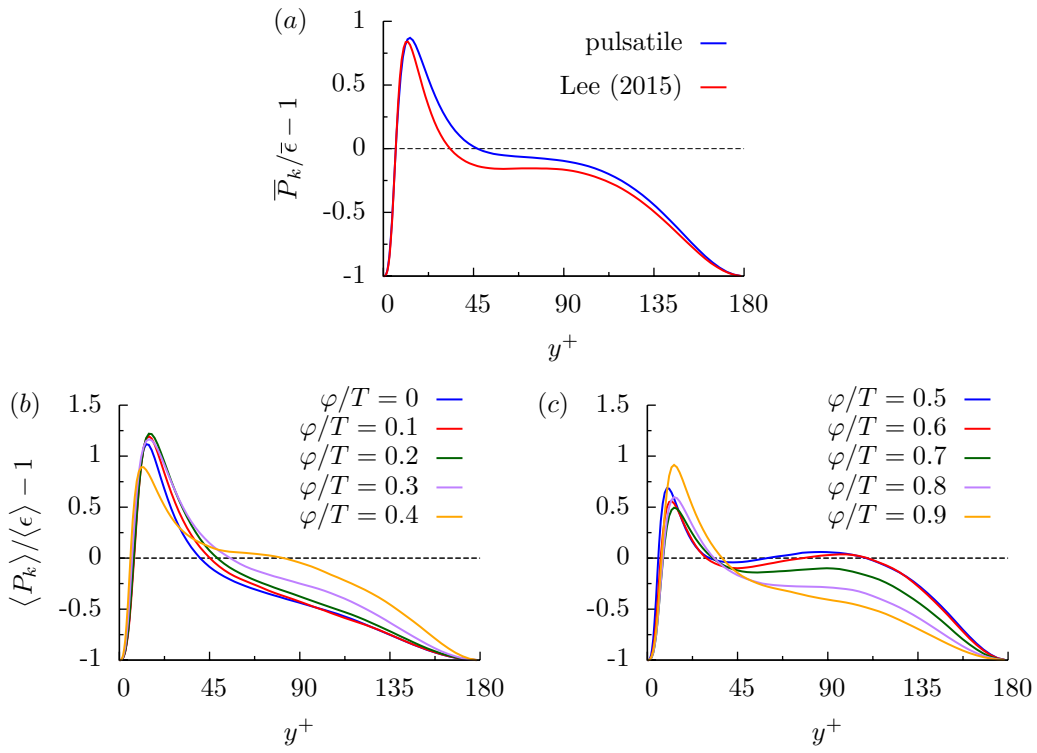

Figure 3.18: (a) Time-averaged balance of production and dissipation $\overline{P}_k/\overline{\epsilon}-1$. Blue line is present pulsatile simulation and red line is steady simulation by Lee & Moser [65] at $Re_\tau = 180$. Phase-locked balance of production and dissipation $\langle P_k\rangle/\langle\epsilon\rangle-1$ at phase positions (b) $\varphi/T=[0,0.1,0.2,0.3,0.4]$ and (c) $\varphi/T=[0.5,0.6,0.7,0.8,0.9]$.

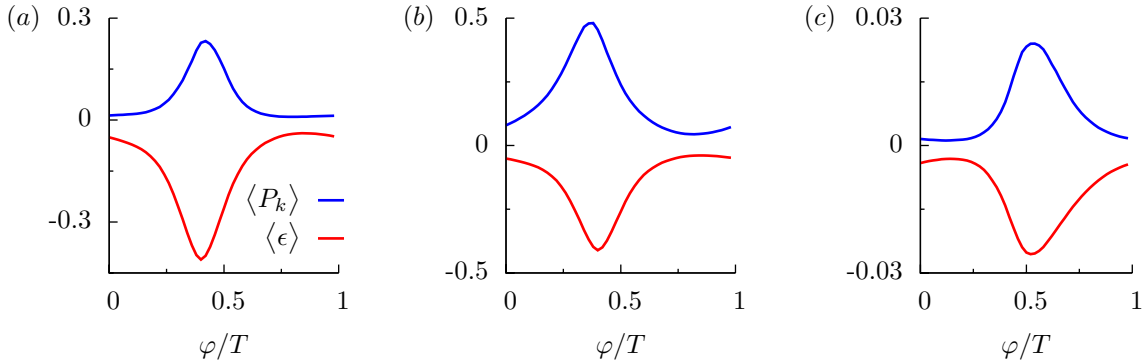

Figure 3.19: Phase-wise variation in production $\langle P_k\rangle$ and dissipation $\langle\epsilon\rangle$ at (a) $y^+\approx 5$, (b) $y^+\approx 21$ and (c) $y^+\approx 120$. Terms are normalized by $\overline{u}_\tau^4/\nu$.

3.3.2 Flow structures

Snapshots of the fluctuating velocity component u'^{+} plotted on a x-z plane at $y^{+} \approx 15$ are shown in figure 3.20. During the late-acceleration period of the pulse ($t/T = 0.2$) turbulent structures are elongate streaks and as the flow decelerates these streaks break into smaller-scale turbulent fluctuations. Referring back to figure 3.14 (b) and (e), during the early period of the pulse when the elongated streaks are present, the streamwise turbulence is increasing while the wall-normal turbulence is stagnant at a low value. The streaks breaking apart into smaller-scale structures corresponds to the rapid increase in wall-normal turbulence seen in figure 3.14 (e). Once flow acceleration starts again during the latter-half of the pulse, the small-scale structures recombine to form larger structures. During this later-period of the pulse, streamwise turbulence starts to increase again while wall-normal turbulence is now decreasing. Finally as peak flow rate is approached, the large structures once again elongate. Referring back to figure 3.19 (b), both production and dissipation rapidly increase as the elongated structures break apart. This is followed by both the production and dissipation terms rapidly decreasing to low values as the small structures reform into the large structures. The spanwise velocity fluctuation u'^{+} at $y^{+} \approx 15$ and temporal positions $t/T = 0$, 0.2, 0.4 and 0.6 is shown in figure 3.21. This figure qualitatively shows that the distance between streaks in the spanwise direction decreases as the flow decelerates and then increases during the acceleration portion of the pulse. For comparison purposes a snapshot of the fluctuating velocity component u'^{+} plotted on a x-z plane at $y^{+} \approx 15$ from a steady channel flow simulation at $Re_{\tau} = 180$ is shown in figure 3.22. For the steady simulation case, the elongated streaks and small-scale fluctuations that occur for the pulsatile simulation are not present.

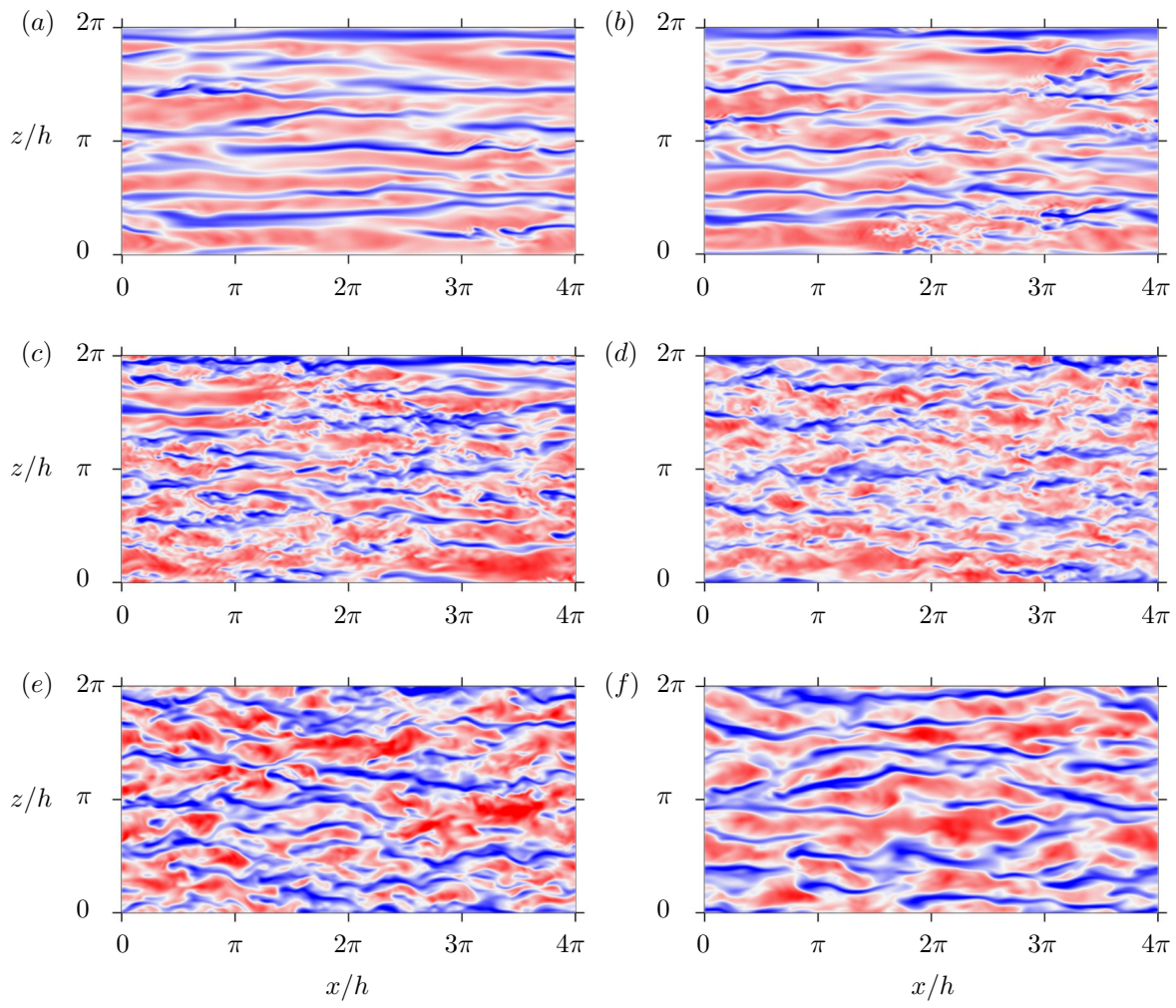

Figure 3.20: Snapshot of the fluctuating velocity component u'^{+} plotted on a x-z plane at $y^{+} \approx 15$ and temporal positions (a) $t/T = 0.2$, (b) $t/T = 0.3$, (c) $t/T = 0.4$, (d) $t/T = 0.5$, (e) $t/T = 0.7$ and (f) $t/T = 0.9$. The time origin is placed at the start of a pulse. Contour levels shown for $-5 \leq u'^{+} \leq 5$ from blue to red.

The phase-locked spanwise correlation function $R_{u'u'}$ at $y^{+} \approx 15$ is shown in figure 3.23. This quantitatively identifies the spacing between the streaks in the spanwise direction during the pulse-cycle, where the location of the minimum value from the correlation function is half of the average width of the streak. The phase-wise variation at $y^{+} \approx 15$ in the spanwise streak spacing is shown in figure 3.24 (a) and the largest spacing occurs as the small-scale

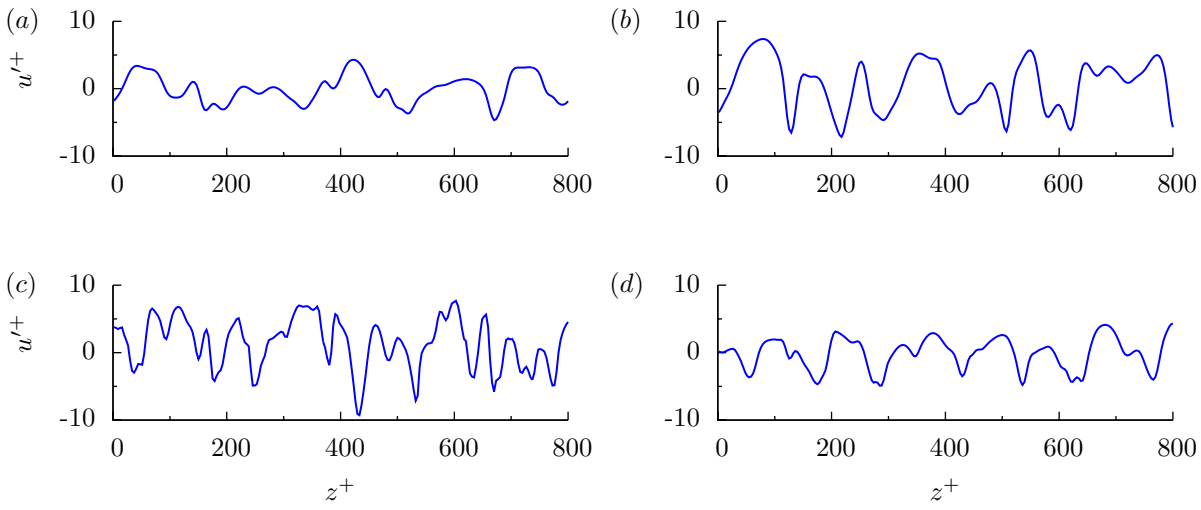

Figure 3.21: Spanwise velocity fluctuation u'^+ at $y^+ \approx 15$ and temporal positions (a) $t/T = 0$, (b) $t/T = 0.2$, (c) $t/T = 0.4$ and (d) $t/T = 0.6$. The time origin is placed at the start of a pulse.

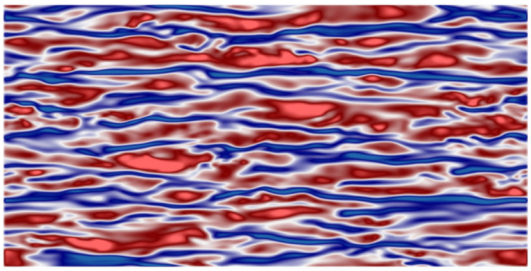

Figure 3.22: From the steady case a snapshot of the fluctuating velocity component u'^+ plotted on a x-z plane at $y^+ \approx 15$. Contour levels shown for $-5 \leq u'^+ \leq 5$ from blue to red.

fluctuations subside during the later period of the pulse. As the elongated streaks are forming during the early period of the pulse, the distance between the streaks rapidly decreases. The spacing reaches a minimum as the streaks break apart into smaller structures. This minimum distance persists for a short period and as the small-scale turbulent subsides there is a rapid increase in spanwise spacing between the structures.

The phase-wise variation at $y^+ \approx 15$ in the minimum value from the spanwise correlation function is shown in figure 3.24 (b). A larger negative value is an indication of more regularly organized streak structures. During the early period of the pulse, when the elongated streaks are present, the minimum value in $R_{u'u'}$ remains relatively constant at a high negative value. The streaks break apart after $\varphi/T = 0.2$ and the minimum value in $R_{u'u'}$ decreases, reaching its smallest negative at approximately $\varphi/T = 0.4$ and signifying a lack of organization in the structures. Once the smallest negative value of $R_{u'u'}$ is reached it will quickly increase during the later-half of the pulse as the small-scale structures recombine.

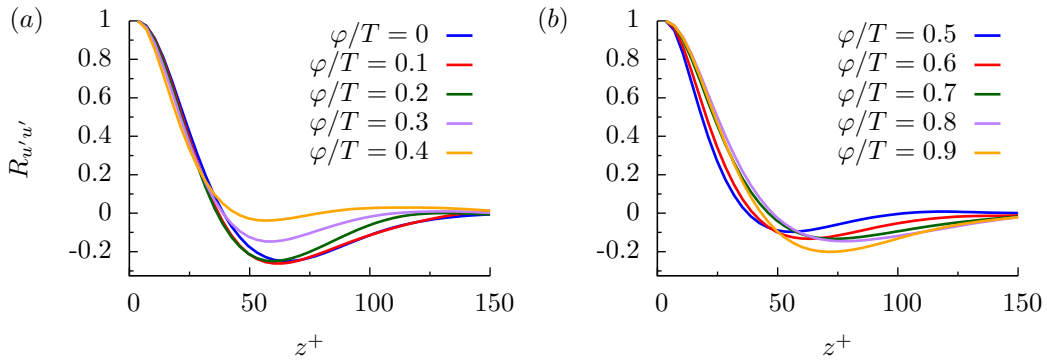

Figure 3.23: Phase-locked spanwise correlation function $R_{u'u'}$ at $y^+ \approx 15$ and phase postions (a) $\varphi/T = [0, 0.1, 0.2, 0.3, 0.4]$ and (b) $\varphi/T = [0.5, 0.6, 0.7, 0.8, 0.9]$.

A log-log plot of the phase-locked spanwise energy spectrum $E_{u'u'}/(\overline{u}_\tau^2 h)$ at $y^+ \approx 15$ is shown in figure 3.25 and a log-linear plot of the pre-multiplied spectrum $k_z E_{u'u'}/\overline{u}_\tau^2$ at $y^+ \approx 15$ is shown in figure 3.26. At the end of the pulse-cycle ($\varphi/T = 0.9$) energy starts to increase within the wavenumber region centered around $k_z h \approx 8$ and there is initially minimal change in the energy at the low and high wavenumber region. During the period of the pulse where the elongated streaks are present ($\varphi/T = 0.1 - 0.2$), minimal change in the energy at the low wavenumber occurs. As the streaks break apart ($\varphi/T = 0.3$), energy

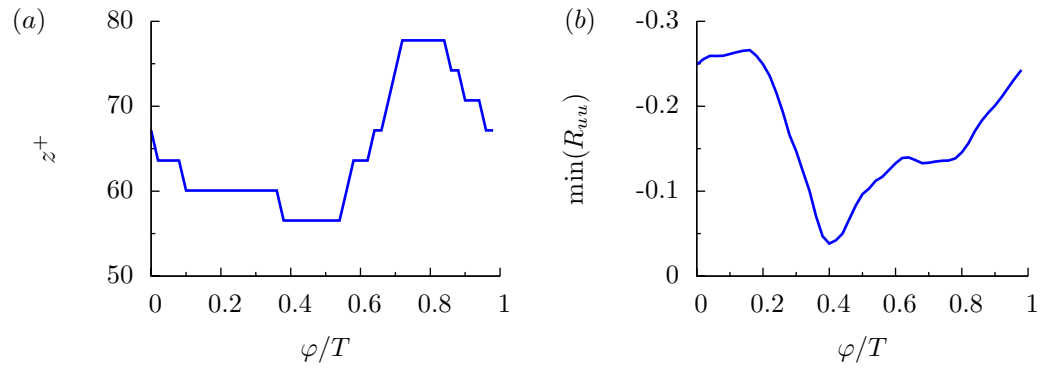

Figure 3.24: Phase-wise variation at $y^+ \approx 15$ in the (a) spanwise streak spacing and (b) minimum value in the spanwise correlation function $R_{u'u'}$.

increases at the low wavenumber region of the spectrum. At $\varphi/T = 0.4$ energy increases at the low and high wavenumber region while it is also decreasing at $k_z h \approx 10$.

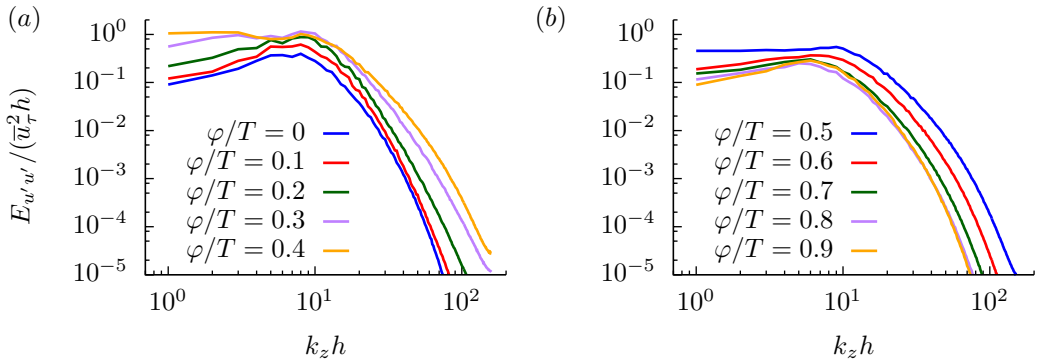

Figure 3.25: Phase-locked spanwise energy spectrum $E_{u'u'}/(\overline{u}_\tau^2 h)$ at $y^+ \approx 15$ and phase postions (a) $\varphi/T = [0, 0.1, 0.2, 0.3, 0.4]$ and (b) $\varphi/T = [0.5, 0.6, 0.7, 0.8, 0.9]$.

Contour plots of the phase-locked pre-multiplied spectrum $k_z E_{u'u'}/\overline{u}_\tau^2$ are shown in figure 3.27 at various phases during the pulse. These figures emphasizes that as the elongated streaks first break down into smaller-scale structures, energy increases in the low wavenumber region of the spectrum. High energy within this region persists for only a short period of the pulse and by $\varphi/T = 0.5$ the low wavenumber energy begins to increase in the outer wall

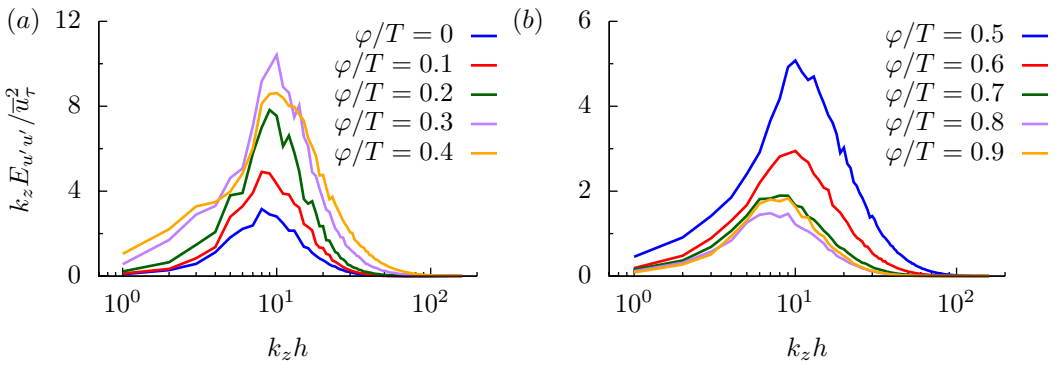

Figure 3.26: Phase-locked spanwise pre-multiplied spectrum $k_z E_{u'u'}/\overline{u}_\tau^2$ at $y^+ \approx 15$ and phase postions (a) $\varphi/T = [0, 0.1, 0.2, 0.3, 0.4]$ and (b) $\varphi/T = [0.5, 0.6, 0.7, 0.8, 0.9]$, .

region.

The phase-locked streamwise correlation function $R_{u'u'}$ at $y^+ \approx 15$ is shown in figure 3.28. As the streaks elongate during the acceleration period of the pulse the correlation function increases. This is followed by the correlation function decreasing once the streaks break down into smaller-scale fluctuations. For the later-half of the pulse cycle, while turbulence is high, there is minimal change in the correlation function.

Figure 3.29 shows a log-log plot of the phase-locked streamwise energy spectrum $E_{u'u'}/(\overline{u}_\tau^2 h)$ at $y^+ \approx 15$ and a log-linear plot phase-locked streamwise pre-multiplied spectrum $k_x E_{u'u'}/\overline{u}_\tau^2$ at $y^+ \approx 15$ is shown in figure 3.30. The pre-multiplied spectrum shows that the length of the domain in the x-direction does not capture the peak in energy at low wavenumbers when the elongated steaks are present during flow acceleration. As the streaks break apart the peak in the pre-multiplied spectrum is captured by the domain length. Although the domain length is insufficient to capture uncorrelated streaks this did not affect the accuracy of the time-averaged turbulent statistics, as shown in figure 3.11. When the elongated streaks are present during the early period of the pulse, there is minimal energy in the high wavenumber

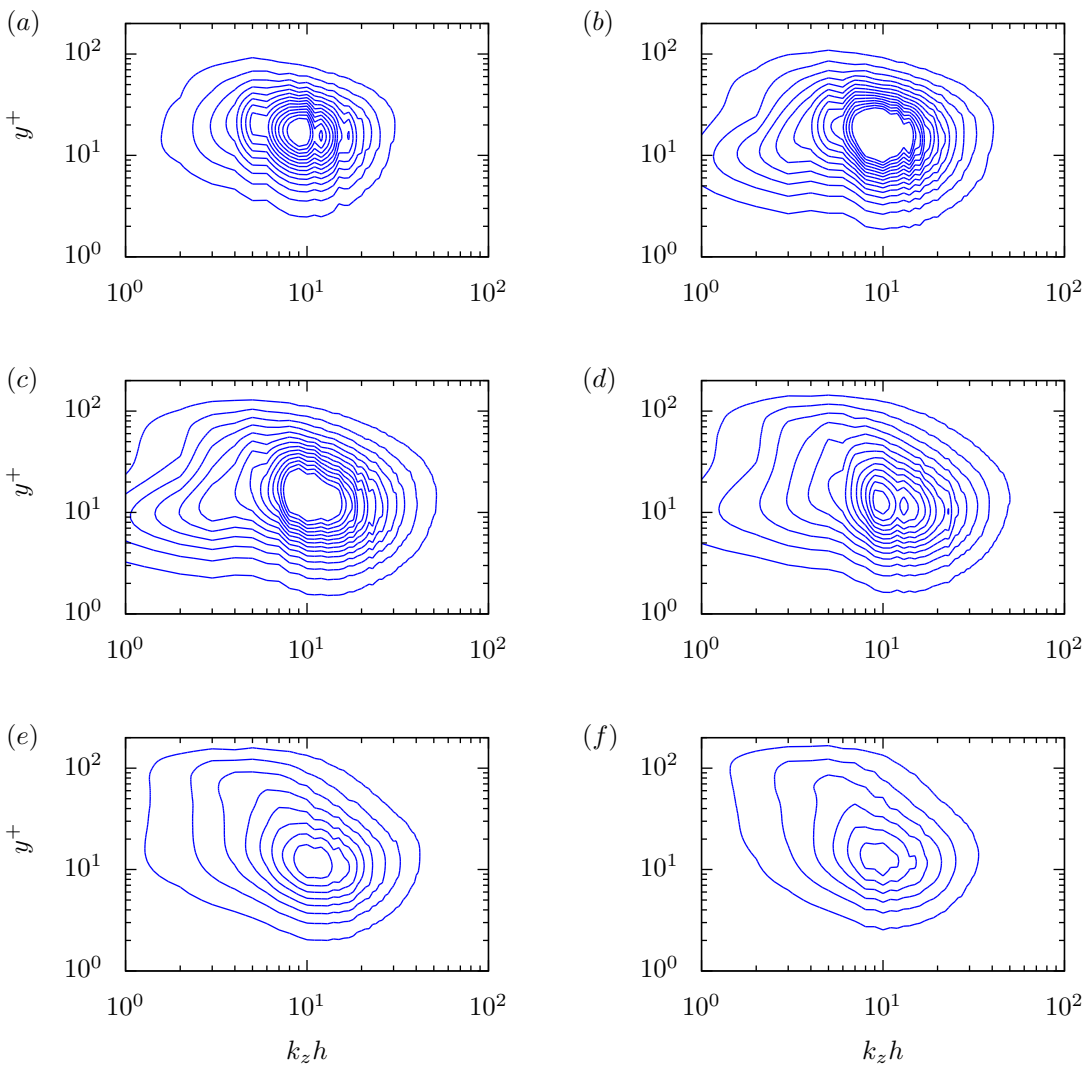

Figure 3.27: Phase-locked spanwise pre-multiplied spectrum $k_z E_{u'u'}/\overline{u}_\tau^2$ at phase postions (*a*) $\varphi/T = 0.2$, (*b*) $\varphi/T = 0.3$, (*c*) $\varphi/T = 0.4$, (*d*) $\varphi/T = 0.46$, (*e*) $\varphi/T = 0.52$ and (*f*) $\varphi/T = 0.58$. Contour level varied from 0.5 to 7 at increments of 0.5.

region. As the elongated streaks break apart, at $\varphi/T = 0.4$ it can be seen low wavenumber energy decreases while high wavenumber energy increases. During the later-half energy at all wavenumbers decreases and at $\varphi/T = 0.9$ it can be seen that low wavenumber energy has started to increase again while the high wavenumber energy is still decreasing. The domain

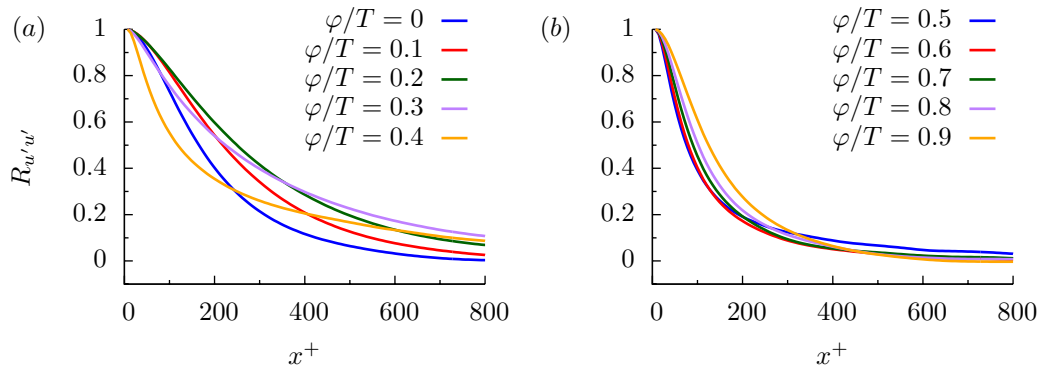

Figure 3.28: Phase-locked streamwise correlation function $R_{u'u'}$ at $y^+ \approx 15$ and phase postions (*a*) $\varphi/T = [0, 0.1, 0.2, 0.3, 0.4]$ and (*b*) $\varphi/T = [0.5, 0.6, 0.7, 0.8, 0.9]$.

length in the x-direction used in the present study is comparable to the x domain length used by He & Seddighi [42] in their study of accelerating channel flow.

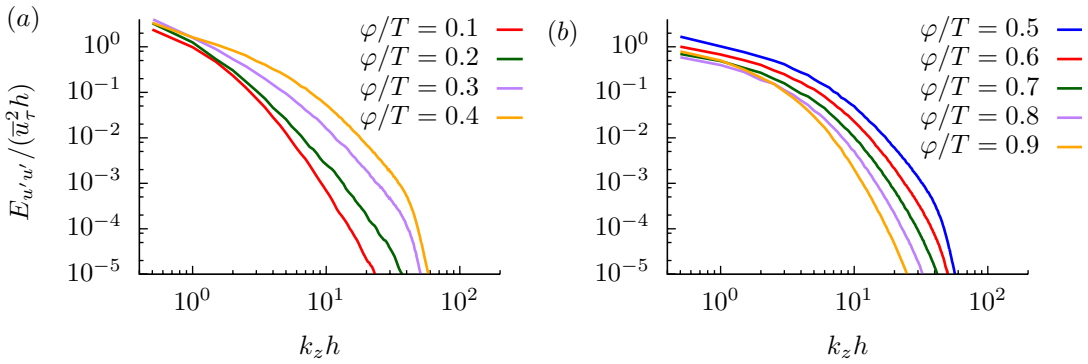

Figure 3.29: Phase-locked streamwise energy spectrum $E_{u'u'}/(\overline{u}_\tau^2 h)$ at $y^+ \approx 15$ and phase postions (*a*) $\varphi/T = [0.1, 0.2, 0.3, 0.4]$ and (*b*) $\varphi/T = [0.5, 0.6, 0.7, 0.8, 0.9]$.

3.3.3 Quadrant analysis

The turbulent shear stress $\langle u'v' \rangle$ can be decomposed into four types of coherent fluid motion, referred to as quadrant components. The first quadrant ($Q1$) is a region of fluid with $u' > 0$ and $v' > 0$ and contains coherent structures that move away from the wall at a high velocity.

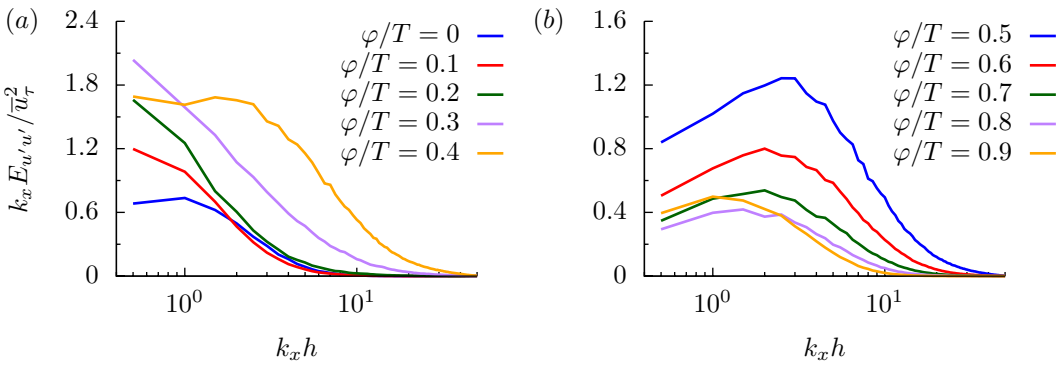

Figure 3.30: Phase-locked streamwise pre-multiplied spectrum $k_x E_{u'u'}/\overline{u}_\tau^2$ at $y^+ \approx 15$ and phase postions (a) $\varphi/T = [0, 0.1, 0.2, 0.3, 0.4]$ and (b) $\varphi/T = [0.5, 0.6, 0.7, 0.8, 0.9]$.

The second quadrant ($Q2$) contains low-speed structures that are being ejected away from the wall and has $u' < 0$ and $v' > 0$. The third quadrant ($Q3$) consists of the inward motion of a low-speed fluid structures and $u' < 0$ and $v' < 0$. Finally the fourth quadrant ($Q4$) has $u' > 0$ and $v' < 0$ and contains high-velocity coherent structure moving towards the wall, sometimes referred to as a sweep event. Only negative turbulent shear events ($Q2$ and $Q4$) contributes to positive TKE production. Time-averaged profiles of $\overline{u'v'}^+$, $\overline{Q2}^+$, $\overline{Q4}^+$ are shown in figure 3.31 (a) and $\overline{Q1}^+$, $\overline{Q3}^+$ are shown in figure 3.31 (b). The sum of the four components giving the turbulent shear stress $\overline{u'v'}^+$. Close to the wall $\overline{Q4}^+$ events exceed $\overline{Q2}^+$ and $\overline{Q1}^+$ events exceed $\overline{Q3}^+$. Away from the wall the opposite trend occurs. The distribution of the time-averaged quadrant components for pulsatile channel flow follows the well-known trend that also occurs for steady channel flow (Kim et al. [54]). At the channel center, although the turbulent shear stress goes to zero the individual quadrant components have non-zero values. Results from Manna et al. [75] showed that at moderate amplitude the time-averaged distribution of the quadrant components are similar to the steady case.

The phase-wise variation in the turbulent shear stress $\langle u'v' \rangle^+$, $\langle Q2 \rangle^+$ and $\langle Q4 \rangle^+$ are

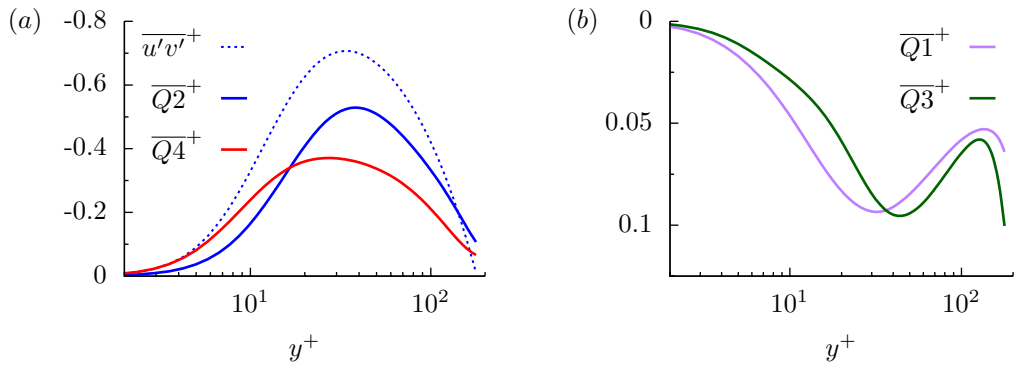

Figure 3.31: Time-averaged profiles of (a) $\overline{u'v'}^+$, $\overline{Q2}^+$, $\overline{Q4}^+$ and (b) $\overline{Q1}^+$, $\overline{Q3}^+$. The sum of the four quadrant components gives the turbulent shear stress $\overline{u'v'}^+$.

shown at $y^+ \approx 5$ and $y^+ \approx 45$ in figure 3.32 (a) and (b), respectively. As shown previously in figure 3.12 (a), close to the wall there is greater phase-lag in the wall-normal component of turbulence compared to the streamwise component and consequently within the wall region, $\langle u'v' \rangle^+$ is relatively small at the start and end phases of the pulse. During the mid-portion of the pulse there is a rapid increase in $\langle u'v' \rangle^+$. It can be seen in figure 3.32 (a) that at $y^+ = 5$, not only are $\langle Q4 \rangle^+$ events more intense, relative to $\langle Q2 \rangle^+$, but the peak value occurs substantially earlier. This results in there being a brief portion of the pulse where the wall region is dominated by high-velocity structures being injected towards the wall. The opposite trend is shown in figure 3.32 (b) where at $y^+ = 45$ the peak in $\langle Q2 \rangle^+$ occur before $\langle Q4 \rangle^+$. Thus the outer region is briefly dominated by low-speed structures being ejected away from the wall.

Figure 3.33 (a) shows the phase-lag $\phi_{\widetilde{Q2}}/T$ and $\phi_{\widetilde{Q4}}/T$. Close to the wall the peak in $\langle Q2 \rangle^+$ events occurs first and the outer region the opposite occurs. The amount of phase-lag remains relatively constant, except at $y^+ \approx 25$ where the phase-lag becomes equal for both types of quadrant events. This phase-lag behavior is further emphasized in figure 3.33 (b)

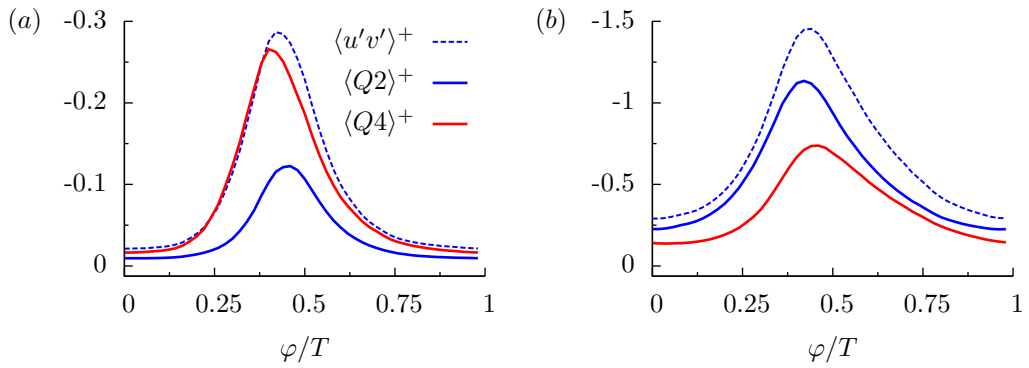

Figure 3.32: Phase-wise variation in the turbulent shear stress $\langle u'v'\rangle^+$, $\langle Q2\rangle^+$ and $\langle Q4\rangle^+$ at (a) $y^+ \approx 5$ and (b) $y^+ \approx 45$.

and (c), where the phase-wise variation in the fraction of $\langle Q2\rangle^+$ and $\langle Q4\rangle^+$ to $\langle u'v'\rangle^+$ at $y^+ \approx 5$ and $y^+ \approx 45$, respectively is shown. The greatest difference between the components occurs slightly after peak flow rate. These observations show similarity to the Seddighi et al. [107] for accelerating channel flow. These authors found that during the late pre-transition and early transition stages there is an increase in $Q4$ events close to the wall with minimal changes in $Q2$ events. The opposite trend was found in the outer region.

The quadrant components of the shear stress are further investigated using a phase-locked joint P.D.F. of the streamwise and wall-normal turbulent fluctuations. Figure 3.34 shows a joint u'-v' P.D.F. at $y^+ \approx 30$. At this location away from the wall, $\langle Q2\rangle$ events are stronger than $\langle Q4\rangle$ and there is approximately equal phase-lag for these components. At $\varphi/T = 0.3$, which corresponds to the elongated streaks starting to break up, there is minimal fluctuation in v'. In addition at this phase there is a greater occurrence of positive u' fluctuations while negative u' fluctuations are less common but can be at a higher intensity. From $\varphi/T = 0.34 - 42$ the joint P.D.F. shows fluctuation in v' increase while there is minimal change in the distribution of u' fluctuations and at $\varphi/T = 0.7$ both u' and v' are decreasing.

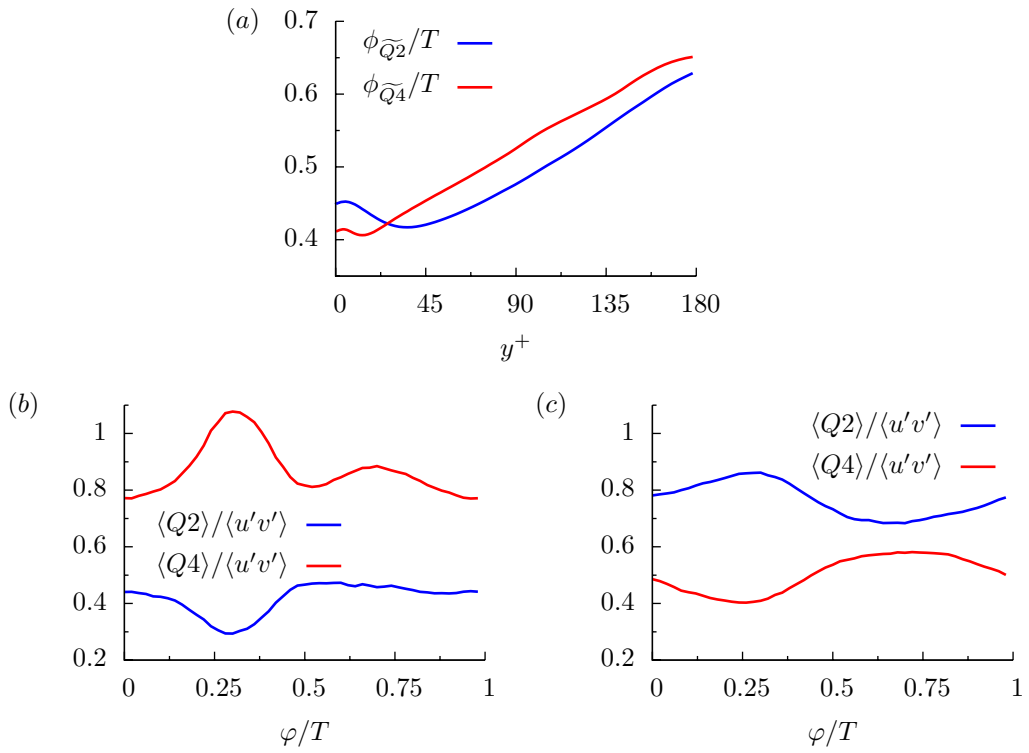

Figure 3.33: (a) Phase-lag $\phi_{\widetilde{Q2}}/T$ and $\phi_{\widetilde{Q4}}/T$. Phase-wise variation in the percent contribution of $\langle Q2\rangle$ and $\langle Q4\rangle$ to the total turbulent shear stress at (b) $y^+ \approx 5$ and (c) $y^+ \approx 45$.

Figure 3.35 shows the phase-locked joint u'-v' P.D.F. at $y^+ \approx 5$. At this wall location, $\langle Q4\rangle^+$ events are stronger and have less phase-lag compared to $\langle Q2\rangle^+$ events. Overall this joint P.D.F. exhibits behavior similar to the joint P.D.F. at $y^+ \approx 30$. A notable difference is that close to the wall there is more phase-lag compared to outer regions in the channel and from $\varphi/T = 0.3 - 0.38$ the fluctuations in u' are still increasing.

3.3.4 DMD applied to channel flow

In the following section the challenges of applying the dynamic mode decomposition (DMD) algorithm to turbulent channel flow data will be discussed. The method has been implemented on both instantaneous and phase-averaged velocity from the pulsatile case and instantaneous

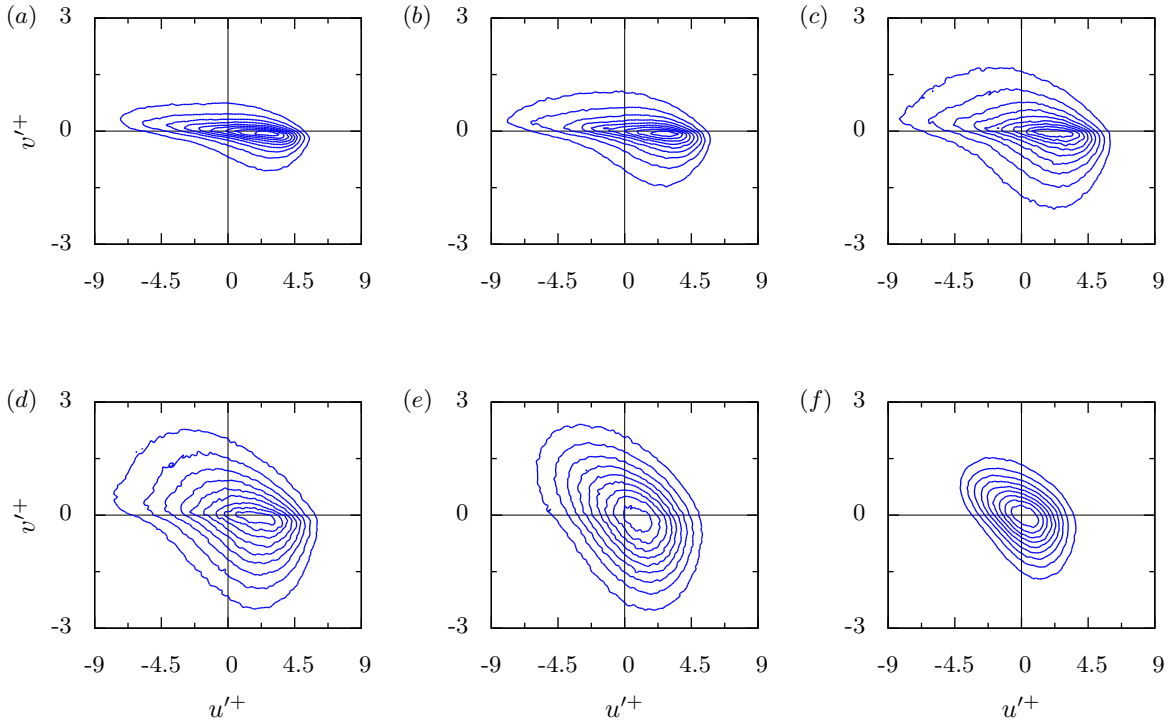

Figure 3.34: Phase-locked joint u'-v' P.D.F. at $y^+ \approx 30$ at phase positions (a) $\varphi/T = 0.3$, (b) $\varphi/T = 0.34$, (c) $\varphi/T = 0.38$, (d) $\varphi/T = 0.42$, (e) $\varphi/T = 0.5$ and (f) $\varphi/T = 0.7$. Contour in between 0.1 and 0.9 maximum probability level at increments of 0.1.

velocity data from the steady case. The purpose of applying DMD to channel flow is to extract coherent motion that corresponds to a particular frequency.

First the effectiveness of DMD is be examined when it is applied to phase-averaged velocity the from the pulsatile case. The DMD algorithm is applied to $m = 25$ snapshots of $\langle u \rangle$ separated by $\Delta t = 0.04/T$. Since the decomposition is performed on $\langle u \rangle$, turbulent oscillations have been removed though phase and spatial averaging and therefore the DMD algorithm is decomposing only periodic oscillations. Each snapshot is store as a column in the matrix $\mathbf{\Psi}$, which is of size 80×25. The resulting weighted inner product matrix $\mathbf{\Psi}^* \mathbf{M} \mathbf{\Psi}$ is of size 25×25 and is relatively inexpensive to compute since the vectors ψ_k contain only

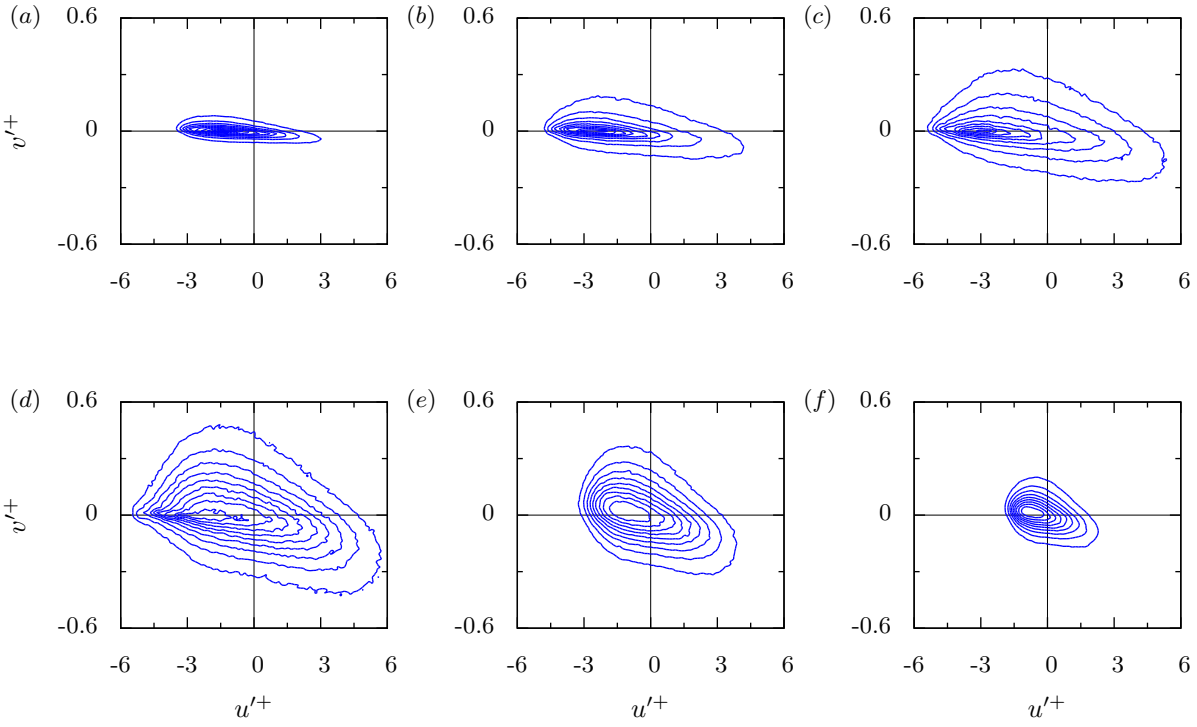

Figure 3.35: Phase-locked joint u'-v' P.D.F. at $y^+ \approx 5$ at phase positions (a) $\varphi/T = 0.3$, (b) $\varphi/T = 0.38$, (c) $\varphi/T = 0.42$, (d) $\varphi/T = 0.46$, (e) $\varphi/T = 0.56$ and (f) $\varphi/T = 0.7$. Contour in between 0.1 and 0.9 maximum probability level at increments of 0.1.

80 entries. A linear-log plot of the DMD amplitude spectrum is shown in figure 3.36 (a). The DMD algorithm computes a mode with a frequency of zero that corresponds to the time-averaged flow and pairs of modes with frequencies that are positive and negative multiples of the pulse period. The mode amplitude quickly decreases as frequency increases. Figure 3.36 (b) shows a plot of the ritz values λ_k and they fall along a unit circle. Modes with ritz values that are on a unit circle have zero growth rates, i.e. mode amplitude remains constant with consecutive oscillations. If the ritz values were within the unit circle that indicates negative growth rate, i.e. mode amplitude decreasing after each oscillation. Figure 3.36 (c) shows the real component of the DMD modes $\Re\big(\boldsymbol{\phi}_k d_k\big)/A_{\widetilde{u}_c}$ for frequencies of $1/T$, $1/(2T)$,

$1/(3T)$ and $1/(4T)$. Modes at frequencies higher than the fundamental only contribute to the phase-averaged velocity close to the wall and this is consistent with the Fourier analysis that identified higher non-linear dynamics close to the wall. Modes at frequencies $\geq 1/(4T)$ do not contribute significantly to the phase-averaged velocity.

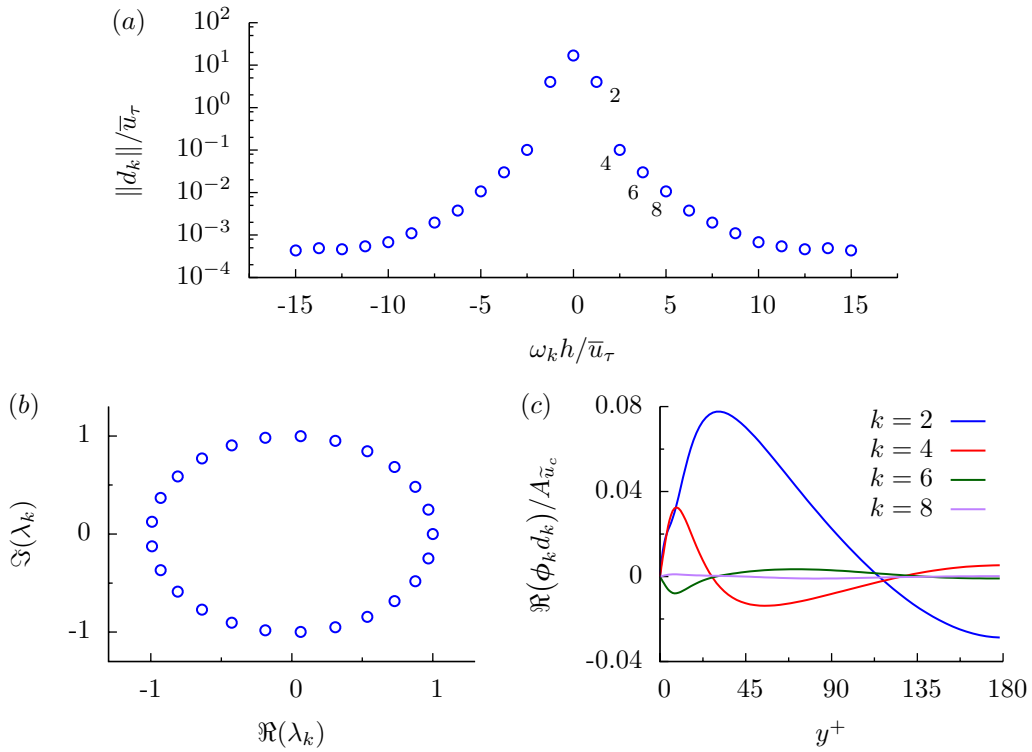

Figure 3.36: DMD calculated from $\langle u \rangle$ using $m = 25$ snapshots separated by $\Delta t = 0.04/T$. (a) Linear-log plot of amplitude spectrum, (b) ritz values and (c) real component of DMD mode $\Re(\boldsymbol{\phi}_k d_k)/A_{\widetilde{u}_c}$ for $k = 2, 4, 6, 8$.

The DMD method is also applied to snapshots of the instantaneous velocity from the steady channel flow case. The DMD calculation is performed using using $m = 469$ snapshots of $\boldsymbol{u}$ separated by $\Delta t^+ = 0.576$ and collected over a sampling interval is $1.5h/u_\tau$. The resulting weighted inner product matrix for this case is of size 469×469 and requires ≈ 115 TB of memory to store. Substantially more computational resources are required in its

calculation, relative to the weighted inner product matrix for the phase-averaged velocity. A log-log plot of amplitude spectrum is shown in figure 3.37 (a) for a frequency range of $\omega_k h/\overline{u}_\tau = 2 - 200$. The ritz values are shown in figure 3.37 (b) to predominantly fall upon a unit circle. Several of the modes have ritz values within the unit circle and this indicates that these modes have relatively large negative growth rate.

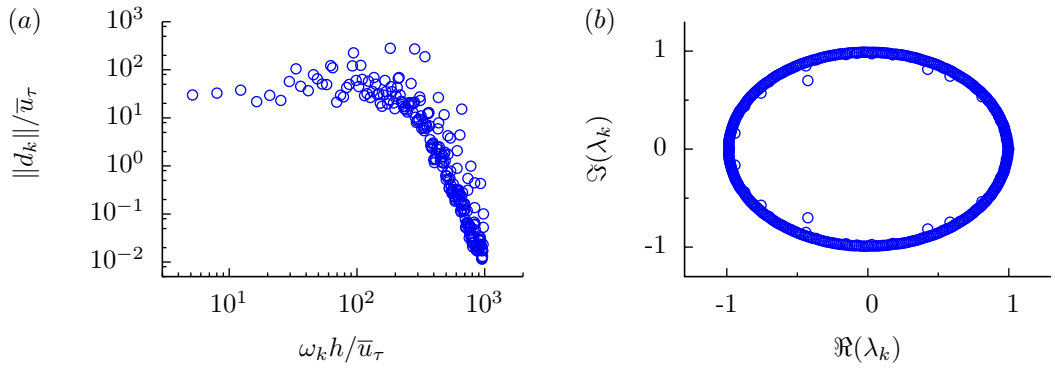

Figure 3.37: Steady simulation. DMD calculated from $\boldsymbol{u}$ using $m = 469$ snapshots separated by $\Delta t^+ = 0.576$. (a) Log-log plot of amplitude spectrum for $\omega_k h/\overline{u}_\tau \in [3, 2000]$ and (b) ritz values. Total length of the sampling interval is $\approx 1.5h/u_\tau$.

A snapshot of the fluctuating streamwise velocity u'^+ plotted on a x-y plane is shown in figure 3.38 (a). Figure 3.38 $(b) - (c)$ shows contours of the streamwise real component of the modes oscillating at frequencies $\omega_k h/\overline{u}_\tau = 20$, 114 and 179, respectively. At $\omega_k h/\overline{u}_\tau = 20$ the mode shows relatively large-scale structures close to the wall and as frequency increases the size of the mode structures decreases.

Several complications arise from applying DMD to instantaneous data from the pulsatile case. Since the period of the pulse is approximately $5h/u_\tau$ a large number of snapshots is required to capture a single pulse period at a small Δt. For example, to capture a single pulse at the same temporal resolution as was done for the above steady case, the DMD

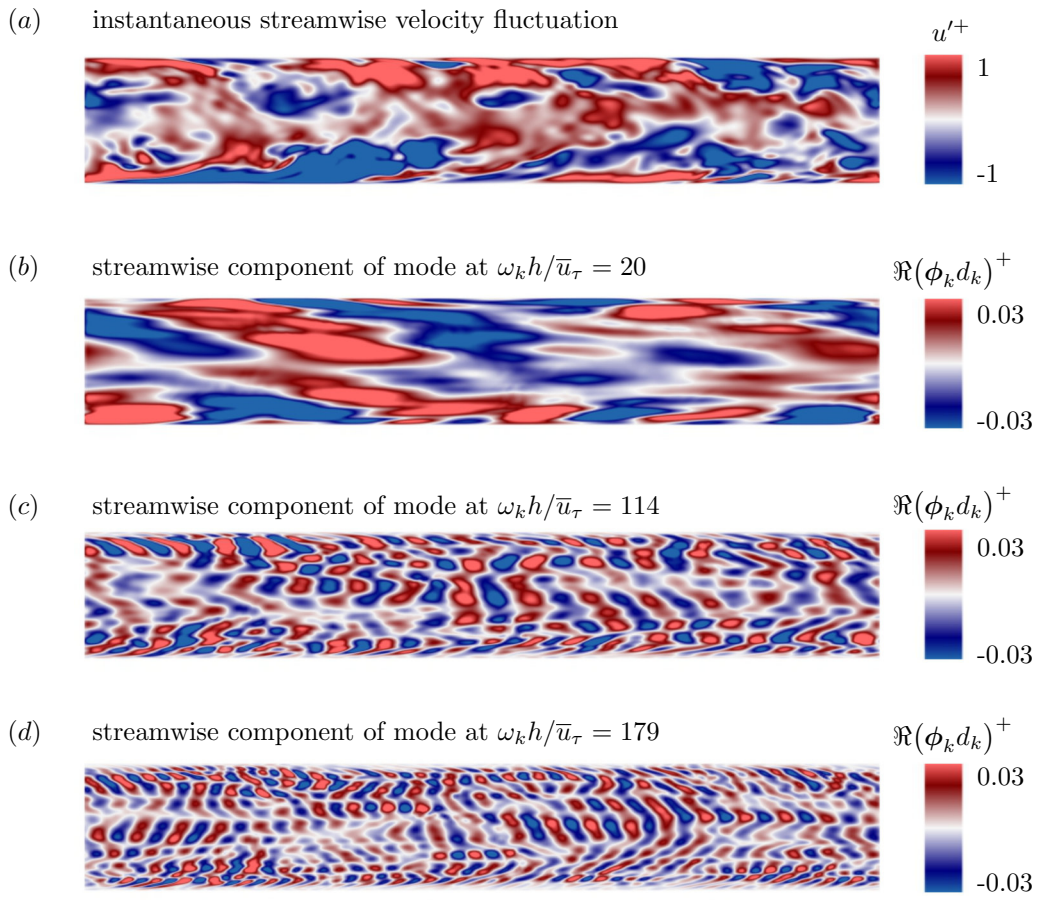

Figure 3.38: Contour plotted on a x-y plane. (a) Snapshot of the flucuating velocity component u'^+. Streamwise component of mode at (b) $\omega_k h/\overline{u}_\tau = 20$, (c) $\omega_k h/\overline{u}_\tau = 114$ and (d) $\omega_k h/\overline{u}_\tau = 179$

requires 1563 snapshots of the instantaneous velocity. In addition it is found that when DMD is applied to turbulent pulsatile data collected over a single pulse, the algorithm does not return the correct pulse frequency. However when DMD is applied to snapshots collected over multiple pulses the correct frequency can be calculated. Figure 3.39 shows the DMD amplitude spectrum calculated from snapshots of $\boldsymbol{u}$ separated by $\Delta t = 0.02/T$ (a) $m = 199$ and (b) $m = 189$. Total length of the sampling interval is $\approx 20h/u_\tau$ and the vertical dashed line in the figure indicates the pulse frequency. Although the sampling interval is large and

higher-frequency motion is not captured by the decomposition, when $m = 199$ (≈ 4 periods) a mode at the dominant pulse frequency is computed by the DMD. However when when $m = 189$ (≈ 3.8 periods) two high amplitude modes are computed with frequencies higher and lower then the pulse frequency. This behavior is presented in chapter 6.

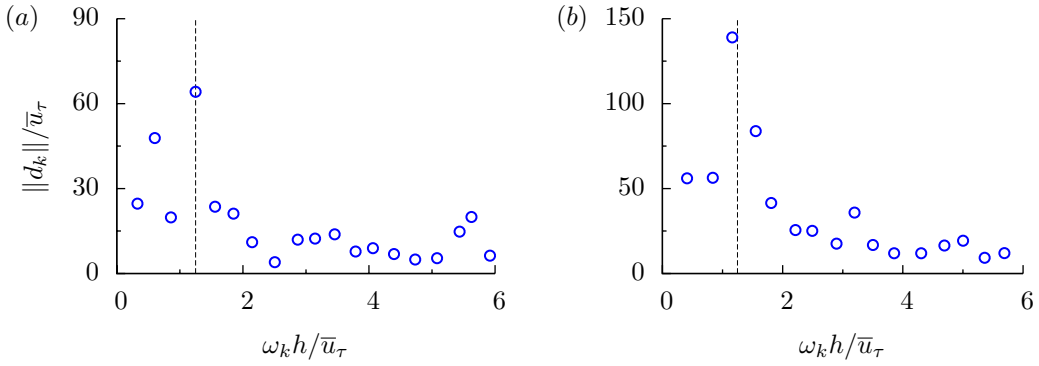

Figure 3.39: DMD amplitude spectrum calculated from snapshots of $\boldsymbol{u}$ separated by $\Delta t = 0.02/T$ (a) $m = 199$ and (b) $m = 189$. Amplitude spectrum for $\omega_k h/\overline{u}_\tau \in [0, 6]$. Total length of the sampling interval is $\approx 20h/u_\tau$ and the vertical dashed line in the figure indicates the pulse frequency.

3.4 Conclusion

In this study pulsatile channel flow was simulated using parameters that are comparable to those found in large artery in the cardiovascular system. Although this study is representative of the highest frequency conditions in arteries, based on the literature on pulsating channel flow it is categorized in the intermediate frequency range. The skin friction, velocity and turbulence all lag behind the pulsatile body force with phase-lag increasing towards the channel center. In the outer region the velocity exhibits single harmonic motion and close to the wall it deviates from this. Since the fluid becomes more turbulent during the deceleration

portion of the pulse this increases the momentum close to the wall. Higher momentum at the wall allows the fluid to resist flow reversal by the pulsating body force. By decomposing the turbulent shear stress into its four quadrant components it is found that these individual components experience varying amounts of phase-lag. There exists a relatively small period of the pulse where the viscous layer is dominated by an excess of $Q2$ events and the opposite occurs in the outer region where it is briefly dominated by $Q4$ events. DMD has been applied to instantaneous and phase-averaged data and some of the challenges arising from this method are discussed.

Chapter 4

The relationship between pulsatile flow impingement and intraluminal thrombus deposition in abdominal aortic aneurysms

Abstract

Direct numerical simulations were performed on four patient-specific AAA geometries and the resulting pulsatile blood flow dynamics were compared to aneurysm shape and correlated with ILT deposition. For three of the cases, turbulent vortex structures impinged/sheared along the anterior wall and along the posterior wall a zone of recirculating blood formed. Within the impingement region the AAA wall was devoid of ILT and remote to this region there was an accumulation of ILT. The high WSS caused by the impact of vortexes is thought to prevent

the attachment of ILT. WSS from impingement is comparable to peak-systolic WSS in a normal-sized aorta and therefore may not damage the wall. Expansion occurred to a greater extent in the direction of jet impingement and the wall-normal force from the continuous impact of vortexes may contribute to expansion. It was shown that the impingement region has low OSI and recirculation zones can have either low or high OSI. No correlation could be identified between OSI and ILT deposition since different flow dynamics can have similar OSI values.

4.1 Introduction

An AAA is a dilatation of the aorta between the renal arteries and the iliac bifurcation. Dilatation weakens the aortic wall making it susceptible to rupture and currently the decision to repair an AAA is based on a diameter criterion of 5.5 cm in men and 5 cm in women. The risk of rupture is significant at sizes greater than 5.5 cm and increases with diameter (Lederle et al. [64]); however, RAAA can have diameters smaller than 5 cm, while others can reach sizes of $10-12$ cm without rupture. The fact that rupture can occur at a wide range of sizes indicates additional criteria could be used to evaluate the susceptibility of AAA rupture.

The tangential force exerted on the arterial wall by blood flow, referred to as WSS, is thought to be an important hemodynamic factor that regulates arterial health. Low WSS and oscillations in blood flow direction are dominant mechanisms that can lead to a deterioration of the arterial wall (Tarbell et al. [116]). The fact that the majority of aortic aneurysms are infrarenal suggests hemodynamics specific to this region trigger the initial aortic dilation. Under resting conditions, only one third of the supraceliac flow rate is directed into the

legs (Ku [58] and WSS is substantially lower in the abdominal segment of the aorta (Tang et al. [115]). Interestingly, it has been shown that patients with a single above-knee leg amputation are more likely to develop AAA (Vollmar et al. [128]). In addition to further lowering WSS in the abdominal aorta, due to reduced blood requirement from the amputated leg, a single above-knee leg amputation causes an asymmetrical flow pattern at the aortic bifurcation. The majority of the blood flow being directed down a single iliac artery of the non-amputated leg causes a higher wall-normal pressure force to be applied along the side with the amputation and expansion was found to be more prevalent on this side.

It is common for ILT to accumulate within AAA. Once a layer of ILT forms the aortic wall is no longer directly exposed to low and oscillating WSS and this cannot be considered the cause of wall deterioration (Lasheras [62]). The aortic wall receives oxygen primarily from luminal blood flow and a layer of ILT may decrease the flow of oxygen (hypoxia), which in turn may decrease wall integrity, making it more susceptible to further expansion or rupture (Vorp et al. [130]). It has been shown that ILT deposition increased AAA growth rate (Parr et al. [88], Wolf et al. [137], Zambrano et al. [143]), regions of the AAA wall with ILT experienced localized hypoxia (Vorp et al. [129] and were thinner with more inflammation (Kazi et al. [53]. Alternatively it has been suggested that ILT is protective and shields the aortic wall from pressure forces (Di Martino et al. [30], Mower et al. [84], Wang et al. [133], Xenos et al. [141]). In Speelman et al. [109] AAA wall stress was lower when a large ILT volume was present but growth rate was also higher. The authors stated that the deterioration of the aortic wall from ILT may be more significant than the hemodynamic forces acting on the wall. It has been suggested that ILT thickness could be used as a criterion, in addition to diameter, when determining risk of rupture (Satta et al. [103]) and ILT deposition in small-sized AAA should

be a factor when considering early surgical repair (Stenbark et al. [111], Wolf et al. [137]).

It is possible that zones of stagnant blood, turbulent fluctuations and flow impingement produce a hemodynamic environment that contributes to AAA expansion, ILT deposition and rupture. As an AAA increases in size adverse hemodynamic conditions may worsen, further increasing the risk of rupture. Since AAA can have a wide variety of shapes, it is possible that particular geometries have greater disturbances in blood flow. Some AAA may dilate to very large sizes while maintaining stable non-disturbed blood flow and therefore could potentially be at a lower risk for rupture. It would be beneficial to be able to identify the flow dynamics associated with particular aortic geometries.

In this current work we computationally investigated pulsatile blood flow dynamics in patient-specific AAA. The study consisted of 23 cases and we focus this chapter on cases 1−4. The results indicate that the impingement of blood flow may prevent ILT deposition and influences the overall aneurysm shape. The remaining 19 cases are referenced to further support this observation and can be found in Appendix A. This work has been published in Lozowy et al. [73].

4.2 Materials and Methods

4.2.1 Model description

Case 1−3 have diameters of 6.8, 6.0 and 11 cm, respectively, and posterior-eccentric ILT of maximum thickness 1.8, 0.4 and 4.4 cm, respectively. For case 3 the ILT becomes circumferential-eccentric in the lower AAA segment. Case 4 has a diameter of 7.4 cm and is

devoid of ILT. The non-dimensional parameters that govern blood flow are the bulk Reynolds number Re_b, Womersley number Wo and the oscillating-to-mean flow rate ratio β, which are, respectively,

$$Re_b = \overline{u}_b D_h / \nu, \tag{4.1}$$

$$Wo = D_h / 2\sqrt{\omega / \nu}, \tag{4.2}$$

$$\beta = u_{osc} / \overline{u}_b. \tag{4.3}$$

Here $\nu = \mu/\rho$ is the kinematic viscosity, with μ and ρ being the dynamic viscosity and density, respectively, $\omega = 2\pi/T$ is the angular frequency, u_{osc} is the amplitude of the oscillating component of the pulse and $\overline{u}_b$ is the time-average of the bulk velocity at the inlet boundary. The length scale used to define Re and Wo is the inlet hydraulic diameter $D_h = 4\mathcal{A}/\mathcal{P}$, where $\mathcal{A}$ and $\mathcal{P}$ are the cross-sectional area and perimeter of the upstream aorta inlet, respectively. Although blood is a non-Newtonian fluid it can be assumed to behave like a Newtonian fluid in large arteries (Ku [58]). Using physiologically-realistic flow conditions $\beta = 5.5$, $\mu = 0.0035$ kg m^{-1} s^{-1}, $\rho = 1050$ kg m^{-3} and $T = 1$ s. The mean and maximum bulk flow rate is 20 ml s^{-1} and 130 ml s^{-1}, respectively. For the cases in this study, Re_b varied from $254-313$ and Wo varied from $16.5-20.5$. The x-axis is placed perpendicular with the axial plane and is referred to as the streamwise direction. The temporal variation in the infrarenal bulk flow rate used in this study is shown in figure 2.6 (a). The term infrarenal refers to the segment of the aorta below the renal arteries. The pulse profile used is from Les et al. [68], where

it was calculated from patients with AAA and the mean infrarenal flow rate was found to be 17.5 ± 5.44 ml s^{-1}. The flow rate used in our study is then slightly above average for patients with AAA.

4.2.2 Simulation details

To satisfy a criterion of having the CFL number < 1 the time-step is fixed at $\Delta t = 2.5 \times 10^{-5}$ s for case 1 and $\Delta t = 5 \times 10^{-5}$ s for cases 2−4. At each time-step the equations were considered converged when the residual became less than 1×10^{-6}. The time-dependent bulk velocity shown in figure 8.2 is implemented at the upstream inlet boundary. A uniform velocity is used as the boundary condition, as opposed to a fully developed profile, since within the aorta only several cm are required for an oscillating boundary layer to develop (Wood [140]) and at no point does the mean component reach a fully developed state (Caro et al. [18]). At the outlet boundaries, downstream in the iliac arteries, a reference pressure of $p = 0$ is imposed and the arterial walls were assumed to be rigid with a no-slip condition. The initial flow field is set to zero and statistics were collected after 5 pulses simulated to remove the affect of initial conditions. The time average of a flow quantity is represented by an overbar and is calculated by averaging over a period defined by $t_i = 5$ s and $t_f = 13$ s.

Unstructured grids are generated composed of prism cells extruded from the wall and tetrahedral cells occupying the interior of the domain. The wall tangent edge length of the first prism cell adjacent to the wall was fixed at 0.002 cm and 15 prism cells were extruded from the wall at an expansion rate of 1.25. The edge length of the interior tetrahedral cells is fixed at 0.065 cm. The size of the grids used in this study varied from 6494498 to 13173579

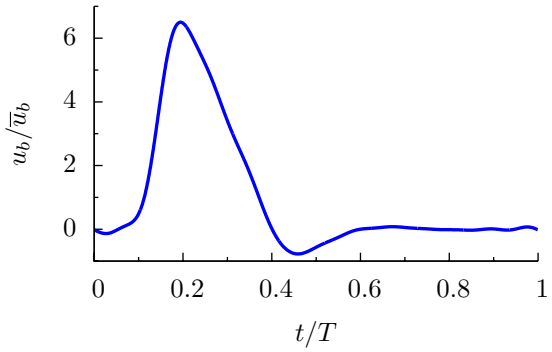

Figure 4.1: Infrarenal aortic bulk flow rate.

and is comparable to those from previous studies (Arzani et al. [3], Les et al. [67], Zambrano et al. [143]). The grid resolution was assessed by comparing the average edge length of a grid cell Δ to the time-averaged Kolmogorov length scale $\overline{\eta} = (\nu^3/\overline{\epsilon})^{1/4}$, where the term $\overline{\eta}$ gives the smallest scale of turbulent motion (Pope [96]). The term $\overline{\epsilon}$ is the time-averaged rate of TKE dissipation and is calculated using the triple decomposition method introduced by Hussain & Reynolds [45]. Each period is segmented into $M = 50$ equidistant phase positions and at each phase $N = 25$ snapshots of the velocity field are collected. The time-average of ϵ is calculated by averaging the 1250 instantaneous snapshots. This procedure was performed for case 3 and $\left(\Delta/\overline{\eta}\right)_{max} = 3.1$, indicating that the smaller turbulent fluctations are resolved by the grid.

4.3 Results

4.3.1 Velocity field

Figure 4.2 shows for case 1, mid-sagittal CTA, instantaneous and time-averaged contours of streamwise velocity plotted on the mid-sagittal section. During systole, the blood flow is predominantly channeled within the AAA. By late-systole, a jet has formed that is directed towards the anterior wall and there is a small zone of recirculating blood along the posterior wall. During diastole, although the bulk flow rate in the abdominal aorta is effectively zero, the high momentum jet structures continue to flow downstream, shearing/impinging against the anterior wall and transition to turbulence. By $t/T = 0.56$ the structures have traversed to the mid-region of the AAA. In the upstream aorta, throughout the cardiac cycle, the blood flow behaves qualitatively similar to the analytical solution shown in figure 2.7. The time-averaged streamwise velocity shows blood flow channeling along the anterior wall and a region of recirculating blood along the posterior wall. Referring to the mid-sagittal CTA, anterior wall is devoid of ILT and the posterior wall exposed to recirculation correlates with ILT deposition.

Figure 4.3 shows for case $2-4$, mid-sagittal CTA, instantaneous coherent structures visualized using the Q-criterion and time-averaged streamlines. During diastole for case 2 and 3, turbulent vortexes shearing along the anterior wall and recirculating blood occurs along the posterior wall. The wall is devoid of ILT at the impingement site and directly below this region ILT accumulates and the posterior wall has considerable ILT. White arrows shown on the CTA indicate the location on the anterior wall ILT starts to accumulate. Case 4 is devoid of ILT and although a jet forms at the neck during systole, the vortexes stagnate at the

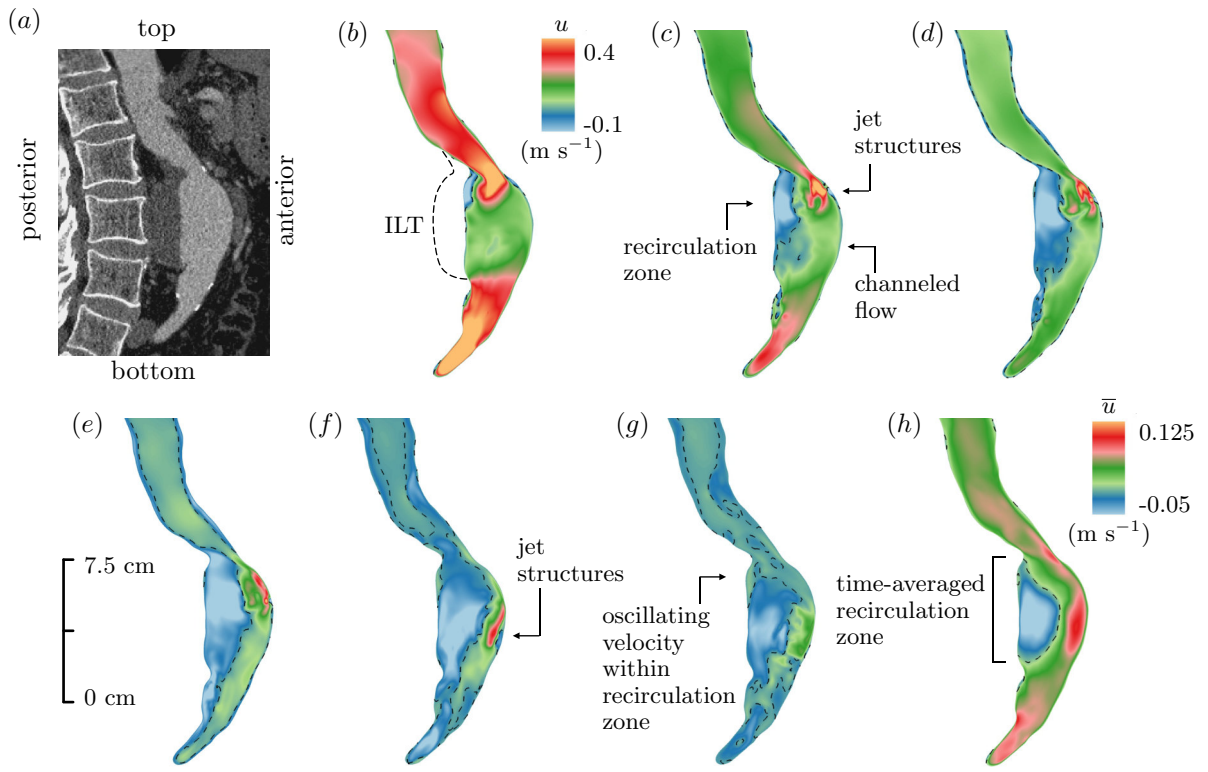

Figure 4.2: Case 1. (a) Mid-sagittal CTA. Instantaneous streamwise velocity at (b) $t/T = 0.24$, (c) $t/T = 0.32$, (d) $t/T = 0.36$, (e) $t/T = 0.4$, (f) $t/T = 0.56$ and (g) $t/T = 0.72$. (h) Time-averaged streamwise velocity. Dashed line in contours seperates regions of positive and negative velocity. Dashed line outside flow channel in (b) shows ILT deposition.

neck region without propagating downstream into the AAA. The time-averaged streamlines indicate the blood flow is predominantly channeled for this case.

Figure 4.4 and 4.5 shows for case 1 and 2, respectively, mid-axial CTA, instantaneous and time-averaged contours of streamwise velocity plotted on the mid-axial section. The jet is initially laminar and transitions to turbulence once it impacts against the wall. White arrows shown on the CTA indicate the location on the wall ILT starts to accumulate. The region of high velocity is devoid of ILT and the edge of this region correlates with the start of ILT accumulation. For case 1, the layer of posterior ILT results in the circular shaped AAA having an oval shaped lumen and the oval shape is tilted in the direction of impingement.

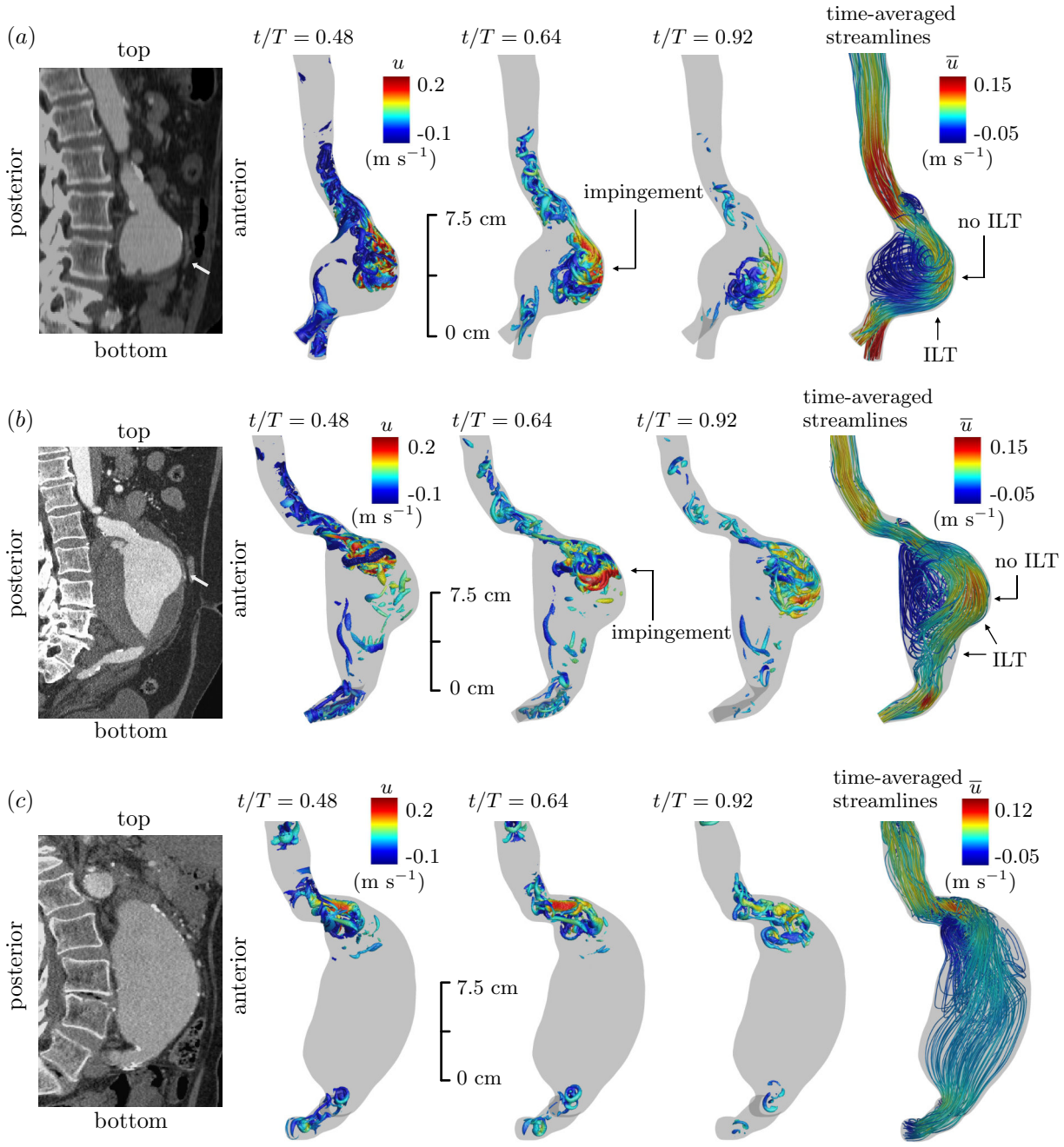

Figure 4.3: Mid-sagittal CTA with white arrow indicating the region on the anterior wall ILT starts to accumulate, instantaneous coherent structures visualized using the Q-criterion and time-averaged streamlines for (*a*) case 2, (*b*) case 3 and (*c*) case 4.

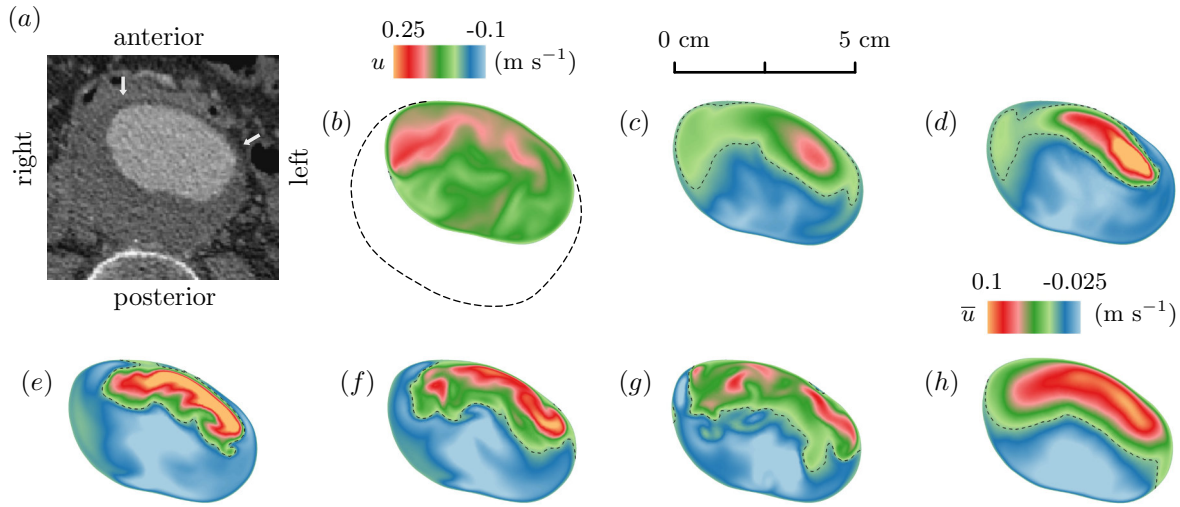

Figure 4.4: Case 1. (a) Mid-axial CTA with white arrows indicating the region on the aortic wall ILT starts to accumulate. Streamwise instantaneous velocity at (b) $t/T = 0.20$, (c) $t/T = 0.4$, (d) $t/T = 0.44$, (e) $t/T = 0.52$, (f) $t/T = 0.60$ and (g) $t/T = 0.72$. (h) Time-averaged streamwise velocity. Dashed line in contour separates regions of positive and negative velocity. Dashed line outside flow channel in (b) shows ILT deposition.

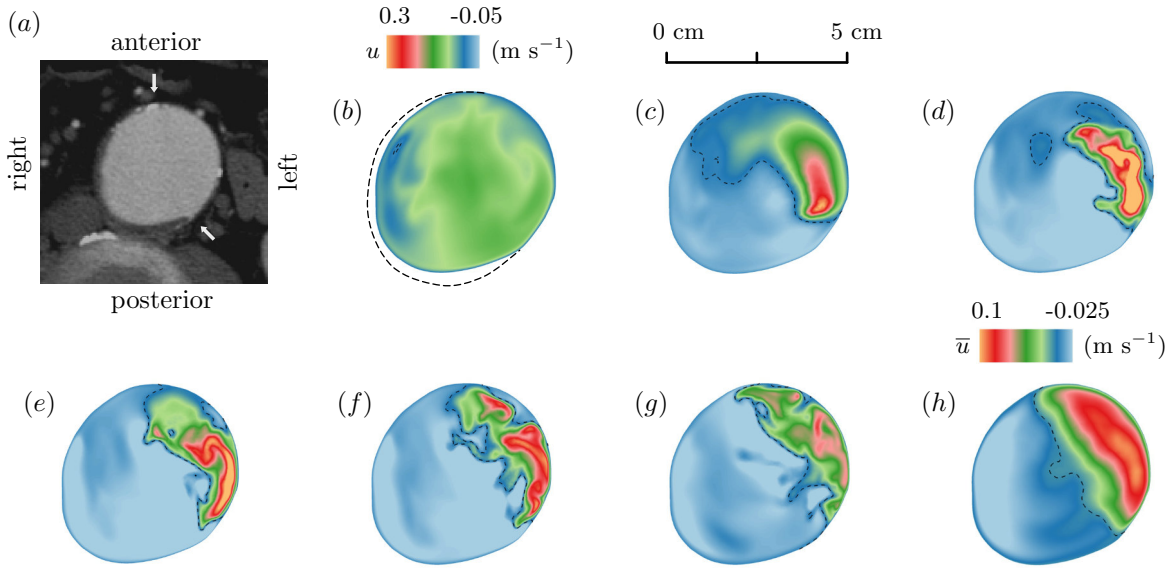

Figure 4.5: Case 2. (a) Mid-axial CTA with white arrows indicating the region on the arterial wall ILT starts to accumulates. Streamwise instantaneous velocity at (b) $t/T = 0.20$, (c) $t/T = 0.36$, (d) $t/T = 0.40$, (e) $t/T = 0.44$, (f) $t/T = 0.48$ and (g) $t/T = 0.56$. (h) Time-averaged streamwise velocity. Dashed line in contour separates regions of positive and negative velocity. Dashed line outside flow channel in (b) shows ILT deposition.

4.3.2 Wall shear stress

The peak WSS calculated from the analytical solution in figure 2.7 is 2.4 N m^{-2} and this value will be used as a reference. Figure 4.6 shows for case 1, anterior facing surface contours of $\tau_{w,x}$ at various times during diastole. From late-systole to early-systole of the next pulse the blood flow reverses in direction close to the wall and this results in the streamwise-component of WSS having low and negative values for a majority of the cardiac cycle. Regions of elevated $\tau_{w,x}$ correspond to the impact of vortexes against the wall. The peak WSS magnitude within the AAA occurs at $t/T = 0.52$ and is $\|\boldsymbol{\tau}_w\| = 3.4$ N m^{-2}. Although WSS caused by impingement is substantially higher then the surrounding regions in the AAA, it is comparable to the peak value obtained from the analytical solution. In the upstream aorta, peak WSS varies based on aortic diameter but is similar to the value predicted by the analytical solution.

Figure 4.7 shows for case 2, the streamwise-component of WSS plotted along the circumference of the axial slice shown in figure 4.5. At peak-systole, $\tau_{w,x}$ is low and uniform along the circumference. During late-systole, $\tau_{w,x}$ continues to be low but has reversed in direction

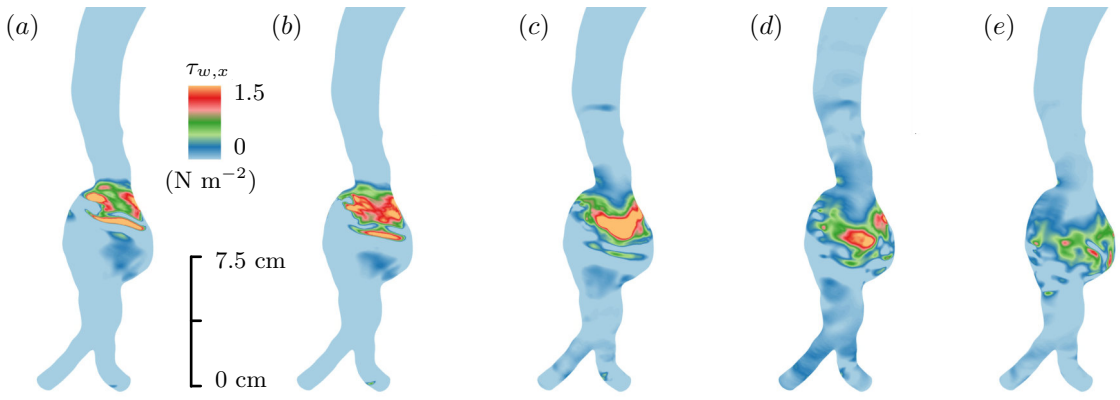

Figure 4.6: Case 1. Anterior facing surface contour of the instantaneous streamwise-component of WSS at (*a*) $t/T = 0.4$, (*b*) $t/T = 0.44$, (*c*) $t/T = 0.52$, (*d*) $t/T = 0.6$ and (*e*) $t/T = 0.72$. Light blue colour indicates $\tau_{w,x} \leq 0$.

along the posterior-right side. During diastole, turbulent vortexes shear pass the anterior-left side causing high and fluctuating WSS.

Surface contours of OSI for case $1-4$, are shown in figure 4.8 $(a)-(d)$. Since a uniform velocity was imposed at the inlet, OSI is low directly downstream of the inlet. Once an oscillating boundary layer develops, OSI is high within the straight segments of the aorta. For cases $1-3$, the continuous blood motion from impingement causes low OSI within this region. Case 2's recirculation zone has low OSI, indicating continuous upstream motion caused by the jet's downstream motion on the opposite side. The recirculating zone for cases 2 and 3 contain regions with both high and low OSI values. High OSI within a recirculation zone is the result of an oscillating velocity similar to that shown in figure 4.2 (d). For cases 2 and 3, directly below the impingement region OSI remains low and the lower anterior wall for case 3 has high OSI. For case 4, aside from the neck region, OSI is predominantly high within the AAA.

Surface contours of normalized transWSS are shown for cases $3-4$ in figure 4.8 $(e)-(f)$. Within the straight segments of the aorta transWSS is low and this indicates that although the blood flow is highly oscillatory, the oscillations occur along a single axis. Within the impingement region, transWSS is high combined with low OSI. This indicates the instantaneous WSS vector fluctuates about the dominant axis and the fluctuation remains directed along the dominant flow direction. Although case 4 has a large lumen, transWSS is predominantly low, indicating laminar blood flow within the AAA. At most wall locations, an inverse relationship was found between OSI and transWSS.

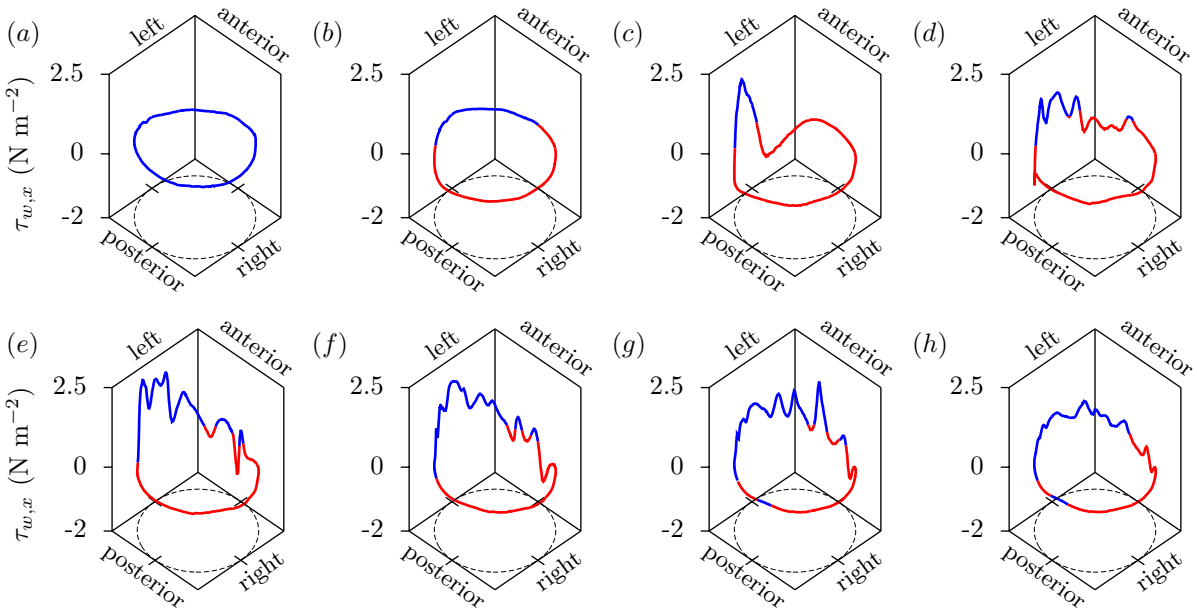

Figure 4.7: Case 2. Instantaneous streamwise-component of WSS plotted along the circumference of the mid-axial slice shown in Fig. 4.5a at (a) $t/T = 0.20$, (b) $t/T = 0.32$, (c) $t/T = 0.40$,(d) $t/T = 0.48$, (e) $t/T = 0.52$, (f) $t/T = 0.56$, (g) $t/T = 0.60$ and (h) $t/T = 0.64$. Blue and red color distinguishes positive and negative values, respectively.

4.4 Discussion

Results are presented from simulations of pulsatile blood flow in four medium-to-large-sized AAA. It was found that a jet forms at the AAA neck during systole. For cases 1−3, during diastole turbulent vortexes from the jet continue to circulate within the AAA and impinge against the anterior wall with a zone of recirculating blood forming along the posterior wall. It can be seen in figures 4.3, 4.4 and 4.5 that the impingement site is devoid of ILT and there is a build-up in ILT remote from this region. Figure 4.7 shows that within the AAA, WSS caused by impingement is substantially higher than peak-systolic WSS. We present an argument that high WSS from the impact of a vortex prevents the attachment of ILT to the aortic wall.

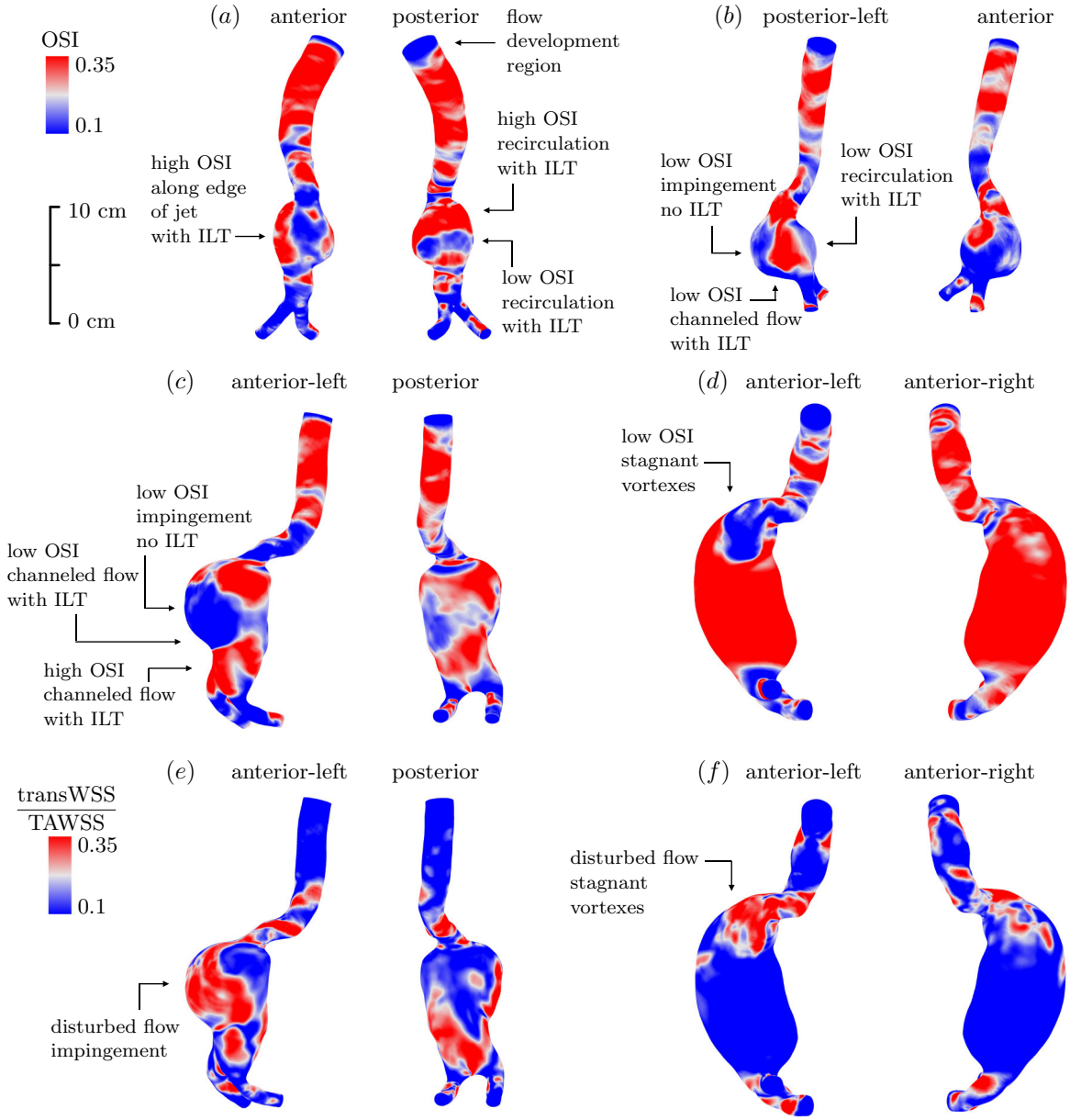

Figure 4.8: Surface contour of OSI for (a) case 1, (b) case 2, (c) case 3 and (d) case 4. Surface contour of normalized transWSS for (e) case 3 and (f) case 4.

It has been established by previous studies that recirculating blood correlates with vascular disease. Regions of recirculating blood have been shown to develop atherosclerosis in carotid bifurcation (Zarins et al. [144]) and ILT in intracranical aneurysms (Ray et al. [98]). Doyle et al. [33] investigated the growth and rupture in an AAA and it was shown that low WSS corresponded with the region with AAA growth, ILT deposition and rupture. Zambrano et al. [143] studied ILT growth in a group of 14 various sized AAA and observed ILT deposition occurred in regions with low WSS and ILT accumulation began in a localized region before spreading out other regions. Since our present study only used a single static CTA for each case, it does not provide any new insight into the hemodynamic cause of ILT deposition. Rather our study identified a hemodynamic factor that may locally prevent the accumulation of ILT.

It has been suggested high WSS from impingement in intracranial aneurysms contributes to growth and rupture (Meng et al. [78]) and Dolan et al. [31] defined high WSS as greater than 3 N m^{-2}. Although our simulations showed WSS from impingement is relatively high, it is comparable to peak-systolic WSS in a straight normal-sized aorta. Therefore, vortexes shearing along the wall may not directly damage the aorta. Caro et al. [18] suggested increased cardiac output from exercise would raise WSS and have a protective effect against atherogenesis. It has been shown exercise conditions raised WSS and lowered OSI within the abdominal aorta (Tang et al. [115], Taylor et al. [118]). Similar results were found to occur in AAA (Suh et al. [113], Les et al. [67]) with it being suggested this would reduce AAA growth (Les et al. [67]) or the accumulation of ILT (Zambrano et al. [143]). Exercise promoting aortic health by raising WSS is consistent with the concept of high shear from impingement locally preventing ILT. An increased cardiac output is not considered a cardiovascular risk

and this supports the hypothesis that impingement does not cause shearing damage.

It can be seen in figure 4.8 that cases 1−3 experience greater expansion on the side the flow structures impact. Although the continuous impact of these vortexes may have a positive effect by locally preventing ILT, the wall-normal force exerted by these impacts could contribute to expansion. This is consistent with a previous finding that AAA from patients with single above-knee leg amputations were more likely to expand on the side with the amputation due to asymmetric blood flow (Vollmar et al. [128]) and it was suggested by Lashera [62] that tensional stresses, and not shear stresses, are the cause of AAA remodeling. Since impingement was found to occur primarily during diastole, the vortexes are relatively slow-moving compared to peak-systole flow velocity. It can be speculated that although their impact may gradually influence expansion, it has insufficient force to be the cause of mechanical failure (rupture) in the wall. In our previous work, we examined the location of rupture in a group of 7 RAAA (Boyd et al. [15]), and found that although high pressure and WSS occurred at the impingement site, rupture occurred in regions dominated by low WSS, recirculating blood and ILT deposition.

For this study a total of 23 AAA cases with diameters greater than 5 cm were simulated. The AAA size, ILT location and impingement location if present, are summarized in table 4.1. Additional CFD results for these cases is shown in Appendix A. It is observed that blood flow impingement similar to cases 1−3 only occurs in AAA with medium-to-large-sized lumen and requires a sudden expansion in lumen cross-sectional area at the neck. For AAA geometries with small-sized lumen or gradual increases in lumen diameter at the neck, flow structures stagnant at the neck (similar to what was seen with case 4). Irrespective of the size or shape of an AAA, during peak-systole the blood flow is channeled and predominantly laminar. The

case	sex	maximum AAA diameter (cm)	neck angulation (degrees)	maximum ILT thickness (cm)	ILT deposition location	impingement location
1	M	6.8	45	1.8	posterior	anterior
2	M	6.0	45	0.4	posterior-right	anterior-left
3	M	11.0	60	4.4	posterior	anterior
4	M	7.4	80	0.0	-	-
5	F	5.0	45	0.5	right	anterior-left
6	M	5.3	25	1.0	anterior	-
7	F	5.5	60	1.0	circumferential-anterior	-
8	M	5.5	40	1.4	posterior	anterior
9	M	8.0	45	2.8	circumferential-posterior	-
10	F	5.4	70	0.0	-	left
11	M	6.5	30	4.0	anterior	-
12	M	5.5	20	2.0	right	left
13	M	6.9	35	2.8	anterior	-
14	M	5.7	45	0.4	anterior-left	-
15	F	6.6	0	2.0	circumferential-anterior	-
16	M	5.5	0	1.0	posterior	-
17	M	5.7	50	1.0	posterior	anterior
18	M	5.5	20	0.4	posterior-left-right	-
19	M	5.9	15	1.0	circumferential	-
20	F	5.5	20	2.4	anterior	-
21	M	9.2	75	0.8	right	left
22	M	8.0	80	0.0	-	-
23	M	5.5	20	2.8	anterior	-

Table 4.1: Patient information. Further detail on these cases can be found in appendix A.

time-averaged velocity field gives an overall description of the hemodynamics, but does not fully capture the disturbed flow dynamics that can occur during late-systole and diastole. For example, figure 4.2 shows the size of the recirculation zone varies with time and figure 4.6 shows the region of high WSS moves along with the vortexes as they flow downstream.

Impingement is found to occur in 9 cases with the jet structures always flowing in the direction the neck angles the blood flow. For 8 of these cases, ILT of various thickness is present remote from the impingement site. Six cases have anterior-eccentric ILT and one case has circumferential-eccentric ILT. For these cases, a thick layer of ILT results in a small-sized

lumen flow channel and the blood flow is stable without impingement or recirculation. From a single static CTA, it cannot be identified what hemodynamic factors would cause ILT to deposit on the anterior wall. The remaining 7 cases experience flow dynamics similar to case 4, where there is no impingement and minimal ILT. Again this study does not identify why AAA similar to case 4 would develop.

Previous studies have shown it to be more common for ILT to be anterior-eccentric in AAA (Hans et al. [41], Pillari et al. [94], Metaxa et al. [79]). Since our study showed impingement is primarily directed towards the anterior wall, this could indicate that the shape that leads to impingement is less common compared to other AAA shapes. In Metaxa et al. [79] it was found that AAA with posterior-eccentric ILT have lower growth rates compared to AAA with anterior-eccentric ILT. Although impingement may contribute to expansion, the possible removal of ILT deposition along the anterior wall may result in a overall slower rate of growth compared to AAA with a thick layer of anterior-eccentric ILT. Despite case 4 having a large lumen, its blood flow is predominantly non-disturbed and no ILT deposition was present. As such, it may represent a type of AAA geometry that is at lower risk of further growth and rupture.

The question was raised in Peiffer et al. [92] as to whether high OSI and low WSS adequately describe relevant blood flow features. Since WSS is proportional to diameter, in general WSS decreases as AAA size increases. Although OSI provides a useful description of the flow dynamics, we believe within AAA it is not the correct metric to use when identifying abnormal hemodynamics. It should be noted that a wide variety of pulse profiles and values for Re_b and Wo can occur within the cardiovascular system. Any observations made for AAA hemodynamics may not hold for different cardiovascular locations. For example,

typical non-dimensional parameters in intracranical aneurysms are $Re_b = 436$, $Wo = 1.8$ and $\beta = 0.6$ (Valen-Sendstad et al. [125]). Although Re_b is similar between these cardiovascular locations the large differences in Wo and β will produce vastly different flow dynamics, i.e., in intracranical arteries high OSI may be an indication of disturbed flow behavior (Meng et al. [78]). Below is a summary of the observed flow dynamics compared with OSI and ILT deposition.

- At the location the jet structures impinge OSI is low, WSS and transWSS are high and the wall is devoid of ILT. Simply from this observation it could be concluded that low OSI has an preventative affect on ILT deposition; however, we believe that the mechanism is the shearing caused by the impact of vortexes and low OSI is only a consequence of this flow.

- For cases 2 and 3 directly below the impingement region OSI remains low and ILT accumulates. The blood flow in this region can be described as channeled and unidirectional.

- For case 3 along the lower segment of the anterior wall there is a thick layer of ILT and OSI is high. While case 4 has predominantly high OSI and there is no ILT. This flow can be described as a attached boundary layer that oscillates in direction. Figure 4.8a and b show that along the edge of the impingement region, blood flow exhibits this behavior and ILT is present.

- Zones of recirculating blood are characterized by low time-averaged velocity flowing opposite to the dominant flow direction. Figure 4.8a shows the recirculation zone can

have distinct regions of both low and high OSI, and these variations do not appear to affect ILT thickness.

From this study a direct correlation could not be identified between OSI and ILT deposition or AAA shape. This is due to different flow dynamics having similar OSI values. Arzani et al. [6] performed a study on ILT growth in 10 small-sized AAA and regions with low OSI experienced the most ILT growth. Low OSI was thought to represent recirculating blood and this is consistent with what we observed in the recirculation zone of case 2. A similar observation was made by ORourke et. al. [85] where, in three small-sized AAA, there was a correlation between regions with low OSI and ILT growth. Since both of these studies used small-sized AAA, they may have observed more normally channeled flow and not the greater disturbances in flow that can occur in larger AAA.

A limitation of this study is the model excluded arteries that branch off of the aorta and instead implemented the infrarenal flow rate at the supraceliac level in the aorta. Disturbances in the blood flow have been observed at the renal arteries (Ku [57]). Since the bulk flow rate is effectively zero during diastole, these flow disturbances would stagnate at the renal arteries and not propagate downstream pass the AAA neck. Therefore it is unlikely that the inclusion of visceral arteries would not appreciably alter our results.

In conclusion, this study showed that high WSS from the impingement of vortexes is associated with an absence of ILT deposition. It is unlikely that impingement is beneficial, as the continuous impact of vortexes could, over an extended period of time, be contributing to AAA expansion. The continuous downstream motion from the vortexes results in low-velocity recirculation on the opposite side and this flow dynamic increases the likelihood of a layer

of posterior-eccentric ILT forming. Wall hypoxia is potentially caused by the layer of ILT preventing adequate oxygen diffusion and this results in the deterioration of the posterior aortic wall; the typical location of aortic rupture (Hans et al. [41]). It would be beneficial to further investigate how the risk of rupture for an AAA with impingement and posterior-eccentric ILT compares to an AAA with stable blood flow and a layer of anterior-eccentric ILT.

Chapter 5

Turbulent vortex flow effects intraluminal thrombus deposition and expansion in abdominal aortic aneurysms

5.1 Abstract

Numerical simulations were performed in two patient-specific AAA using CTA measurements taken over several years. The growth of the AAA and change in ILT deposition was compared with the blood flow dynamics. For both of these patients the simulations identify that a jet of turbulent blood flow forms at the neck during late-systole. Later into the cardiac cycle, the jet vortexes continue to circulate and come into contact with the wall. No ILT

was found at the location of vortex impingement where blood flow sheared against the wall. In recirculation zones the blood flow could either be laminar or turbulent. ILT formation appears to begin accumulating in the laminar region of the of the recirculation zone, whereas the presence of turbulent vortexes within a recirculation zone may prevent the attachment of ILT to the wall. One of the two cases experienced appreciable AAA growth and since minimal ILT was present within the AAA as the growth occurred, it is suspected that impingement of vortexes was the primary cause of growth. For the other patient the jet vortexes shearer along the wall without directly impinging and this patient experienced less growth.

5.2 Introduction

AAA rupture is associated with high rates of morbidity and mortality. Elective AAA repair takes place when certain aortic diameter criteria are met. Aortic diameter as a primary criterion in the decision to repair is imperfect, as some AAA rupture below operative thresholds, while others reach extreme sizes without rupture. The infrarenal aorta is the most susceptible to aneurysmal dilation and it has been suggested that pathologic hemodynamic changes in this region promote aortic dilation. Hemodynamics may be further disturbed as the aneurysm grows, leading to regions of flow recirculation and low and oscillating WSS. It is well known that oscillatory WSS can promote endothelial injury (Tarbell et al. [116]), whereas low WSS is characterized by inflammatory infiltration (Zarins et al. [144]). It has also been shown that ILT deposition inhibits vascular smooth muscle cell synthesis of collagen (Levene et al. [69], Kazi et al. [53]) has greater inflammatory infiltrate, and may promote thinning of the aortic wall (Burke et al. [16], Adolph et al. [1]).

Relative aortic wall hypoxia has been postulated in regions of high ILT deposition (Vorp et al. [130], Vorp et al. [131]) and has been suggested as a mechanism for aortic wall expansion, degeneration, and rupture. A better understanding of the effect of hemodynamics on AAA growth and rupture is needed, as is a more sophisticated method of predicting rupture risk.

We have previously used CFD to model laminar blood flow in ruptured human AAA and showed that rupture occurs in zones of flow recirculation where WSS is relatively low and ILT deposition is more abundant (Boyd et al. [15]). In the present study we used CFD to model pulsatile aortic blood flow conditions in the growth of 6 human AAA to test the hypothesis that ILT deposition and aortic expansion mediated by vortex flow.

A better understanding of the effect of hemodynamics on the interaction between AAA growth and ILT deposition is needed, as is a more sophisticated method of predicting rupture risk. In the present study we examined the growth of three AAA and used CFD to model pulsatile aortic blood flow conditions in two of the cases to test the hypothesis that ILT deposition and aortic expansion is mediated by vortex flow. Growth data for the first case is presented without supporting CFD flow results since the lumen is small-sized and the flow dynamics are not suspected to deviate from normal aortic flow. In Appendix A from this thesis, several examples of CFD data from similar sized AAA can be found.

5.3 Methods

5.3.1 Model description

Three patients with infrarenal AAA underwent a series of 3 CTA assessments over a period of surveillance ranging from 3 to 5 years. The AAA were followed for 1.5, 5 and 3 years for cases 1, 2 and 3, respectively. Three separate measurements of aortic diameter and maximal ILT deposition were made in the proximal and distal thirds of the aorta, as well as at the mid-point between the lowest renal artery and the aortic bifurcation for each case at each time point. At each time point, thickness and location of ILT deposition, as well as aortic diameter changes in the proximal, mid and distal AAA were measured and CFD-predicted pulsatile aortic blood flow are performed on case 2 and 3.

5.3.2 Simulation details

To satisfy a criterion of having the CFL number less than 1 the time-step was fixed at $\Delta t = 4 \times 10^{-5}$ s. The time-dependent bulk velocity shown in figure 8.2 is implemented at the upstream inlet boundary. Unstructured grids are generated composed of prism cells extruded from the wall and tetrahedral cells occupying the interior of the domain. The wall tangent edge length of the first prism cell adjacent to the wall was fixed at 0.002 cm and 15 prism cells were extruded from the wall at an expansion rate of 1.25. The edge length of the interior tetrahedral cells is set to 0.065 cm. The initial flow field was set to zero and statistics were collected after 5 pulses simulated to remove the effect of initial conditions. The time average of a flow quantity is represented by an overbar and is calculated by averaging over a period defined by $t_i = 5$ s and $t_f = 13$ s.

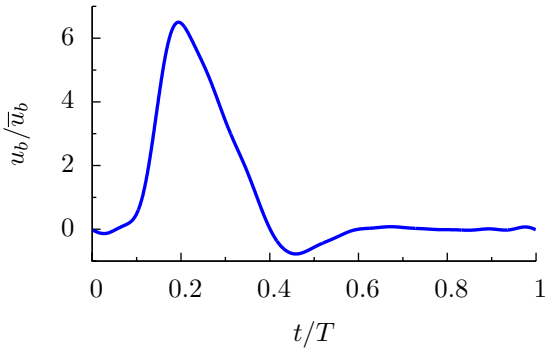

Figure 5.1: Infrarenal aortic bulk flow rate.

5.4 Results

5.4.1 Growth

Figure 5.2 shows CTA for on a mid-axial plane at (a) 0 months, (b) 12 months and (c) 19 months for case 1. Flow simulations are not performed for this case. In this case, the AAA initially has a small-sized luminal diameter ($\approx$ 3 cm) that does not deviate substantially from that of a non-aneurysmal aorta. Based on observations from the previous chapter and the appendix from this thesis, AAA with this type of lumen have predominately laminar

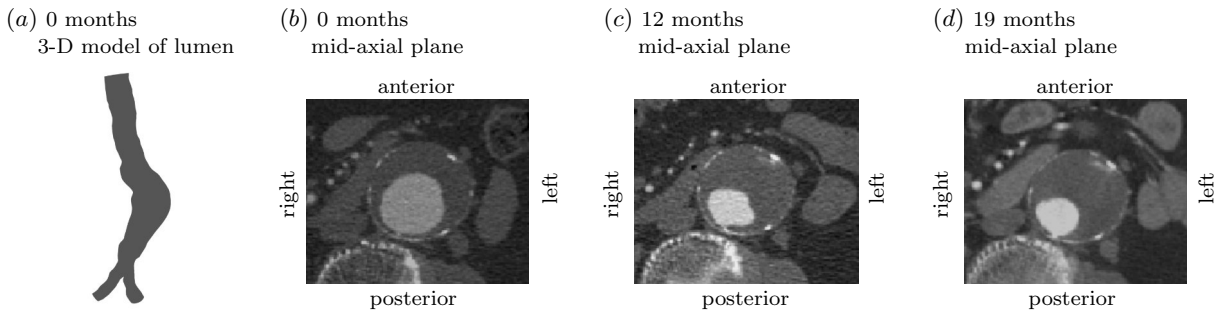

Figure 5.2: Case 1. (a) 3-D model of lumen rotated 45 degrees to left of anterior-posterior and reconstructed from CTA at 0 months. CTA on mid-axial plane at (b) 0 months, (c) 12 months and (d) 19 months.

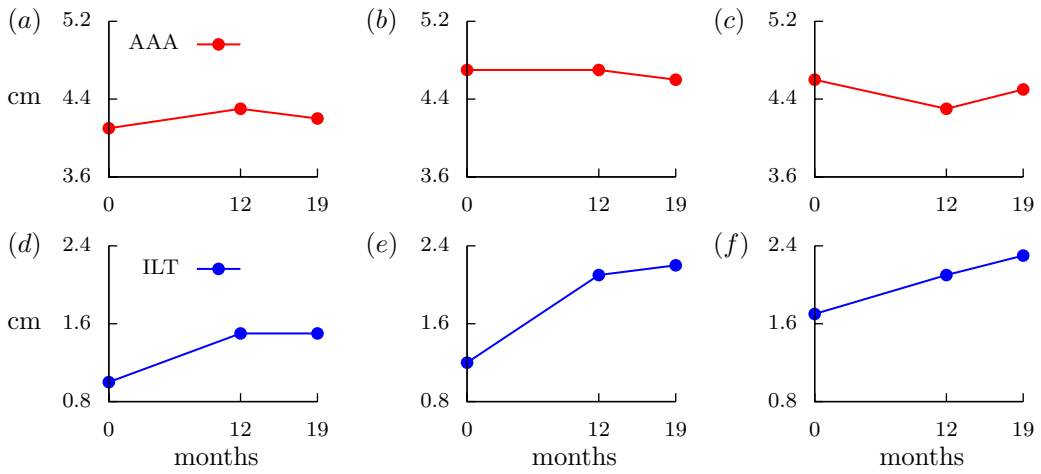

Figure 5.3: Case 1. Change in maximum AAA diameter at (a) below neck, (b) mid-plane and (c) above bifurcation. Change in maximum ILT thickness at (d) below neck, (e) mid-plane and (f) above bifurcation.

non-disturbed flow. It is expected that the flow in this case does not experience substantial aortic wall impingement, recirculation or turbulence. The ILT deposition is anterior-eccentric and over the 19 months there is a substantial accumulation of ILT on the anterior and left wall with minimal accumulation on the posterior and right wall. The change in AAA shape is further examined in figure 5.3 where the change in maximum AAA diameter and maximum ILT thickness measured at three distances from the neck. The size of the AAA does not change substantially during this period but there is a increase in ILT at all measurement locations.

Figure 5.4 shows the change in maximum AAA diameter and maximum ILT thickness measured at three distances from the neck for case 2. At all measurement locations there is a close to linear increase in AAA diameter over the 57 month period. At the measurement location below the neck, there is a moderate increase in ILT over the first 45 months. At the mid-plane there is substantially less ILT accumulation and effectively no ILT accumulated

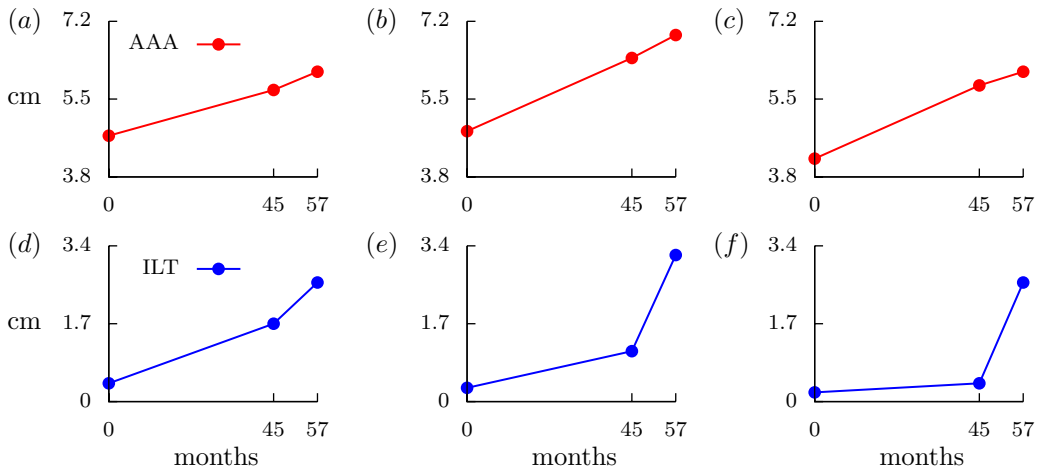

Figure 5.4: Case 2. Change in maximum AAA diameter at (a) below neck, (b) mid-plane and (c) above bifurcation. Change in maximum ILT thickness at (d) below neck, (e) mid-plane and (f) above bifurcation.

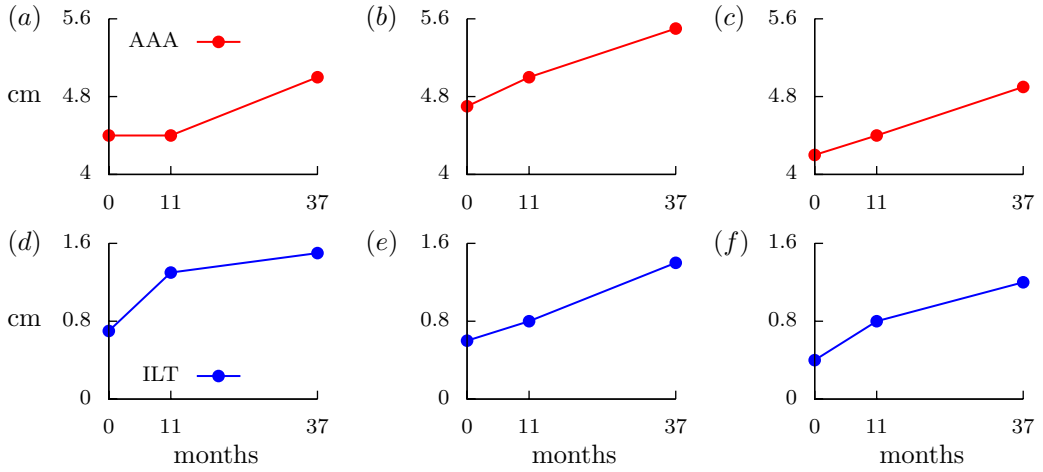

Figure 5.5: Case 3. Change in maximum AAA diameter at (a) below neck, (b) mid-plane and (c) above bifurcation. Change in maximum ILT thickness at (d) below neck, (e) mid-plane and (f) above bifurcation.

above the bifurcation within the first 45 months. From months 45 to 57 there is substantial ILT accumulation at all three measurement locations. In particular for the mid-aneurysm and distal AAA, the majority of the ILT forms within the last 12 months.

Figure 5.5 shows the change in maximum AAA diameter and maximum ILT thickness measured at three distances from the neck for case 3. At the mid-plane and lower region, there is a close to linear increase in AAA diameter and ILT thickness over the 37 month period. Below the neck, during the first 11 months, there is a substantial increase in ILT without a increase in diameter. From 11 to 37 months, below the neck there is minimal change in ILT thickness but AAA diameter increases during this time period. Images of the CTA for case 2 and 3 are shown along with velocity data in the following section.

Growth measurements were taken from an additional three AAA cases (data not shown). Although the increase in ILT deposition over time was not linear, there was an overall positive correlation between AAA growth and ILT deposition.

5.4.2 Velocity field

Figure 5.6 $(a) - (c)$ shows instantaneous coherent structures visualized using the Q-criterion (Hunt et al. [44]) for the three CTA measurements for case 2. The Q-criterion identifies regions with high vorticity and thus can be used to visualize turbulent flow structures. The flow is visualized at the start of diastole ($t/T = 0.48$) and the end of diastole ($t/T = 0.88$). During systole a jet forms at the neck of the AAA and during diastole turbulent structures from the jet continue to circulate within the AAA. Further detail on the formation of this jet and the overall flow dynamics in AAA with large-sized lumen can be found in Lozowy et al. [73]. At 0 months (figure 5.6 (a)), from late-systole to mid-diastole, turbulent vortexes impinge/shear along the anterior-right side and laminar recirculating blood is present along the posterior-left side. The angulation in the neck directs the jet vortexes towards the anterior-right wall. On

the opposition side, during this period of the pulse, laminar low-velocity upstream blood recirculation occurs. By the start of diastole, the jet vortexes have been transported further downstream and impact above the iliac bifurcation. Afterwards during late-diastole, the flow structures recirculate upstream along the posterior-left wall. The vortexes make a complete revolution, exposing the entirety of the AAA wall to turbulent blood flow. Over the next 45 months there is a substantial increase in lumen size. Since the lumen is now larger, the jet structures no longer make a complete revolution. Figure 5.6 (b) shows the jet structures now only shear along the lower portion of the posterior-right side and the region of the lumen on the posterior-left side below the neck is now only exposed to laminar recirculating blood during the cardiac-cycle. At 57 months, the rapid increase in ILT has confined the blood flow to a smaller volume and the now the entire lumen contains persistent turbulent blood flow throughout diastole.

Figure 5.6 (d) shows for case 3, reconstructed at 0 months, instantaneous coherent structures visualized using the Q-criterion are shown for the at various times during late-systole and diastole. Similar to the previous case, a jet forms at the neck during late-systole. Since there is minimal angulation in the neck and the jet structures do not directly impinge and instead only shear along the left wall. During late-systole and early-diastole, the right wall is exposed to laminar recirculation. The jet structures impact above the iliac bifurcation and recirculate on the right side during late-diastole, exposing the lower and mid-region of the right wall to turbulent vortexes. The vortexes do not reach the upper right side and this region is exposed to only laminar recirculating blood during the cardiac-cycle. Over time the lumen decreases in size, however, the flow dynamics do not change substantially at 11 and 37 months (not shown).

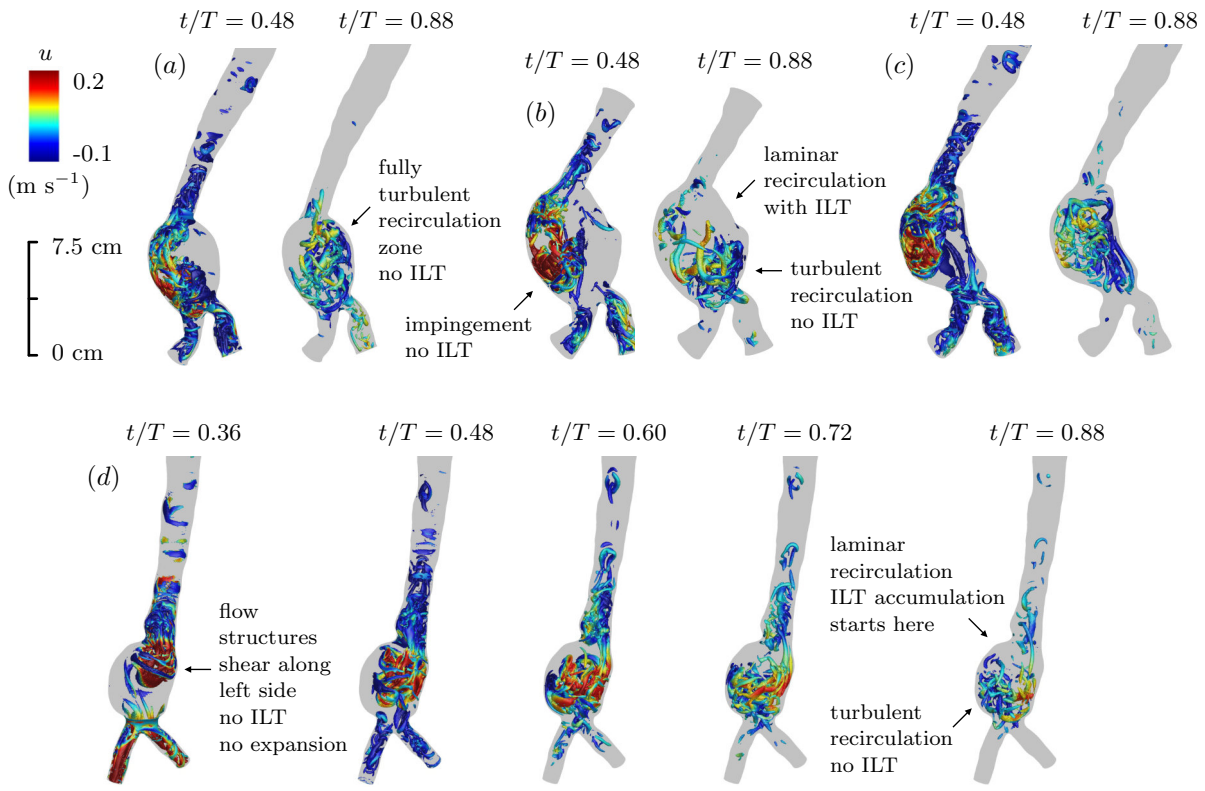

Figure 5.6: Instantaneous coherent structures visualized using the Q-criterion. Case 2 at (a) 0 months, (b) 45 months and (c) 57 months. (d) Case 3 at 0 months.

Figure 5.7 $(a)-(i)$ shows axial CTA and contours of the time-averaged streamwise velocity for case 2. The process of time-averaging removes time-dependent flow features such as vortexes and provides an overall representation of the flow dynamics that occur during a pulse. As the AAA grows over time, the anterior side is always exposed to high time-averaged velocity and the posterior side is always exposed to recirculating blood. Figure 5.7 $(a)-(c)$ show at 0 months there is effectively no ILT within the AAA. Figure 5.7 $(d)-(f)$ show at 45 months, in addition to the AAA increasing in size, a ILT layer has formed along the the left and posterior walls below the neck. At the mid-plane, moderate ILT accumulation occurred in the region between the impingement and recirculation zone and above the bifurcation

there is effectively no ILT present. Figure 5.7 $(g)-(i)$ show at 57 months there was a substantial increase in ILT and the lumen is now irregular in shape. The region of the anterior wall exposed to high velocity is the only region that ILT does not accumulate during the 57 months. Figure 5.7 $(j)-(k)$ shows for case 2, mid-sagittal CTA and contours of the time-averaged streamwise velocity at 0 and 45 months, respectively and this figure emphasizes the substantial increase in AAA size that occurs without build-up in ILT. The angulation in the neck directs the jet of blood towards the anterior wall and the AAA expands out it this direction; however, the spine likely prevents AAA expansion in the posterior direction.

Time-averaged velocity contours and CTA are shown for case 3 on mid-coronal planes in figure 5.8 $(a)-(c)$ and mid-axial planes in figure 5.8 $(d)-(f)$. The right wall is exposed to recirculating blood and ILT accumulates first below the neck on the right side and progressively spreads down the right wall. The lumen volume reduces over time and no ILT accumulation or AAA expansion occurs on the left side.

5.4.3 Wall shear stress

High and fluctuating WSS occurs at any location than a jet vortex impacts or shears along the wall. An example of this is shown in figure 5.9, where for case 3 the instantaneous streamwise-component of WSS plotted at various times during the cardiac cycle along the circumference of the axial slice shown in figure 5.8 (d) (mid-plane and 0 months). At peak-systole, WSS is positive in the x-direction and during diastole, vortex structures shear along the left wall causing high and fluctuating WSS. The WSS caused by the shearing of vortexes is appreciably higher then the peak systolic value. Similar correlation between vortex shearing

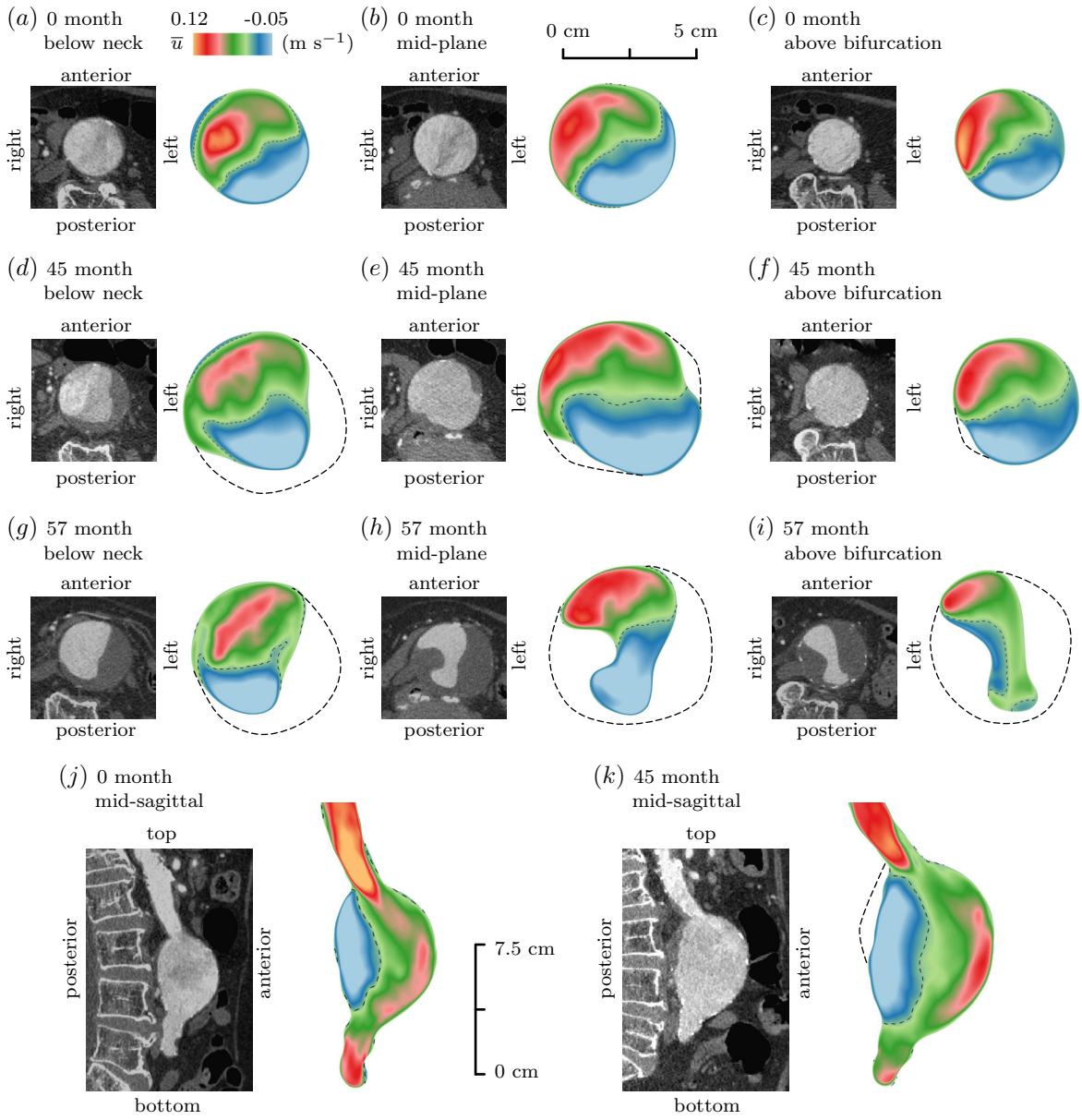

Figure 5.7: Case 2. Axial CTA and time-averaged streamwise velocity. (a) 0 months below neck, (b) 0 months mid-plane, (c) 0 months above bifurcation, (d) 45 months below neck, (e) 45 months mid-plane, (f) 45 months above bifurcation, (g) 57 months below neck, (h) 57 months mid-plane and (i) 57 months above bifurcation. Mid-sagittal CTA and time-averaged streamwise velocity at (j) 0 months and (k) 45 months. Dashed lines within the lumen separate regions of positive and negative velocity. Dashed line outside flow channel show the location of ILT deposition.

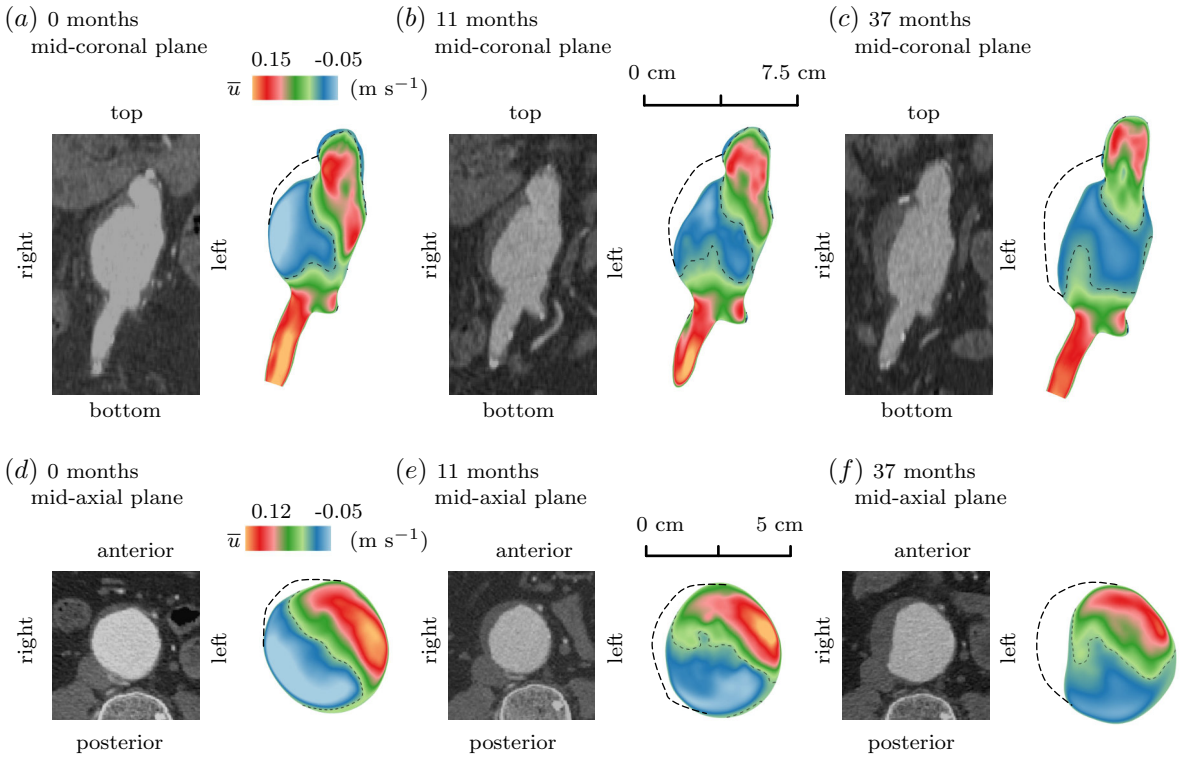

Figure 5.8: Case 3. CTA and time-averaged streamwise velocity. (a) 0 months mid-coronal plane, (b) 11 months mid-coronal plane, (c) 37 months mid-coronal plane, (d) 0 months mid-axial plane, (e) 11 months mid-axial plane and (f) 37 months mid-axial plane. Dashed lines within the lumen separate regions of positive and negative velocity. Dashed line outside flow channel show the location of ILT deposition.

and high WSS is found to occur for case 2 and in particular at 0 months, the entire AAA wall for case 2 is exposed to high WSS. In addition the oscillatory shear index (OSI) is found to be relatively high in regions of laminar recirculation, while turbulent recirculation has a lower OSI, mostly due to the unidirectional motion of the vortexes. Further discussion on OSI in large-sized AAA can be found in Lozowy et al. [73].

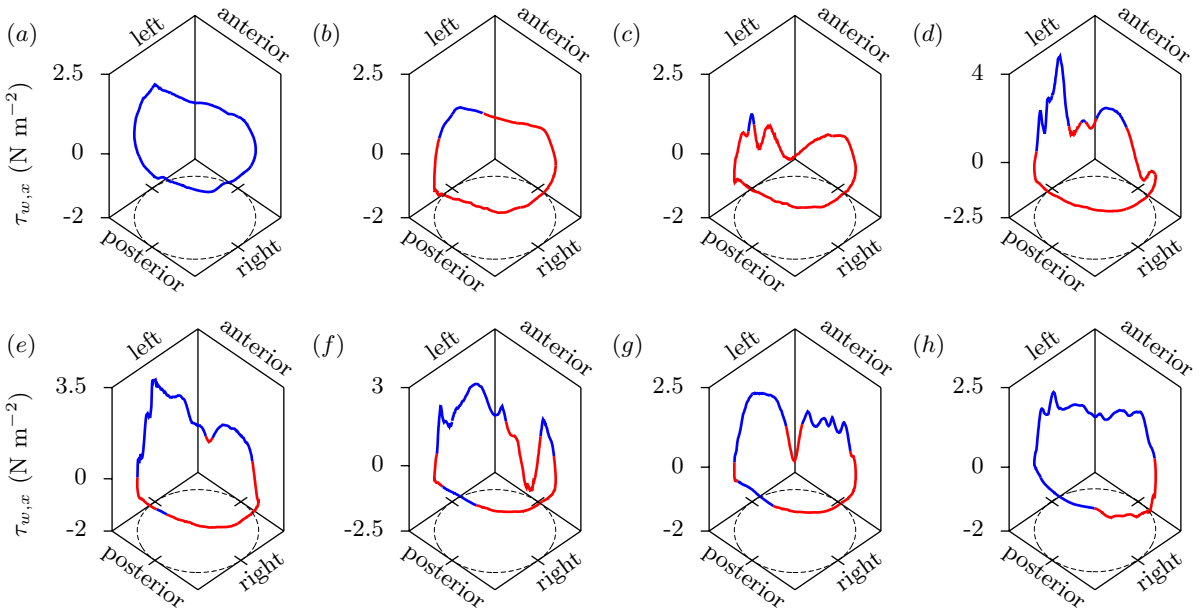

Figure 5.9: Case 3 at 0 months. Instantaneous streamwise-component of WSS plotted along the circumference of the mid-axial slice shown in Fig. 5.8 (d) at (a) $t/T = 0.20$, (b) $t/T = 0.32$, (c) $t/T = 0.36$,(d) $t/T = 0.4$, (e) $t/T = 0.44$, (f) $t/T = 0.48$, (g) $t/T = 0.52$ and the (h) $t/T = 0.72$. Blue and red color distinguishes positive and negative values, respectively.

5.5 Discussion

In this chapter, simulations of pulsatile blood flow in two medium-sized AAA are performed and the results are compared with the change in AAA shape and ILT deposition over time. Growth from an additional case is presented without CFD simulation results. In the previous chapter it was suggested that high WSS from the impact of turbulent vortexes prevents the attachment of ILT to the wall. In addition, it was hypothesized that the higher wall-normal pressure force from impingement causes an gradual expansion in size and this expansion occurs in the direction that the neck angles the jet of blood flow. Although high WSS from impingement prevents ILT, it is suspected that it is not sufficiently high to cause shearing damage to the AAA wall. The continuous downstream blood motion from the jet, results in

a zone of recirculating blood forming on the opposite side. Recirculating blood is potentially a hemodynamic environment that favors ILT deposition, where cellular material becomes trapped within this region for several cardiac-cycles. Once a layer of ILT forms it could potentially cause the AAA wall to deteriorate and this leads to further expansion and eventual rupture.

Case 1 has a small lumen flow channel and anterior-eccentric ILT. Although flow simulations are not performed for this case, based on the fact that the lumen is small-sized with a initial diameter of ≈ 3 cm, the blood flow is expected to be laminar and stable. This case does not grow in size over 19 months but does experiences an increase in ILT thickness on the anterior and effectively no increase in ILT on the posterior wall. It is not apparent why ILT deposition would favor the anterior and not posterior wall. It has been observed to be more likely for anterior-eccentric ILT to occur in AAA (Hans et al. [41], Pillari et al. [94], Metaxa et al. [79]). AAA with posterior-eccentric ILT have also been identified to have lower growth rates when compared to AAA with anterior-eccentric ILT (Metaxa et al. [79]). A layer of ILT could weaken the AAA wall and this deterioration in wall integrity may lead to expansion. When an AAA only has posterior-eccentric ILT the presence of the spine prevents expansion in the posterior direction and the lack of ILT on the anterior wall could limit expansion in the anterior direction.

For case 2 the AAA grew at a relatively constant rate, however, ILT deposition does not follow this trend and a majority of the ILT accumulates within the last 12 months of the 57 month period. The simulation from the initial CTA show turbulent vortexes from the jet circulate within the lumen exposing the entirety of the wall to high and turbulent WSS. This AAA is devoid of ILT and it is suggested that the shearing from these vortexes

prevents its attachment to the wall. During the 45 month interval between the first and second CTA, there was a substantial increase in size and minimal increase in ILT deposition. Previous studies have found that a high ILT load increases growth rate (Parr et al. [88], Wolf et al. [137], Zambrano et al. [143]); however, since ILT was not present during this time period it cannot be considered the cause of AAA growth. The impact of jet vortexes against the wall is suspected to be the primarily cause of expansion. Referring to figure 5.6 (a) and (b) the AAA appears to be expanding to a greater extent in the direction the neck angles the jet of blood flow.

At 45 months, the increase in AAA size has changed the flow dynamics considerably and jet vortexes no longer recirculate to the upper region on the posterior-left. There continues to be no ILT accumulation along the anterior-right, reinforcing the argument that high WSS prevents ILT deposition. Below the neck on the posterior-left side, the recirculating blood is laminar and ILT develops within this region (figures 5.7 (d)). In the more distal AAA, minimal ILT developed (figure 5.7 (e) and (f)) and this suggests that turbulent vortexes within the recirculation zone prevent ILT deposition. Since only one CTA was taken over this period it is not know if ILT accumulated below the neck gradually or suddenly over the 45 months. Based on this hypothesis, first the AAA gradually increases in size and once the AAA reaches a critical size the flow conditions change from turbulent to laminar. Once the blood flow reverts back to laminar within the AAA, there is a rapid increase in ILT at wall regions exposed to laminar flow.

During the 12 months between the second and third CTA, the AAA size continues to increase. Remote from the impingement region, there is a substantial build-up in ILT during this period (figure 5.7 (g)$-$(i)). At 57 months, the entire lumen contains highly turbulent

blood flow and the ILT along the left and right side is now exposed to high WSS from turbulent vortexes (figure 5.6 (c)). This observation contradicts the assertion that high WSS from turbulent vortexes prevents ILT deposition. Based on this hypothesis, turbulence fluctuations against the wall should have prevented ILT from forming in this region. A possible explanation is that high WSS prevents the initial attachment of ILT to the AAA wall. Once a well-developed layer of ILT has formed, it continues to spread out from the initial location, irrespective of the hemodynamic environment. An example of high-velocity adjacent to ILT can be seen in figure 5.7 (h). Although no CTA measurements were taken after 57 months, it can be speculated that the layer of ILT would continue to thicken, leaving only a small blood flow channel on the anterior side and a thick layer of poster-eccentric ILT.

For case 3, the AAA initially expanded toward the right side. Since there was no flow impingement and initially no ILT on the right side, it is not clear why the AAA would have initially expanded in this direction. Jet vortexes shear along the left wall and then recirculate along the right wall without reaching the upper right side. During the first 11 months, figure 5.8 shows that there is a substantial increase in ILT below the neck and it can be seen in figure 5.6 (d) that this increase occurs within the laminar region of the recirculation zone. From 11 to 37 months, ILT continues to accumulate and spread down the right side. High and turbulent WSS occured along the left wall. No ILT accumulated within this region and there is no apparent expansion in the left direction.

In previous work by Zambrano et al. [143] ILT growth was studied in 14 AAA of various sizes. They found that ILT deposition occurred in regions with low WSS and ILT accumulated at the same rate as AAA growth. This is not consistent with case 2 from this study, where although AAA growth occurred at a linear rate, ILT growth did not. Another interesting

finding from Zambrano et al. [143] is that recirculation zones with high-velocity near the wall were less likely to develop ILT, while a recirculation zone that consisted primarily of low-velocity would experience greater ILT accumulation. This finding is consistent with our data, where the region of a recirculation zone comprised of jet structures does not develop ILT. It is important to recognize, in contrast to the present study, that time-averaging the velocity field gives an overall description of the velocity field, but it does not capture the instantaneous dynamics and certain flow features such as the motion of turbulent vortexes will not be represented. In Arzani et al. [6] greater ILT deposition was found to occur at wall regions with low OSI and these regions were viewed as zones of persistent recirculation. In their study AAA diameter was less than 5 cm and it is possible that the more extreme flow conditions presented in large AAA cases did not occur in their study. In a study by Doyle et al. [33] it was found that AAA growth, ILT deposition and eventual rupture correlated with a wall region with low WSS.

The results from these cases show that AAA recirculation zones can consist of two types of flow dynamics and both types can be present within a single recirculation zone. The first type of recirculation zone can be comprised of low-velocity laminar blood flow. This flow dynamic is caused by the continuous downstream motion from the jet causing low-velocity upstream blood motion on the opposite side. In the present study, this region was found to coincide with the location where ILT developed. For the two cases presented here, this type of recirculation occurs below the neck on the posterior side. The second type of recirculation zone is comprised of turbulent vortexes. This flow dynamic is caused by turbulent structures from the jet recirculating on the side opposite of impingement. There is no accumulation of ILT within this region.

The following observations can be made in regards to flow impingement and its influence on AAA shape. The impingement of jet structures against the wall contributes to AAA expansion. It is suspected that the wall-normal pressure force from the impact of vortexes is causing the expansion and that growth will occur in the direction of impingement. If the neck is not angulated it is possible for the jet structures to shear along the wall without directly impinging. The wall is then exposed to high and fluctuating WSS this does not cause aortic wall deterioration and expansion will not occur at this location.

A significant assumption used in this study is a mean infrarenal flow rate of 20 ml s^{-1} is used. Based on Les et al. [68] this value is above the mean value of 17.5 ml s^{-1} that they found for patients with AAA. Patient-specific flow rate data was not available for this study. If a higher or lower flow rate had been used in this study it would affect the distance the flow structures traverse within the AAA and the intensity of the turbulence. Conclusions from this study could potentially change if the patients infrarenal flow rate is substantially lower than the value used in the simulation.

In conclusion, the results from this chapter provide support to the argument that high WSS from the impingement of vortexes prevent the initial attachment of ILT to the AAA wall. Within the laminar region of a recirculation zone, ILT is shown to develop and the presence of turbulent vortexes within a recirculating zone appears to be preventive. The accumulation of ILT did not occur at the same rate as AAA enlargement and is apparently more associated with a particular hemodynamic environment and flow conditions can change as an AAA increases in size. Although the results indicate turbulent recirculation may prevent the initial attachment of ILT to the wall, this study potentially suggests that once a well-developed layer of ILT forms, it continues to thicken irrespective of the presence of

turbulent vortexes. Detailed flow analysis is performed on two cases. A larger study would be beneficial to substantiate these results.

Chapter 6

Turbulent pulsatile blood flow in a medium sized abdominal aorta aneurysm

Abstract

Pulsatile simulations are performed on a medium-sized patient-specific AAA. Two types of turbulent flow occur for this case. Within the upstream neck region a zone of turbulent recirculating vortexes is present and within the AAA's body a jet forms on the anterior-right side. Initially the jet is laminar and during late-systole it transitions-to-turbulence. Although flow rate is affectively zero during diastole, the jet structures continue to flow downstream and by the end of the pulse the jet structures have mostly relaminarized. The downstream motion of the jet results in large region of laminar recirculating blood along the posterior side. DMD is applied to the instantaneous velocity field, with snapshots collected over four blood pulses.

A low-order representation of the velocity field is reconstructed using the mean and dominate harmonic modes. This reconstructed velocity field is found to consist of a single large-scale structure, where as the instantaneous velocity field is composed of small-sized turbulent fluctuations. Substantially more than four pulses are required to obtain phase-averaged statistics and therefore, DMD can be used as an alternative to phase averaging when only data from a small number of pulses is available.

6.1 Introduction

The vascular disease, AAA occurs due to a combination of both biological and hemodynamic factors (Tarbell [116]). The biological factors, such as cholesterol, smoking, high blood pressure, act throughout the entire cardiovascular system but vascular disease only occurs at certain locations (Lasheras [63]). Generally these locations are arteries with shapes that differ from a straight artery, i.e. bends, arches and bifurcations. It has been conjected that the adverse blood flow dynamics that develop at these locations play an important role in the development vascular disease. Adverse blood flow behavior includes dynamics such as recirculation, impingement and turbulence.

Blood flow in arteries consists of a mean flow rate superimposed with oscillating harmonics. For a healthy abdominal aorta the geometry is effectively a straight pipe and the pulsatile flow will be laminar and repeat every pulse with minimal changes. In diseased aorta, such as AAA, the geometry can cause the blood flow to transition to turbulence. For these cases, there are turbulent oscillations superimposed on the periodic component and the blood flow could transition from laminar to turbulent and then back to laminar.

The objective of this study was to investigate the transition to turbulence in an AAA. The patient-specific geometry chosen here contains an AAA with a contorted and conical neck and a sudden expansion in aortic diameter distal to the neck. Since both of these features are present in a single case it is possible to compare how they influence the hemodynamics. The second objective was to investigate whether DMD is a useful method in analyzing cardiovascular flows. The DMD method segments the blood flow into modes that are oscillating at specific frequencies. Thus it can potentially be used to remove the high-frequency turbulent oscillations and the resulting velocity field consists of only the low-frequency large-scale hemodynamics. This patient-specific AAA have been previously presented in Lozowy et. al. [73] and additional flow dynamic, such as wall shear stress, oscillating shear index and time-averaged velocity are documented there.

6.2 Materials and Methods

6.2.1 Model description

For this case, using the hydraulic diameter at the inlet boundary as the length scale, $Re_b = 315$ and $Wo = 16.5$. The infrarenal aortic bulk flow rate used for this simulation is from Les et al. [68] and is shown in figure 2.6 (a). The mean and maximum bulk flow rate is 20 ml s^{-1} and 130 ml s^{-1}, respectively. The x-axis is placed perpendicular to the axial plane and is referred to as the streamwise direction. Figure 6.2 shows the patient-specific geometry used in this study. In the neck region, upstream of the AAA, the aorta becomes contorted. In addition the neck is conical, where the diameter first decreases then increases prior to the

AAA. The maximum diameter of the AAA is 6 cm and have a thin layer of ITL having a maximum thickness 0.4 cm along the posterior-right side and the bottom of the bulge on the anterior-left side. There is no ILT deposition along the anterior-left side of the AAA. Figure 6.2 also gives the location of data probes on axial planes, where the velocity signal is monitored. Using standard CTA orientation, the left and right sides are flipped on axial slices.

6.2.2 Simulation details

To satisfy the criterion of having the CFL number < 1 the time-step was fixed at $\Delta t = 4 \times 10^{-5}$ s. The time-dependent bulk velocity shown in figure 8.2 is implemented at the upstream inlet boundary. An unstructured grid is generated composed of prism cells extruded from the wall and tetrahedral cells occupying the interior of the domain. The wall tangent edge length of the first prism cell adjacent to the wall was fixed at 0.002 cm and 15 prism cells were extruded from the wall at an expansion rate of 1.25. The edge length of the interior tetrahedral cells is set to 0.055 cm. This interior cell edge length is the same as that used in studies by Arzani et al. [3], Les et al. [67] and Zambrano et al. [143] The number of grid cells used in this study is 12043646 and in the following section the grid resolution is assessed in the results section using the Kolmogorov length scale. Each pulse is segmented into $M = 50$ equidistant phase positions and at each phase $N = 80$ snapshots of the flow field are collected. These snapshots are used to calculate the phase-averaged velocity, TKE and TKE dissipation rate. The storage of 4000 instantaneous velocity fields requires approximately 1.6 TB of storage.

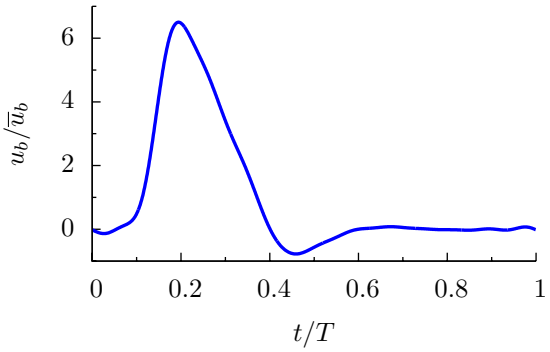

Figure 6.1: Infrarenal aortic bulk flow rate.

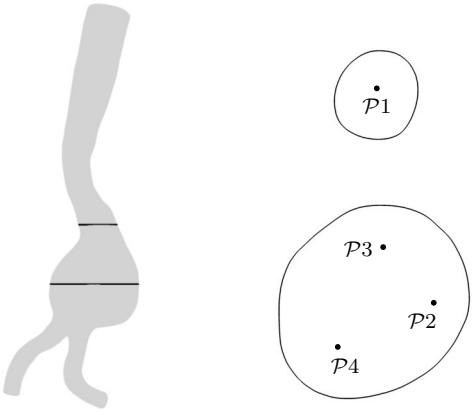

Figure 6.2: AAA geometry and location of probes $\mathcal{P}1 - \mathcal{P}4$.

6.3 Results

6.3.1 Blood flow dynamics

In this section, since instantaneous quantities are stochastic and vary with every pulse, they are presented as a function of the time unit t. When a quantity is phase-averaged it repeats exactly every pulse and therefore these quantities are presented by their phase position φ with the pulse. Figure 6.3 $(a) - (h)$ shows contours of the instantaneous velocity magnitude $\|\boldsymbol{u}\|/\overline{u}_b$

plotted on a vertical plane that has been positioned so that it intersects with the dominate direction of the flow structures. During early-systole there exists a favorable pressure gradient (FPG) across the aorta accelerating the blood flow, i.e. pressure is highest at the aortic inlet and decreases downstream. Peak blood flow rate occurs at $t/T = 0.19$ and it can be seen in figure 6.3 (a) that by $t/T = 0.24$ a laminar recirculation zone has formed in the neck region and distal to the neck a laminar jet is forming that angles towards the anterior wall. On the posterior side distal to the neck the blood flow has started to separate. However, at $t/T = 0.24$ insufficient time has passed for flow structures to develop downstream within the body of the AAA and the blood flow is uniform. During late-systole an adverse pressure gradient (APG) decelerates the blood velocity; however, during this period of the pulse that the jet continues to progress downstream and transitions to turbulence, as shown in figure 6.3 $(b) - (d)$. Additionally during late-systole the recirculation zone in the neck transitions to turbulence. The blood flow in the straight segment of the upstream aorta remains laminar for the entire cardiac cycle. During diastole the pressure gradient across the abdominal aorta is effectively zero and there is no bulk blood flow movement into the iliac arteries. At this point in the cardiac cycle two dominant hemodynamics are present; a zone of stagnant turbulent vortexes recirculating within the neck and a group of turbulent jet vortexes flow downstream within the AAA's body. Within the neck region, the vortexes are moderately pulled upstream by the reversal in bulk flow direction that occurs during early-diastole. From early-to-mid-diastole these vortexes dissipate, resulting in laminar blood flow at this location by mid-diastole. The flow behavior within the body of the AAA is substantially different than the neck. Since pressure is inversely proportional to the diameter of a pipe, the late-systole APG within the AAA is substantially less compared to what occurs in the

smaller diameter upstream aorta. The turbulent jet vortexes have sufficient momentum to overcome the late-systole APG and during diastole they maintain the momentum required to circulate within the AAA; where as, the remainder of the blood flow in the abdominal aorta contains effectively no momentum during diastole. Unlike the turbulent structures in the neck, the jet vortexes do not remain at a single location and instead they continue to flow downstream on the anterior-left side. This causes laminar low-velocity blood flow to be pushed upstream on the posterior-right side. The velocity of the jet vortexes gradually decrease as they flow downstream and by the end of the cardiac cycle the jet vortexes have traversed to the iliac arteries and relaminarized, as shown in figure 6.3 (h).

The velocity field is further examined on a mid-axial plane positioned in the center on the AAA's body. Figure 6.4 $(a) - (d)$ shows contours of the phase-averaged streamwise velocity $\langle u \rangle$ and figure 6.4 $(e) - (h)$ shows the instantaneous streamwise turbulent fluctuation u'. The phase-average gives the component of the velocity field that repeats every pulse while the turbulent fluctuation gives a stochastic component. At peak-systole the velocity is low, uniform and laminar within the mid-axial plane (not shown). By late-systole $(t/T = 0.38)$ the jet can be seen impacting against the left AAA wall. During diastole both the phase-averaged velocity and the turbulent fluctuations spread from the left to the anterior side of the wall. The periodic and turbulent flow structures are confined to the jet region on the anterior-left side. The remainder of the cross-section contains laminar low-velocity upstream motion during diastole.

The blood flow dynamics are examined at various probe locations that are shown in figure 6.2. Probe $\mathcal{P}1$ is located within the neck region and probe $\mathcal{P}2$ is located on the left side of the AAA's body within the path the dominate jet structures traverse. Probe $\mathcal{P}3$ is located

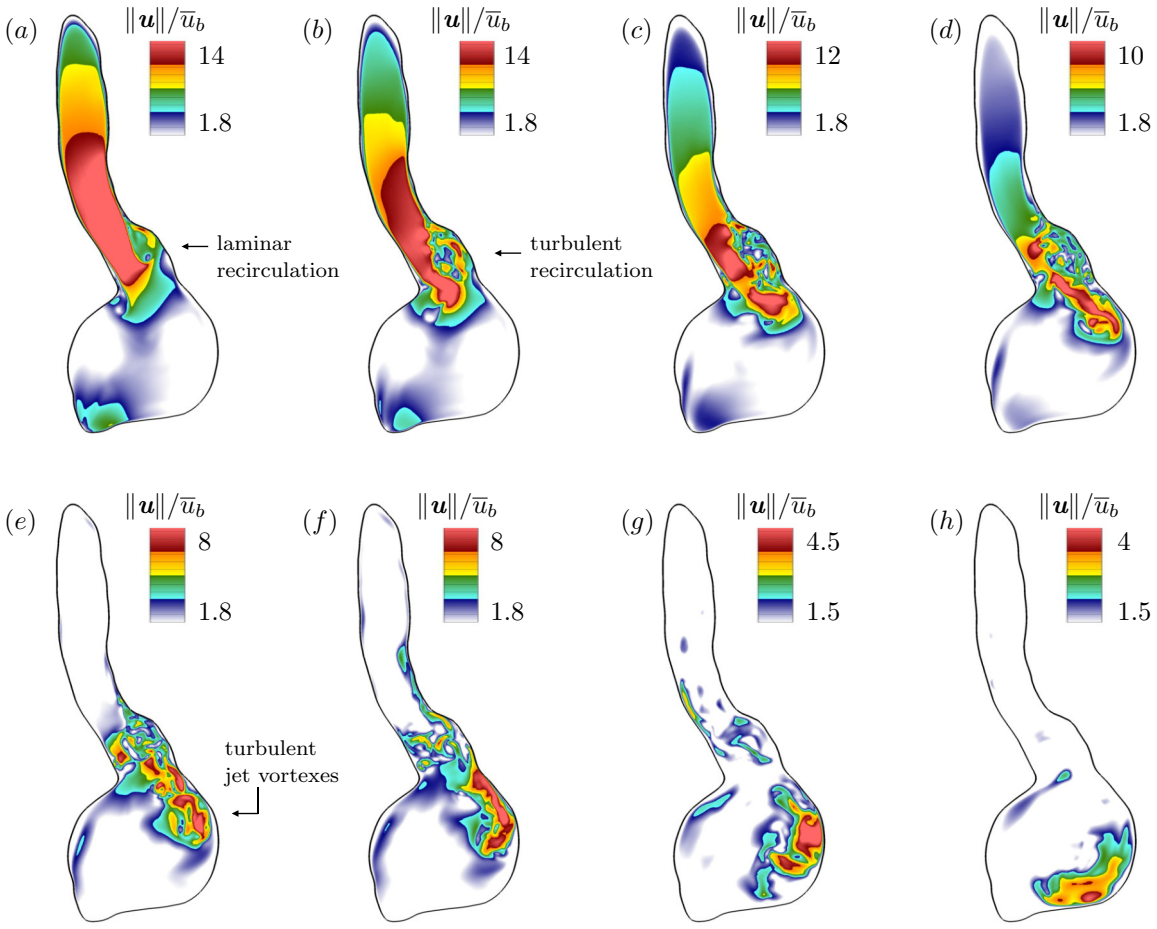

Figure 6.3: Instantaneous velocity magnitude $\|\boldsymbol{u}\|/\overline{u}_b$ at (a) $t/T = 0.24$, (b) $t/T = 0.28$, (c) $t/T = 0.32$, (d) $t/T = 0.36$, (e) $t/T = 0.4$, (f) $t/T = 0.44$, (g) $t/T = 0.6$ and (h) $t/T = 0.76$. Contours plotted on a vertical plane that is positioned so that it intersects with the dominate flow direction. The time origin is placed at the start of a pulse.

on the anterior side of the AAA's body and probe $\mathcal{P}4$ in located within the recirculation zone. Figure 6.5 $(a) - (d)$, shows the temporal variation in the streamwise velocity $u/\overline{u}_b$ and the phase-wise variation $\langle u \rangle/\overline{u}_b$ at points $\mathcal{P}1 - \mathcal{P}4$. At all probe locations, the blood flow is laminar during the flow acceleration period of early-systole. At $\mathcal{P}1$ as the blood flow decelerates during mid to late-systole it transitions-to-turbulence and by early-diastole the turbulence has mostly dissipated with only large-scale turbulent oscillations remaining. At

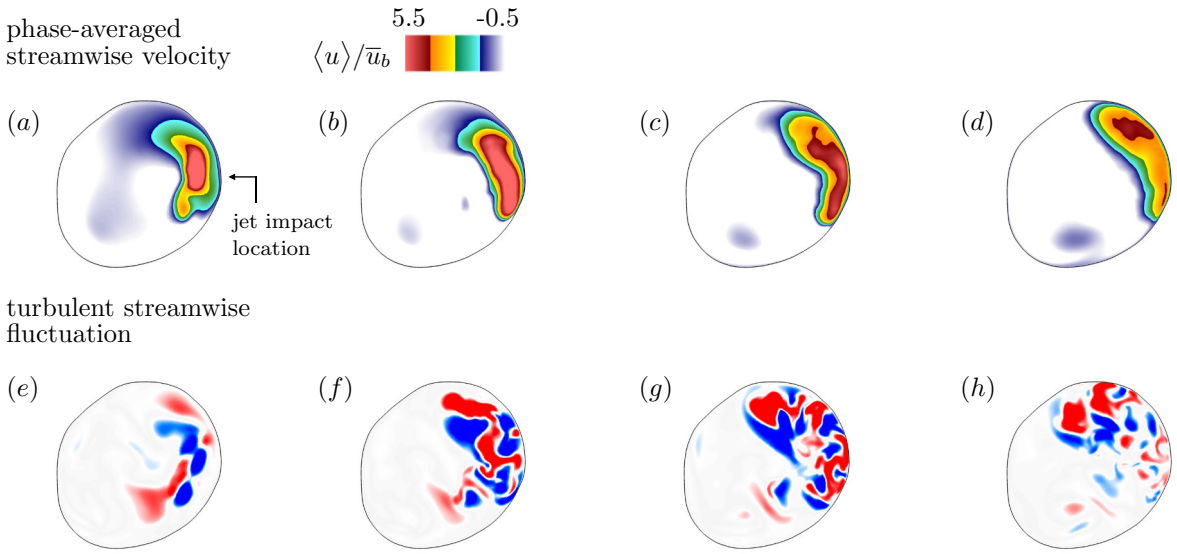

Figure 6.4: Streamwise phase-averaged velocity $\langle u \rangle / \overline{u}_b$ at phase positions (a) $\varphi/T = 0.38$, (b) $\varphi/T = 0.42$, (c) $\varphi/T = 0.48$. and (d) $\varphi/T = 0.56$. Streamwise turbulent fluctuation $u'/\overline{u}_b$ at temporal positions (e) $t/T = 0.38$, (f) $t/T = 0.42$, (g) $t/T = 0.48$, (h) $t/T = 0.56$ and contour levels shown for $-1.5 \leq u'/\overline{u}_b \leq 1.5$ from blue to red. The sum of $\langle u \rangle$ and u' gives the instantaneous streamwise velocity. Contours plotted on a mid-axial plane. The time origin is placed at the start of a pulse.

both $\mathcal{P}2$ and $\mathcal{P}3$, there is a relatively small peak in the velocity that occurs at peak-systole flow rate. This is followed by a series of large fluctuations during diastole as flow structures traverse past the probe locations. At $\mathcal{P}2$, the large fluctuation corresponds to the movement of a large-scale structure that repeats every cardiac cycle. Superimposed on this periodic structure are smaller-scale turbulent fluctuations. Since probe $\mathcal{P}3$ is located on the anterior side, the periodic jet structure miss this location and the phase-averaged velocity remains low. Instead the blood flow is dominated by turbulent fluctuations at $\mathcal{P}3$. By qualitatively comparing the velocity at $\mathcal{P}2$ and $\mathcal{P}3$ it can be observed that the periodic and turbulent fluctuations are comparable in intensity and without phase-averaging it would be difficult to distinguish between these oscillations. Probe $\mathcal{P}4$ is located in a region with predominately

laminar recirculation and therefore there is minimal difference between the phase-averaged and instantaneous velocity. The velocity at probe $\mathcal{P}4$ is negative (upstream motion) during a majority of the cardiac cycle and only becomes positive during peak systole.

The phase-wise variation in the TKE, calculated as $\left\langle \boldsymbol{u}' \cdot \boldsymbol{u}' \right\rangle / (2\overline{u}_b^2)$ and is shown at $\mathcal{P}1 - \mathcal{P}4$ in figure 6.6. The term $\phi_{\widetilde{\boldsymbol{u}' \cdot \boldsymbol{u}'}}/T$ giving the phase-lag in the peak TKE. At $\mathcal{P}1$ TKE increases rapidly during late-systole and reaches a peak value at $\varphi/T = 0.36$. The TKE deceases rapidly and is then followed by a more gradual decease that persists into mid-diastole. Within the AAA's body the turbulence moves along with large-scale periodic jet structures and at $\mathcal{P}2$ there is a very rapid spike in TKE corresponding to the turbulent jet vortexes traversing past this location. The blood at this location does not necessarily transition to turbulence, rather existing turbulence that was first produced distal to the neck has been advected to this location. The peak value occurs at $\varphi/T = 0.38$ and similar to $\mathcal{P}1$, there is a gradual decease in TKE that persists into mid-diastole. Unlike the neck region, only part of this decrease is caused by the TKE dissipation and a substantial portion of the TKE reduction is caused by vortexes being advected to a different location. At $\mathcal{P}3$, from early to mid-diastole there is a gradual increase in TKE with the peak value is delayed until $\varphi/T = 0.58$. This gradual increase in TKE is caused by turbulent vortexes spreading out from the left wall towards the anterior wall. Within the recirculation zone at $\mathcal{P}4$ there is effectively no TKE during the cardiac cycle.

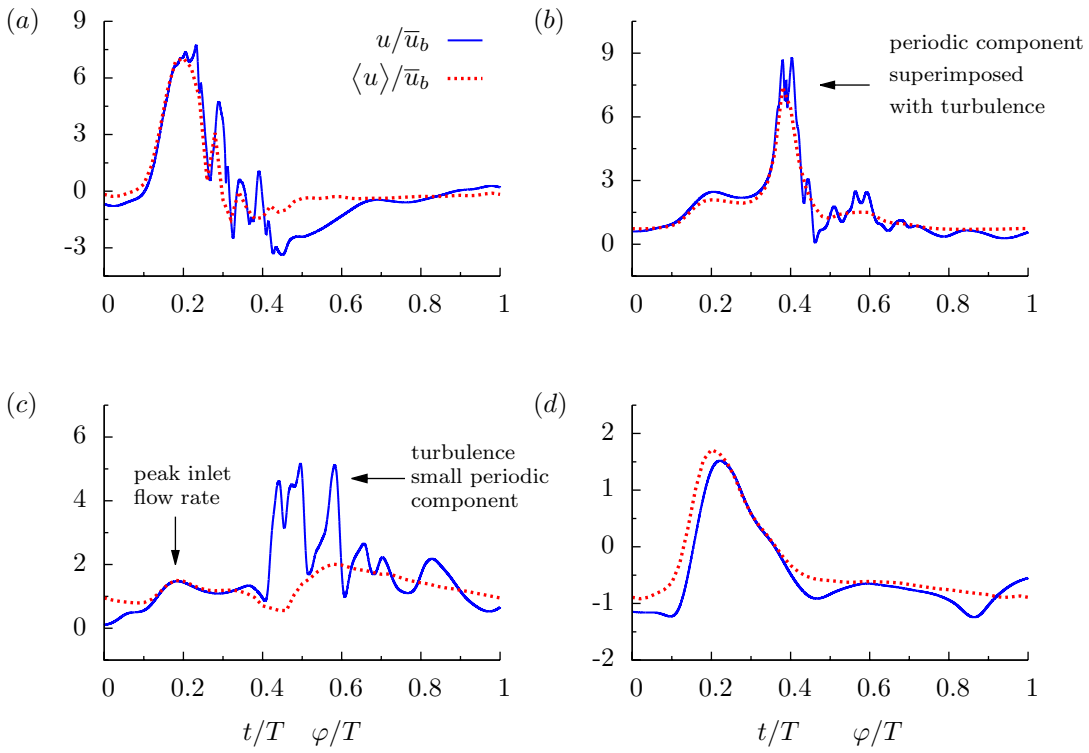

Figure 6.5: Temporal variation in $u/\overline{u}_b$ and phase-wise variation in $\langle u \rangle/\overline{u}_b$ at (a) $\mathcal{P}1$, (b) $\mathcal{P}2$, (c) $\mathcal{P}3$ and (d) $\mathcal{P}4$. The time origin is placed at the start of a pulse.

6.3.2 DMD spectrum

The DMD algorithm is applied to snapshots of the instantaneous (blue circle) and phase-averaged (red circle) velocity field and the amplitude spectrum for both of these decompositions is shown in figure 6.7 (a) and (b). In general mode amplitude decreases as frequency increases and a vertical line in 6.7 (b) shows the cut-off for frequencies higher then the 12-term Fourier series boundary condition applied at the inlet.

DMD from phase-averaged velocity field

For the phase-averaged velocity field the DMD algorithm is performed on $m = 49$ snapshots collected over a single cardiac cycle at a sampling rate of $\Delta t = 0.02/T$. The resulting matrix

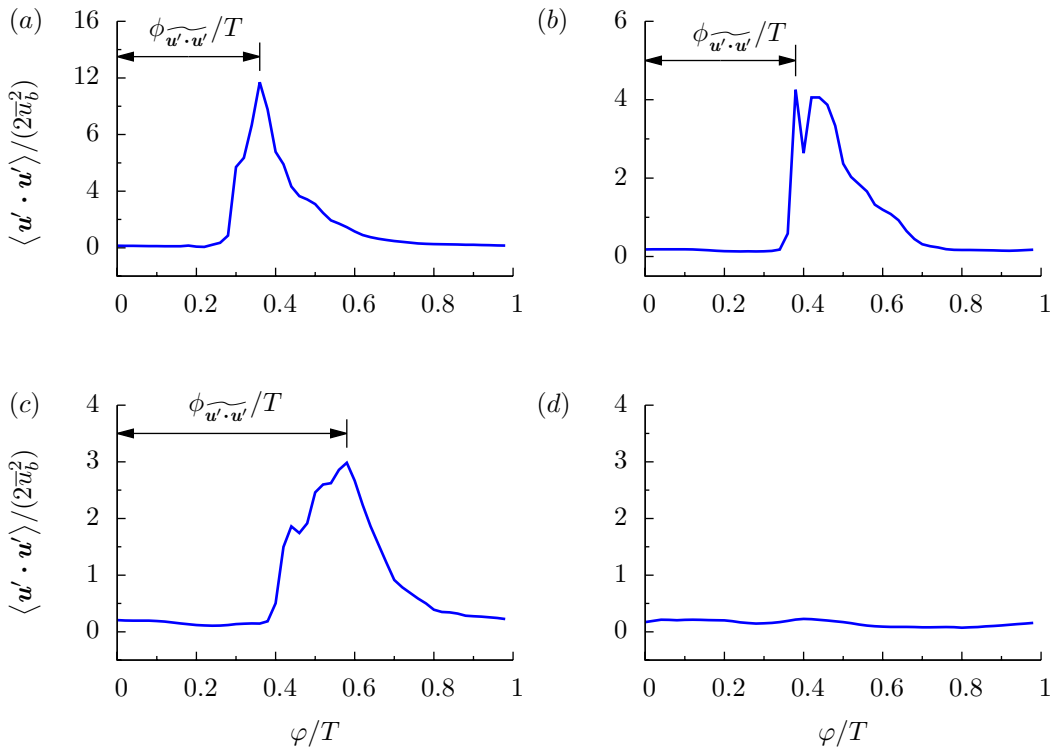

Figure 6.6: Phase-wise variation in TKE $\langle \boldsymbol{u}' \cdot \boldsymbol{u}' \rangle / (2\overline{u}_b^2)$ at (a) $\mathcal{P}1$, (b) $\mathcal{P}2$, (c) $\mathcal{P}3$ and (d) $\mathcal{P}4$. The phase-lag in the peak TKE is given by $\phi_{\widetilde{\boldsymbol{u}'\cdot\boldsymbol{u}'}}/T$.

$\boldsymbol{\Psi}$ is of size 36130938×49, with each column $\boldsymbol{\psi}_m$ containing the x, y and z component of velocity at each grid point for a given snapshot. Storing a matrix of this size requires approximately 20 GB of storage. Since the phase-averaged velocity field is calculated by averaging 80 instantaneous velocity fields, flow oscillations associated with turbulence have already been removed and only periodic oscillations are present. The algorithm returns a mode with a zero frequency that corresponds to the mean velocity field and pairs of modes with positive and negative frequencies. Since the snapshots from this decomposition span a single pulse, the smallest frequency returned is $\pm 1/T$ and the highest frequency is given by the Nyquist criterion and will be $\pm 2/\Delta t$. In figure 6.7 (b) it can be seen that the amplitude of the high-frequency modes quickly approaches zero as the frequency increase. Thus only several

low-frequency modes contain a majority of the energy from the phase-averaged velocity

DMD from instantaneous velocity field

For the instantaneous velocity field the DMD algorithm is performed on $m = 197$ snapshots collected over four pulse cycles at a sampling rate of $\Delta t = 0.02/T$. For this decomposition, the matrix $\mathbf{\Psi}$ is of size 36130938×197 and storing a matrix of this size requires approximately 80 GB of storage Since the DMD algorithm does not distinguish between turbulent and periodic oscillations, the modes from the instantaneous velocity contain a mixture of both oscillation types. Since the snapshots from this decomposition span approximately four pulses, the smallest frequency mode returned is approximately $\pm 4/T$. The zero frequency mode and dominate harmonic mode are labeled in figure 6.7 (a). It can be seen that there is a clear distinction where modes at multiples of the pulse frequency have a higher amplitude compared to the modes that are not multiples of the pulse frequency. The mode at the pulse frequency $1/T$ is at a similar amplitude for both the instantaneous and phase-averaged velocities. At frequencies $2/T$, $4/T$ and $8/T$ the amplitude of the DMD modes computed from the instantaneous velocity are substantially higher than the phase-averaged velocity. This indicates that these low-frequency modes, computed from the instantaneous velocity field, contain energy from a mixture of both periodic and turbulent oscillations. This has been qualitatively verified by reconstructing the modes and identifying the presence of turbulent fluctuations within the low-frequency modes computed from the instantaneous velocity.

Growth rate spectrum

Figure 6.7 (c) shows the growth rate spectrum from the DMD using the instantaneous (blue circle) and phase-averaged (red circle) velocity field. All of the modes have negative growth rates, indicating decay in the amplitude over consecutive periods. For both the instantaneous and phase-averaged velocity DMD, the growth rate for the dominate harmonic mode is relatively close to zero, i.e. for this mode the amplitude experiences relatively no decay over multiple oscillations. Figure 6.8 shows the ritz values (eigenvalues from DMD) and it can be seen that they predominately fall upon a unit circle for both the instantaneous and phase-averaged velocity. Ritz values within the unit circle indicate negative growth rates.

6.3.3 Reduced-order reconstruction of the flow field

A reduced-order reconstruction of the flow field is performed using the mode with zero-frequency ($m = 1$) and the modes at the pulse frequency ($m = 2, 3$), i.e.

$$\boldsymbol{u}_{1-3}^{\mathrm{dmd}} = \sum_{m=1}^{3} \boldsymbol{\phi}_m d_m \exp\left(\alpha_k t_j + \mathrm{i}\omega_k t_j\right) \qquad j = (1 \cdots m). \tag{6.1}$$

The modes $\boldsymbol{\phi}_m$ have been calculated using $m = 197$ snapshots of the instantaneous velocity field separated by $\Delta t = 0.02/T$. This reconstruction provides an idealized representation of the transient flow dynamics, since flow structures that are oscillating at frequencies other then the dominate pulse frequency have been removed. The oscillating structures that have been removed contain both periodic and turbulent motion. Figure 6.9 shows contours of the reduced-order reconstruction of the velocity magnitude and blood flow within the body of the AAA now consists of a single large-scale structure that gradually flows downstream; where

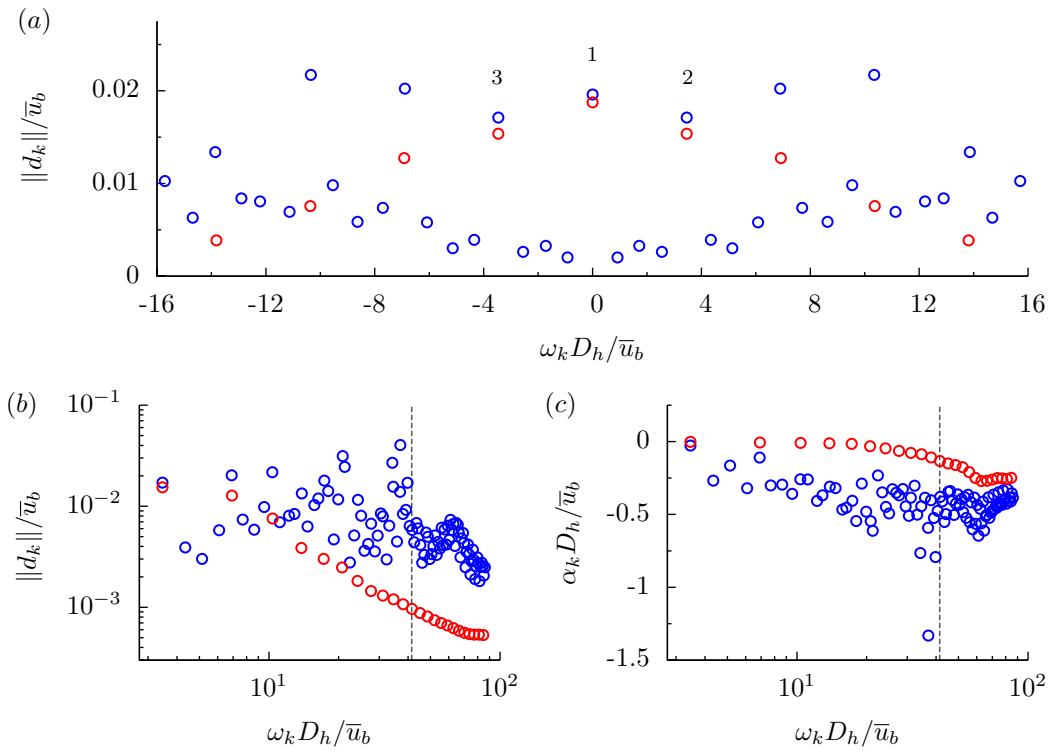

Figure 6.7: Blue circle is DMD calculated from $m = 197$ snapshots of $\boldsymbol{u}$ separated by $\Delta t = 0.02/T$. Red circle is for DMD calculated from $m = 49$ snapshots of $\langle \boldsymbol{u} \rangle$ separated by $\Delta t = 0.02/T$. (a) Amplitude spectrum for $\omega_k D_h/\overline{u}_b \in [-18, 18]$. (b) Log-log plot of amplitude spectrum for $\omega_k D_h/\overline{u}_b \in [2.75, 100]$. (c) Log-linear plot of growth rate spectrum for $\omega_k D_h/\overline{u}_b \in [2.75, 100]$. Vertical dashed line indicates the cut-off for frequencies higher than the inlet boundary Fourier series.

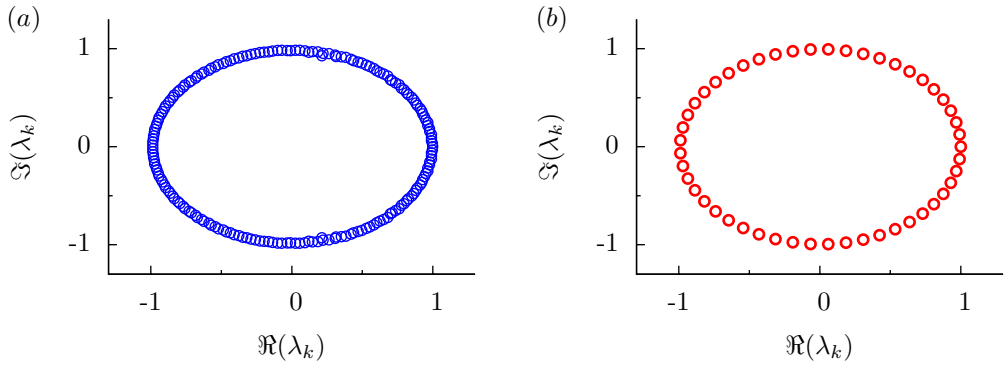

Figure 6.8: Ritz values from (a) instantaneous velocity field and (b) phase-averaged velocity field.

as, the instantaneous velocity field (figure 6.3) consists of a group of vortexes that comprise this single flow structure. Within the neck the higher-frequency turbulent oscillations are removed from the flow field. Figure 6.10 shows reduced-order reconstruction streamwise velocity plotted on mid-axial plane. The phase-averaged velocity shown in figure 6.4 closely resembles the reduced-order reconstruction and differences represent periodic oscillations at frequencies higher than the pulse frequency.

6.3.4 Effect of number of snapshots on DMD

In the previous section a reduced-order reconstruction of the instantaneous velocity field is performed using snapshots collected over four pulses. The rationale behind collecting snapshots over four pulses is that it is found when DMD is applied to the instantaneous velocity field and the snapshots are collected over only one pulse, irrespective of Δt the dominant frequency is always under predicted. Similar behavior has been observed in chapter 3 when DMD was applied to pulsatile flow in a channel. Table 6.1 summarizes the frequency of the dominant harmonic mode for data collected over a single pulse at various sampling frequencies. Reducing the sampling interval from $\Delta t = 0.01/T$ to $\Delta t = 0.0016/T$ did not yield improvement in the accuracy of the computed frequency. However, when DMD is applied to the phase-averaged velocity, with snapshots collected over a single pulse and relatively large sampling intervals of $\Delta t = 0.02/T$ and $\Delta t = 0.04/T$, the exact pulse frequency is returned. This suggests that the presence of turbulent oscillations hampers the robustness of the DMD algorithm from extracting the exact pulse frequency. This limitation can be seen in figure 6.11, where a log-log plot of the DMD amplitude spectrum is shown for snapshots of

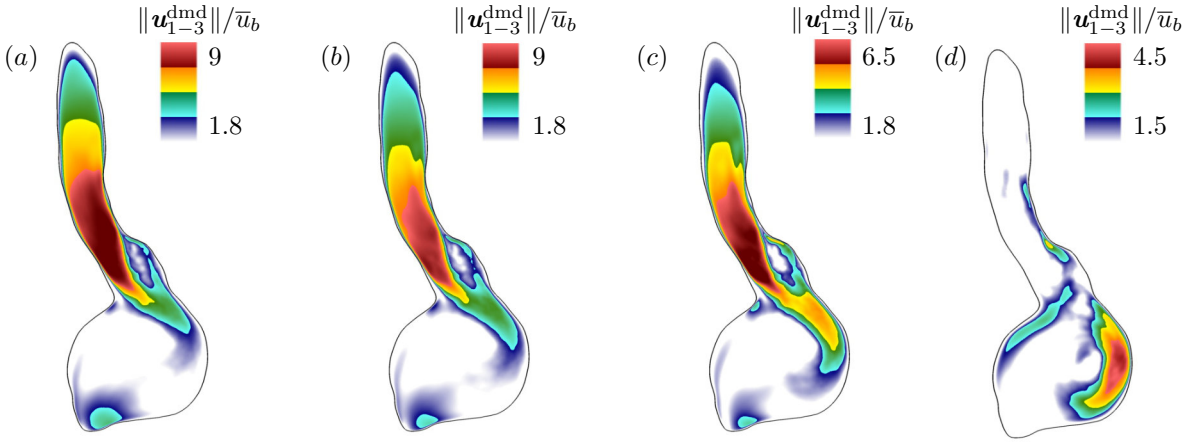

Figure 6.9: Reduced-order reconstruction of the velocity magnitude $\|\boldsymbol{u}_{1-3}^{\mathrm{dmd}}\|/\overline{u}_b$ at temporal positions (a) $t/T = 0.28$ or $j = 15$, (b) $t/T = 0.34$ or $j = 18$, (c) $t/T = 0.4$ or $j = 21$ and (d) $t/T = 0.6$ or $j = 31$. Contours plotted on a vertical plane that is positioned so that it intersects with the dominate flow direction. The time origin is placed at the start of a pulse.

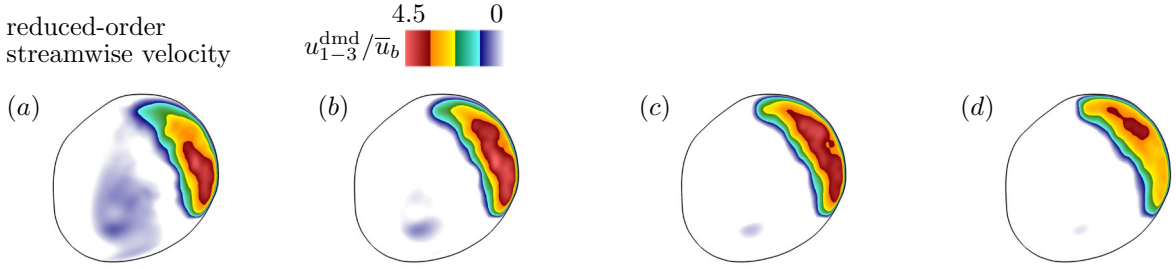

Figure 6.10: Reduced-order reconstruction of the streamwise velocity $u_{1-3}^{\mathrm{dmd}}/\overline{u}_b$ at temporal positions (a) $t/T = 0.38$ or $j = 20$, (b) $t/T = 0.48$ or $j = 25$, (c) $t/T = 0.56$ or $j = 29$ and (d) $t/T = 0.66$ or $j = 34$. Contours plotted on a mid-axial plane. The time origin is placed at the start of a pulse.

the instantaneous velocity collected over a single pulse at a sampling rate of $\Delta t = 0.0016/T$ (blue circle). Storing $m = 625$ snapshots for the matrix requires approximately 250 GB of storage. For comparison purposes the figure includes the amplitude spectrum computed from phase-averaged data (red circle). It can be observed from this figure that the modes from the instantaneous velocity are substantially misaligned with the frequency computed from the

phase-averaged velocity. The flow structures associated with the dominate pulse frequency are split between several different frequencies.

Figure 6.12 (a) shows the effect the number of snapshots has on the frequency of the dominant harmonic mode when the DMD algorithm is applied to the instantaneous velocity field with a sampling interval of $\Delta t = 0.02/T$. When the length of the sampling period is four blood pulses the frequency of the dominant harmonic mode oscillates, at a relatively low amplitude, about the correct value. As the length of the sampling period is decreased the oscillations worsen. In particular when the sampling period is less than 2 blood pulses DMD cannot be used to reliably compute the correct pulse frequency. Figure 6.12 (b) shows that as the length of the sampling period is decreased the growth rate of the dominate mode becomes a larger negative number. This behavior where DMD is sensitive to the number of snapshots used but insensitive to the interval in between snapshots is similar to an observation found in Sarmast et al. [102].

Figure 6.13 shows the effect of the number of snapshots on the frequency and growth rate of the dominant harmonic mode when the DMD algorithm is applied to the phase-averaged velocity field with a sampling interval of $\Delta t = 0.02/T$. Unlike the instantaneous velocity, when the sampling interval is only a single blood pulse the DMD correctly outputs the pulse frequency and the growth rate is effectively zero. If the sampling period is decreased

	DMD from instantaneous velocity			DMD from phase-averaged velocity	
	$\boldsymbol{u}$, $m = 51$, $\Delta t = 0.02/T$	$\boldsymbol{u}$, $m = 201$, $\Delta t = 0.005/T$	$\boldsymbol{u}$, $m = 625$, $\Delta t = 0.0016/T$	$\langle \boldsymbol{u} \rangle$, $m = 25$, $\Delta t = 0.04/T$	$\langle \boldsymbol{u} \rangle$, $m = 49$, $\Delta t = 0.02/T$
$\omega_2 T/(2\pi)$	0.89	0.91	0.91	1	1

Table 6.1: Summary of the frequency of the dominate harmonic mode computed by DMD for different sampling intervals. Data collected over a single blood pulse.

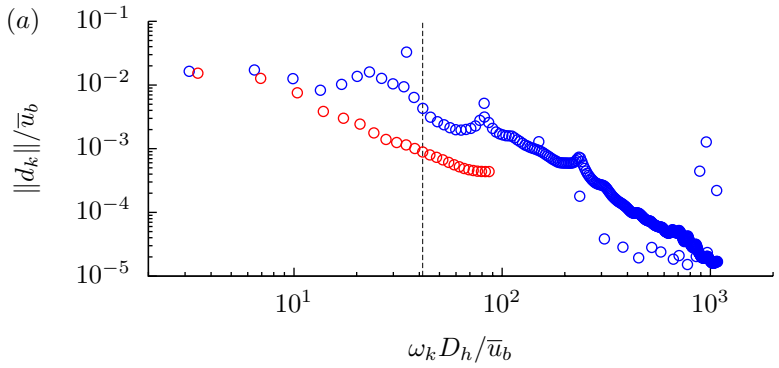

Figure 6.11: Blue circle is DMD calculated from $m = 625$ snapshots of $\boldsymbol{u}$ separated by $\Delta t = 0.0016/T$. Red circle is for DMD calculated from 49 snapshots $\langle \boldsymbol{u} \rangle$ separated by $\Delta t = 0.02/T$. Amplitude spectrum for $\omega_k D_h/\overline{u}_b \in [2, 2000]$. Vertical dashed line indicates the cut-off for frequencies higher than the inlet boundary Fourier series.

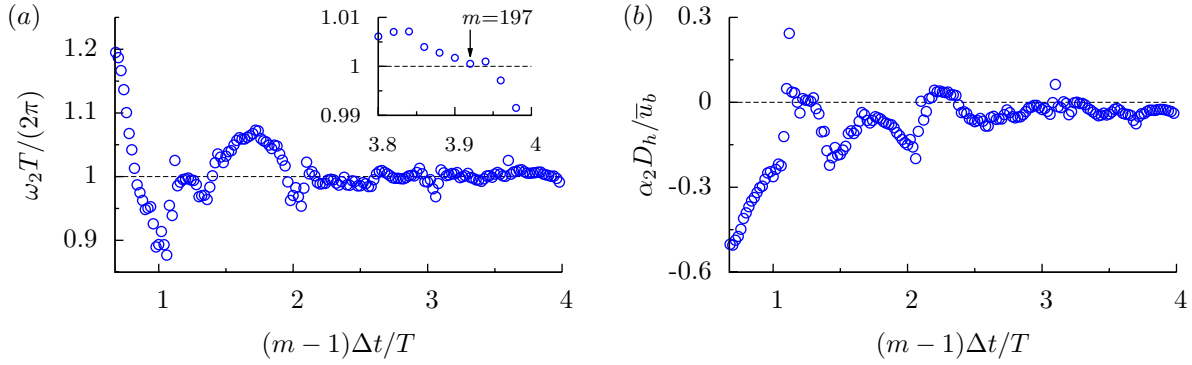

Figure 6.12: Effect of m on the (a) angular frequency and (b) growth rate of the dominant harmonic mode. DMD was calculated from snapshots of $\boldsymbol{u}$ separated by $\Delta t = 0.02/T$.

below the pulse period, the correct dominant pulse frequency is still returned and the growth rate remains close to zero. When the sampling period is reduced further below $0.75T$ the computed pulse frequency is not returned and growth rate becomes more negative. This behavior was previously observed in Chen et al. [21] where it was also observed that the correct frequency can be returned by DMD without the snapshots spanning a entire period. In Iyer & Mahesh [48] when DMD was applied to low-Reynolds number vortex shedding

from a cylinder the exact shedding frequency was shown to be returned by DMD.

6.3.5 Convergence of phase-averaged statistic

Figure 6.14 qualitatively compares the reduced-order reconstruction of the streamwise velocity computed at $t/T = 0.48$ to the phase-averaged streamwise velocity at $\varphi/T = 0.48$ with the number of snapshots used to compute the phase-average being $n = 4$. The contours are plotted on a mid-axial plane. When $n = 4$ it is easily identified that $\langle u \rangle / \overline{u}_b$ has not statistically converged. Contrast this to the reduced-order reconstruction of the streamwise velocity, where removing flow motion at frequencies higher than the fundamental results in a relatively smooth contour. Figure 6.15 shows the convergence of $\langle u \rangle$ at probe location $\mathcal{P}3$ as the number of snapshots is increased. Although up to 80 snapshots are used the statistic has not converged at this point.

6.3.6 Kolmogorov length scale

The Kolmogorov length scale gives an approximate order of magnitude of the smallest turbulent fluctuation (Pope [96]). The time-average $\Delta/\overline{\eta}$ gives an overall representation length scale of the velocity fluctuations that occur within the AAA during a pulse. Concentrated on the anterior-left side of the AAA's body $\Delta/\overline{\eta}$ is approximately 1.5 and within the neck region $\Delta/\overline{\eta}$ is approximately 2. The time-average of the dissipation is calculated by averaging the $M = 50$ phase-averaged values. The phase-wise variation in $\Delta/\langle \eta \rangle$ is shown in figure 6.16 at probes $\mathcal{P}1 - \mathcal{P}3$. The phase-averaged value gives a representation of how the turbulent length scale varies and relatively high values for $\Delta/\langle \eta \rangle$ can occur briefly during the cardiac

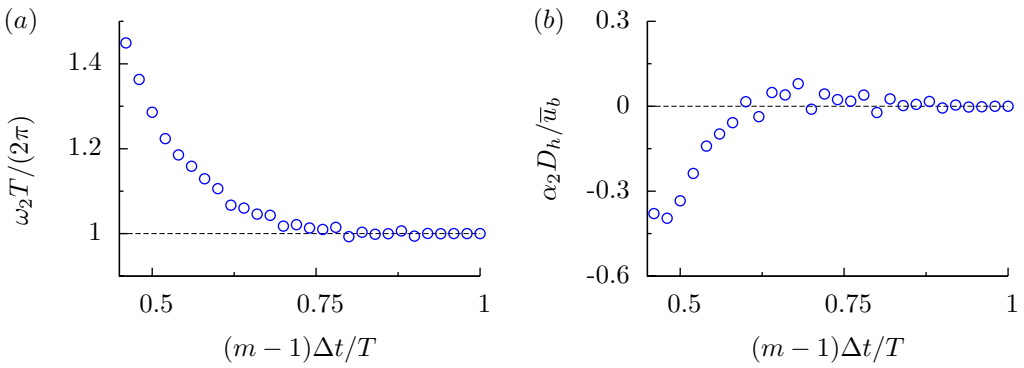

Figure 6.13: Effect of m on the (a) angular frequency and (b) growth rate of the dominant harmonic mode. DMD was calculated from snapshots of $\langle \boldsymbol{u} \rangle$ separated by $\Delta t = 0.02/T$.

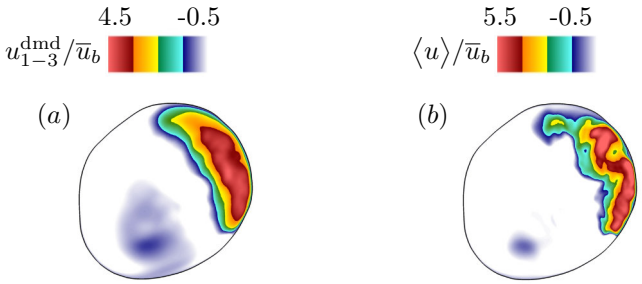

Figure 6.14: (a) Reduced-order reconstruction of the streamwise velocity u_{1-3}^{dmd} at $t/T = 0.48$. Snapshots used for DMD are collected over 4 pulses at a sampling interval of $\Delta t = 0.02/T$. (b) Phase-averaged streamwise velocity $\langle u \rangle/\overline{u}_b$ at $\varphi/T = 0.48$ computed over 4 periods. Contours plotted on a mid-axial plane.

cycle.

6.4 Discussion

In the present study DMD and triple decomposition are applied to the numerical simulation of blood flow in a medium-sized patient-specific AAA. Two interesting geometric features are present that cause the blood flow to transition to turbulence; namely a contorted and conical neck and the sudden expansion in AAA diameter distal to the neck. Both of these

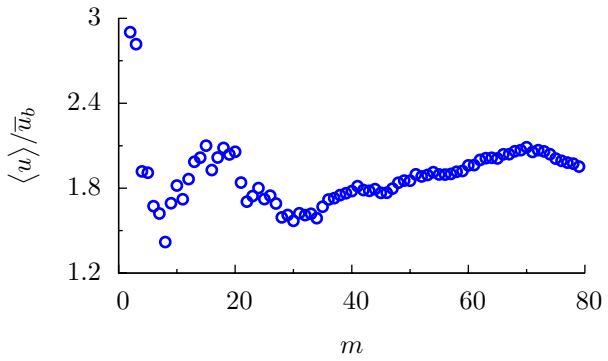

Figure 6.15: Convergence of the phase-averaged velocity $\langle u \rangle / \overline{u}_b$ at phase position $\varphi/T = 0.56$ and probe $\mathcal{P}3$ as the number of snapshots m used for the averaging is increased.

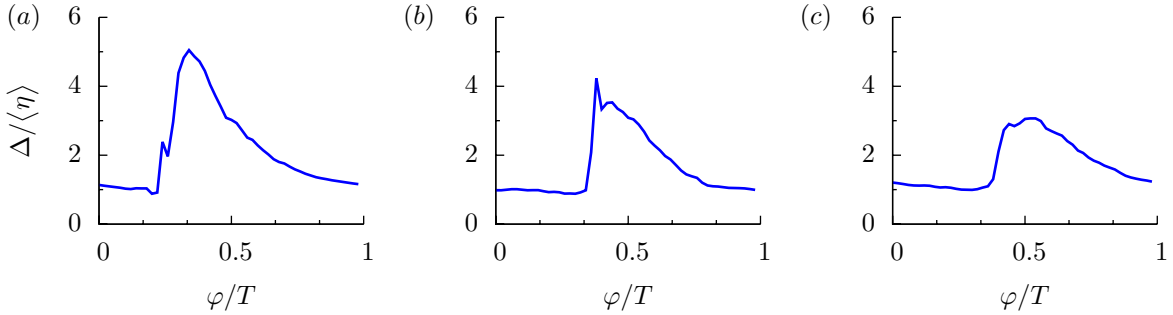

Figure 6.16: Phase-wise variation in the ratio of the grid cell average edge length to the phase-averaged Kolmogorov length scale $\Delta / \langle \eta \rangle$ at (a) $\mathcal{P}1$, (b) $\mathcal{P}2$ and (c) $\mathcal{P}3$.

features cause blood flow dynamics that differ from a healthy aorta and because they occur in a single case it is possible to contrast the different flow dynamics they cause.

As the blood flow accelerates during early-to-mid-systole, no notable flow features are present other then a recirculation zone that has formed within the neck region and a jet has started to form distal to neck. After peak-systole the recirculating blood within the neck transitions to turbulence and these turbulent vortexes stagnate in the neck region. Further downstream, in the AAA's body, the jet becomes turbulent and continues to circulate within the AAA during diastole. Unlike the neck region, where the turbulence is primarily confined

to a single location, the turbulent vortexes flow downstream, along the anterior-left wall and the turbulence from the jet vortexes is present for a majority of the pulse. Although the turbulence within the neck region exists for a shorter period of the pulse, its fluctuations are at a substantially higher intensity. In the work by Cantwell & Coles [17], the vortex shedding from a cylinder was described as turbulent vorticity that accumulates within large-scale coherent structures. This also describes the flow dynamics of the jet that forms with the AAA.

In Lozowy et al. [73] it was found that jets similar to this case only occur for aortic shapes when there is a sudden expansion in lumen cross-sectional area. For AAA with small-sized lumen or gradual increases in lumen cross-sectional area, the late-systole APG is strong enough to stagnate any jet vortexes at the neck. In a canonical study of oscillating flow in a pipe at $Wo = 13$ and $Re_D = 11460$ by Feldmann & Wagner [34], it was shown that as the flow accelerates i.e., has a FPG the turbulence is dampened. During flow decelerating the pressure gradient is adverse and there was a substantial increase in turbulent fluctuations. This type of flow behavior appears to continue in patient-specific arteries. Lantz et al. [61] observed fully disturbed blood flow in the aorta arch by the end of systole and stable flow during peak flow rate. In a numerical simulation of blood flow in a normal left ventricle by Chnafa et al. [22], peak volume-averaged turbulent kinetic energy did not occur until mid-diastole. Similar behavior has also been shown to occur in AAA by Poelma et al. [95]. The flow dynamics that occurred in this study show many similarities with the simplified eccentric stenosed tube at $Wo = 7.5$ observed by Varghese et al. [127]. The stenosis causes a long turbulent jet to form and since the stenosis was eccentric the jet is directed towards the wall. The turbulence persisted as the flow decelerated and by the end of the pulse the

turbulence in the stenosed tube had dissipated. However the results from this study are not fully applicable to AAA. Within the normal-sized aorta diameter $\approx$ 2 cm and $Wo \approx 15$, instead the study by Varghese et al. [127] is representative of stenosed blood flow further downstream in the common iliac artery where diameter $\approx$ 1 cm and $Wo \approx 7.5$. Reducing Wo by one half is equivalent to increasing the period of the blood pulse by a factor of four. At a Womersley number of 15, there would be substantially less time for a long turbulent jet to form and it can be expected that only a short jet will form.

The second component of this study evaluates DMD as a method for studying cardiovascular flows. As shown in chapter 2 in figure 2.6, a blood pulse can be represented as the summation of harmonic oscillations at progressively higher frequencies (Fourier series). DMD segments the velocity field into modes that contain the flow structures oscillating at a specific frequency. In the present study DMD is used to reconstruct a reduced-order representation of the velocity field so that it contains transient motion at only the dominate pulse frequency. This is beneficial to the study of cardiovascular flows as it allows for the dominate flow structures to be easily identified. DMD shares similarities with triple decomposition (Mezic [80]), which segments the velocity field is into periodic and turbulent components.

It is shown that if phase-averaging is performed only using four pulses the statistic is not close to being converged. An advantage that DMD has over triple decomposition is that it requires only a small number of pulses to collect the required snapshots. In this study only four pulses are used for DMD while 80 are used for phase averaging. A disadvantage that DMD has is it is not possible to fully reconstruct the phase-averaged velocity from DMD modes since the higher frequency modes contain both periodic and turbulent oscillations. This observation is made clear by viewing the velocity signal in figure 6.5 (b) and (c), since the

periodic and turbulent oscillations are qualitatively similar. Another disadvantage of DMD is the algorithm is not guaranteed to output a mode at the exact pulse frequency. When computing DMD from snapshots of the instantaneous velocity field collected over a single pulse, the correct pulse frequency is under predicted. Decreasing the time interval between snapshots did not improve this outcome. However, when the instantaneous snapshots are collected over 4 blood pulse, the frequency of the dominant DMD mode converged to the correct pulse frequency.

DMD can be viewed as an alternative to triple-decomposition since the velocity reconstruction using the mean and dominate harmonic it is qualitatively similar to the phase-averaged velocity field. In general DMD can be performed using less computational resources than what is required to simulate the large number of pules required to statistically average $\langle \boldsymbol{u} \rangle / \overline{u}_b$. In this study $m = 80$ snapshots were used to calculate the phase-averages and in Chnafa et al. [22] $m = 30$ were used. There are also computational challenges in calculating the inner product matrix $\widehat{\boldsymbol{\Psi}}^* \widehat{\boldsymbol{\Psi}}$ used in the DMD algorithm. A detailed discussion on these challenges in calculating this matrix can be found in Belson et al. [100]. As the number of snapshots is increased the computational resources used to calculate the DMD symmetric inner product matrix increases approximately by a power squared. Significantly more CPU resources are required to compute DMD when $n = 625$ snapshots are used compared to $n = 200$ snapshots.

A typical tetrahedral cell edge length used in AAA studies is set at 5.5 mm (Arzani et al. [3], Les et al. [67], Zambrano et al. [143]) and this is the length used in this study. To evaluate the suitability of this edge length to fully resolve turbulent fluctuations, it is compared to the time and phase-averaged Kolmogorov length scale. This length scale represents the smallest length of turbulent fluctuation and ideally the edge length of a grid

cell should be of $\mathcal{O}(\eta)$ (Moin and Mahesh [82]). In general the results from this study indicate that an edge length of 5.5 mm is suitable to resolve a majority of the turbulence for this patient-specific AAA. At peak turbulence, the phase-averaged Kolmogorov length scale decreases and the scale of the turbulence is less resolved by the grid, however, at no point during the pulse does $\Delta/\langle\eta\rangle$ exceed an order of magnitude. A smaller grid size better resolves the smaller-scale turbulent fluctuation but at the same time increasing the grid resolution significantly increases the computational costs and it is unlikely that this would qualitatively change the results from this study. The time-averaged Kolmogorov length scale is a more lenient criterion to evaluate the grid resolution and for this study the grid resolution is closer to this criterion.

Since the blood flow in AAA is transitioning to and from turbulence, it is not clear which is a more suitable length scale, the time or phase-averaged value of η. In a study on non-pulsatile flow in a backward facing step by Barri et al. [9], $\Delta/\overline{\eta}$ did not exceed ≈ 4 with a majority of the domain having $\Delta/\overline{\eta} < 3$. A backward facing step is a geometry that shares similarities with AAA. In a study of blood flow in heart value by Min Yun et al. [142], Δ/η was resolved to approximately 2. Since the blood flow rate is higher as it exits the heart and valve geometry contributes to the turbulence approximately 2 orders of magnitude more grid cells are required to achieve this resolution. This highlights the computational challenge in fully resolving the Kolmogorov length scale of complex geometries, even at a low-Reynolds number. The amount of turbulence that can occur in an AAA is dependent on the shape of an AAA. As shown in Lozowy et al. [73], it is possible for large AAAs to also have predominately laminar flow throughout the pulse cycle. Thus, the required grid resolution can vary based on AAA shape.

A limitation of the reduced-order reconstruction performed using DMD is that the sampling interval between snapshots is only $\Delta t = 0.02/T$ (50 snapshots per pulse). At this sampling rate the decomposition would not produce modes that capture the higher frequency flow motion. Although the method returns a dominant harmonic mode at the pulse frequency, it is likely that the higher frequency modes would be better resolved if a smaller sampling interval is used.

In conclusion this study highlighted two types of aortic flow; turbulent recirculation within the neck region and a jet comprised of turbulent vortexes that circulate within the AAA's body during diastole. Phase averaging can decompose vascular flow into its periodic and turbulent components but requires a large number of pulses to achieve statistically converged results. It is demonstrated that DMD can be used as a alternative to phase averaging where the flow can be reconstructed as a single harmonic that is comparable to the phase-averaged velocity.

Chapter 7

Low wall shear stress predominates at sites of abdominal aortic aneurysm rupture

Abstract

Objective: Aortic diameter as the primary criterion in the decision to repair AAAs has drawbacks as some rupture below size thresholds, whereas others reach extreme size without rupture. Predictions of static aortic wall stress have also failed to reliably predict rupture potential. The objective of this study was to computationally assess blood flow characteristics at the site of infrarenal AAA rupture. On the basis of the finite element literature correlating rupture location with high static local wall stress, we hypothesized that a computational fluid dynamics approach would also demonstrate rupture at regions of high pressure and WSS.

Methods: Three-dimensional AAA geometry was generated from computed tomography

angiography images of seven ruptured AAAs. Aortic blood flow velocity, pressure, and WSS were computationally determined. Flow characteristics at the site of rupture were determined and compared across all cases.

Results: AAA size at the time of rupture was 8.3 ± 0.9 cm. Only three of the seven AAAs ruptured at the site of maximal diameter. Blood flow velocity in the aneurysmal aorta showed dominant flow channels with zones of recirculation, where low WSS predominated. Regardless of aneurysm size or configuration, rupture occurred in or near these flow recirculation zones in all cases. WSS was significantly lower and thrombus deposition was more abundant at the site of rupture.

Conclusions: This computational study was the first to assess blood flow characteristics at the site of infrarenal AAA rupture in realistic aortic geometries. In contradiction to our initial hypothesis, rupture occurred not at sites of high pressure and WSS but rather at regions of predicted flow recirculation, where low WSS and thrombus deposition predominated. These findings raise the possibility that this flow pattern may lead to thrombus deposition, which may elaborate adventitial degeneration and eventual AAA rupture.

Clinical Relevance: Aortic diameter as the primary criterion in the decision to repair AAAs has drawbacks as some AAAs rupture below size thresholds, whereas others grow to large sizes without rupture. Computational fluid dynamics was used to model blood flow in ruptured human AAAs. Rupture occurred in regions of low wall shear stress, where flow recirculation and thrombus deposition predominated, suggesting that prolonged interaction of circulating factors with the vascular endothelium may lead to wall degeneration. An understanding of the interplay between wall shear stress and vascular remodeling will ultimately lead to a better understanding of AAA development, growth, and rupture potential.

7.1 Introduction

Rupture of an AAA has an associated mortality of 90% (Patel et al. [89]). In general, AAAs are repaired when they meet certain size criteria (aortic diameter 5.5 cm in men and 5.0 cm in women) or when they become symptomatic or rupture (Chaikof et al. [19]). Use of aortic diameter as the primary criterion in the decision to intervene fails to take into consideration AAAs that rupture at sizes below operative thresholds (Reed et al. [99]), particularly in women (Wilson et al. [136]), and fails to account for AAAs that reach extreme size without rupture (Doyle et al. [32]). Furthermore, aortic diameter is a static measure that does not take into consideration the dynamic interactions between local physical forces and the biology of the aortic wall. Pulsatile pressure changes may result in unsteady turbulent stresses, with regions of high and low WSS that may damage the endothelium and contribute to AAA formation and the degradation of the aneurysm wall (Moore et al. [52], Meng et al. [78], Davies et al. [26]).

There has been considerable finite element (FE) structural analysis modeling the physical characteristics of the AAA wall using computed tomography reconstructions (Di Martino et al. [29], Fillinger et al. [35], Fillinger et al. [36], Thubrikar et al. [121]). These studies examined the effect of mechanical wall stress (WS) and revealed features that affect AAA mechanics, including tortuosity, asymmetry, presence of ILT, and wall thickness (Kleinstreuer & Li [55], Taylor et al. [119], Bonert et al. [14], Chatziprodromou et al. [20], Zarins et al. [144]). Although these FE methods have the potential to improve rupture prediction, they employ a static measure of WS that fails to take into account that rupture occurs not at maximal failure pressure but rather at normal aortic pressures (Mohan & Melvin [81], Lee

& Haut [66], Purslow [97]). Unfortunately, the correlation of the magnitude of static WS with the tensile strength of the aneurysm wall has yet to consistently predict the outcome for specific AAA geometries (Caro et al. [18], Glagov et al. [39], Zarins et al. [145]) because it fails to take into consideration the effect of hemodynamic factors, such as WSS, in assessing AAA growth and rupture potential.

There currently is no truly reliable way to evaluate the susceptibility of a particular AAA to rupture. Understanding of local hemodynamic factors in specific AAAs may lead to a better prediction of rupture potential. The purpose of this study was to computationally simulate aortic blood flow in RAAAs to correlate local hemodynamic factors of blood flow velocity, pressure, and WSS with rupture location. On the basis of evidence from the FE literature, we hypothesized that a CFD investigation would confirm the location of AAA rupture at regions of high pressure and WSS. This work has been published in Boyd et al. [15].

7.2 Method

Thin-slice (2.5-mm) CTA images of the infrarenal aorta were obtained for one non-aneurysmal aorta and seven RAAAs. Patients with RAAAs were stable enough to undergo CTA before urgent repair. Rupture location was determined at time of repair and was independently determined from CTA images. The blood was assumed to be an incompressible fluid with Newtonian properties. Blood density and dynamic viscosity are $\rho = 1050$ kg m^{-3} and $\mu = 0.0035$ kg m^{-1} s^{-1}, respectively. The inner walls of the aorta are assumed to be rigid with a no-slip condition.

The constant bulk flow rate used in this chapter is qualitatively representative of the time average of pulsatile flow in the abdominal aorta. The bulk Reynolds number is $Re_b = 250$ and is defined as $Re_b = 2R\rho u_b/\mu$, where length scale $R = 1.2$ cm is the upstream aortic inlet radius (aortic neck) and $u_b = 0.0347$ m/s is the bulk velocity. The flow rate used in this study is comparable to the mean value that occurs during a adominal aortic blood pulse. It is assumed here that a steady flow simulation performed using the mean flow rate is comparable to the time-average from a pulsatile simulation. At the upstream inlet, Poiseuille flow was assumed. The WSS at the inlet was 0.04 N m^{-2} and was calculated from $\text{WSS}_{inlet} = 4\mu u_b/R$. WSS varies as a function of vessel diameter, with WSS increasing in smaller vessels. Unstructured grids composed of tetrahedral and prism cells were generated using commercial grid generation software (version 17.2, Pointwise, Fort Worth, Tex). The number of cells varied from 1.9 million to 4.6 million, depending on the size of the RAAA. For the surface contours, pressure was expressed as $P^* = (P - P_{inlet})/P_D$, where $P_D = 0.5\rho u_b^2$, and WSS* indicates that magnitude of the WSS has been normalized by WSS_{inlet}.

Predicted aortic blood flow velocity, localized pressure variation, and WSS profiles were obtained for all cases. By CFD convention, lower values are represented by the blue end of the color spectrum, whereas higher values are represented by the red end of the spectrum. Relative differences in flow velocity profiles, pressure, and WSS were compared between patients.

7.3 Results

Predicted blood flow in the normal aorta under non-pulsatile simulation conditions demonstrated a channeled pattern with a characteristic increase in flow velocity at the aortic bifurcation (figure 7.1, (a)). Predicted aortic pressure loss and WSS in the normal aorta (figure 7.1, (b) and (c), respectively) were uniform, with an increase in WSS and a characteristic decrease in pressure toward the iliac bifurcation. The observed local variation in WSS is predominantly a function of the variation in vessel diameter and, to a lesser extent, flow channeling due to the modest tortuosity of the aorta.

The seven RAAA patients (four men, three women) had fusiform AAAs with varied shapes, and none had associated iliac artery aneurysms. The average AAA size at rupture was 8.3 ± 0.91 cm. Aortic neck angulation ranged from 0 to 80 degrees. Only three of the seven RAAAs ruptured at the site of maximal diameter.

In all seven RAAAs, the blood flow was characterized by a dominant flow channel with associated zones of low-velocity recirculation flow (figure 7.2 (a)). Recirculation flow

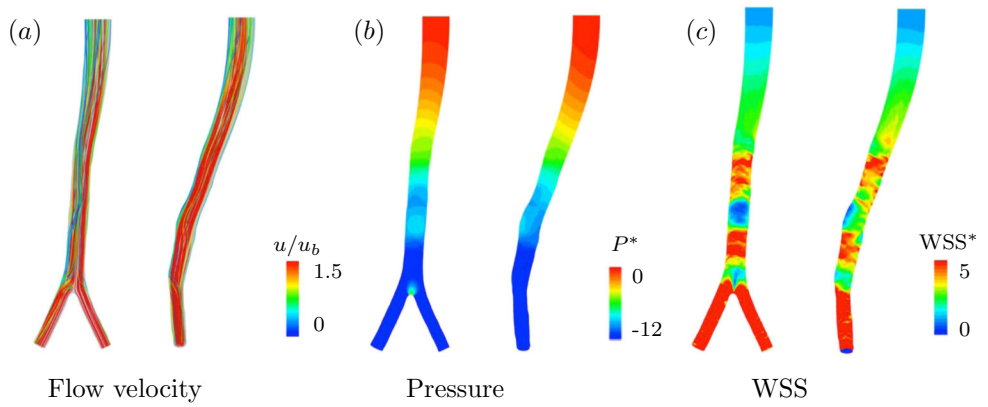

Figure 7.1: Predicted (a) velocity (u/u_b), (b) pressure (P^*), and (c) wall shear stress (WSS*) in normal adult aorta. Anterior-posterior and lateral views are shown.

shows a vortex pattern with flow direction at times opposite to the dominant flow channel. RAAAs with larger diameters had greater recirculation flow, whereas a smaller RAAA was associated with less recirculation flow (patient 3, figure 7.2 (a)), similar to the flow seen in the nonaneurysmal aorta (figure 7.1). The dominant flow channel was associated with higher velocity flow and a high relative pressure within the aneurysm sac. Predicted maximal aortic sac pressure occurred at the site where the main flow channel impinged on the aortic wall (figure 7.2 (b)), typically the anterior aortic wall (figure 7.2 (a)). The predicted WSS was maximal at the site of dominant flow channel impingement, with relatively low WSS predominating elsewhere in the aneurysm (figure 7.2 (c)). The region of highest WSS was on the aortic wall opposite to the site of rupture in five of seven RAAA cases. WSS at the site of maximal impingement was calculated as 0.197 ± 0.040 N m^{-2}, whereas at the actual site of rupture, the regional WSS was significantly reduced at 0.02 ± 0.006 N m^{-2}. In all cases of RAAA, the rupture occurred in a low WSS region and in most cases in association with zones of flow recirculation and not at the site of maximal pressure and WSS (figure 7.2 (b) and (c)).

In figure 7.2, fewer velocity streamlines are visualized to more clearly show the location of the dominant flow channel and regions of low velocity flow in relation to the site of aortic rupture. In each case, with the exception of patient 3, the area of rupture is clearly seen in relation to the site of recirculating, low-velocity blood flow. In patient 3, aortic rupture occurred at the border of the dominant flow channel and the recirculation zone. In this case, there is a large component of vortex flow involving the entire lumen, and the dominant flow channel is not pronounced as in the other cases.

Figure 7.4 shows axial CTA images of rupture location (white arrows, panel 1) contrasted

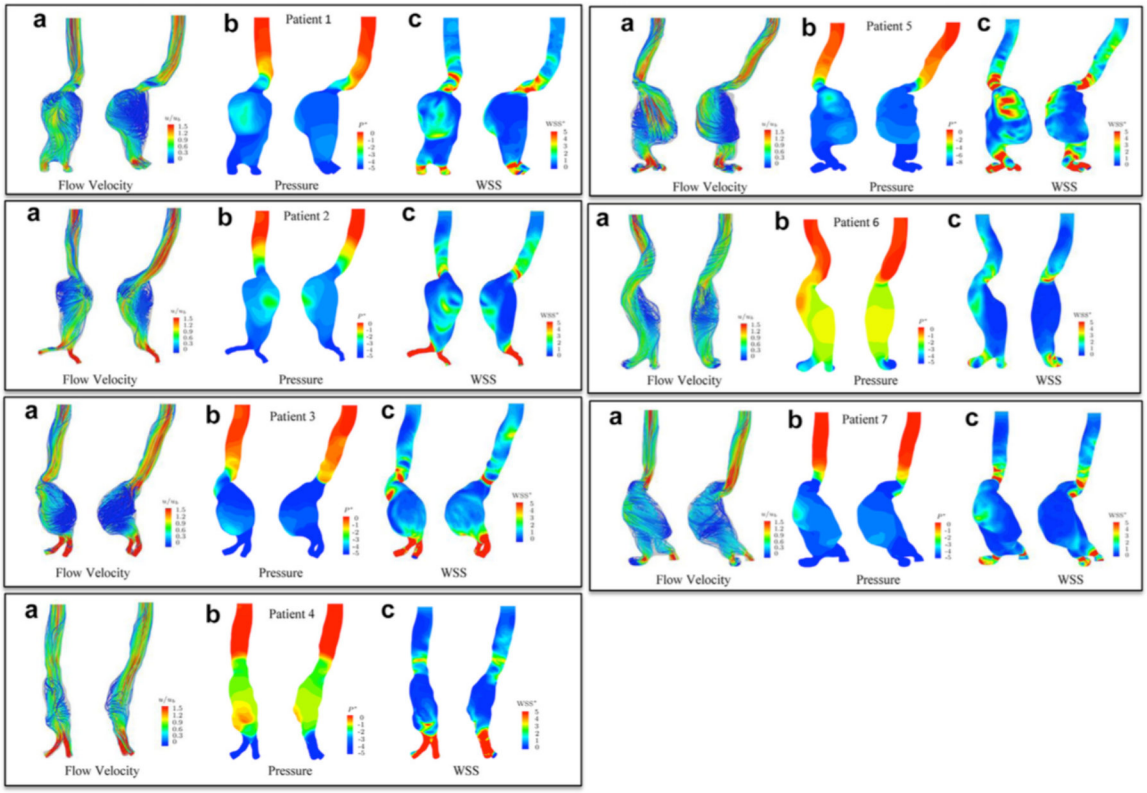

Figure 7.2: Predicted (a) velocity (u/u_b), (b) pressure (P^*), and (c) wall shear stress (WSS*) in the seven cases of ruptured abdominal aortic aneurysms (RAAAs). Anterior-posterior and left lateral views are shown. Lower values are represented by the blue end of the spectrum, whereas red indicates higher values.

with normalized velocity profiles (panel 2) indicating the nature of flow at the site of rupture (black arrows). These velocity data show zones of slower or reverse flow that corresponds to regions of low WSS depicted in figure 7.2 (c).

The site of the dominant flow channel impingement on the aortic wall was nearly devoid of ILT in all cases with an average thickness of 0.2 $\pm$ 0.1 cm, in contrast with the site of rupture, which showed significantly more thrombus deposition, with an average of 2.6 $\pm$ 1.8 mm of thrombus.

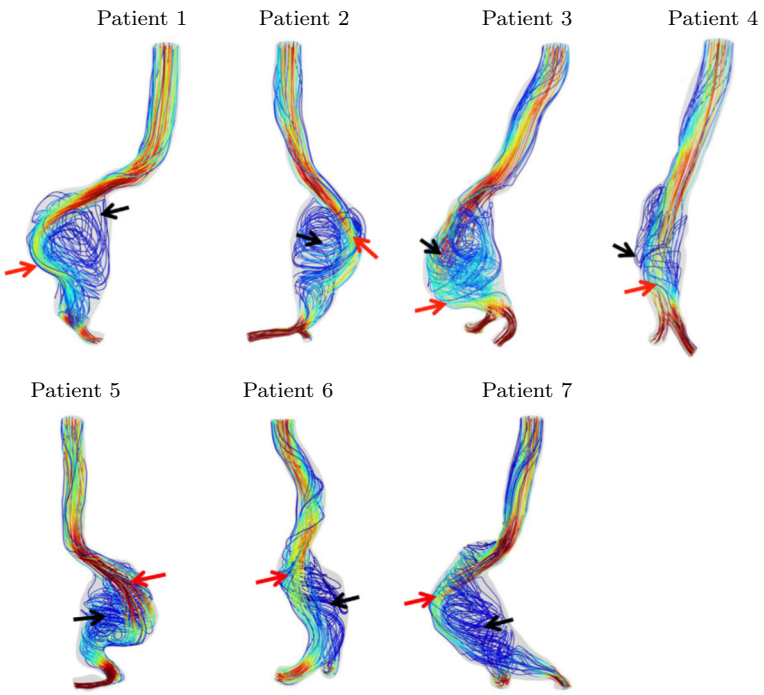

Figure 7.3: Velocity profile streamlines are shown for seven ruptured abdominal aortic aneurysms (RAAAs). Images have been rotated in the X/Y direction, if required, to more clearly demonstrate the dominant flow channel, zone of flow recirculation, and rupture location within each AAA: 45 degrees to right of anterior-posterior (patients 1, 3, 4, and 7); 90 degrees to left of anterior-posterior (patient 6); 45 degrees to left of anterior-posterior (patient 2); and anterior-posterior projection (patient 5). The black arrows indicate the location of rupture, whereas red arrows indicate site of dominant flow channel impingement of the aortic wall. Lower velocity values are represented by colors toward the blue end of the spectrum, whereas red indicates higher values.

7.4 Discussion

This CFD study was the first to describe predicted blood flow velocity, pressure, and WSS in the geometry of seven infrarenal RAAAs. Aortic rupture occurred in areas of reduced flow velocity and in most cases in recirculation zones, where low WSS and ILT deposition predominated. This is in direct contradiction to FE studies, in which rupture was predicted to occur at areas of high localized WS, not WSS. Unlike FE analysis, which is more applicable to static structural aortic wall mechanics, CFD is a numerical method that provides a dynamic

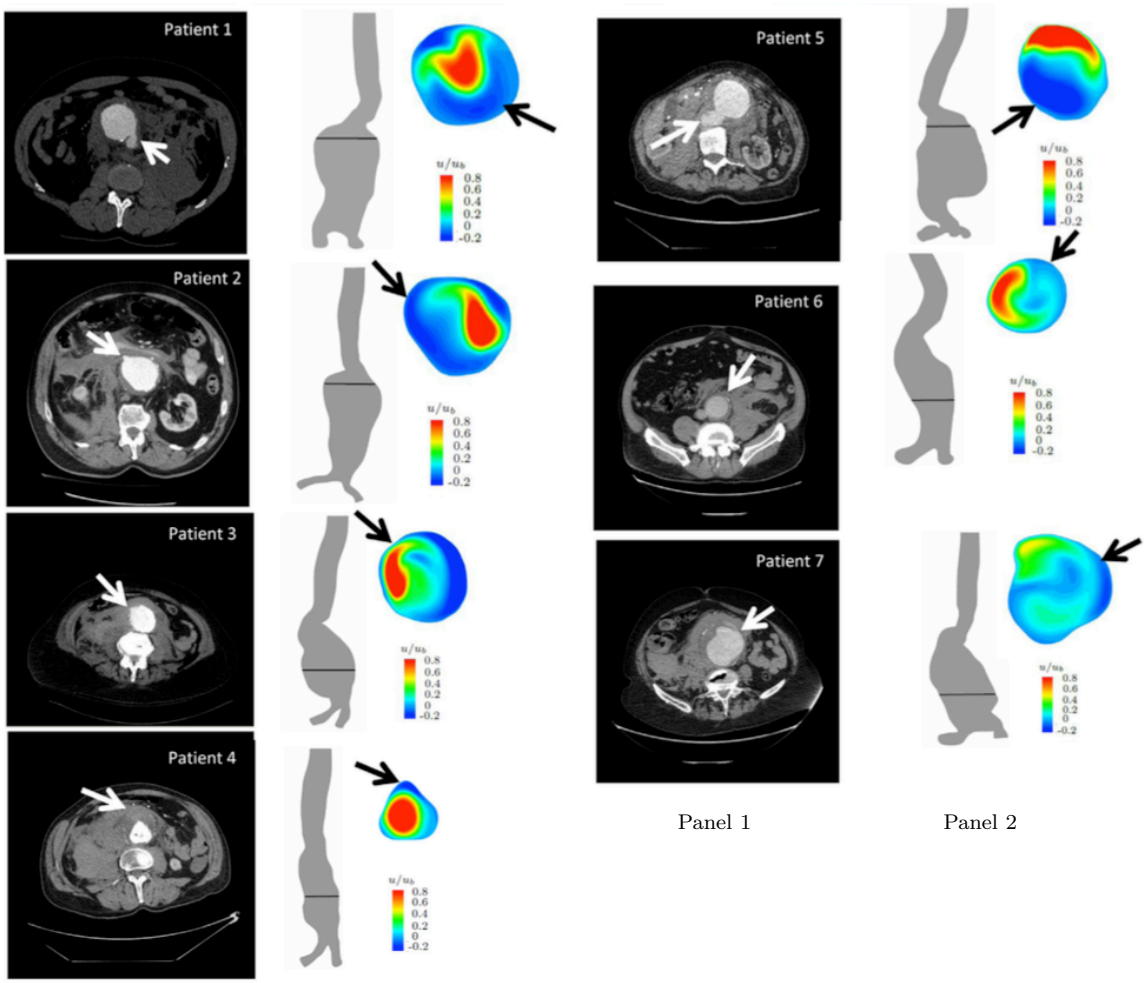

Figure 7.4: Panel 1, Axial computed tomography angiography (CTA) images of seven ruptured abdominal aortic aneurysms (RAAAs), indicating the location of rupture (white arrows). Panel 2, Anterior-posterior AAA flow channel silhouettes, indicating level of rupture (black line), and cross-sectional images of normalized velocity profiles, indicating the location of rupture (black arrows).

prediction of aortic flow characteristics, such as WSS.

This study was limited by assuming rigid and impermeable aortic walls, non-pulsatile Newtonian blood characteristics, and negligible effect of visceral branches. In addition, to compare across AAAs, we assumed a uniform resting cardiac output as we did not have access to patient-specific blood flow rates. One normal aorta, which showed relatively stable, non-recirculating flow under the conditions modeled, was included. Velocity, pressure, and WSS data on non-ruptured AAAs (not presented) have similar flow patterns and thrombus deposition as in RAAAs. In this study, each RAAA serves as its own control, i.e. comparison of the flow dynamics within the AAA at the ruptured and non-ruptured regions.

In spite of these limitations, this model showed characteristic vortex flow in all RAAAs and allowed a comparison of flow characteristics at the site of rupture. The shape and configuration of the RAAA were well represented by the three-dimensional reconstruction, which preserved the relative size and shape differences between individual RAAAs.

Although only seven RAAAs were examined, this is the largest study to date employing CFD to predict flow characteristics in the geometry of actual RAAAs. Aortic rupture did not occur at the site of maximal diameter as only three of seven cases ruptured near the maximal cross-sectional area (figure 7.4, patients 2, 3, and 7), demonstrating that size and static aortic WS are insufficient to predict the propensity to rupture. In the one case in which rupture did not occur at a region of predominantly low velocity and WSS (patient 3), the site of rupture still did not coincide with the point of maximal flow channel impingement, where WSS and pressure are relatively high. In this case, there was a more marked vortex flow involving the entire aortic lumen, and rupture occurred at the border of the dominant flow channel and recirculation zone. The reason for this difference is not known, but future work on modeling

pulsatile blood flow in these geometries may provide answers about the effect of oscillating WSS on rupture. Regardless of this discrepancy, this CFD study provides novel information about the relationship between blood flow hemodynamics and rupture location in realistic AAA geometries that has not previously been reported.

Most aortic aneurysms develop in the infrarenal segment of the aorta, suggesting that specific hemodynamics or aortic wall constituents predispose this portion of the aorta to aneurysmal expansion and rupture. It is possible that exposure of the infrarenal aorta to changes in WSS leads to pathologic changes that promote aortic dilation. WSS hemodynamics may be further disturbed as the aneurysm grows, leading to regions of flow recirculation and oscillating WSS (Zarins et al. [144], Caro et al. [18], Glagov et al. [39]). It is well known that high WSS can promote endothelial injury (Langille & ODonnell [60]), whereas low WSS is characterized by inflammatory infiltration (Chatziprodromou et al. [20]).

It has been suggested that ILT may act to reduce AAA WS and to protect the AAA from rupture (Di Martino et al. [29]); however, it has been shown that ILT inhibits vascular smooth muscle cell synthesis of collagen (Levene et al. [69], Pietila & Jaakkola [93]), is associated with a thinner aortic wall, and has greater numbers of macrophages and inflammatory cells (Kazi et al. [53], Burke et al. [16], Adolph et al. [1]). Relative aortic wall hypoxia has been postulated in regions of high ILT deposition (Vorp et al. [130], Vorp et al. [131]) and has been suggested as a mechanism for aortic wall expansion and degeneration.

In our study, all cases of aortic rupture occurred in regions with relatively more ILT deposition, which is in contradiction to FE analysis, in which ILT has been suggested to be protective against rupture. Although low WSS is unlikely to directly cause aortic rupture, it is possible that continued deposition of ILT occurs at sites with lower velocity and WSS.

This ILT deposition may lead to alterations in the local environment that elaborate loss of adventitial integrity through inflammatory or ischemic changes. Although the process of AAA growth and rupture is likely multifactorial, with pressure playing a significant role in aortic expansion, the adventitia may weaken and rupture preferentially at these sites.

7.5 Conclusion

This CFD study was the first to model aortic blood flow in realistic geometries of RAAAs. In contradiction to our original hypothesis, rupture location coincided with regions of predicted low WSS and flow recirculation, not with regions of high pressure and WS as predicted by FE analysis. The reason for this discrepancy is not yet known. Future studies examining the interplay between alterations in WSS in pulsatile flow and its effect on vascular endothelial remodeling will lead to a better understanding of AAA development and growth and may ultimately provide better prediction of AAA rupture potential.

Chapter 8

Influence of abdominal aortic aneurysm shape on hemodynamics

Abstract

Direct numerical simulation was performed on two patient-specific AAA using physiologically realistic flow conditions. The patients have AAA with diameters of approximately 5 and 11 cm, respectively. The blood flow hemodynamics are shown to consist of large-scale periodic structures and the flow transitions from laminar-to-turbulent and back to laminar during a pulse. Transition does not occur until after the maximum flow rate has been reached and turbulence persists in the AAA after the bulk flow decelerates to a laminar condition. For both cases, a jet of blood forms at the AAA throat and impinges against the arterial wall at the site of maximal aortic diameter. During the pulse structures shear across the AAA causing locally high WSS. It is shown that the cases have substantially different hemodynamics. The smaller sized AAA has faster moving flow structures, higher WSS, higher turbulent kinetic energy, and the blood spirals down the AAA toward the iliac arteries. In the larger sized

AAA, the blood flow channels down on the anterior side and a large recirculation zone forms on the posterior side. A large recirculation zone causes low WSS, which is known to promote atherosclerosis.

8.1 Introduction

AAA formation and growth occurs due to a combination of biological and hemodynamic factors (Lasheras [63]). A known hemodynamic factor is the frictional drag exerted by blood flow on the arterial wall, referred to as wall shear stresses (WSS). Stable unidirectional WSS is associated with healthy, intact vascular endothelium, whereas low flow with oscillating WSS is associated with atherosclerosis (Tarbell et al. [116]). Evidence also suggests that high WSS with sharp spacial gradients (Dolan et al. [31]) can damage the arterial wall. Low oscillating WSS is primarily caused by zones of recirculating blood and high WSS by blood flow impingement. Since the abdominal aorta is generally a uniform cylindrical shape in most cases the flow would remain laminar. However the shape of an AAA could cause the blood flow to transition-to-turbulence increasing the oscillation in the flow direction and causing higher WSS. The influence of vascular shape on turbulence is not well understood and the goal of this study is to numerically calculate physiological blood flow in two patient-specific AAAs to determine if there is a notable different in the flow structures and turbulence intensity between the cases. Previous work on physiological blood flow in patient-specific arteries includes the experimental study by Stamatopoulos et al. [110] and the numerical study by Les et al. [67], Valen-Sendstad et al. [125] and Arzania & Shaddenb [4].

8.2 Method

The geometry of the two patients, referred to as case 1 and case 2, is shown in figure 8.1. Case 1 has an AAA diameter approaching the size criterion of 5 cm and case 2 has a AAA diameter that has dilated to over 11 cm, well beyond the size threshold. For both cases, the aorta contorts as it leads into the AAA.

To ensure the CFL number less than 1, the time step was fixed at $\Delta t = 5 \times 10^{-5}$ s during a pulse. The time-dependent bulk velocity shown in figure 8.2 is implemented at the upstream inlet boundary. The simulation is performed on 48 processors. An unstructured grids have been generated composed of 3078214 and 4462192 tetrahedral and prism cells for case 1 and case 2, respectively. The velocity field was set to zero for the initial conditions and the flow is allowed to develop over 5 pulses. The blood pulse was segmented into $m = 25$ phase positions and phase-averaged statistics were calculated by ensemble averaging $n = 50$ snapshots. The time-averaged quantities were then calculated by averaging the $m = 25$ phase-averaged quantities. In the previous chapters the numerical grid is evaluated by comparing the edge length of a grid cell to the Kolmogorov length scale. In this chapter the grid has been

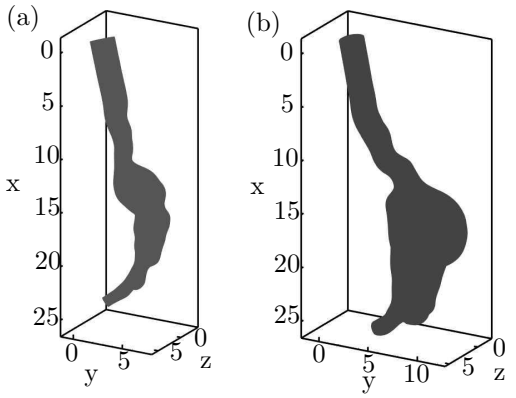

Figure 8.1: Geometry for (a) case 1 and (b) case 2. Units are in cm.

evaluated by comparing the grid edge length to the maximum friction velocity at the inlet boundary. The wall tangent and normal edge length of the first prism cell adjacent to the wall is $\Delta s_t = 0.005$ cm and $\Delta s_n = 0.075$ cm, respectively. Using the maximum WSS at the inlet boundary to scale the grid spacing in viscous units, $\Delta s_t^+ = 0.8$ and $\Delta s_n^+ = 11.6$. The superscript $^+$ denotes scaling with the viscous length ν/u_τ, where u_τ is the friction velocity. From the wall 14 prism cells are extruded at an expansion rate of 1.1. The tetrahedral cells that occupy the remainder of the domain have a viscous edge length of $\Delta s^+ = 11.6$. These normalized lengths are similar to what was used in chapter 3 for channel flow.

8.3 Results

Figure 8.3 shows isosurfaces of instantaneous coherent structures for case 1 visualized using the λ_2 criterion of Jeong & Hussain ([50]). During systole flow structures form at the AAA throat and by mid systole impinge against the arterial wall at the site of maximal aortic diameter. The structures spiral within the AAA, shearing against the arterial wall and breaking down into smaller turbulent structures. During diastole the bulk flow through the AAA is effectively zero but the turbulent structures continue to spiral making approximately 1.5 revolutions during a pulse. Since the diameter of the AAA is larger than the upstream aorta, the local Wo is higher, increasing the prevalence of unsteady inertia forces in the AAA. At the start of diastole the reversal of the bulk flow direction causes some of the coherent structures in the aorta to be pulled upstream. By the end of diastole the turbulent structures are dissipating and the process begins again with the next pulse. Figure 8.4 shows isosurfaces of instantaneous coherent structures for case 2 visualized using the λ_2 criterion. Similar to

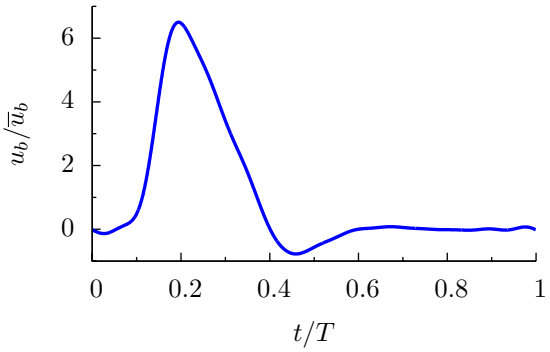

Figure 8.2: Infrarenal aortic bulk flow rate.

case 1, flow structures form at the AAA throat but it is not until early diastole that the jet impinges against the arterial wall and breaks down into a turbulent flow. During diastole the turbulent structures continue to flow downstream, shearing along the anterior side of the AAA. Since the AAA is larger, relative to case 1, a greater amount of time is required for the vortexes to traverse the AAA and it is not until systole of the next pulse that the structures are ejected from the AAA into the iliac arteries. Similar to case 1, the site of maximal aortic diameter is the location the structures impinge.

Surface contours of WSS are shown for case 1 at $\phi/T = 0.4$ and case 2 at $\phi/T = 0.56$ in figure 8.5 and 8.6, respectively. It can be seen in figure 8.5 (a) and figure 8.6 (a) large structures of positive and negative $\langle \tau_{w,x} \rangle$ shear across the AAA with the magnitude of $\langle \tau_{w,x} \rangle$ being higher for case 1. Figure 8.5 (b) and figure 8.6 (b) show the instantaneous turbulent WSS x-component $\tau'_{w,x}$. For both cases fluctuations in $\tau'_{w,x}$ are localized to the proximity of the large structures and follows the structures movement as they shear across the AAA. Figure 8.5 (c) and figure 8.6 (c) show the phase-averaged quantity $\tau_{w,x,rms}$. For case 1, $\tau_{w,x,rms}$ occupies a larger surface area of the AAA and is at a higher intensity, relative to case 2.

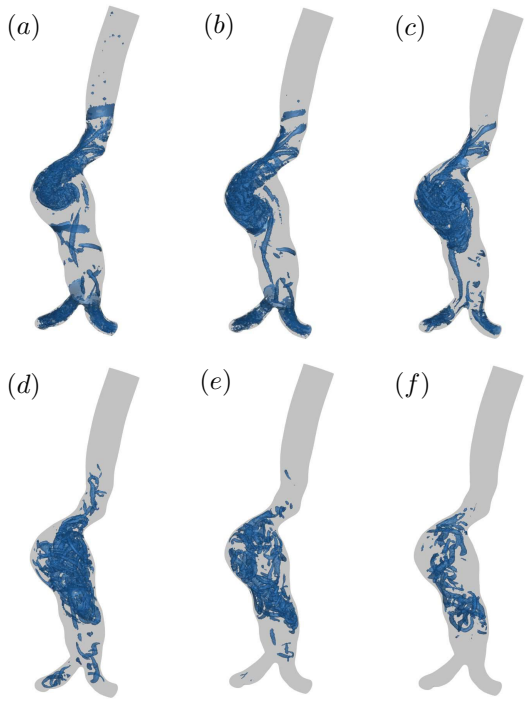

Figure 8.3: Case 1 isosurfaces of instantaneous coherent structures visualized using the λ_2 criterion at temporal positions (a) $t/T = 0.28$, (b) $t/T = 0.32$, (c) $t/T = 0.40$, (d) $t/T = 0.56$, (e) $t/T = 0.72$ and (f) $\phi/T = 0.88$.

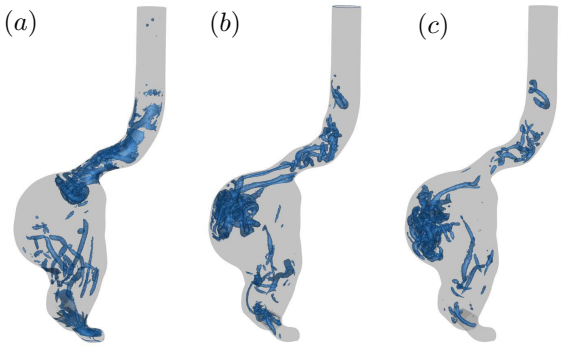

Figure 8.4: Case 2 isosurfaces of instantaneous coherent structures visualized using the λ_2 criterion at temporal positions (a) $t/T = 0.32$, (b) $t/T = 0.60$ and (c) $t/T = 0.80$.

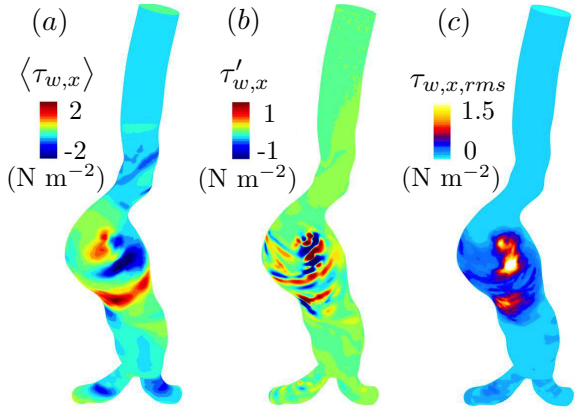

Figure 8.5: Case 1 surface contours of (a) phase-averaged WSS $\langle \tau_{w,x} \rangle$, (b) instantaneous WSS fluctuation $\tau'_{w,x}$ and (c) root mean square of WSS fluctuation $\tau_{w,x,rms}$ at phase position $\phi/T = 0.4$.

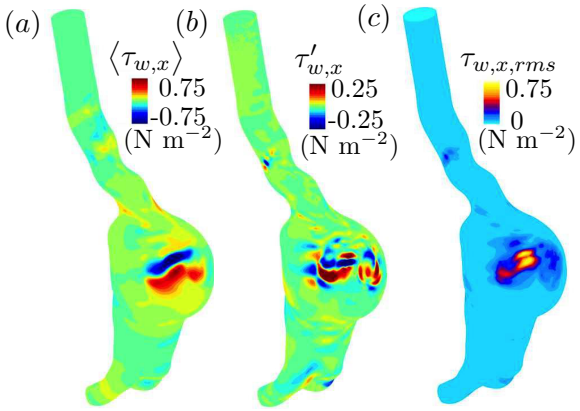

Figure 8.6: Case 2 surface contours of (a) phase-averaged WSS $\langle \tau_{w,x} \rangle$, (b) instantaneous WSS fluctuation $\tau'_{w,x}$ and (c) root mean square of WSS fluctuation $\tau_{w,x,rms}$ at phase position $\phi/T = 0.56$.

The phase-averaged TKE is calculated as $\left\langle \boldsymbol{u}' \cdot \boldsymbol{u}' \right\rangle / (2\overline{u}_b^2)$. Figure 8.7 shows for case 1 $\left\langle \boldsymbol{u}' \cdot \boldsymbol{u}' \right\rangle / (2\overline{u}_b^2)$ on a mid-coronal plane. High TKE is not present in the AAA until late systole and it spirals within the AAA following the path of the flow structures. During diastole $\left\langle \boldsymbol{u}' \cdot \boldsymbol{u}' \right\rangle / (2\overline{u}_b^2)$ dissipates in intensity. Figure 8.8 shows for case 2 $\left\langle \boldsymbol{u}' \cdot \boldsymbol{u}' \right\rangle / (2\overline{u}_b^2)$ on a mid-sagittal plane. High TKE is not present in the AAA until early diastole and similar to case 1 the TKE follows the path of the flow structures and dissipates during late diastole. Case 2 has a zone of $\left\langle \boldsymbol{u}' \cdot \boldsymbol{u}' \right\rangle / (2\overline{u}_b^2)$ on its posterior side that persists at a low intensity throughout diastole. In Figure 8.8 (a) and (b) it can be seen for case 2 that TKE is first produced at the shear layer between the high velocity jet and the lower velocity fluid in the AAA. High TKE occurs adjacent to where the AAA bulges and on the posterior side TKE is relatively low. During diastole TKE propagates downstream on the anterior side and dissipates in intensity. For both cases there is a phase-lag between the highest flow rate and the formation of TKE, but this phase-lag is more profound for case 2. Turbulence is low during early-to-mid systole and begins to increase in the AAA during late-systole. Figure 8.9 shows for case 2 isosurfaces of instantaneous turbulent components of velocity visualized by $u' = -0.5\overline{u}_b$ (blue) and $u' = 0.5\overline{u}_b$ (red). The turbulent fluctuations are attached to the large-scale coherent structures and the turbulent fluctuations spread out during diastole. In the upstream aorta relatively no turbulence is visualized.

Figure 8.10 shows surface contours of $\left\langle C_p \right\rangle$ at various phase positions during the pulse. At $\phi/T = 0.16$ there is a favorable pressure gradient (FPG) across the aorta and AAA, corresponding to the acceleration portion of systole. At $\phi/T = 0.28$ there is a adverse pressure gradient (APG) across the aorta and AAA, corresponding to the deceleration portion of systole. Figure 8.10 (a) and (b) show qualitatively that the pressure drop across the AAA

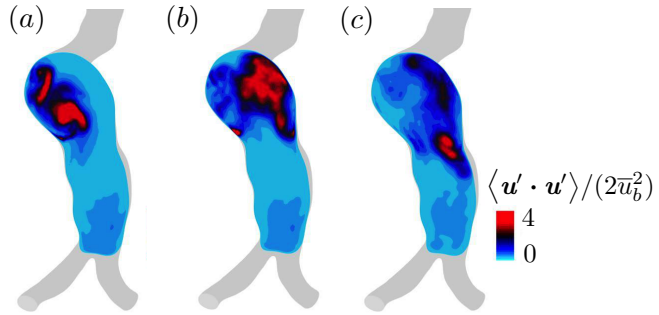

Figure 8.7: Case 1 contours of phase-averaged TKE $\langle \boldsymbol{u}' \cdot \boldsymbol{u}' \rangle / (2\overline{u}_b^2)$ on a mid-coronal plane at phase positions (a) $\phi/T = 0.36$, (b) $\phi/T = 0.44$ and (c) $\phi/T = 0.52$.

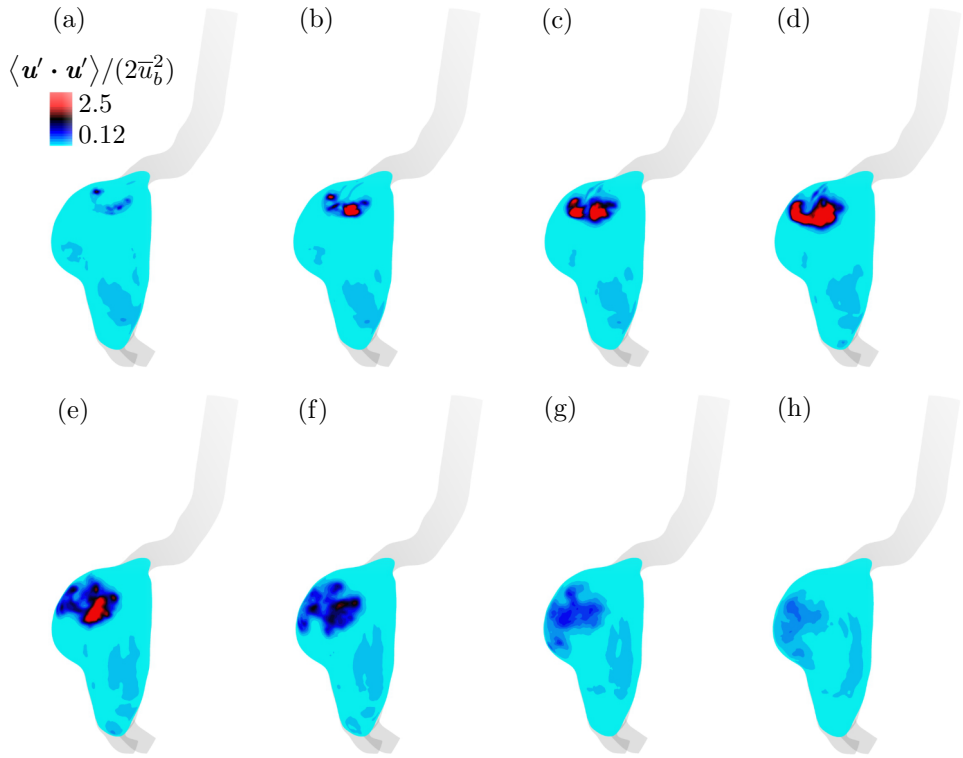

Figure 8.8: Case 2 contour of phase-averaged TKE $\langle \boldsymbol{u}' \cdot \boldsymbol{u}' \rangle / (2\overline{u}_b^2)$ on a mid-sagittal plane at phase positions (a) $\phi/T = 0.36$, (b) $\phi/T = 0.4$, (c) $\phi/T = 0.44$, (d) $\phi/T = 0.48$, (e) $\phi/T = 0.56$, (f) $\phi/T = 0.64$, (g) $\phi/T = 0.72$ and (h) $\phi/T = 0.96$.

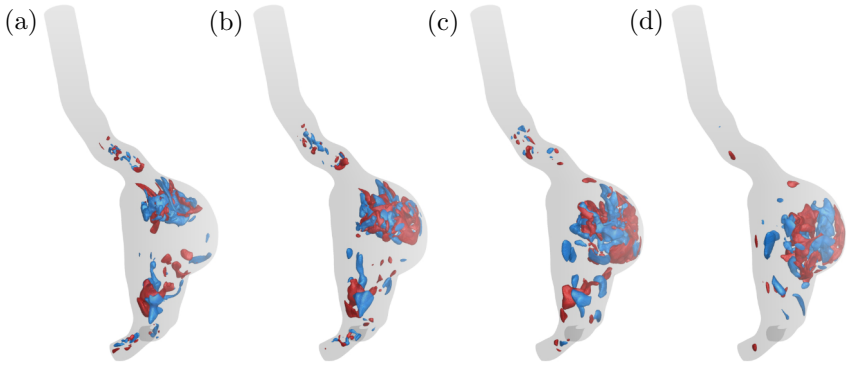

Figure 8.9: Case 2 isosurfaces of instantaneous turbulent velocity fluctuation $u' = 0.5\overline{u}_b$ (red) and $u' = -0.5\overline{u}_b$ (blue) at temporal positions (a) $t/T = 0.44$, (b) $t/T = 0.56$, (c) $t/T = 0.72$ and (d) $t/T = 0.96$.

is less relative to the upstream aorta. The reduced pressure drop during late-systole leads to the continued fluid motion in the AAA during diastole. Since the flow in the AAA is channeled during systole, $\langle C_p \rangle$ is approximately uniform along a cross-sectional slice of the AAA. During diastole the flow rate is low, relative to systole, and the pressure drop across the aorta and AAA is also comparably low. At $\phi/T = 0.48$ and 0.72 on the anterior side of the AAA $\langle C_p \rangle$ is locally high due to the impingement of flow structures.

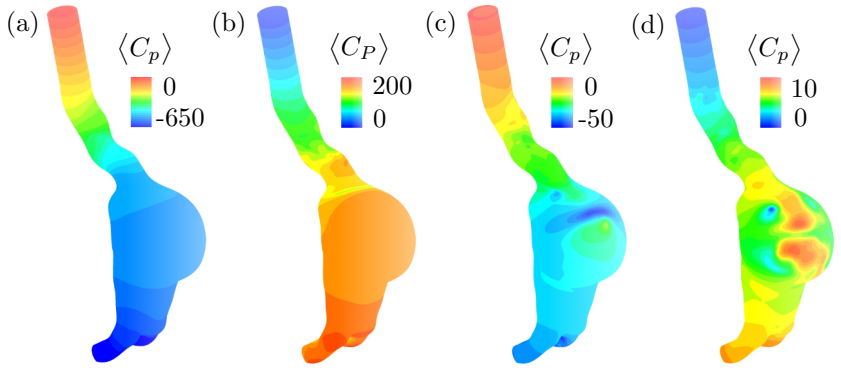

Figure 8.10: Case 2 surface contour of phase-averaged pressure coefficient $\langle C_p \rangle$ at phase positions (a) $\phi/T = 0.16$, (b) $\phi/T = 0.28$, (c) $\phi/T = 0.48$ and (d) $\phi/T = 0.72$.

The time-averaged streamlines are shown for case 1 in figure 8.11 (a) and case 2 in figure 8.11 (b). Time averaging removes the time-dependent flow structures and gives an overall description of the flow field and the hemodynamic forces acting on the arterial wall. For case 1 the time-averaged flow field consists of a jet that impinges against the arterial wall and spirals down the length of the AAA. There is no zone of separated recirculating flow for case 1. The time-averaged streamlines for case 2 show that the flow also impinges against the arterial wall, however instead of spiraling like case 1, the blood flows downstream on the anterior side and a large zone of recirculating blood forms on the posterior side. For both cases the AAA bulges at the location the time-averaged streamlines impinge.

The time-averaged TKE is shown for case 1 on a x-z plane at y = 5.3 cm in figure 8.12 (a) and case 2 on a x-y plane at x = 1.6 cm in figure 8.12 (b). It can be seen that for case 1, high $\overline{\boldsymbol{u}' \cdot \boldsymbol{u}'}/\overline{u}_b^2$ occupies a majority of the AAA's volume and the highest $\overline{\boldsymbol{u}' \cdot \boldsymbol{u}'}/\overline{u}_b^2$ occurs along the centre axis of the AAA. For case 2 a zone of high $\overline{\boldsymbol{u}' \cdot \boldsymbol{u}'}/\overline{u}_b^2$ occurs on the anterior side in the AAA's bulge and occupies a relatively small amount of the total AAA volume. A smaller zone of lower intensity $\overline{\boldsymbol{u}' \cdot \boldsymbol{u}'}/\overline{u}_b^2$ occurs on the posterior side. Overall $\overline{\boldsymbol{u}' \cdot \boldsymbol{u}'}/\overline{u}_b^2$

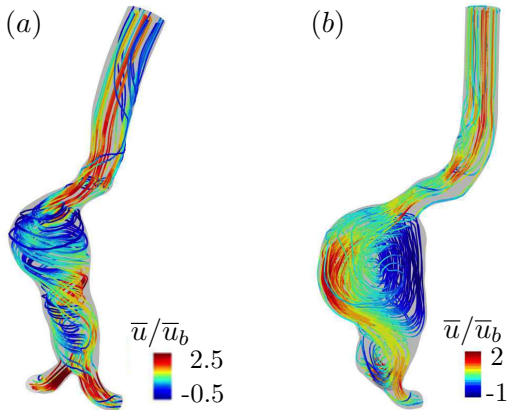

Figure 8.11: Time-averaged streamlines for (a) case 1 and (b) case 2.

for case 1 it is substantially higher and occupies at larger amount of the total AAA volume, relative to case 2.

8.4 Conclusions

Direct numerical simulation has been performed on two patient-specific AAA. The hemodynamics vary considerably between the cases and the flow is found to be comprised of complex periodic and turbulent structures. To analyze the phase-variation during a pulse the velocity was decomposed into it's instantaneous turbulent and phase-averaged component. For both cases the blood flow transitions from laminar-to-turbulent and back to laminar during a pulse. There is considerable phase-lag between the maximum flow rate and the formation of turbulent flow structures in the AAA. During systole, for both cases, a jet forms at the AAA's throat and impinges against the arterial wall with the AAA appearing to bulge at the impingement location. During diastole, when the bulk flow through the AAA is $\approx$ zero, the velocity in the AAA is not zero and the flow structures continue to shear across the arterial wall. High WSS and TKE occurs in the proximity of the flow structures. The following

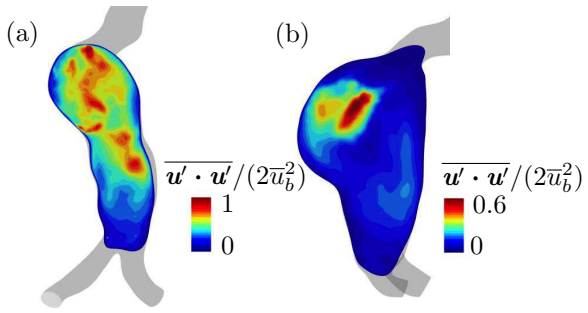

Figure 8.12: Contours of time-averaged TKE $\overline{\boldsymbol{u}' \cdot \boldsymbol{u}'}/(2\overline{u}_b^2)$ for (a) case 1 on a mid-coronal plane and (b) case 2 on a mid-sagittal plane.

differences exist between the two cases:

- For case 1 the flow transitions-to-turbulence during late systole and for case 2 during early diastole. For both cases the turbulence has mostly dissipated by early systole of the next pulse.

- Overall the flow velocity is higher in case 1's AAA. This results in faster moving flow structures, higher WSS and TKE. High TKE occupies a larger amount of the AAA volume for case 1.

- For case 1 the blood flow spirals within the AAA and for the time-averaged flow there is no zone of separated recirculating blood. For case 2 the blood flows downstream on the anterior side and a large zone of recirculating blood forms on the posterior side.

Within the scope of the two AAA studied here the moderately sized AAA has higher turbulence and WSS. However the larger-sized AAA has a large recirculation zone which is not present in the moderately-sized AAA. Physiologically both high turbulence and a large recirculation zone could damage the arterial wall.

Chapter 9

Conclusion

9.1 Conclusions of the work

The primary contribution of this thesis is that it provides greater insight into the types of blood flow dynamics that can occur in AAA. This has been achieved by performing numerical simulations on the blood flow in 32 patient-specific AAA shapes. The hemodynamics from this dataset have been compared to biological features, such as ILT deposition, growth and rupture location. The risk of rupture is known to increase substantially for AAA diameters > 5 cm but the exact reason for this is not known. The hypothesis that was tested in this thesis is that blood flow dynamics become more adverse as AAA size increases and this could contribute to increased risk of rupture. The results from this thesis identify that adverse hemodynamics are dependent on diameter, along with several other AAA geometric features.

It is found that when AAA have small-sized lumens, the blood flow behaves qualitatively similar to a normal-sized abdominal aorta. Although these patients may have AAA with diameters diameters > 5 cm, the accumulation of ILT along the aortic wall constricts the

diameter of the lumen flow channel. Turbulence can still occur in AAA with small-sized lumen but it is often confined to a small region and the turbulence will quickly dissipate. As the lumen increases in size the hemodynamics in an AAA deviate progressively more from a healthy aorta. For cases that have a sudden expansion in cross-sectional area distal to the neck, a jet of turbulent blood forms at the neck that often impinges and shears against the arterial wall. Since the late-systole adverse pressure gradient (APG) decreases as AAA diameter increases, the late-systole inertia forces are insufficient to decelerate the jet structures. The severity of the impingement does not necessarily increase with lumen size and in fact it is found to be less intense in large-sized AAA. This is due in part to there being a greater distance from the neck to the AAA wall in large-sized cases. It is possible for large-sized AAA to also experience gradual increases in lumen cross-sectional area. For these cases, despite the large lumen size, the jet structures are stagnant at the neck and the blood flow downstream in the AAA is predominately laminar. Two additional types of abnormal flow dynamics are identified in AAA. The first of these is a zone of turbulent recirculating vortexes that forms in the conical neck. A conical neck refers to the upstream region of the AAA where the aorta becomes constricted and angulated. The turbulent structures stagnant in the neck region and unlike the jet vortexes do not move within the AAA. The second is a region of low-velocity recirculating blood that is caused by the downstream motion of the jet vortexes pushing the fluid on the opposite side upstream.

The work in this study provides evidence that laminar recirculating blood promotes ILT growth. This observation came from comparing hemodynamcs from a serial growth study. No ILT formed within a recirculation zone with turbulent vortexes. Within the same recirculation zone, the region with laminar flow corresponded with the region of ILT

accumulation. The accumulation of ILT is likely caused by both biological and hemodynamic factors therefore it may not be possible to identify a single hemodynamic cause that is valid for all patients. A hemodynamic factor that prevents the attachment of ILT to the wall is identified by this study to be high WSS from the impingement of vortexes. For medium to large-sized AAA that also experiences the impingement of turbulent jet vortexes, the region of the wall that experienced the impact of flow structures is always found to be devoid of ILT. Directly away from the wall region, ILT is found to be present. This leads to the conclusion that the elevated shear from a vortex prevents the initial attachment of ILT to the wall. This has not been observed previously in the literature since most previous studies have focused primarily on small-sized AAA and these jet vortexes would not be present. Another reason this has not been observed is that it is common for studies to focus only on the time-averaged velocity field and as such instantaneous flow dynamics, such as the movement of vortexes, are not discussed in the literature. One would suspect that a vortex shearing against the arterial wall would cause damage and possibly lead to a deterioration in wall integrity; however, since vortex impingement primarily occurs during diastole, the vortexes are relatively slow moving and the intensity of the shear is comparable to peak WSS that occurs in a normal-sized aorta. This leads to the speculation that vortex shearing does not cause damage the wall and instead the shear has a positive effect by preventing ILT accumulation. That said, in general AAAs with impingement are found to be expanding in the direction of impingement and if shearing is not the cause of this expansion it must be the wall-normal pressure force caused by the impact of vortexes. Since the vortexes are at a low-velocity this expansion is likely to occur gradually over a extended period of time. From this study no AAA with impingement experienced ILT at the impingement site. All AAAs

with impingement were growing in the direction that the flow structures impact. Another downside to AAA experiencing impingement is that it is often coupled with a recirculation zone along the opposite side and recirculating blood can cause ILT deposition.

Low and oscillating WSS is thought to be a dominant mechanism that contributes to vascular disease. It is common in vascular studies to calculate the oscillatory shear index (OSI) and link this parameter to ILT deposition or atherosclerosis. Studies that have attempted to link OSI to ILT in AAA have found a correlation between low OSI and ILT deposition. This is opposite to the original theory regarding blood flow oscillations. It is identified that there are several different types of flow dynamics that can occur in AAAs and that different flow types can have similar OSI values. For example regions of vortex impingement have low OSI and are devoid of ILT. A single recirculation zone can contain regions with both low and high OSI. This further demonstrates the limitation of using OSI by itself to identify adverse blood flow dynamics.

Triple decomposition is used to segment pulsatile turbulent flow into its periodic and turbulent components. Another segmentation method investigated in this work is dynamic mode decomposition (DMD) where the velocity field is decomposed into modes that give the flow structures oscillating at a specific frequency. At most cardiovascular locations the flow is laminar and only periodic oscillations are present. In large or diseased arteries the flow can transition to turbulence and there is a turbulent component superimposed onto the periodic oscillation. In this study the DMD algorithm is used to remove frequencies other then the pulse frequency from the velocity field. This allows for a better representations of the flow dynamics, where the reconstructed velocity field consists of a single large-scale vortex. Small-scale vortexes that oscillate at frequencies higher than the pulse frequency are

excluded from the reconstruction. The DMD method produces results that are comparable to the phase-average; however, since periodic and turbulent oscillation can be at the same frequency, the phase-average cannot be fully calculated using DMD. Since fewer pulses are required to collect the data for DMD, compared to triple decomposition, it may be more applicable to clinic applications.

9.2 Future work

The research presented in this thesis has importance for future research. The work can be advance in the following ways:

- The abdominal aorta is one of the largest diameter vessels in the cardiovascular system with $Wo \approx 15$ and therefore pulsatile inertia forces have a substantial effect of the hemodynamics. Within the AAA the diameter is larger still and inertia is even more significant. Aneurysms occur in various locations in the cardiovascular system. For intracranial aneurysms $Wo \approx 2$ inertia forces have substantially less influence on the blood flow dynamics. The large difference in Wo results in AAA and intracranial aneurysms having different flow dynamics. A detailed comparative study on the blood flow dynamics in diseased arteries at various Wo values would be beneficial.

- The AAA simulations in this thesis assumed rigid walls and simulated only the blood flow. The hemodynamic forces (pressure and WSS) then cause stress within the arterial wall and this wall stress is ultimately what causes expansion. Combining both the numerical simulation of the blood flow and wall stress in the arterial wall would give

more insight into the cause of AAA growth. This type of simulation is referred to as fluid-structure interaction.

- The grid resolution in this study is compared to the Kolmogorov length scale. Although the ratio was reasonable when viewed as a time-averaged quantity, at certain points during the pulse the Kolmogorov length scale was substantially smaller then the average edge length of a grid cell. A smaller grid resolution at locations with high turbulence could give a better representation of the smaller-scale turbulent fluctuations. It is unlikely that a higher grid resolution would substantially change the fist-order velocity calculations. However, a finer grid resolution combined with $n >> 80$ pulses would likely be required to accurately calculate the higher-order turbulent quantities, such as the terms in the transport equation for turbulent kinetic energy.

- Simulations were performed on pulsatile channel flow at $Wo = 15$. It would be beneficial to perform multiple simulations at a wide range of Wo, pulse amplitudes and Reynolds numbers. However one of the computational challenges of deceasing Wo is that it lengthens the pulse period. Since a large number of pulses are required for phase-averaging this increases the length of the simulation. Increasing the amplitude of the pulse could result in the phase-averaged velocity reversing in direction during the deceleration period of the pulse and this would produce interesting flow physics. Further work could be performed using DMD on steady and pulsatile channel flow.

Appendix A

In this appendix results from cases $5-23$ from chapter 4 are presented. The results include time-averaged streamlines, mid-axial CTA and time-averaged streamwise velocity plotted on the mid-axial slice.

For cases 6, 7, 9, 11, 13, 16, 20 and 23, although the AAA have the diameters greater than 5 cm the presence of ILT deposition reduces the size of the lumen flow channel to that of a normal-sized abdominal aorta. As a result of this the blood flow within the AAA for these cases is non-disturbed and behaves similar to the analytical solution shown in figure 2.7. The ILT is predominately located along the anterior wall. Although the blood flow is non-disturbed in the AAA, if the neck region is contorted, turbulence will occur during late-systole. Any turbulence structures that form within the neck stagnant at this location and dissipate by mid-diastole. No conclusions can be made from the hemodynamics as to why these AAA form and it is likely that biological factors play a dominate role. The presence of ILT likely weakens the arterial wall and this is contributing to the expansion. However, it is not possible to identify the mechanisms that caused ILT to accumulate along the wall in the first place.

Cases 5, 8, 10, 12 and 17 experience a sudden expansion in lumen cross-sectional area

distal to the neck. This feature causes a jet to form during systole and the jet structures continue to circulate within the AAA during diastole. For case 5, due to the contortion in the neck, turbulent flow structures spiral within the AAA and make a complete revolution. This exposes the majority of the AAA wall to turbulent shear. Similar flow dynamics occur for case 10 and the turbulent vortexes first shear down the anterior side and then recirculate up along the posterior side. For both of these cases relatively no ILT is present. The blood flow also spirals for case 17, but the vortexes only revolve approximately 180 degrees. The left side that is exposed to turbulent vortexes is devoid of ILT and ILT has accumulated along the right side where the blood flow is laminar and stagnant. Cases 8, 12 and 17 also experience blood flow impingement and this region is devoid of ILT and ILT has accumulated along the wall exposed to recirculating blood.

Although cases 14, 15, 18, 19 and 22 have relatively large-sized lumen, the AAA lumen diameter gradual increases after the neck. This causes the jet structures to stagnant distal to the neck during early-diastole and the blood flow is predominately non-disturbed downstream in the AAA. These cases have little to no ILT deposition.

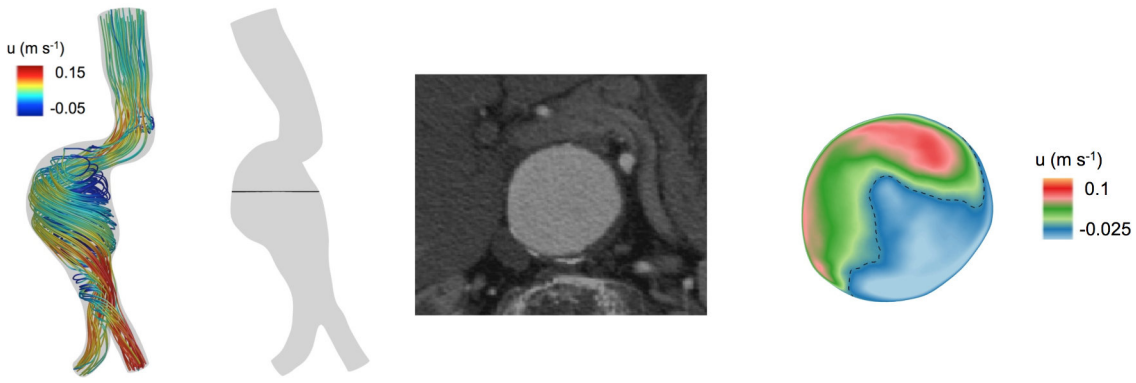

Figure 1: Case 5. Maximum diameter 5 cm. Maximum ILT thickness 0.5 cm. ILT located along right wall. Impingement occurred along anterior-left.

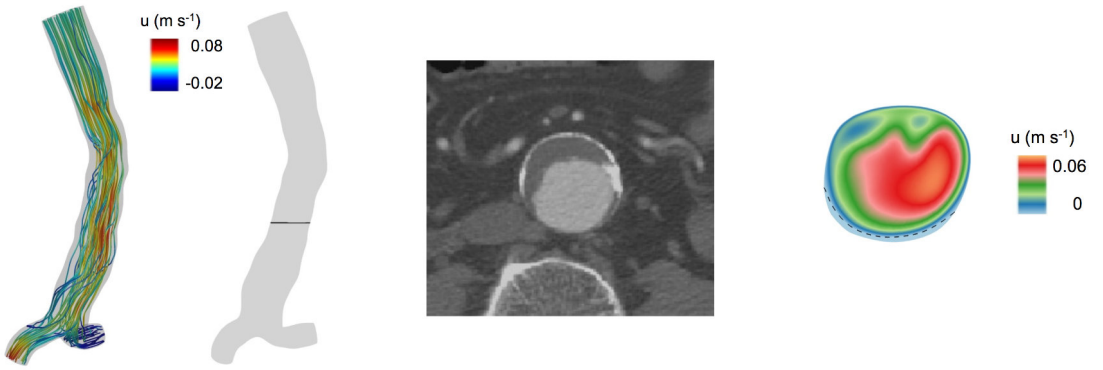

Figure 2: Case 6. Maximum diameter 5.3 cm. Maximum ILT thickness 1.0 cm. ILT located along anterior wall. No impingement.

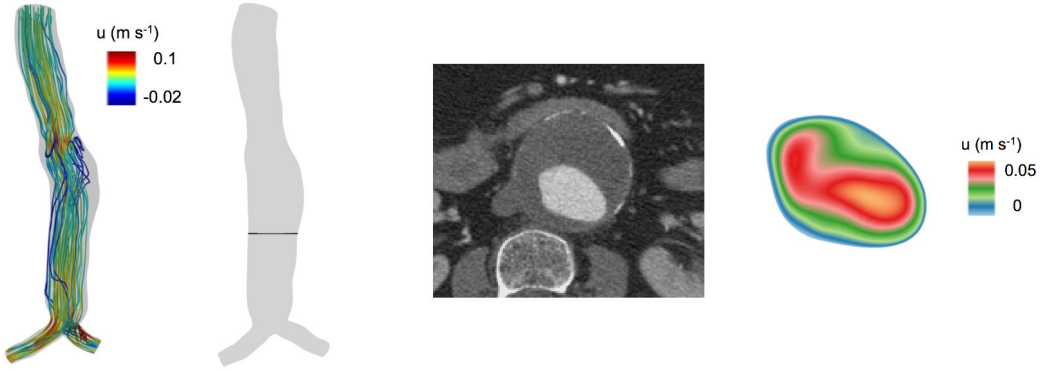

Figure 3: Case 7. Maximum diameter 5.5 cm. Maximum ILT thickness 1.4 cm. ILT circumferential-anterior. No impingement.

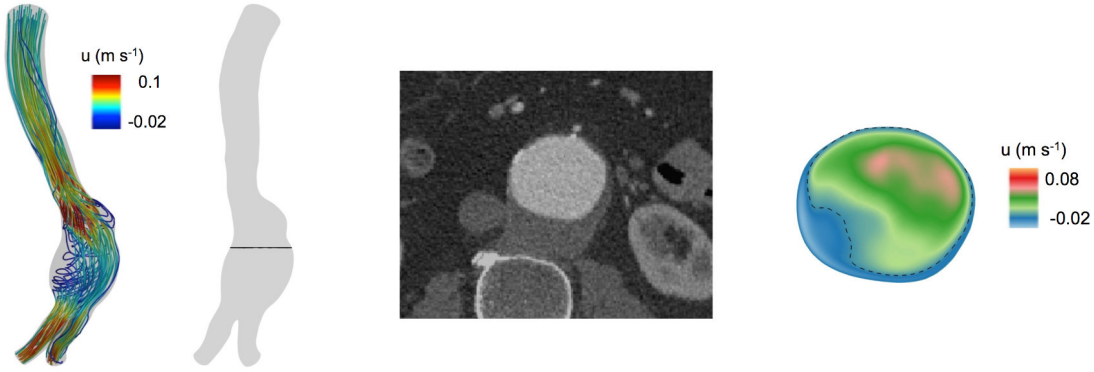

Figure 4: Case 8. Maximum diameter 5.5 cm. Maximum ILT thickness 1.4 cm. ILT located along posterior wall. Impingement occurred along anterior.

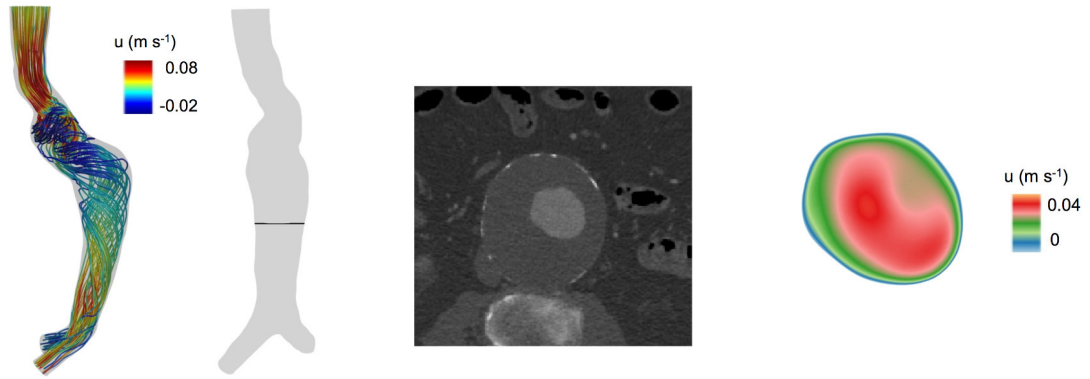

Figure 5: Case 9. Maximum diameter 8 cm. Maximum ILT thickness 2.8 cm. ILT circumferential-posterior. No impingement.

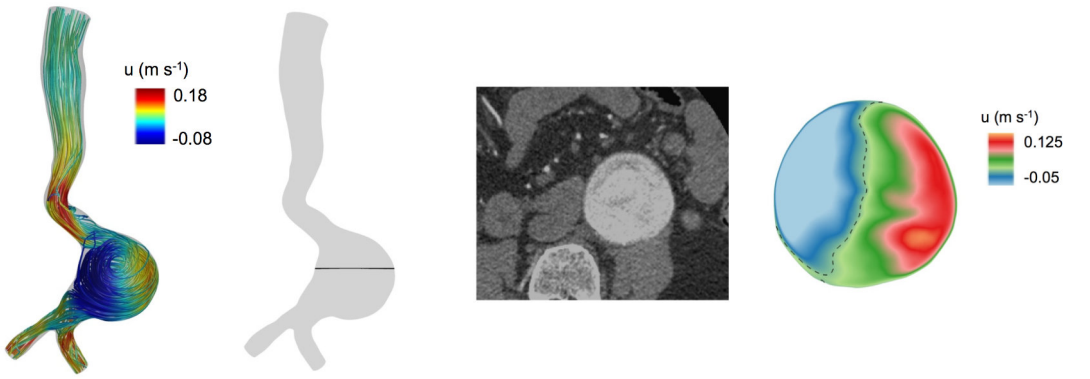

Figure 6: Case 10. Maximum diameter 5.4 cm. No ILT. Impingement occured along left.

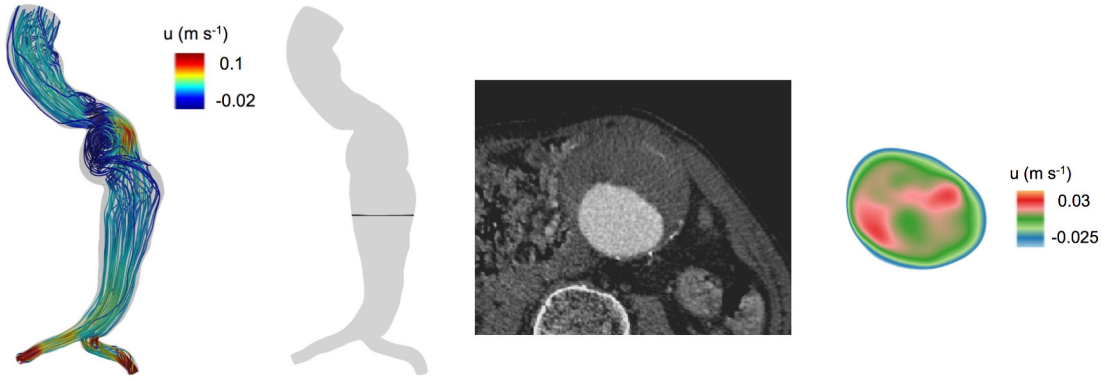

Figure 7: Case 11. Maximum diameter 6.5 cm. Maximum ILT thickness 4 cm. ILT located along anterior wall. No impingement.

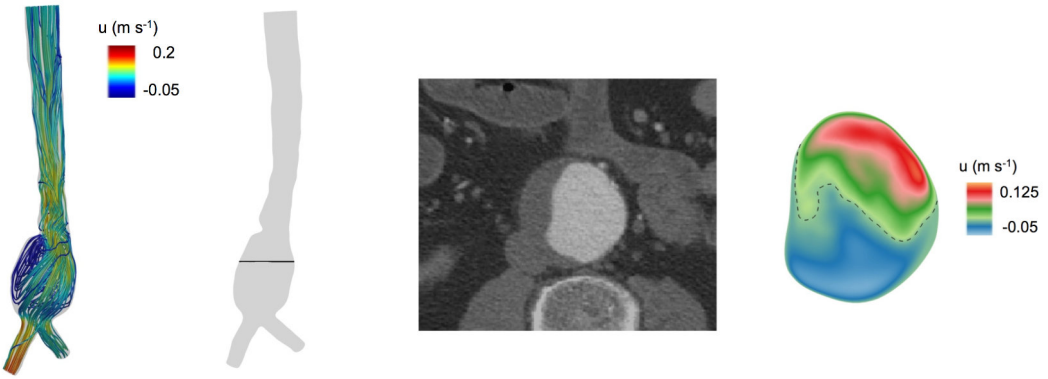

Figure 8: Case 12. Maximum diameter 5.5 cm. Maximum ILT thickness 2 cm. ILT located along right. Impingement occured along anterior-left.

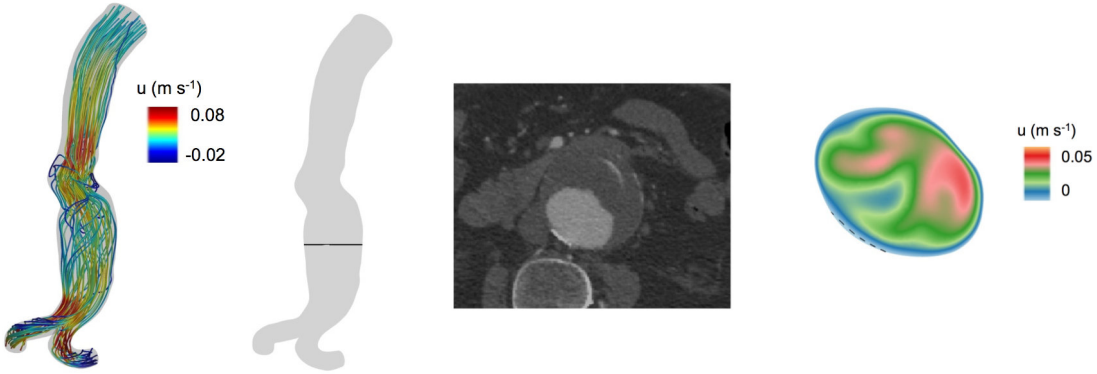

Figure 9: Case 13. Maximum diameter 6.9 cm. Maximum ILT thickness 2.8 cm. ILT located along anterior wall. No impingement.

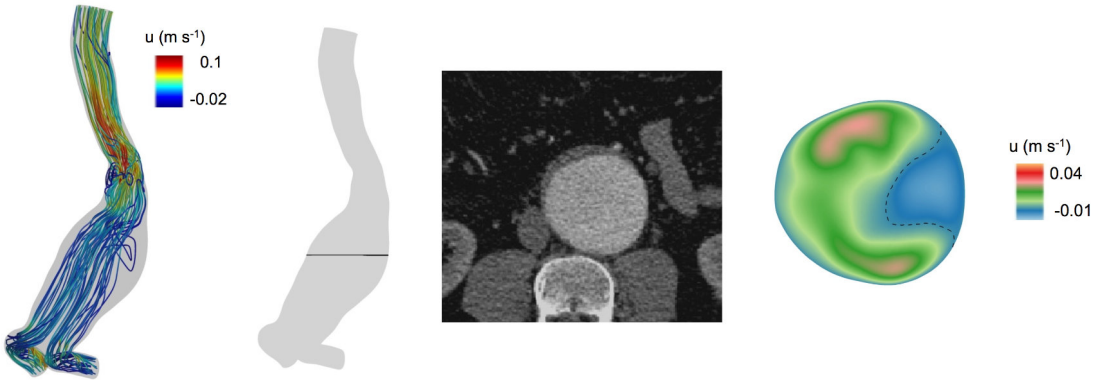

Figure 10: Case 14. Maximum diameter 6.9 cm. Maximum ILT thickness 2.8 cm. ILT located along anterior wall. No impingement.

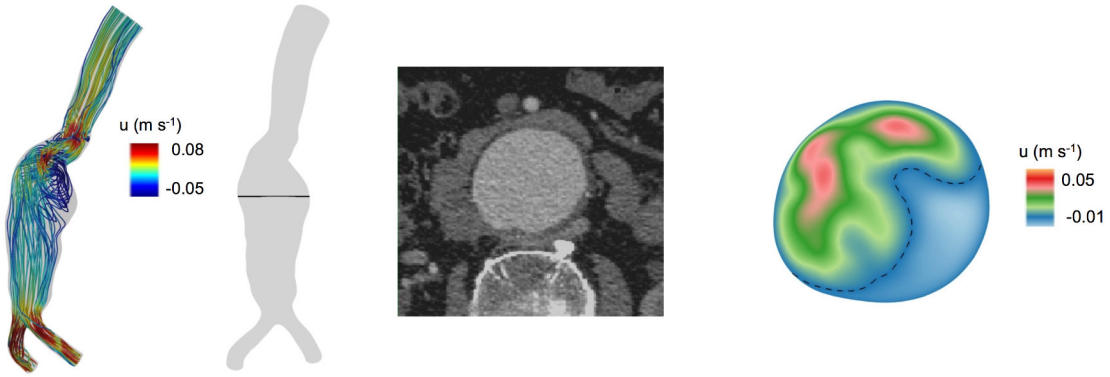

Figure 11: Case 15. Maximum diameter 6.9 cm. Maximum ILT thickness 2.8 cm. ILT located along anterior wall. No impingement.

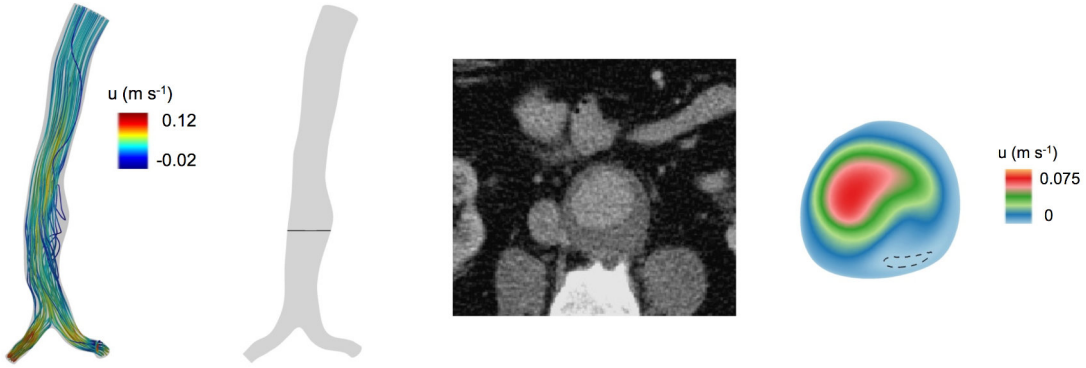

Figure 12: Case 16. Maximum diameter 5.5 cm. Maximum ILT thickness 1 cm. ILT located along posterior wall. No impingement.

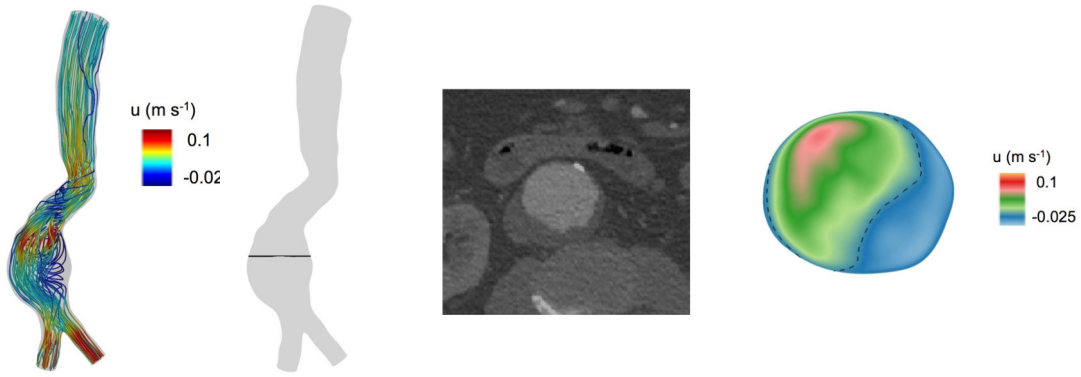

Figure 13: Case 17. Maximum diameter 5 cm. Maximum ILT thickness 1 cm. ILT located along posterior wall. Impingement occured along anterior wall.

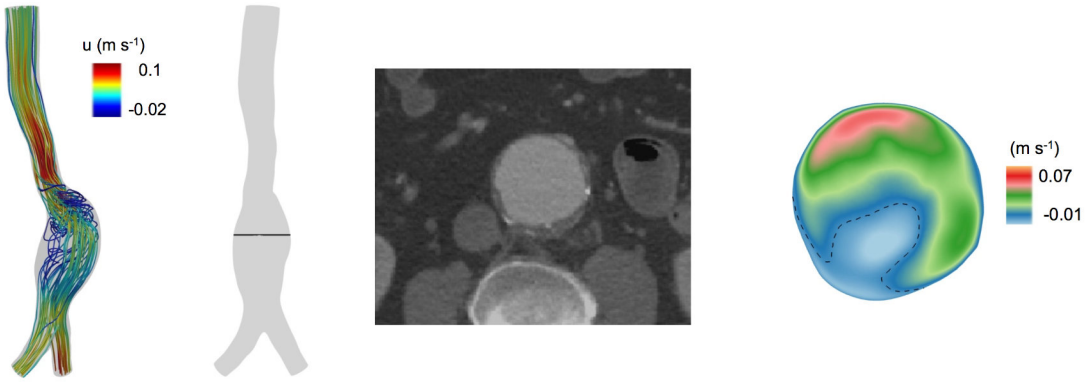

Figure 14: Case 18. Maximum diameter 5.5 cm. Maximum ILT thickness 2.4 cm. ILT located along posterior-left-right wall. No impingement.

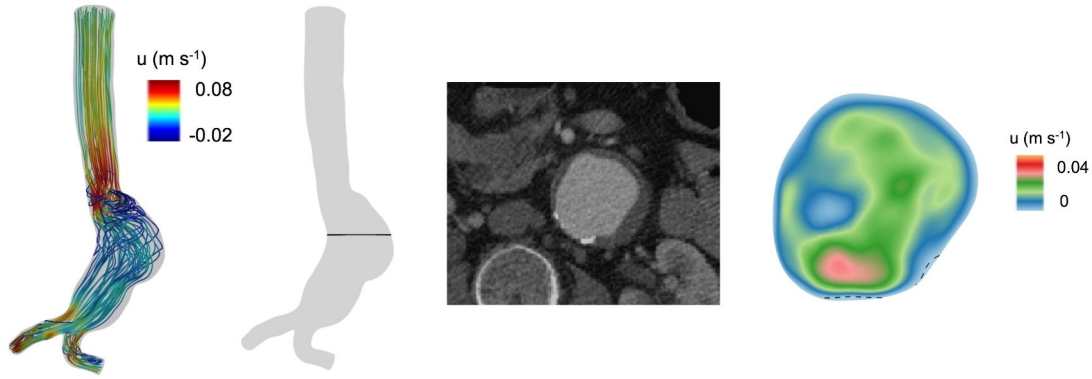

Figure 15: Case 19. Maximum diameter 5.9 cm. Maximum ILT thickness 0.4 cm. Circumferential ILT. No impingement.

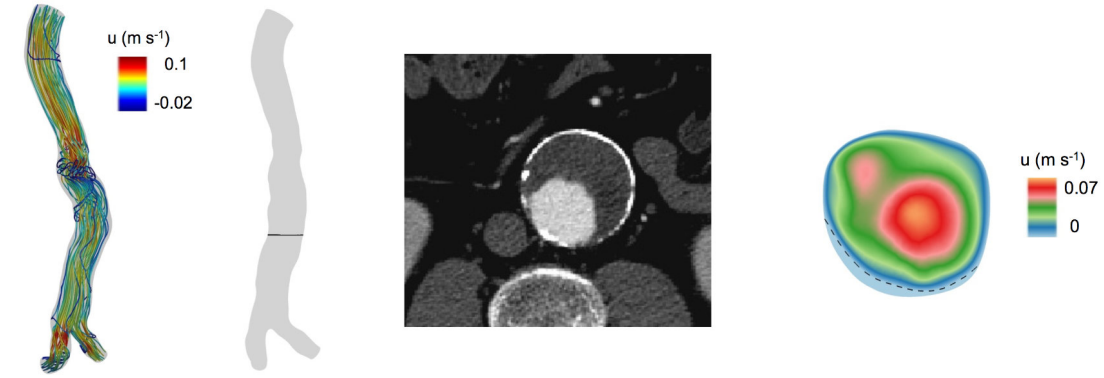

Figure 16: Case 20. Maximum diameter 5.5 cm. Maximum ILT thickness 2.4 cm. ILT located along anterior wall. No impingement.

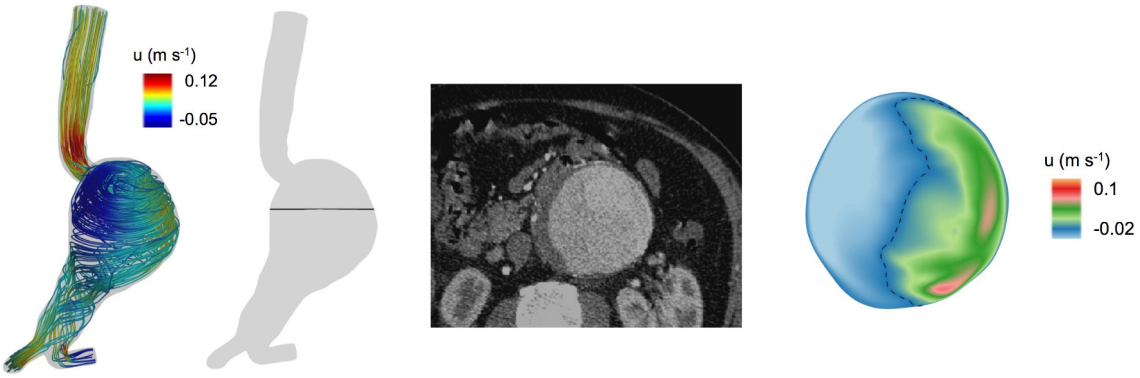

Figure 17: Case 21. Maximum diameter 9.2 cm. Maximum ILT thickness 0.8 cm. ILT located along posterior wall. Impingement occured along anterior wall.

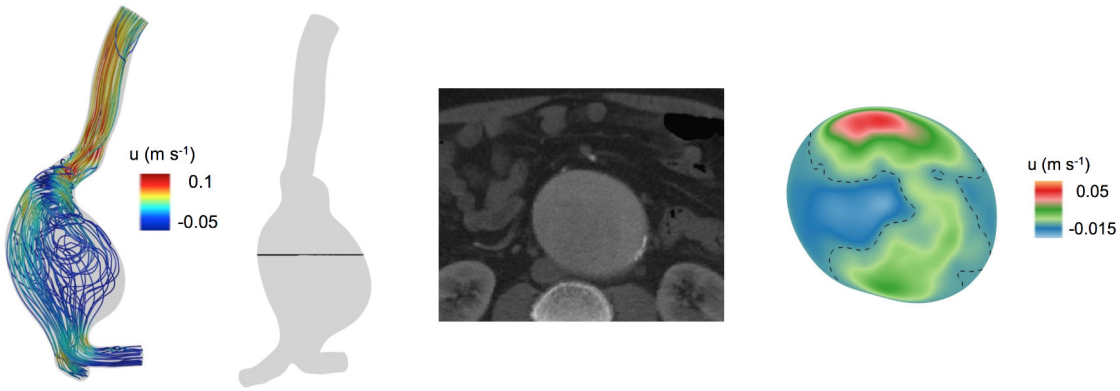

Figure 18: Case 22. Maximum diameter 8 cm. No ILT. No impingement.

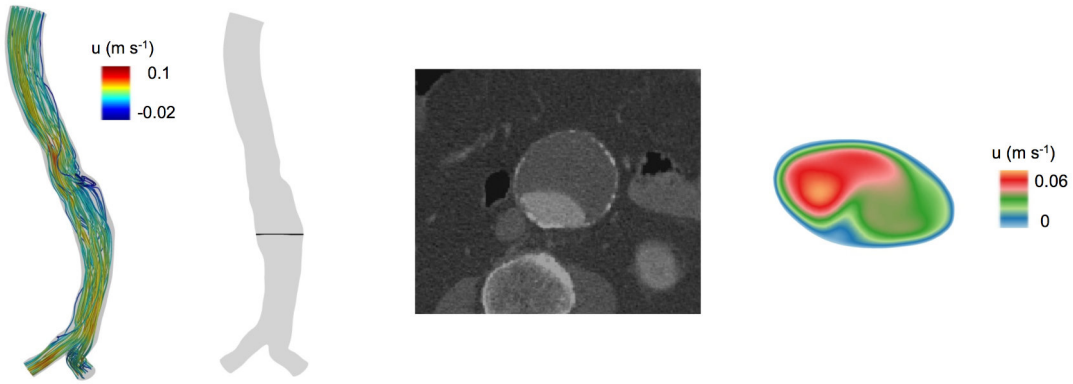

Figure 19: Case 23. Maximum diameter 5.5 cm. Maximum ILT thickness 2.8 cm. ILT located along anterior wall. No impingement.

Bibliography

[1] R. Adolph, D. A. Vorp, D. L. Steed, M. W. Webster, M. V. Kameneva, and S. C. Watkins. Cellular content and permeability of intraluminal thrombus in abdominal aortic aneurysm. *J. Vasc. Surg.*, 25:916–926, 1997.

[2] A. Arzani, A. M. Gambaruto, G. Chen, and S. C. Shadden. Lagrangian wall shear stress structures and near-wall transport in high-schmidt-number aneurysmal flows. *J. Fluid Mech.*, 790:158–172, 2016.

[3] A. Arzani, A. S. Les, R. L. Dalman, and S. C. Shadden. Effect of exercise on patient specific abdominal aortic aneurysm flow topology and mixing. *Int. J. Numer. Methods Biomed. Eng.*, 30(2):280–295, 2014.

[4] A. Arzani and S. C. Shadden. Characterization of the transport topology in patient-specific abdominal aortic aneurysm models. *Phys. Fluids*, 24(8), 2012.

[5] A. Arzani and S. C. Shadden. Characterizations and correlations of wall shear stress in aneurysmal flow. *J. Biomech. Eng.*, 138, 2016.

[6] A. Arzani, G.-Y. Suh, R. L. Dalman, and S. C. Shadden. A longitudinal comparison of hemodynamics and intraluminal thrombus deposition in abdominal aortic aneurysms.

Am. J. Physiol.Heart Circ. Physiol., 2014.

[7] S. Bagheri, P. Schlatter, P. J. Schmid, and D. S. Henningson. Global stability of a jet in crossflow. *J. Fluid Mech.*, 624:33–44, 2009.

[8] E. Barocio, B. C. Pal, N. F. Thornhill, and A. R. Messina. A dynamic mode decomposition framework for global power system oscillation analysis. *IEEE transactions on power systems a publication of the Power Engineering Society*, 30:2902–2912, 2015.

[9] M. Barri, G. K. El Khoury, H. I. Andersson, and B. Pettersen. Dns of backward-facing step flow with fully turbulent inflow. *Int. J. Numer. Meth. Fluids*, 64:777–792, 2009.

[10] C. Basciano, C. Kleinstreuer, S. Hyun, and E. A. Finol. A relation between near-wall particle-hemodynamics and onset of thrombus formation in abdominal aortic aneurysms. *Ann. Biomed. Eng.*, 39:2010–2026, 2010.

[11] E. Berger, M. Sastuba, D. Vogt, B. Jung, and H. B. Amor. Estimation of perturbations in robotic behavior using dynamic mode decomposition. *Advanced Robotics*, 29:331–343, 2015.

[12] K. Bhaganagar. Direct numerical simulation of unsteady flow in channel with rough walls. *Phys. Fluids*, 20, 2008.

[13] J. Biasetti, T. C. Gasser, M. Auer, U. Hedin, and F. Labruto. Hemodynamics of the normal aorta compared to fusiform and saccular abdominal aortic aneurysms with emphasis on a potential thrombus formation mechanism. *Ann. Biomed. Eng.*, 38:380–390, 2010.

[14] M. Bonert, R. L. Leask, J. Butany, C. R. Ethier, J. G. Myers, K. W. Johnston, and et al. The relationship between wall shear stress distributions and intimal thickening in the human abdominal aorta. *Biomed. Eng.*, 2:18, 2003.

[15] A. J. Boyd, D. C. Kuhn, R. J. Lozowy, and G. P. Kulbisky. Low wall shear stress predominates at sites of abdominal aortic aneurysm rupture. *J. Vasc. Surg.*, 63(6):1613–1619, 2016.

[16] B. Burke, A. Giannoudis, K. Corke, D. Gill, M. Wells, L. Ziegler-Heitbrock, and et al. Hypoxia-induced gene expression in human macrophages: Implications for ischemic tissues and hypoxia-regulated gene therapy. *Am. J. Pathol.*, 163:1233–1243, 2003.

[17] B. Cantwell and D. Coles. An experimental study of entrainment and transport in the turbulent near wake of a circular cylinder. *J. Fluid Mech.*, 136:321–374, 1983.

[18] C. G. Caro, J. M. Fitz-Gerald, and R. C. Schroter. Atheroma and arterial wall shear observation, correlation and proposal of a shear dependent mass transfer mechanism for atherogenesis. *Proc. R. Soc. London. Ser. B Biol. Sci.*, 177:109–133, 1971.

[19] E. L. Chaikof, D. C. Brewster, R. L. Dalman, M. S. Makaroun, K. A. Illig, G. A. Sicard, and et al. The care of patients with an abdominal aortic aneurysm: the society for vascular surgery practice guidelines. *J. Vasc. Surg.*, 50:32–49, 2009.

[20] I. Chatziprodromou, A. Tricoli, D. Poulikakos, and Y. Ventikos. Haemodynamics and wall remodelling of a growing cerebral aneurysm: a computational model. *J. Biomech.*, 40:412–426, 2007.

[21] K. K. Chen, J. H. Tu, and C. W. Rowley. Variants of dynamic mode decomposition: Boundary condition, koopman, and fourier analyses. *J. Nonlinear Sci.*, 22:887–915, 2012.

[22] C. Chnafa, S. Mendez, and F. Nicoud. Image-based simulations show important flow fluctuations in a normal left ventricle: What could be the implications? *Ann. Biomed. Eng.*, 44:3346–3358, 2016.

[23] I. Choutapalli, A. Krothapalli, and J. H. Arakeri. An experimental study of an axisymmetric turbulent pulsed air jet. *J. Fluid Mech.*, 631:23–63, 2009.

[24] R. L. Dalman, M. M. Tedesco, J. Myrers, and C. A. Taylor. Aaa disease: Mechanism, stratification, and treatment. *Ann. N.Y. Acad. Sci.*, pages 92–109, 2006.

[25] S. M. Damian. *An Extended Mixture Model for the Simultaneous Treatment of Short and Long Scale Interfaces*. PhD thesis, Universidad Nacional Del Litoral, 2006.

[26] P. F. Davies, T. Mudel, and K. A. Barbee. A mechanism for heterogeneous endothelial responses to flow in vivo and in vitro. *J. Biomech.*, 28:1553–1560, 1995.

[27] E. de Villiers. *The Potential of Large Eddy Simulation for the Modeling of Wall Bounded Flows*. PhD thesis, Imperial College of Science, Technology and Medicine, 2006.

[28] P. DiAchille, G. Tellides, C. A. Figueroa, and J. D. Humphrey. A haemodynamic predictor of intraluminal thrombus formation in abdominal aortic aneurysms. *Proc. R. Soc. A*, 470, 2014.

[29] E. S. DiMartino, G. Guadagni, A. Fumero, G. Ballerini, R. Spirito, P. Biglioli, and et al. Fluid-structure interaction within realistic three dimensional models of the aneurysmatic aorta as a guidance to assess the risk of rupture of the aneurysm. *Med. Eng. Phys.*, 23:647–655, 2001.

[30] E. S. DiMartino, S. Mantero, F. Inzoli, G. Melissano, D. Astore, R. Chiesa, and R. Fumero. Biomechanics of abdominal aortic aneurysm in the presence of endoluminal thrombus: experimental characterisation and structural static computational analysis. *Eur. J. Vasc. Endovasc. Surg.*, 15:290–299, 2016.

[31] J. M. Dolan, J. Kolega, and H. Meng. High wall shear stress and spatial gradients in vascular pathology: A review. *Ann. Biomed. Eng.*, 41:1411–1427, 2012.

[32] B. J. Doyle, A. Callanan, P. E. Burke, P. A. Grace, M. T. Walsh, D. A. Vorp, and et al. Vessel asymmetry as an additional diagnostic tool in the assessment of abdominal aortic aneurysms. *J. Vasc. Surg.*, pages 443–54, 2009.

[33] B. J. Doyle, T. M. McGloughlin, E. G. Kavanagh, and P. R. Hoskins. From detection to rupture: a serial computational fluid dynamics case study of a rapidly expanding, patient-specific, ruptured abdominal aortic aneurysm. *In: Computational Biomechanics for Medicine*, pages 53–68, 2014.

[34] D. Feldmann and C. Wagner. Direct numerical simulation of fully developed turbulent and oscillatory pipe flows at re=1440. *Journal of Turbulence*, 32:1–28, 2012.

[35] M. F. Fillinger, S. P. Marra, M. L. Raghavan, and F. E. Kennedy. Prediction of rupture risk in abdominal aortic aneurysm during observation: wall stress versus diameter. *J. Vasc. Surg.*, 37:724–732, 2003.

[36] M. F. Fillinger, M. L. Raghavan, S. P. Marra, J. L. Cronenwett, and F. E. Kennedy. In vivo analysis of mechanical wall stress and abdominal aortic aneurysm rupture risk. *J. Vasc. Surg.*, 36:589–597, 2002.

[37] D. L. Fry. Certain chemorheologic considerations regarding the blood vascular interface with particular reference to coronary artery disease. *Circulation*, 40:38–57, 1969.

[38] W. K. George. *Lectures in Turbulence for the 21st Century*. 2013.

[39] S. Glagov, C. Zarins, D. P. Giddens, and D. N. Ku. Hemodynamics and atherosclerosis. insights and perspectives gained from studies of human arteries. *Arch. Pathol. Lab. Med.*, 112:1018–1031, 1988.

[40] J. F. Hale, D. A. McDonald, and J. R. Womersley. Velocity profiles of oscillating arterial flow, with some calculations of viscous drag and the reynolds number. *J. Physiol.*, 128:629–640, 1955.

[41] S. S. Hans, O. Jareunpoon, M. Balasubramaniam, and G. B. Zelenock. Size and location of thrombus in intact and ruptured abdominal aortic aneurysms. *J. Vasc. Surg.*, 41:584–588, 2005.

[42] S. He and M. Seddighi. Turbulence in transient channel flow. *J. Fluid Mech.*, 715:60–102, 2013.

[43] X. He and D. N. Ku. Pulsatile flow in the human left coronary artery bifurcation: average conditions. *J. Biomech. Eng.*, 118:74–82, 1996.

[44] J. C. R. Hunt, A. Wray, and P. Moin. Eddies, stream, and convergence zones in turbulent flows. *Center for Turbulent Research*, CTR-S88, 1988.

[45] A. K. M. F. Hussain and W. C. Reynolds. The mechanics of an organized wave in turbulent shear flow. *J. Fluid Mech.*, 41:241–258, 1970.

[46] F. P. Incropera and D. P. DeWitt. *Fundamental of heat and mass transfer*. Wiley, 2002.

[47] R. I. Issa. Solution of the implicitly discretized fluid flow equation by operator-splitting. *J. Comput. Phys.*, 62(1):40–65, 1985.

[48] P. S. Iyer and K. Mahesh. A numerical study of shear layer characteristics of low-speed transverse jets. *J. Fluid Mech.*, 790:275–307, 2016.

[49] H. Jasak. *Error analysis and estimation for the finite volume method with applications to fluid flows*. PhD thesis, Imperial College of Science, Technology and Medicine, 1996.

[50] J. Jeong and F. Hussain. On the identification of a vortex. *J. Fluid Mech.*, 285:69–94, 1995.

[51] M. R. Jovanovi, P. J. Schmid, and J. W. Nichols. Sparsity-promoting dynamic mode decomposition. *Phys. Fluids*, 26, 2014.

[52] J. E. Moore Jr., E. Burki, A. Suciu, S. Zhao, M. Burnier, H. R. Brunner, and et al. A device for subjecting vascular endothelial cells to both fluid shear stress and circumferential cyclic stretch. *Ann. Biomed. Eng.*, 22:416–422, 1994.

[53] M. J. Kazi, T. P. Religa, J. Roy, P. Eriksson, U. Hedin, and J. Swedenborg. Influence of intraluminal thrombus on structural and cellular composition of abdominal aortic aneurysm wall. *J. Vasc. Surg.*, 38:1283–1292, 2003.

[54] J. Kim, P. Moin, and R. Moser. Turbulence statistics in fully developed channel at low reynolds number. *J. Fluid Mech.*, 177:133–166, 1987.

[55] C. Kleinstreuer and Z. Li. Analysis and computer program for rupture risk prediction of abdominal aortic aneurysms. *Biomed Eng*, 5:19, 2006.

[56] D. Koole, H. J. A. Zandvoort, A. Schoneveld, A. Vink, J. A. Vos, L. L. van den Hoogen, J.-P. P. M. de Vries G. Pasterkamp andF. L. Moll, and J. A. van Herwaarden. Intraluminal abdominal aortic aneurysm thrombus is associated with disruption of wall integrity. *J. Vasc. Surg.*, 57:77–83, 2013.

[57] D. N. Ku. Flow patterns in the abdominal aorta. *J. Vasc. Surg.*, 9:309–316, 1989.

[58] D. N. Ku. Blood flow in arteries. *Annu. Rev. Fluid Mech.*, 29(1):399–434, 1997.

[59] D. N. Ku, D. P. Giddens, C. K. Zarins, and S. Glagov. Pulsatile flow and atherosclerosis in the human carotid bifurcation. positive correlation between plaque location and low oscillating shear stress. *Arterioscler. Thromb. Vasc. Biol.*, 5:293–302, 1985.

[60] B. L. Langille and F. ODonnell. Reductions in arterial diameter produced by chronic decreases in blood flow are endothelium-dependent. *Science*, 231:405–407, 1986.

[61] J. Lantza, R. Gardhagen, and M. Karlsson. The biomechanics of arterial aneurysms. *Medical Engineering and Physics*, 34:1139–1148, 2012.

[62] J. C. Lasheras. The biomechanics of arterial aneurysms. *Annu. Rev. Fluid Mech.*, 39:293–319, 2007.

[63] J. C. Lasheras. Haemodynamic stresses and the onset and progression of vascular diseases. *J. Fluid Mech.*, 664:1–4, 2010.

[64] F. A. Lederle, G. R. Johnson, S. E. Wilson, D. J. Ballard, W. D. Jordan Jr., J. Blebea, F. N. Littooy, J. A. Freischlag, D. Bandyk, J. H. Rapp, A. A. Salam, and I. Veterans Affairs Cooperative Study. Rupture rate of large abdominal aortic aneurysms in patients refusing or unfit for elective repair. *JAMA*, 287:2968–2972, 2002.

[65] M. Lee and R. D. Moser. Haemodynamic stresses and the onset and progression of vascular diseases. *J. Fluid Mech.*, 774:395–415, 2015.

[66] M. C. Lee and R. C. Haut. Strain rate effects on tensile failure properties of the common carotid artery and jugular veins of ferrets. *J. Biomech.*, 25:925–927, 1992.

[67] A. S. Les, S. C. Shadden, C. A. Figueroa, J. M. Park, M. M. Tedesco, R. J. Herfkens, R. L. Dalman, and C. A. Taylor. Quantification of hemodynamics in abdominal aortic aneurysms during rest and exercise using magnetic resonance imaging and computational fluid dynamics. *Ann. Biomed. Eng.*, 38:1288–1313, 2010.

[68] A. S. Les, J. J. Yeung, G. M. Schultz, R. J. Herfkens, R. L. Dalman, and C. A. Taylor. Supraceliac and infrarenal aortic flow in patients with abdominal aortic aneurysms: mean flows, waveforms, and allometric scaling relationships. *Card. Eng. Tech.*, 1:39–51, 2010.

[69] C. Levene, R. Kapoor, and G. Heale. The effect of hypoxia on the synthesis of collagen and glycosaminoglycans by cultured pig aortic endothelium. *Atherosclerosis*, 44:327–337, 1982.

[70] C. Loudon and A. Tordesillas. The use of the dimensionless womersley number to characterize the unsteady nature of internal flow. *J. Theor. Biol.*, 191:63–78, 1998.

[71] R. J. Lozowy, D. C. S. Kuhn, and A. J. Boyd. Numerical simulation of abdominal aortic aneurysm rupture. *Canadian Society of Mechanical Engineering Congress*, 2012.

[72] R. J. Lozowy, D. C. S. Kuhn, and A. J. Boyd. Influence of abdominal aortic aneurysm shape on hemodynamics. *European Research Community on Flow, Turbulence and Combustion*, 2014.

[73] R. J. Lozowy, D. C. S. Kuhn, A. A. Ducas, and A. J. Boyd. The relationship between pulsatile flow impingement and intraluminal thrombus deposition in abdominal aortic aneurysms. *Card. Eng. Tech.*, 8:57–69, 2017.

[74] V. L. Marrero, J. A. Tichy, and O. S. K. E. Jansen. Spectral dynamic of pulsating turbulent pipe flow. *Computers and Fluids*, 37, 2008.

[75] V. L. Marrero, J. A. Tichy, and O. S. K. E. Jansen. Pulsating pipe flow with large-amplitude oscillations in the very high frequency regime. part1. time-averaged analysis. *J. Fluid Mech.*, 700, 2012.

[76] V. L. Marrero, J. A. Tichy, and O. S. K. E. Jansen. Numerical study of purely viscous non-newtonian flow in an abdominal aortic aneurysm. *J. Biomech. Eng.*, 136, 2014.

[77] D. A. McDonald. The relation of pulsatile pressure to flow in arteries. *J. Physiol.*, 27:533–552, 1955.

[78] H. Meng, V. M. Tutino, J. Xiang, and A. Siddiqui. High wss or low wss? complex interactions of hemodynamics with intracranial aneurysm initiation, growth, and rupture: toward a unifying hypothesis. *AJNR Am. J. Neuroradiol.*, 35:1254–1262, 2014.

[79] E. Metaxa, N. Kontopodis, K. Tzirakis, C. V. Ioannou, and Y. Papaharilaou. Effect of intraluminal thrombus asymmetrical deposition on abdominal aortic aneurysm growth rate. *J. Endovasc. Ther.*, 22(3):406–412, 2013.

[80] I. Mezic. Spectral properties of dynamical systems, model reduction and decompositions. *Nonlinear Dynamics*, 41:309–325, 2005.

[81] D. Mohan and J. W. Melvin. Failure properties of passive human aortic tissue.2- biaxial tension tests. *J. Vasc. Surg.*, 16:31–44, 1983.

[82] P. Moin and K. Mahesh. Direct numerical simuation: A tool in turbulence research. *Annual Review of Fluid Mechanics*, 30:539–578, 1998.

[83] E. Motheau, F. Nicoud, and T. Poinsot. Mixed acousticentropy combustion instabilities in gas turbines. *J. Fluid Mech.*, 749:542–576, 2014.

[84] W. R. Mower, W. R. W. J. Quinones, and S. S. Gambhir. Effect of intraluminal thrombus on abdominal aortic aneurysm wall stress. *J. Vasc. Surg.*, 26:602–608, 1997.

[85] M. J. O'Rourke, J. P. McCullough, and S. Kelly. An investigation of the relationship between hemodynamics and thrombus deposition within patient-specific models of abdominal aortic aneurysm. *Proc. Inst. Mech. Eng.*, 226:548–564, 2012.

[86] P. K. Papadopoulos and A. P. Vouros. Pulsating turbulent pipe flow in the current dominated regime at high and very-high frequencies. *International Journal of Heat and Fluid Flow*, 58:54–67, 2016.

[87] D. J. Parkin, M. C. Thompson, and J. Sheridan. Highly resolved pulsatile flows through prosthetic heart valves using the entropic lattice-boltzmann method. *J. Fluid Mech.*, 739:94–123, 2014.

[88] A. Parr, M. McCann, B. Bradshaw, A. Shahzad, P. Buttner, and J. Golledge. Thrombus volume is associated with cardiovascular events and aneurysm growth in patients who have abdominal aortic aneurysms. *J. Vasc. Surg.*, 53:28–35, 2011.

[89] M. I. Patel, D. T. Hardman, C. M. Fisher, and M. Appleberg. Current views on the pathogenesis of abdominal aortic aneurysms. *J. Am. Coll. Surg.*, 181:371–382, 1995.

[90] E. M. Pedersen, H.-W. Sung, and A. P. Yoganathan. Influence of abdominal aortic curvature and resting vesus exercise conditions on velocity fields in the normal abdominal aortic bifurcation. *J. Biomech. Eng.*, 116:347–353, 1994.

[91] V. Peiffer, S. J. Sherwin, and P. D. Weinberg. Computation in the rabbit aorta of a new metricthe transverse wall shear stressto quantify the multidirectional character of disturbed blood flow. *J. Biomech.*, 46:2651–2658, 2013.

[92] V. Peiffer, S. J. Sherwin, and P. D. Weinberg. Does low and oscillatory wall shear stress correlate spatially with early atherosclerosis? a systematic review. *Cardiovasc. Res.*, 99:242–250, 2013.

[93] K. Pietila and O. Jaakkola. Effect of hypoxia on the synthesis of glycos- aminoglycans and collagen by rabbit aortic smooth muscle cells in culture. *Atherosclerosis*, 50:183–190, 1984.

[94] G. Pillari, J.B. Chang, J. Zito, J.R. Cohen, K. Gersten, and A. Rizzo. Computed tomography of abdominal aortic aneurysm. an in vivo pathological report with a note on dynamic predictors. *Arch. Surg.*, 123:727–732, 1988.

[95] C. Poelma, P. N. Watton, and Y. Ventikos. Transitional flow in aneurysms and the computation of haemodynamic parameters. *J. R. Soc. Interface*, 12, 2015.

[96] S. B. Pope. *Turbulent Flows*. Cambridge University Press, 2000.

[97] P. P. Purslow. Positional variations in fracture toughness, stiffness and strength of descending thoracic pig aorta. *J. Biomech.*, 16:947–953, 1983.

[98] V. L. Rayz, L. Boussel, M. T. Lawton, G. Acevedo-Bolton, L. Ge, W. L. Young, R. T. Higashida, and D. Saloner. Numerical modeling of the flow in intracranial aneurysms: prediction of regions prone to thrombus formation. *Ann. Biomed. Eng.*, 36:1793–1804, 2008.

[99] W. W. Reed, J. W. Hallett Jr., M. A. Damiano, and D. J. Ballard. Learning from the last ultrasound. a population-based study of patients with abdominal aortic aneurysm. *Arch. Intern. Med.*, 157:2064–2068, 1997.

[100] B. B. Belson J. H. Tu C. W. Rowley. Algorithm 945: modred a parallelized model reduction library. *ACM Trans Math Softw.*, 138:1–23, 2014.

[101] C. W. Rowley, I. Mezic, S. Bagheri, P. Schlatter, and D. S. Henningson. Spectral analysis of nonlinear flows. *J. Fluid Mech.*, 641:115–127, 2009.

[102] S. Sarmast, R. Dadfar, R. F. Mikkelsen, P. Schlatter, S. Ivanell, J. N. Sorensen, and D. S. Henningson. Mutual inductance instability of the tip vortices behind a wind turbine. *J. Fluid Mech.*, 755:705–731, 2014.

[103] J. Satta, E. Laara, and T. Juvonen. Intraluminal thrombus predicts rupture of an abdominal aortic aneurysm. *J. Vasc. Surg.*, 23:737–739, 1996.

[104] P. Scandura, C. Faraci, and E. Foti. A numerical investigation of acceleration-skewed oscillatory flows. *J. Fluid Mech.*, 808:576–613, 2016.

[105] P. J. Schmid. Dynamic mode decomposition of numerical and experimental data. *J. Fluid Mech.*, 656:5–28, 2010.

[106] A. Scotti and U. Piomelli. Numerical simulation of pulsating turbulent channel flow. *Phys Fluids*, 13, 2001.

[107] M. Seddighi, S. He, A. E. Vardy, and P. Orlandi. Direct numerical simulation of an accelerating channel flow. *Flow Turbulence Combust.*, 92:473–502, 2013.

[108] L. Sirovich. Turbulence and the dynamics of coherent structures. part i. coherent structures. *Q. Appl. Math.*, 45:561–571, 1987.

[109] L. Speelman, G. W. H. Schurink, E. M. H. Bosboom, J. Buth, M. Breeuwer, and F. N. van de Vosse. The mechanical role of thrombus on the growth rate of an abdominal aortic aneurysm. *J. Vasc. Surg.*, 51:19–26, 2010.

[110] C. Stamatopoulos, D. S. Mathioulakis, Y. Papaharilaou, and A. Katsamouris. Experimental unsteady flow study in a patient-specific abdominal aortic aneurysm model. *Exp. Fluids*, 50:1695–1709, 2011.

[111] J. Stenbaek, B. Kalin, and J. Swedenborg. Growth of thrombus may be a better predictor of rupture than diameter in patients with abdominal aortic aneurysms. *Eur. J. Vasc. Endovasc. Surg.*, 20:466–499, 2000.

[112] G. Y. Suh, A. S. Les, A. S. Tenforde, S. C. Shadden, R. L. Spilker, J. J. Yeung, C. P. Cheng, R. J. Herfkens, R. L. Dalman, and C. A. Taylor. Quantification of particle residence time in abdominal aortic aneurysms using magnetic resonance imaging and computational fluid dynamics. *Ann. Biomed. Eng.*, 39:864–883, 2010.

[113] G. Y. Suh, A. S. Tenforde, S. C. Shadden, R. L. Spilker, C. P. Cheng, R. J. Herfkens, R. L. Dalman, and C. A. Taylor. Hemodynamic changes in abdominal aortic aneurysms with increasing exercise intensity using mr exercise imaging and image-based computational fluid dynamics. *Ann. Biomed. Eng.*, 39:2186–2202, 2011.

[114] L. R. J. Sundstrom, B. G. Mulu, and M. J. Cervantes. Wall friction and velocity measurements in a double- frequency pulsating turbulent flow. *J. Fluid Mech.*, 788:521–548, 2016.

[115] B. T. Tang, C. P. Cheng, M. T. Draney, N. M. Wilson, P. S. Tsao, R. J. Herfkens, and C. A. Taylor. Abdominal aortic hemodynamics in young healthy adults at rest and during lower limb exercise: quantification using image-based computer modeling. *Am. J. Physiol. Heart Circ. Physiol.*, 291:H668–H676, 2006.

[116] J. M. Tarbell, Z. Shi, J. Dunn, and H. Jo. Fluid mechanics, arterial disease, and gene expression. *Annu. Rev. Fluid Mech.*, 46:591–614, 2014.

[117] S. F. Tardu, G. Binder, and R. F. Blackwelder. Turbulent channel flow with large-amplitude velocity oscillations. *J. Fluid Mech.*, 267:109–151, 1994.

[118] C. A. Taylor, C. P. Cheng, L. A. Espinosa, B. T. Tang, D. Parker, and R. J. Herfkens. In vivo quantification of blood flow and wall shear stress in the human abdominal aorta during lower limb exercise. *Ann. Biomed. Eng.*, 30:402–408, 2002.

[119] C. A. Taylor, T. J. R. Hughes, and C. K. Zarins. Finite element modeling of three-dimensional pulsatile flow in the abdominal aorta: relevance to atherosclerosis. *Ann. Biomed. Eng.*, 26:975–987, 1998.

[120] C. A. Taylor, T. J. R. Hughes, and C. K. Zarins. Effect of exercise on hemodynamic conditions in the abdominal aorta. *J. Vasc. Surg.*, 29:1077–1089, 1999.

[121] M. J. Thubrikar, F. Robicsek, M. Labrosse, V. Chervenkoff, and B. L. Fowler. Effect of thrombus on abdominal aortic aneurysm wall dilation and stress. *J. Cardiovasc. Surg.*, 44:67–77, 2003.

[122] J. H. Tu. *Dynamic Mode Decomposition: Theory and Applications*. PhD thesis, Princeton University, 2013.

[123] J. H. Tu and C. W. Rowley. An improved algorithm for balanced pod through an analytic treatment of impulse response tails. *Journal of Computational Physics*, 16:5317–5333, 2012.

[124] S. Uchida. The pulsating viscous flow superposed on the steady laminar motion of incompressible fluid in a circular pipe. *Z. Angew. Math. Phys.*, 7:403–422, 1955.

[125] K. Valen-Sendstad, K. Mardal, M. Mortensen, B. A. P. Reif, and H. P. Langtangen. Direct numerical simulation of transitional flow in a patient-specific intracranial aneurysm. *J. Biomech.*, 44:2826–2832, 2011.

[126] N. Varble, J. Xiang, N. Lin, E. Levy, and H. Meng. Flow instability detected by high-resolution computational fluid dynamics in fifty-six middle cerebral artery aneurysms. *J. Biomech.*, 138(6), 2016.

[127] S. S. Varghese, S. H. Frankel, and P. F. Fischer. Direct numerical simulation of stenotic flows. part 2. pulsatile flow. *J. Fluid Mech.*, 528:281–318, 2007.

[128] J. F. Vollmar, E. Paes, P. Pauschinger, E. Henze, and A. Friesch. Aortic aneurysms as late sequelae of above-knee amputation. *Ann. Biomed. Eng.*, 2:834–835, 1989.

[129] D. A. Vorp, W. J. Federspiel, and M. W. Webster. Does laminated intraluminal thrombus within abdominal aortic aneurysm cause anoxia of the aortic wall? *J. Vasc. Surg.*, 23:540–541, 1996.

[130] D. A. Vorp, P. C. Lee, D. H. Wang, M. S. Makaroun, E. M. Nemoto, S. Ogawa, and M. W. Webster. Association of intraluminal thrombus in abdominal aortic aneurysm with local hypoxia and wall weakening. *J. Vasc. Surg.*, 34:291–299, 2001.

[131] D. A. Vorp, D. H. Wang, M. W. Webster, and W. J. Federspiel. Effect of intraluminal thrombus thickness and bulge diameter on the oxygen diffusion in abdominal aortic aneurysm. *J. Biomech. Eng.*, 120:579–583, 1998.

[132] A. W. Vreman and J. G. M. Kuerten. Comparison of direct numerical simulation databases of turbulent channel flow at $re = 180$. *Phys Fluids.*, 26:015102, 2014.

[133] D. H. Wang, M. S. Makaroun, M. W. Webster, and D. A. Vorp. Effect of intraluminal thrombus on wall stress in patient-specific models of abdominal aortic aneurysm. *J. Vasc. Surg.*, 36:598–604, 2002.

[134] H. G. Weller, G. Tabor, H. Jasak, and C. Fureby. A tensorial approach to computational continum mechanics using object-oriented techniques. *Comput. Phys.*, 620(12):620–631, 1998.

[135] C. Weng, S. Boij, and A. R. Hanifi. Numerical and theoretical investigation of pulsatile turbulent channel flows. *J. Fluid Mech.*, 792:98–133, 2016.

[136] K. A. Wilson, A. J. Lee, A. J. Lee, P. R. Hoskins, F. G. R. Fowkes, C. V. Ruckley, and et al. The relationship between aortic wall distensibility and rupture of infrarenal abdominal aortic aneurysm. *J. Vasc. Surg.*, 37:112–117, 2003.

[137] Y.G. Wolf, W. S. Thomas, F. J. Brennan, W. G. Goff, M. J. Sise, and E. F. Bernstein. Computed tomography scanning findings associated with rapid expansion of abdominal aortic aneurysms. *J. Vasc. Surg.*, 20:529–535, 1994.

[138] J. R. Womersley. Method for the calculation of velocity, rate of flow and viscous drag in arteries when the pressure gradient is known. *J. Physiol.*, 127:553–563, 1955.

[139] N. B. Wood. *Development of hot film anemometry for measurement of blood velocity profiles in arteries*. PhD thesis, University of London, 1991.

[140] N. B. Wood. Aspects of fluid dynamics applied to the larger arteries. *J. Theor. Biol.*, 199:137–161, 1999.

[141] M. Xenos, N. Labropoulos, S. Rambhia, Y. Alemu, A. Tassiopoulos, N. Sakalihasan, and D. Bluestein. Progression of abdominal aortic aneurysm towards rupture: Refining clinical risk assessment using a fully coupled fluidstructure interaction method. *Ann. Biomed. Eng.*, 43:139–153, 2014.

[142] B. Min Yun, L. P. Dasi, C. K. Aidun, and A. P. Yoganathan. Highly resolved pulsatile flows through prosthetic heart valves using the entropic lattice-boltzmann method. *J. Fluid Mech.*, 754:122–160, 2014.

[143] B. A. Zambrano, H. Gharahi, C. Lim, F. A. Jaberi, J. Choi, W. Lee, and S. Baek. Association of intraluminal thrombus, hemodynamic forces, and abdominal aortic

aneurysm expansion using longitudinal ct images. *Ann. Biomed. Eng.*, 44:1502–1514, 2016.

[144] C. K. Zarins, D. P. Giddens, B. K. Bharadvaj, V. S. Sottiurai, R. F. Mabon, and S. Glagov. Carotid bifurcation atherosclerosis. quantitative correlation of plaque localization with flow velocity profiles and wall shear stress. *Circ. Res.*, 53:502–514, 1983.

[145] C. K. Zarins, M. A. Zatina, D. P. Giddens, and D. N. Ku. Shear stress regulation of artery lumen diameter in experimental atherogenesis. *J. Vasc. Surg.*, 5:413–420, 1987.

[146] T. Zhou, Y. Zhou, M. W. Yiu, and L. P. Chua. Three-dimensional vorticity in a turbulent cylinder wake. *Experiments in Fluids*, 35:459–471, 2003.